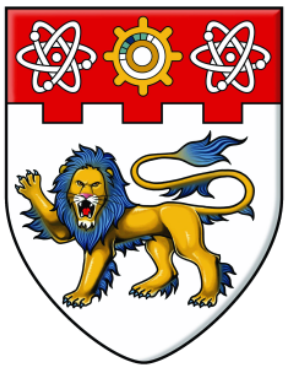

NANYANG TECHNOLOGICAL UNIVERSITY

NATURE-INSPIRED ENHANCED MICROSCALE HEAT TRANSFER IN MACRO GEOMETRY

GOH AIK LING

INTERDISCIPLINARY GRADUATE SCHOOL
ENERGY RESEARCH INSTITUTE @ NTU (ERI@N)

2016

NATURE-INSPIRED
ENHANCED MICROSCALE HEAT TRANSFER
IN MACRO GEOMETRY

GOH AIK LING

Interdisciplinary Graduate School
Energy Research Institute @ NTU (ERI@N)

A thesis submitted to the Nanyang Technological University
in partial fulfilment of the requirement for the degree of
Doctor of Philosophy

2016

Statement of Originality

I hereby certify that the work embodied in this thesis is the result of original research and has not been submitted for a higher degree to any other University or Institution.

2 August 2016

. . . . . .

Date

. . . . . .

Goh Aik Ling

Abstract

The microchannel heat sink is known to offer superior heat transfer capabilities. However, microchannel cooling is generally not applied on a large-scale basis, mainly due to the complex and non-economical nature of microfabrication processes. In 2013, Kong and Ooi developed a system for microscale heat transfer in macro geometry, and showed that heat transfer coefficients comparable to that of typical microchannels can be achieved, without involving complex and costly manufacturing methods.

The present Ph.D. research study aims to develop a novel nature-inspired configuration to enhance the microscale heat transfer in macro geometry using conventional machining processes, and formulate working correlations to evaluate the heat transfer and pressure drop for practical applications. The nature-inspired geometrical enhancement profiles are designed to be simple, such that their geometries are mathematically quantifiable in the correlations and can be machined conventionally.

In the present study, a 300 μm annular microchannel of 30 mm length with a constant heat transfer area of 1885 mm^2 is formed by securing a cylindrical non-heated insert of mean diameter 19.4 mm within a heated cylindrical pipe of internal diameter 20 mm. Introduced on the insert surface, the enhancement profiles are the Inverted Fish Scale (IFS) and Fish scale (FS) profiles, which are inspired by fish scales, and the Durian (D) profiles, which are inspired by a thorny tropical fruit. The enhancement profiles serve to increase the heat transfer coefficient by disturbing the velocity and thermal boundary layers, and promoting early laminar-to-turbulent flow transition.

Both physical measurements and numerical simulations have been carried out in this Ph.D. research study. A measurement system has been designed, fabricated, instrumented and commissioned for data collection. The system provides accurate pressure and heat transfer measurements with a mean discrepancy of 7.8% and 13.4%, respectively, as well as consistent pressure and heat transfer measurements within 0.57% and 0.39%, respectively. In addition, a conjugate heat transfer numerical model has been developed using a Computational Fluid Dynamics (CFD) code. The numerical model is validated through the comparison of its predictions with the measurements, which shows a mean discrepancy of 8.5% and 20.2%, respectively, for the pressure drop and heat transfer.

The investigations have been carried out for plain and enhanced annular microchannels with a fixed mean channel height (H) of 300 μm using liquid-phase water. About 600 steady-state measurements have been collected, using 22 microchannel profiles, up to 27 flow conditions ($350 \lesssim Re \lesssim 4{,}600$) for each profile, and 2 wall heat fluxes of 13.3 and 53.0 W/cm^2. The 22 profiles include 7 for each of the three nature-inspired enhanced microchannel series, and the Plain microchannel. The measurements for the Plain microchannel are used as the basis to determine the extent of heat transfer enhancement.

Within the nature-inspired enhanced IFS, FS and D microchannel series, the effects of two geometrical ratios are studied. They are the ratio of scale/thorn height (e) to mean channel height (H), and the ratio of scale/thorn pitch (P) to scale/thorn height (e). In the first study, four e/H ratios of 0.1, 0.3, 0.5 and 0.7 are employed, with a fixed P/e ratio of 10. In the second study, four P/e ratios of 5, 10, 15 and 20 are employed, with a fixed e/H ratio of 0.5. A larger e/H ratio corresponds to a narrower minimum gap through which the fluid flows, while a lower P/e ratio corresponds to a larger number of scale/thorn protrusions of the same height, for a fixed microchannel length. These two

ratios are formulated such that they mathematically quantify the geometrical enhancement profiles and could eventually be incorporated into the proposed working correlations.

The results show that enhanced microscale heat transfer effects have indeed been achieved in macro geometry, using conventional machining processes. The highest convective heat transfer coefficient achieved in the whole study is 52.8 $kW/m^2 \cdot K$, at 6.5 L/min ($Re \approx 4280$) using the IFS microchannel with a scale height (e) of 0.21 mm and scale pitch (P) of 2.1 mm. This means that this IFS microchannel profile is able to remove heat flux of up to 375 W/cm^2, for a temperature difference of 71 K. The highest pressure drop in the whole study is 3.3 bars, which can be easily overcome by a commercially available pump. In terms of the thermo-hydraulic performance, the D microchannel performs the best, with a thorn height (e) of 0.21 mm and thorn pitch (P) of 2.1 mm. Given a fixed heat transfer surface area and pumping power, this profile can improve the heat transfer capacity by 67% relative to the Plain microchannel, at Reynolds number of about 2,350.

Most importantly, working correlations have been proposed to evaluate the average Nusselt number and friction factor for the nature-inspired enhanced IFS, FS and D microchannels. The mathematical form of the new correlations follows that of existing classical correlations, but with an additional term, which is a function of e/H ratio and P/e ratio, added to account for the effect of the scale/thorn protrusions. The correlations are formulated based on about 600 steady-state measurements, as well as the underlying physics which governs the heat transfer and flow behaviours, within the scope of investigation.

The present Ph.D. work brings the research a significant step closer to the successful development of a compact microchannel heat exchanger with large heat duty at competitive costs.

Acknowledgements

The author expresses her sincere gratitude to her supervisors, Professor Ooi Kim Tiow and Professor Ulrich Stimming, for their guidance during the past four years. Professor Ooi not only inspired the author to pursue a Ph.D. degree and motivated her during difficult times, but also imparted much wisdom on life to her. Professor Stimming is always encouraging and supportive whenever the author approaches him for help. She also wishes to thank her mentor, Associate Professor Wong Teck Neng, for his helpful and valuable advice.

The author expresses her appreciation to Nanyang Technological University (NTU), Singapore, for the financial support during the past four years. This Ph.D. research is also funded by the National Research Foundation, Singapore, under its Campus for Research Excellence and Technological Enterprise (CREATE) programme.

The author is immensely grateful to the following people who have supported her in her research. Her seniors, Dr. Kong Kian Shing and Dr. Alison Subiantoro, were good role models and shared valuable knowledge with her. The students whose final year projects she mentored provided much assistance in the experimental and numerical sections. They are Mr. Lai Sze Ming, Mr. Aw Wee Earn, Mr. Edwin Ang Ching Jitt, Mr. Lim Teck Siang, Mr. Cheng Kai Xian, Mr. Tan Phei Chieh, Mr. Han Bo and Mr. Foo Yu Ping.

The author appreciates the technical support from the lab technicians, Mr. Roger Lee, Mr. Edward Yeo, Mr. Lawrence Ang and Mr. Kong Seng Ann, at the School of Mechanical and Aerospace Engineering (MAE), NTU. She also appreciates the administrative support from the school staff, including Ms. Jean Wee from MAE, Ms. Lily Lim from ERI@N, as well as Ms. Ellen Heng and Ms. Lena Tay from the Interdisciplinary Graduate School.

The author is thankful for the Ph.D. friends she has made during the past four years. Their friendship and camaraderie play an important role in brightening up her days during this Ph.D. journey. They include Youjin, Linyan, Lichun, Li Zhong, Liu Zhe, Pui Mun, Aung and many others. She is also thankful for her long-time friends, who remind her of the importance to have a good work-life balance. They include Suyi, Lay Wang, Xiao Hui, Song Hua, Hong Ern, Jean, Chin Siang and many others.

The author is thankful to Kai Liang for sharing a happy journey with her since they first met.

Most importantly, the author expresses her heartfelt appreciation to her parents, grandparents and Marilyn. She is thankful to have them by her side through the many ups and downs of life. She is also thankful to her extended family, including her uncles, aunts and cousins, for the close relationships.

Thanks to the support from everyone, the author successfully completed this Ph.D. research study.

Table of Contents

List of Figures

List of Tables

List of Appendix Figures

Nomenclature

Latin Symbol

A	Heat transfer surface area [m^2]
A_c	Cross-sectional area [m^2]
c_p	Specific heat [J/kg·K]
D	Diameter [m]
D_h	Hydraulic diameter [m]
E_f	Normalised friction factor (f/f_{Plain}) [-]
E_{Nu}	Normalised Nusselt number (Nu/Nu_{Plain}) [-]
e	Scale/thorn height [m] (Refer to Figure 3-5)
f	Darcy friction factor [-]
H	Mean channel height [m] (Refer to Figure 3-5)
h	Average heat transfer coefficient [$W/m^2 \cdot K$]
h_e	Enthalpy per unit mass [J/kg]
k	Thermal conductivity [W/m·K]
L	Channel length [m]
$\dot{m}$	Mass flow rate [kg/s]
Nu	Average Nusselt number [-]
P	Scale/thorn pitch [m] (Refer to Figure 3-5)
p	Pressure [Pa]
Pr	Prandtl number [-]
Q	Volumetric flow rate [m^3/s]
q	Heat input [W]
r^*	Ratio of inner to outer diameter of annulus [-]
Re	Reynolds number [-]
S_M	Momentum source [$kg/m^2 \cdot s^2$]
S_E	Energy source [$kg/m \cdot s^3$]
T	Temperature [K]
$\boldsymbol{U}$	Velocity vector [m/s]
u	Velocity [m/s]
y^+	Dimensionless wall distance [-]
z	Axial location [m]
z_{hy}^*	$z/(D_h\, Re)$ [-]

Greek symbol

δ	Velocity boundary layer thickness [m]
δ_t	Thermal boundary layer thickness [m]
ε^*	Dimensionless surface roughness [-]
η	Thermo-hydraulic performance $((Nu/Nu_{Plain})/(f/f_{Plain})^{1/3})$ [-]
ρ	Density [kg/m^3]
τ	Stress tensor [Pa]
μ	Dynamic viscosity [Pa·s]

Subscript

app	Apparent
bulk	Bulk fluid
c	Copper
D	Durian profile
FS	Fish Scale profile
f	Fluid
hy	Hydrodynamic
i	Inlet
IFS	Inverted Fish Scale profile
m	Mean
o	Outlet
Plain	Plain profile
r	Radial
th	Thermal
w	Wall

Chapter 1 Introduction

This chapter presents an introduction of the Ph.D. research study. First, the motivation to delve into this research topic is established. Second, the objectives of this Ph.D. research study are clearly stated. Third, the scope of work to be accomplished in order to achieve the stated objectives is defined. Fourth, the organisation of the thesis is outlined.

1.1 Motivation for Research

Microscale passages are commonly observed in nature, such as the lungs and kidneys in living beings. The improved efficiency of the transport processes is due to the increased area-to-volume ratio of the microscale passages. Following the advancement of the electronics industry in the 20th century, the scientific community underwent a paradigm shift from macroscale to microscale systems. Tuckerman and Pease [1] ignited interest in this research topic in 1981 when they displayed the capability of microchannels with hydraulic diameter of about 100 μm to remove a heat flux of up to about 790 W/cm^2. The key benefits of microscale cooling include significant size reductions in practical devices, as well as low unit costs of microfluidic structures during mass production [2]. The present study adopts the generally accepted convention of ≤ 1 mm as the definition of microchannel dimension [3–6].

Microchannel cooling generally involves two-phase flow boiling, as well as single-phase liquid cooling in copper or silicon micro geometry [7]. While two-phase flow boiling appears to be a good choice in fulfilling the projected demand of 1000 W/cm^2 in advanced electronic cooling applications, considering the higher transport efficiency, the primary challenge to the practical implementation of evaporative microscale heat exchangers lies in flow

boiling instabilities [8]. On the other hand, there is great potential for single-phase liquid flow with heat transfer enhancement features to achieve comparable cooling performance to two-phase flow systems, and yet avoid the complexity and high pumping power requirement of the latter [9]. The first successful implementation of enhanced heat transfer in microchannels was by Kishimoto and Sasaki [10] in 1987. Even till today, there still exists a strong research need for enhanced microscale single-phase liquid flow. As concurred by Kandlikar et al. [8] in 2013, the research in this area is critical in the successful development of microscale thermal devices, where increased convective heat transfer coefficient and reduced pressure drop are required.

Another current research need is the application of microscale heat transfer phenomena to conventionally-sized heat exchangers, by replacing the macroscale passages with microscale passages. The three potential benefits include reduction in physical size, material cost and fabrication cost. Since the microscale heat transfer is expected to provide higher heat transfer coefficients than the conventionally-sized heat exchanger, a smaller heat transfer area is needed. Hence, a smaller heat exchanger is required. This is an advantage in applications where space is a constraint, such as an offshore platform or a chemical plant. Furthermore, constructing a smaller heat exchanger saves material costs and resources. In addition, microchannels are currently fabricated using costly microfabrication technologies, including microelectromechanical systems (MEMS) and photolithographic-based processes [3]. If conventional machining techniques such as turning, milling and cutting can be used to produce microchannels, this would significantly reduce fabrication costs. Therefore, the research efforts would result in the development of compact microchannel heat exchangers with large heat duty at competitive costs.

In 2013, Kong and Ooi [11] proposed the concept of securing a cylindrical insert of mean diameter 19.4 mm within a circular pipe of internal diameter 20 mm. An annular microchannel is thus created by combining the two conventionally-sized macro geometries, which can be separately manufactured through conventional machining processes. For a microchannel gap size of 300 µm, the investigation reported a heat transfer coefficient of at least 20 $kW/m^2 \cdot K$ at Reynolds number of 5200. Since the heat transfer effects are comparable to that of typical microchannels, the feasibility of achieving microscale heat transfer effects in macro geometry is demonstrated. The comprehensive research work is documented in the Ph.D. thesis of Kong [12].

The present Ph.D. research study aims to extend the Ph.D. work of Kong, by developing a novel configuration for enhanced microscale heat transfer in macro geometry. In this study, the enhancement profiles are introduced on the insert surface, while the heat is supplied to the flow via the circular pipe of a fixed heat transfer surface area. Therefore, heat transfer is improved by increasing the convective heat transfer coefficient, for a constant heat transfer surface area. The enhancement profiles serve to increase the convective heat transfer coefficient by disturbing the velocity and thermal boundary layers. In addition, working correlations for Nusselt number and friction factor for the new configurations are proposed, which are useful in the practical design of microchannel heat exchangers.

The novelty of the present study lies in the enhancement of microscale heat transfer in macro geometry, where the enhancement profiles are designed through inspiration from nature. This revolutionary science is also known as biomimicry. As human knowledge reaches a bottleneck, it is humbling to accept that mankind is but a part of nature. Undeniably, the most sustainable and efficient systems are found in life forms that have been evolving and adapting to changing conditions for more than 3.8 billion years to date. While

designing the enhancement profiles, geometries which naturally cause significant flow disturbances are prudently selected, studied and adapted to fulfil the design objectives.

The academic value of the present study comes from the analysis of the heat transfer and flow phenomena for microscale flow in macro geometry, as well as the physics behind the enhanced microscale heat transfer phenomena for the nature-inspired geometrical profiles. The industrial value of the present study comes from the newly proposed working correlations. Therefore, it is believed that the present Ph.D. research work offers significant contributions to both the scientific community as well as the engineering industry.

1.2 Objectives

The main objective in the present Ph.D. research study is to develop a novel nature-inspired configuration to enhance the microscale heat transfer in macro geometry using conventional machining methods, and formulate working correlations to evaluate the heat transfer and pressure drop for practical applications. This is achieved by fulfilling the following requirements:

- To achieve microscale heat transfer effects in macro geometry using single-phase liquid water.
- To achieve high convective heat transfer coefficient values in excess of 10 $kW/m^2 \cdot K$ for a microchannel with mean gap of 300 μm.
- To enhance the microscale heat transfer effects through improving the convective heat transfer coefficient for a fixed heat transfer surface area, using passive heat transfer augmentation techniques.
- To design nature-inspired enhancement geometries based on the concept of biomimicry, so as to cause disturbance to the flow and thereby enhance heat transfer.
- To design simple enhancement geometries such that they are mathematically quantifiable and can be easily manufactured at relatively low costs using conventional machining processes.

- To keep the pressure drop within a limit of 3.5 bars, such that the pumping requirement can be easily met by a commercially available pump.
- To develop working correlations for the average Nusselt number and friction factor, to be used in the design of compact microchannel heat exchangers.

1.3 Scope of Work

In order to achieve the objectives stated earlier in Section 1.2, the tasks to be accomplished are as follows:

- To review existing classical theory for forced convective internal flow in a conventionally-sized flow passage, as well as critically evaluate the state-of-the-art studies conducted on enhanced heat transfer in single-phase liquid flow in microchannels. The former provides a good understanding of the underlying concepts on convective heat transfer phenomena, while the latter presents an overview of the history, up-to-date developments and research needs in the field. The preceding work on microscale heat transfer in macro geometry is carefully examined, so as to identify past challenges and areas of improvement, in order to advance this research topic. In addition, the revolutionary science of biomimicry is studied, and designs inspired by nature are employed to enhance the microscale heat transfer in macro geometry.

- To develop a conjugate heat transfer numerical model using an available Computational Fluid Dynamics (CFD) computational code. In the early stage of the present study, the preliminary results are used to assist in the design of the measurement apparatus and operating procedures, as well as the data reduction method. Subsequently, the numerical results are used to provide useful insight into the flow field and temperature distribution, which cannot be directly and completely observed from the measurement system. These insights are valuable in explaining the physics behind the enhanced microscale heat transfer phenomena.

- To design, fabricate, instrument and commission a measurement system for data collection. First, the test module is designed and custom-made such that it comprises the microchannel of interest and is capable of providing a heat flux of up to 160 W/cm^2. Next, the supporting equipment to complete the flow loop is carefully selected, procured and installed. They include the chiller to pump and cool the working fluid, the filter to remove contaminants, as well as the pipeline and fittings. For the purpose of the present study, the flow system is designed to provide a pressure drop of up to 3.5 bars and volumetric flow rate of up to 10 L/min. The heat supply system, the measuring devices for temperature, pressure, flow and current, as well as the data acquisition system are also procured and assembled to establish a functional measurement system.

- To collect steady-state measurements to investigate if the enhanced microscale heat transfer effects have been achieved in the present study. About 600 steady-state measurements have been collected for a smooth annular microchannel with a mean gap size of 300 μm using single-phase liquid water. The independent variables include 22 microchannel profiles, Reynolds number range of 350-4,600, and wall heat flux of 13.3 and 53.0 W/cm^2. The dependent variables include the convective heat transfer coefficient, pressure drop, Nusselt number, friction factor, and thermo-hydraulic performance. The preparation work prior to data collection includes calibration of the critical measuring devices, dimension inspection of the critical components and validation of the measurement system.

- To analyse the steady-state measurements for the Plain microchannel, and verify that the microscale heat transfer effects have indeed been achieved in macro geometry, without involving complex and costly manufacturing methods. This is characterised by the high convective heat transfer coefficient values in excess of 10 kW/m^2·K. In addition, the measured results are compared with classical predictions to confirm the applicability of the continuum theory to microchannel flows. The laminar and turbulent flow regimes are also identified, along with the laminar-to-turbulent flow transition.

- To analyse the steady-state measurements for the nature-inspired enhanced microchannel series, namely the Inverted Fish Scale (IFS), Fish Scale (FS) and the thorny Durian (D) microchannel series. The physics behind the heat transfer and flow phenomena are examined as well. In addition, working correlations are proposed to evaluate the average Nusselt number and friction factor for the enhanced microchannel configurations. The correlations are formulated based on the 600 steady-state measurements, as well as the underlying physics which governs the heat transfer and flow behaviours, within the scope of investigation.

1.4 Organisation of Thesis

The Ph.D. thesis is organised as follows:

Chapter 1, which is this chapter, presents an introduction of the Ph.D. research study. It includes the research motivation, objectives and scope, as well as the organisation of the thesis.

Chapter 2 critically evaluates existing state-of-the-art literature relevant to the present study. The first two sections review the classical theory for forced convective internal flow in conventionally-sized circular and annular channels, in terms of hydrodynamic and thermal considerations. The third section summarises the investigations conducted on enhanced heat transfer in single-phase liquid flow in microchannels to date. The key focus is on passive heat transfer enhancement techniques, as well as performance quantification over a non-enhanced channel. An overview of studies on microchannels is also presented, along with the comparison with classical theory. The fourth section introduces the revolutionary science of biomimicry, which would be employed to enhance the microscale heat transfer in macro geometry. The fifth section identifies the research gaps based on the findings from the literature review.

Chapter 3 explains the research methodology used in the present study. The first section describes how the enhanced microscale heat transfer is achieved in macro geometry. The second and third sections detail the selection of independent and dependent parameters, respectively. The independent variables include the channel profile, Reynolds number and heat flux. The dependent variables include convective heat transfer coefficient, pressure drop, Nusselt number, friction factor and thermo-hydraulic performance.

Chapter 4 describes the three-dimensional numerical conjugate heat transfer model used in the present study. The discussion includes the Computational Fluid Dynamics code, governing equations, model simplification, turbulence model, mesh settings, boundary conditions and convergence criteria. The numerical model is validated through the comparison of its predictions with the measurements.

Chapter 5 describes the measurement system used in the present study, which was entirely designed, fabricated and commissioned by the author. The flow loop which connects all the components is first outlined, followed by the detailed specifications of each component. The main components include the chiller, filter, test module, heat supply system, measuring devices and data acquisition system. Calibration of the critical measuring devices and dimension inspection of the critical components is presented. The operational limits of the measurement system are also summarised. Next, the data reduction procedure is presented, along with the uncertainty analysis. Lastly, validation of the measurement system is carried out to demonstrate that the pressure and heat transfer measurements are accurate and consistent.

Chapter 6 presents the measured results for the Plain annular microchannel, with a gap size of 300 μm. The first section demonstrates that high heat transfer coefficient values, which are comparable to those in a typical microchannel, can

be achieved in macro geometry without involving complex and costly manufacturing methods. The second and third sections compare the measured results with predictions from the classical theory, and discuss the possible reasons for any deviation. The fourth section identifies the laminar-to-turbulent flow transition regime in the present study based on the flow and heat transfer behaviour, and compares it with those from the classical theory. The fifth section distinguishes the flow regime based on the hydrodynamic and thermal entrance lengths.

Chapter 7 presents the results for the Inverted Fish Scale (IFS) microchannel series. In the IFS configuration, the scales are arranged to oppose the flow direction in the attempt to cause maximum flow disturbances, and therefore enhance the heat transfer coefficient. The IFS geometrical profile is quantified by the scale height (e) and scale pitch (P). For a fair comparison with the Plain microchannel, the mean flow gap (H) is kept constant at 300 μm. The chapter first presents the measured convective heat transfer coefficient and pressure drop for all the IFS microchannels. Second, a comparison between the measured and numerical results is presented. Third, the effects of e/H ratio and P/e ratio on Nusselt number, friction factor and thermo-hydraulic performance are studied. The physical mechanisms behind the heat transfer and flow phenomena are examined using the flow field, as well as velocity and temperature distributions, from the numerical results.

Chapter 8 presents the results for the Fish Scale (FS) microchannel series. In the FS configuration, the scales are arranged in a streamlined configuration, so as to achieve minimal flow disturbances, and therefore lower friction losses. The FS geometrical profile is also quantified by the scale height (e) and scale pitch (P). The organisation of this chapter is the same as that of Chapter 8. In addition, this chapter also highlights the differences between the results for the IFS and FS microchannels.

Chapter 9 presents the results for the thorny Durian (D) microchannel series. Inspired by the thorn-covered husk of a tropical fruit, which is regarded as the king of fruits in Southeast Asia, the thorny durian-inspired profile shows potential to create flow disturbances and enhance heat transfer, while keeping the friction losses low due to the smooth wavy flow path. The D geometrical profile is quantified by the thorn height (e) and thorn pitch (P). The organisation of this chapter is the same as that of Chapter 8 and 9. In addition, this chapter also highlights the differences between the results for the durian-inspired D microchannels and the scale-inspired IFS and FS microchannels.

Chapter 10 presents the newly proposed working correlations to evaluate the average Nusselt number and friction factor for the nature-inspired enhanced IFS, FS and D microchannels. The mathematical form of the new correlations follows that of existing classical correlations, but with an additional term added to account for the effect of the scale/thorn protrusions. The correlations are formulated based on about 600 steady-state measurements, as well as the underlying physics which governs the heat transfer and flow behaviours, within the scope of investigation. These correlations are useful in the design of compact microchannel heat exchangers.

Chapter 11 concludes the work accomplished by the author during the course of the Ph.D. research study, and summarises the key findings of this research work. The results for the Plain, Inverted Fish Scale (IFS), Fish Scale (FS) and Durian (D) microchannels are first individually concluded, before the newly proposed correlations for the average Nusselt number and friction factor are listed. After a thoughtful reflection on the key findings from the present study, the opportunities and strategies for future work are identified and recommended.

Chapter 2 Literature Review

This chapter critically evaluates existing state-of-the-art literature which is relevant to the present study. The first two sections review the classical theory for forced convective internal flow in conventionally-sized circular and annular channels, in terms of hydrodynamic and thermal considerations. The third section summarises the investigations conducted on enhanced heat transfer in single-phase liquid flow in microchannels to date. The key focus is on passive heat transfer enhancement techniques, as well as performance quantification over a non-enhanced channel. An overview of studies on microchannels is also presented, along with the comparison with classical theory. The fourth section introduces the revolutionary science of biomimicry, which would be employed to enhance the microscale heat transfer in macro geometry. The fifth section identifies the research gaps based on the findings from the literature review.

2.1 Classical theory for Circular Channel

2.1.1 Forced Convective Internal Flow

The main interest in forced convective internal flow is to determine the total heat transfer rate. It may be calculated using Newton's law of cooling:

$$Q = hA(T_s - T_m) \tag{2-1}$$

where h is average convective heat transfer coefficient, A is surface area over which the heat transfer occurs, T_s is surface temperature and T_m is mean fluid temperature.

The problem of convection is therefore to find the average convective heat transfer coefficient. However, the complexity of the problem lies in that this

coefficient depends on surface geometry and flow conditions, on top of fluid properties [13]. The multi-factor dependence is mainly due to the fact that convection heat transfer is closely related to the boundary layers that develop on the internal pipe surface.

The two boundary layers of interest are velocity boundary layer and thermal boundary layer. The velocity boundary layer is a result of the difference between free stream velocity and zero surface velocity; while the thermal boundary layer is a result of the difference between free stream temperature and surface temperature. Friction factor is associated with velocity boundary layer; whereas convective heat transfer coefficient is associated with thermal boundary layer.

2.1.2 Hydrodynamic Consideration

2.1.2.1 Velocity Boundary Layer

The concept of a boundary layer originated with Ludwig Prandtl in 1904 [14]. He inferred from experimental evidence that a thin layer exists near a solid boundary where viscous effects are at least as important as inertia effects, even if fluid viscosity is low.

Figure 2-1 shows the development of velocity boundary layer for laminar flow in a circular pipe. In the hydrodynamic entrance region, the boundary layer grows in the direction of fluid flow. Within the boundary layer, viscous effects are important and fluid flow near the stationary wall is impeded. Outside the boundary layer, there is an inviscid core where fluid flow is accelerated by virtue of mass conservation. The boundary layer then merges at $x_{fd,h}$ for a sufficiently long pipe. In the fully developed region, viscous effects apply over the entire cross section, and the velocity profile is independent of x.

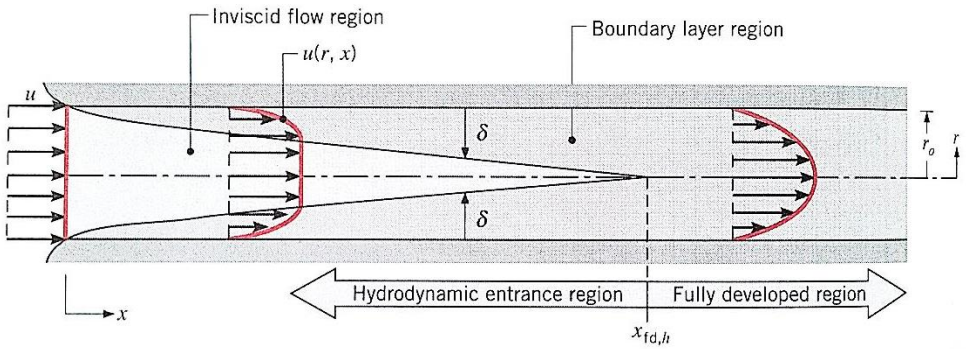

Figure 2-1: Laminar, hydrodynamic boundary layer development in a circular pipe [13]

For laminar flow in circular pipe, fully developed velocity profile is parabolic. This is on the condition that flow is incompressible and has constant fluid properties. The parabolic velocity profile can be derived by solving the x-component of Navier-Stokes equation in cylindrical coordinates. For turbulent flow, however, fully developed velocity profile is flatter due to turbulent mixing in the radial direction. Figure 2-2 illustrates the difference in the velocity profiles.

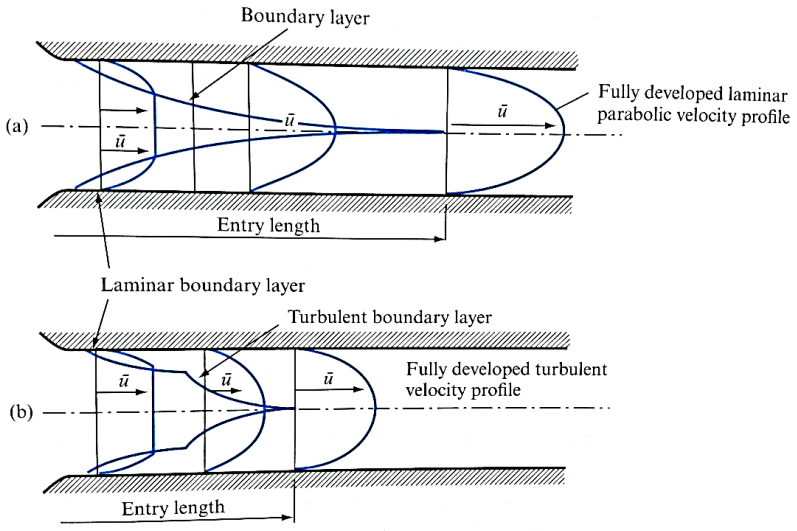

Figure 2-2: (a) Laminar and (b) Turbulent boundary layer development in circular tube [15]

The turbulent mixing in the radial direction can be seen in Figure 2-3. There are three distinct regions: the laminar sublayer, turbulent core and buffer layer. In the laminar sublayer, the fluid particles flow orderly in the axial direction. In the turbulent core, fluid chunks move in a chaotic manner. These eddying motions cause intense mixing of the fluid. The buffer layer serves as a transition between the laminar sublayer and turbulent core. It is also the region in which the mean velocity profile exhibits a logarithmic behaviour [16].

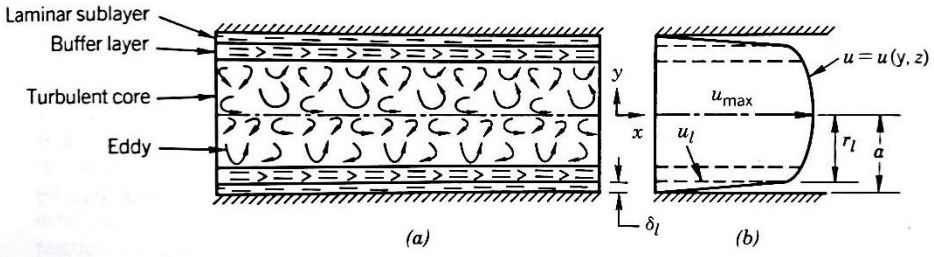

Figure 2-3: Fully developed turbulent flow in a smooth pipe [14]

The extent of the hydrodynamic entrance region depends on whether the flow is laminar or turbulent. This in turn is determined by Reynolds number. Reynolds number for flow in circular pipe is defined as:

$$Re_D \equiv \frac{\rho u_m D}{\mu} \tag{2-2}$$

where u_m is the mean fluid velocity, and D is the pipe diameter.

Mean fluid velocity is defined from the conservation of mass as:

$$u_m \equiv \frac{\dot{m}}{\rho A_c} = \frac{\int_{A_c} \rho u(r)\, dA_c}{\rho A_c} = \frac{\int_0^{r_o} \rho u(r) 2\pi r\, dr}{\rho \pi {r_o}^2} \tag{2-3}$$

where $\dot{m}$ is mass flow rate, ρ is density of fluid and A_c is the cross-section area.

In a fully developed internal flow, the critical Reynolds number corresponding to the onset of turbulence is approximately 2,300 [13]. The transition to turbulence is likely to begin in the developing boundary layer of the hydrodynamic entrance region. To achieve fully turbulent conditions, a much higher Reynolds number, of approximately 10,000, is required. The above is valid for smooth pipes.

For laminar flow ($Re_D \lesssim 2300$), the hydrodynamic entry length $x_{fd,h}$ can be obtained from [13]:

$$\left(\frac{x_{fd,h}}{D}\right)_{lam} \approx 0.05\, Re_D \tag{2-4}$$

For turbulent flow, there is no general expression for the entry length. However, it is found to be approximately independent of Reynolds number. As a simplified first approximation [17]:

$$10 \lesssim \left(\frac{x_{fd,h}}{D}\right)_{turb} \lesssim 60 \tag{2-5}$$

2.1.2.2 Friction Factor

Another interest in forced convective internal flow is to determine the pump power required to sustain the flow. It depends on the pressure drop across the length of the pipe, which may be computed by:

$$\Delta p = f\, \frac{L}{D_h}\, \frac{1}{2} \rho\, u_m^2 \tag{2-6}$$

where f is friction factor, ρ is density of fluid, u_m is mean fluid velocity, L is the length of pipe and D_h is hydraulic diameter of pipe. For circular pipes, hydraulic diameter is simply the inner pipe diameter.

Eqn. (2-6) is arises from the definition of friction factor, also known as Moody or Darcy friction factor:

$$f \equiv \frac{-(dp/dx)D}{\rho {u_m}^2/2} \tag{2-7}$$

On the other hand, friction coefficient, also known as Fanning friction factor, is defined as:

$$C_f \equiv \frac{\tau_s}{\rho {u_m}^2/2} \tag{2-8}$$

where τ_s is the surface shear stress, which is related to the surface velocity gradient by Eqn. (2-9) for circular pipe:

$$\tau_s = -\mu \left.\frac{dv_x}{dr}\right|_{r=r_o} \tag{2-9}$$

where μ is dynamic viscosity of fluid.

Friction factor is related to friction coefficient by: $f = 4C_f$. Friction factor is more commonly used by civil and mechanical engineers, whereas the latter is generally used by chemical engineers.

Eqn. (2-6) is usually used for cases where the flow is fully developed. Eqn. (2-10), on the other hand, takes into account the entrance region and computes the total pressure drop from the pipe inlet to a certain point along the pipe. This gives rise to the apparent friction factor, f_{app}. The incremental pressure defect, K(x) represents the combined effect of wall shear and change in momentum due to the developing velocity profile. This value increases monotonically from 0 at the pipe entrance to a constant value $K(\infty)$ in the developed region.

$$\Delta p = f_{app}\ \frac{L}{D}\ \frac{1}{2}\rho\ u_m^2 = f\ \frac{L}{D}\ \frac{1}{2}\rho\ u_m^2 + K(x)\frac{1}{2}\rho\ u_m^2 \tag{2-10}$$

Figure 2-4 illustrates the variation of local friction factor along the pipe for laminar flow. The velocity boundary layer affects surface velocity gradient along *x*, which in turn affects friction factor. In the hydrodynamic entrance region, velocity boundary layer is constantly developing with increasing *x*. As the viscous effects penetrate further into the pipe centre, the layer of particles nearer to the wall becomes increasingly impeded along *x*. This implies that magnitude of surface velocity gradient decreases along *x*. By virtue of Eqn. (2-9), surface shear stress and therefore friction factor decreases along *x*. This trend continues until the flow becomes fully developed. Since fully developed velocity profile is independent of *x*, it follows that surface velocity gradient is constant along *x*. This implies that surface shear stress and therefore local friction factor become independent of *x*. The hydrodynamic entry length is defined as the axial distance required to achieve a local friction factor of 1.05 times the fully developed friction factor, or the distance from entrance to the point where the maximum velocity reaches 99% of the fully developed value [18].

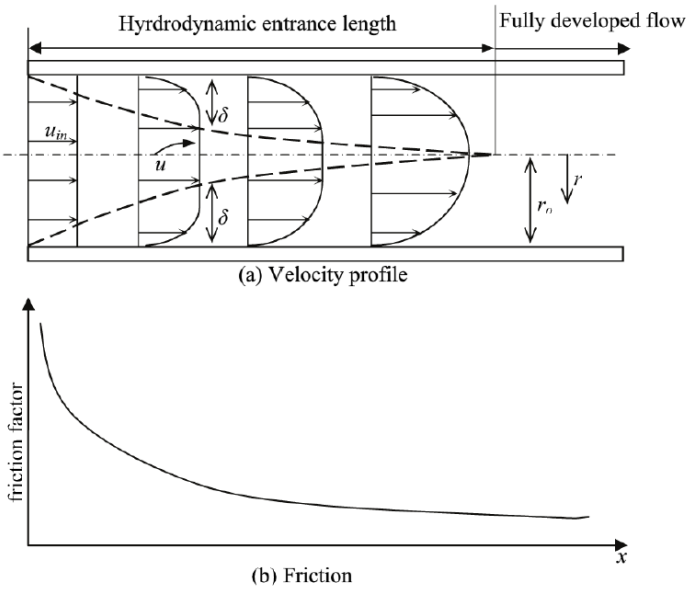

Figure 2-4: Velocity profiles and friction factor variation for laminar flow in a circular tube [19]

Figure 2-5 shows the variation of local friction factor along the pipe for turbulent flow. Regardless of the inlet velocity, the laminar velocity boundary layer develops first. This is followed by the transition to the turbulent boundary layer. Similar to laminar flow, the friction factor become independent of *x* in the fully developed region.

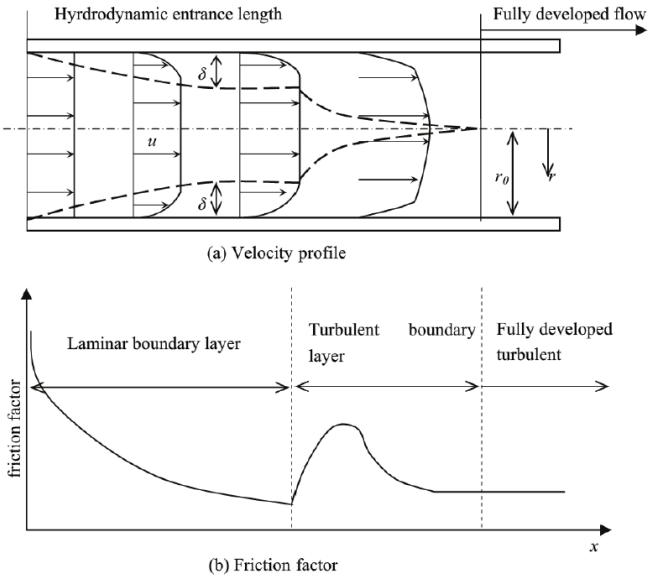

Figure 2-5: Velocity profiles and friction factor variation for turbulent flow in a circular tube [19]

Table 2-1 shows the friction factor correlations for laminar flow. It is observed that for laminar flow, fully developed friction factor is a function of Reynolds number only.

Table 2-1: Darcy friction factors for laminar flow in circular pipes

Laminar Condition	Correlation		Range and Remarks
Developing and fully developed	$f_{app} = [13.76(z_{hy}^*)^{-1/2} + \frac{1.25(z_{hy}^*)^{-1} + 64 - 13.76(z_{hy}^*)^{-1/2}}{1 + 0.00021(z_{hy}^*)^{-2}}] \cdot \frac{1}{Re}$ **Shah and London, 1978 [18]**	(2-11)	
Fully developed	$f = \frac{64}{Re_D}$ **Derivation [13]**	(2-12)	$Re \leq 2{,}100$

For turbulent flow, however, any surface irregularity disturbs the laminar sublayer and affects the flow. Hence, fully developed friction factor is a strong function of surface roughness, on top of Reynolds number. For the same Reynolds number, it is a minimum for smooth surface condition and increases with increasing surface roughness. As illustrated in Figure 2-6, there are three regimes of turbulent pipe flow, with different friction factor correlations for each regime.

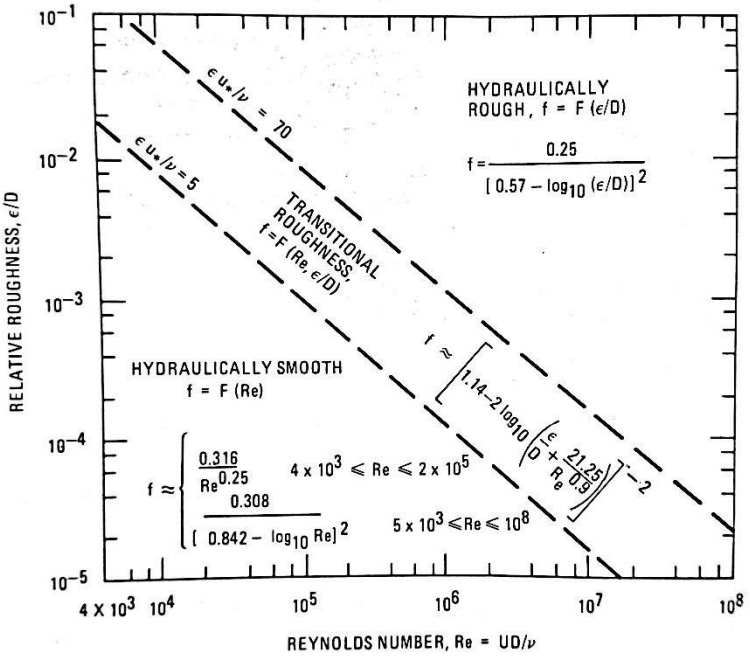

Figure 2-6: Regimes of turbulent pipe flow as a function of Reynolds number and relative surface roughness [20]

Table 2-2 summarises the Darcy friction factor correlations for turbulent flow. Alternatively, fully developed friction factor can be determined from the Moody chart [21], which is valid for both laminar and turbulent flow, as well as for smooth and rough pipes. Furthermore, the Moody chart is applicable to both circular and non-circular pipes, using the definition of hydraulic diameter.

Table 2-2: Darcy friction factors for turbulent flow in circular pipes

Turbulent Condition	Correlation		Remarks
Developing and fully developed, Smooth	$f_{app} = A\,Re^{B}$ $A = 0.3716 + \frac{4.06448}{z/d_h}$ $B = -0.268 - \frac{0.31930}{z/d_h}$ **Phillips, 1987 [22]**	(2-13)	$Re < 28{,}000$
Fully developed, Smooth	$f = 0.316\,Re^{-1/4}$ **Blasius, 1913** [23]	(2-14)	$3000 \leq Re \leq 10^5$ $Re \geq 10^5$ *f* depends only on Reynolds number.
	$f = (0.790 \ln Re - 1.64)^{-2}$ **First Petukhov equation [25]**	(2-15)	$3000 \leq Re \leq 5 \times 10^6$ Single correlation valid over a large Reynolds number range.
Fully developed, Smooth and rough	$\frac{1}{\sqrt{f}} = -2\log\left(\frac{\varepsilon/d_h}{3.7} + \frac{2.51}{Re\sqrt{f}}\right)$ **Implicit Colebrook equation, 1939 [26]**	(2-16)	*f* depends on Reynolds number and relative surface roughness ϵ/D, which is the ratio of mean roughness height to pipe diameter. Also applicable in transition region.
	$\frac{1}{\sqrt{f}} \cong -1.8 \lg\left[\left(\frac{\epsilon/D}{3.7}\right)^{1.11} + \frac{6.9}{Re}\right]$ **Haaland equation, 1983 [21]**	(2-17)	Approximate explicit relation which predicts results within 2% of those from Colebrook equation.

2.1.3 Thermal Consideration

For hydrodynamic considerations, there are only two types of flow: developing and fully developed. However, when thermal effects are considered, the type of flow depends on when the temperature difference is introduced. As shown in Figure 2-7(a), if the temperature difference is introduced after the flow is hydrodynamically developed, then there are three flow regions. They are hydrodynamically developing flow, thermally developing flow, and fully developed flow where both the viscous and heat transfer effects apply over the entire cross-section of the pipe. As shown in Figure 2-7(b) and Figure 2-7(c), if the temperature difference is introduced right at the pipe entrance, then there are

two flow regions. They are simultaneously developing flow, where the velocity and thermal boundary layers start to develop together, and fully developed flow, where both boundary layers are completely developed. Within the simultaneously developing flow region, either one of the velocity and thermal boundary layers may be fully developed first while the other is still developing, depending on the Prandtl number.

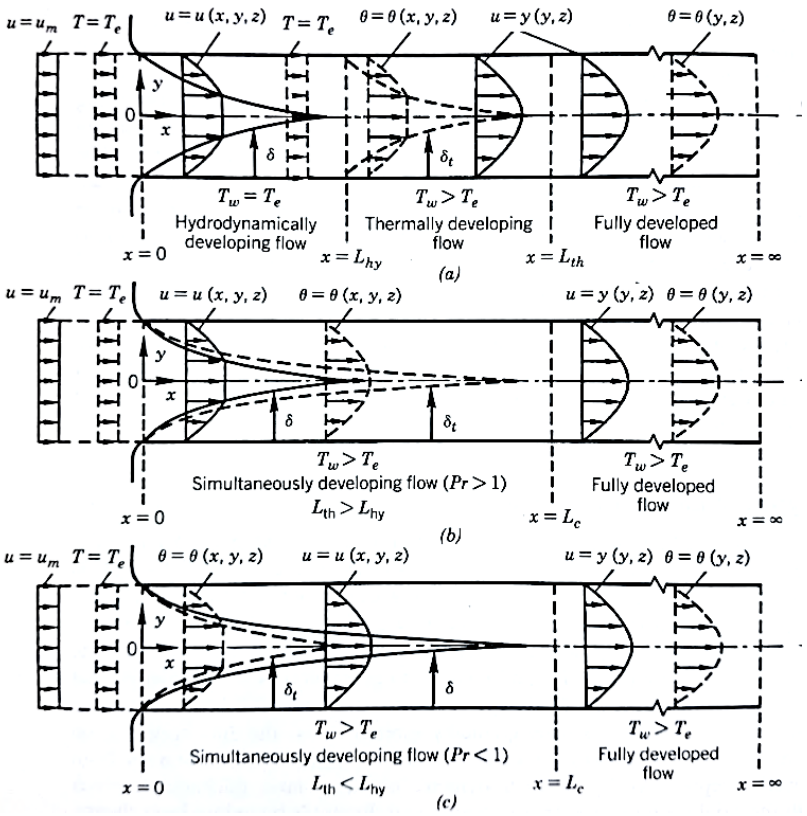

Figure 2-7: Types of laminar flows for constant wall temperature boundary condition [14]

2.1.3.1 Thermal Boundary Layer

In forced convective internal flow, a thermal boundary layer develops when the free stream fluid temperature differs from the surface temperature of the pipe. An example would be cool flow into a hot pipe. When the cool fluid particles come into direct contact with the hot surface, they reach thermal equilibrium

with the surface and assume the surface temperature. These particles then transfer the heat energy to the next layer of cool particles in contact with them. This results in temperature gradients developing in the fluid. This process continues, until the heat transfer effect becomes negligible, at a distance $y = \delta_t$ from the surface.

Figure 2-8 shows the thermal boundary layer development in a heated circular tube [13]. In the fully developed region, the temperature profile depends on the surface condition, which may be constant temperature or constant heat flux. This is unlike the fully developed velocity profile, which has only one no-slip surface condition.

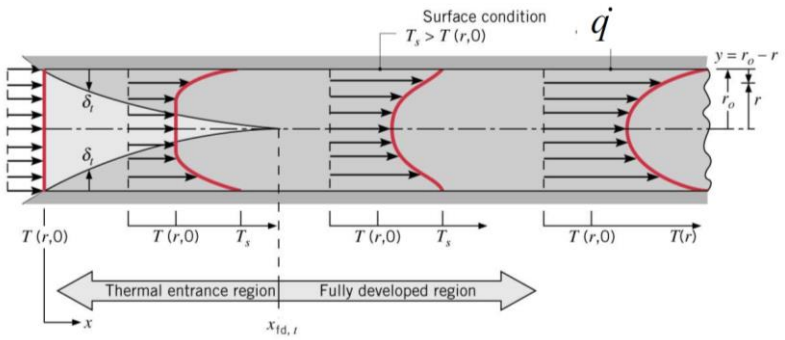

Figure 2-8: Thermal boundary layer development in a heated circular tube [13]

Furthermore, the fully developed temperature profile continues to change with increasing x for both surface conditions. The relative shape of the profile, however, remains constant along x. This can be described by the dimensionless temperature profile, which is defined as:

$$\frac{\partial}{\partial x}\left[\frac{T_s(x) - T(r,x)}{T_s(x) - T_m(x)}\right]_{fd,t} = 0 \qquad (2\text{-}18)$$

where T_s is surface temperature of pipe, T is local fluid temperature, and T_m is mean temperature of fluid over the cross-section of the tube.

For laminar flow ($Re_D \lesssim 2300$), the thermal entry length $x_{fd,t}$ can be obtained from [17]:

$$\left(\frac{x_{fd,t}}{D}\right)_{lam} \approx 0.05\, Re_D Pr \tag{2-19}$$

For turbulent flow, conditions are nearly independent of Prandtl number. As a simplified first approximation [13]:

$$\left(\frac{x_{fd,t}}{D}\right)_{turb} = 10 \tag{2-20}$$

Eqn. (2-4) and Eqn. (2-19) suggest that Prandtl number is an important factor in determining the relative growth of the velocity and thermal boundary layers. In fact, Prandtl number can be approximated as the ratio of δ/δ_t, where δ and δ_t is the velocity and thermal boundary layer thickness, respectively. For example, when $Pr > 1$, $\delta > \delta_t$ and $x_{fd,h} < x_{fd,t}$, as illustrated in Figure 2-9.

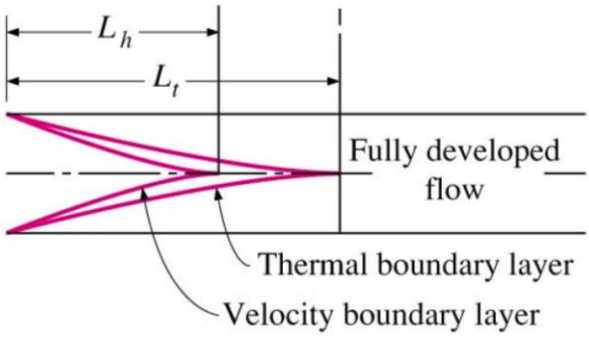

Figure 2-9: Velocity and thermal boundary layer development in a circular tube for *Pr* > 1 [21]

It is also useful to note that, for turbulent flow, the hydrodynamic and thermal entrance lengths are much shorter than those for laminar flow. This implies that, for turbulent flow, correlations for fully developed flow may be used to approximate the dimensionless parameters, without the need to consider the hydrodynamic and thermal entrance regions.

2.1.3.2 Convective Heat Transfer Coefficient

Table 2-3 shows the approximate values of convective heat transfer coefficient *h* under different flow conditions [14]. It is worthy to note that for single-phase liquid water in conventionally-sized channels, the typical *h* values are at most 10 kW/m^2·K. This is also supported by Figure 2-10 [27].

Table 2-3: Typical values of convective heat transfer coefficient [14]

	***h* (W/m^2·K)**	
Fluid	**Free Convection**	**Forced Convection**
Gases	5-30	30-300
Water	30-300	300-10,000
Viscous oils	5-100	30-3,000
Liquid metals	50-500	500-20,000
Boiling water	2,000-20,000	3,000-100,000
Condensing water vapour	3,000-30,000	3,000-200,000

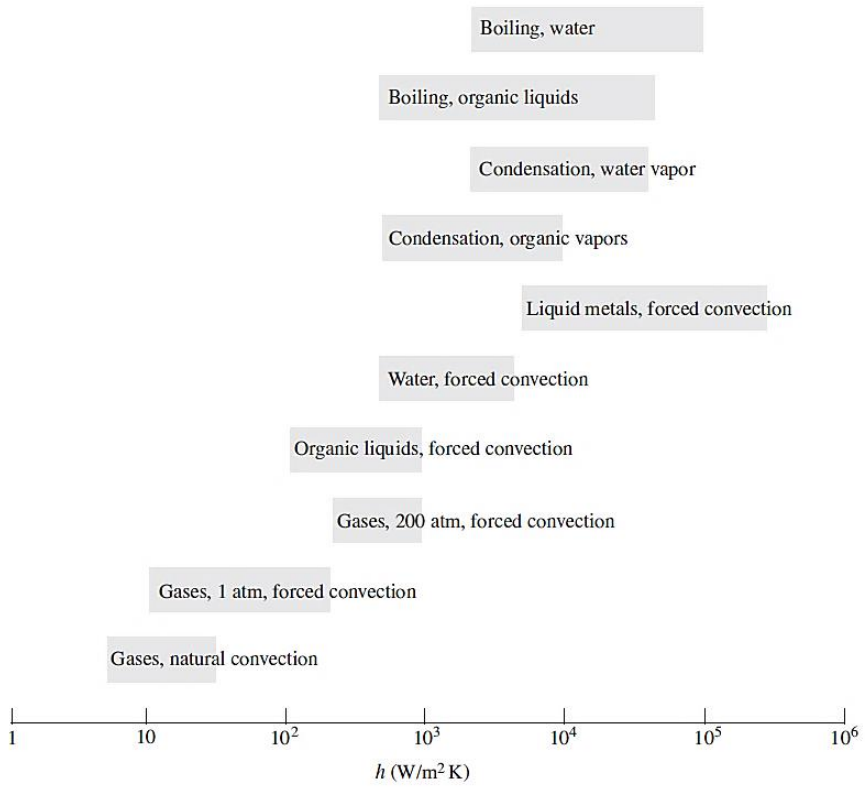

Figure 2-10: Convective heat transfer coefficients for different flow configuration [27]

The local convective heat transfer coefficient h can be found from the knowledge of Nusselt number through the relation:

$$h = \frac{Nuk_f}{D} \tag{2-21}$$

where k_f is fluid thermal conductivity.

Nusselt number is in fact equal to the dimensionless temperature gradient at the wall surface:

$$Nu = \left.\frac{\partial T^*}{\partial r^*}\right|_{r^*=1} \tag{2-22}$$

As illustrated in Figure 2-11, the significance of Nusselt number in thermal boundary layer is similar to that of friction factor in the velocity boundary layer. In the thermal entrance region, thermal boundary layer is constantly developing with increasing x. As the heat transfer effects penetrate further towards the pipe centre, dimensionless wall temperature gradient, ie $\left.\frac{\partial T^*}{\partial r^*}\right|_{r^*=1}$ decreases along x. Consequently, both the Nusselt number and convective heat transfer coefficient decrease along x. This trend continues until the flow becomes thermally fully developed. Since, by definition, fully developed dimensionless temperature profile is independent of x, it follows that both Nusselt number and convective heat transfer coefficient become independent of x. The thermal entrance length is defined as the axial distance required to achieve a local Nusselt number of 1.05 times the fully developed Nusselt number.

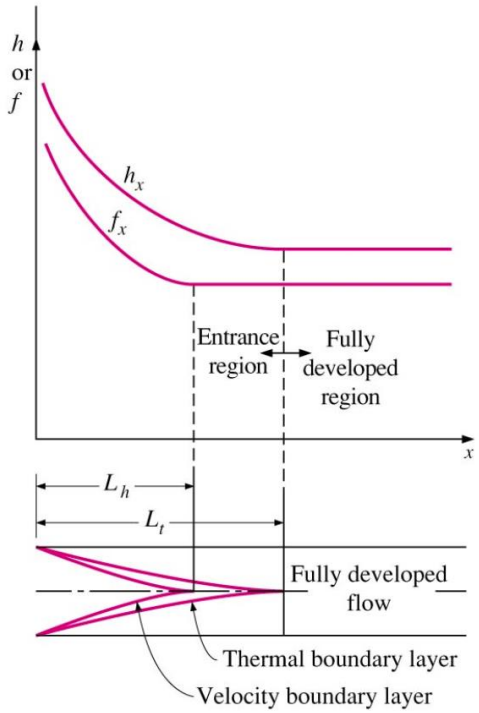

Figure 2-11: Variation of friction factor and convective heat transfer coefficient with velocity boundary layer and thermal boundary layer development for *Pr* > 1 [21]

Table 2-4 summarises the Nusselt number correlations for laminar flow. Unlike fully developed friction factor which is a function of Reynolds number, fully developed Nusselt number is simply a constant.

Table 2-5 summarises the Nusselt number correlations which are applicable to both transitional flow and turbulent flow. Valid for constant surface temperature and constant heat flux boundary conditions, the Nusselt number correlations can be used to obtain estimates of convective heat transfer coefficients.

Table 2-4: Local and average Nusselt numbers for laminar flow in circular pipes

Laminar Conditions	Correlation		Remarks
Fully developed, constant T_s	$Nu = 3.66$ **Derivation [28]**	(2-23)	
Thermally developing, constant T_s	$\overline{Nu} = 3.66 + \frac{0.065 Re\ Pr\ D_h/L}{1 + 0.04[Re\ Pr\ D_h/L]^{2/3}}$ **Edwards, 1979 [29]**	(2-24)	$Pr \lesssim 5$
Thermally developing, constant T_s	$\overline{Nu} = 3.66 + \frac{0.19(Re\ Pr\ D_h/L)^{0.8}}{1 + 0.117(Re\ Pr\ D_h/L)^{0.467}}$ **Hausen, 1959 [30]**	(2-25)	$Re < 2{,}200$
Simultaneously developing, constant T_s	$\overline{Nu} = 1.86\left(\frac{RePrD}{L}\right)^{1/3}\left(\frac{\mu_b}{\mu_s}\right)^{0.14} \geq 3.66$ **Sieder and Tate, 1936 [31]**	(2-26)	$0.60 \leq Pr \leq 5$ $0.0044 \leq (\mu/\mu_s) \leq 9.75$ *Re*<2200 Accounts for viscosity variation due to temperature difference between surface and fluid.
Fully developed, constant q_s	$Nu = \frac{48}{11} = 4.36$ **Derivation [13]**	(2-27)	
Thermally developing, constant q_s	$\overline{Nu} = 1.953(Re\ Pr\ D_h/L)^{1/3}$ for $Re\ Pr\ D_h/L \geq 33.3$ $\overline{Nu} = 4.364 + 0.0722 Re\ Pr\ D_h/L$ for $Re\ Pr\ D_h/L < 33.3$ **Shah and London, 1978 [18]**	(2-28)	$Re < 2{,}200$

Table 2-5: Average Nusselt numbers for turbulent flow in circular pipes

Turbulent Conditions	Correlation		Remarks
Smooth and rough pipes	$Nu = 0.125\, f\, Re_D\, Pr^{1/3}$ **Chilton–Colburn analogy [21]**	(2-29)	Fluid properties computed using bulk mean fluid temperature $T_b = 1/2(T_{in} + T_{out})$
Fully developed, Smooth pipe	$Nu = 0.023\, Re_D^{4/5}\, Pr^{1/3}$ **Colburn equation [21]**	(2-30)	$0.7 \le Pr \le 160$ $Re > 10{,}000$ $L/d_h \ge 10$ Substitute Blasius correlation into Chilton–Colburn analogy
	$Nu = 0.023\, Re_D^{4/5}\, Pr^{n}$ $n = 0.4\ when\ T_{surf} > T_{mean}$ (heating) $n = 0.3\ when\ T_{surf} < T_{mean}$ (cooling) **Dittus–Boelter, 1930 [32]**	(2-31)	$0.60 \le Pr \le 160$ $Re \ge 10{,}000$ $L/d_h \ge 10$ Improved version of Colburn equation
	$Nu = 0.027\, Re_D^{4/5}\, Pr^{1/3} \left(\frac{\mu}{\mu_s}\right)^{0.14}$ **Sieder and Tate, 1936 [31]**	(2-32)	$0.7 \le Pr \le 16{,}700$ $Re \ge 10{,}000$ $L/d_h \ge 10$ Accounts for viscosity variation due to large temperature difference between surface and fluid. Properties are evaluated at T_b except μ_s, which is evaluated at T_s
	$Nu = \frac{(f/8)\, Re_D\, Pr}{1.07 + 12.7\,(f/8)^{0.5}(Pr^{2/3} - 1)}$ **Second Petukhov equation, 1970** $f = \frac{1}{(1.82 \log_{10} Re - 1.64)^2}$ **Filonenko equation, 1954 [33]**	(2-33)	$1 \le Pr \le 2000$ $10^4 < Re_D < 5 \times 10^5$ Slightly complex and applicable for a smaller range, but improves accuracy to less than 10% error.
	$Nu = \frac{(f/8)\,(Re_D - 1000)\, Pr}{1 + 12.7\,(f/8)^{0.5}(Pr^{2/3} - 1)}$ **Gnielinski's equation, 1976 [34]** $f = (0.790 \ln Re - 1.64)^{-2}$ **First Petukhov equation [25]**	(2-34)	$1 \le Pr \le 10^6$ $2300 \le Re \le 5 \times 10^6$ $L/d_h \ge 10$ Improves accuracy of second Petukhov equation at lower Reynolds number Generally preferred in calculations Fluid properties are evaluated at T_b.
	$Nu = \frac{(f/8)\,(Re_D - 1000)\, Pr}{1 + 12.7\,(f/8)^{0.5}(Pr^{2/3} - 1)} \left(\frac{\mu}{\mu_s}\right)^{n}$ $n = 0.11\ when\ T_{surf} > T_{mean}$ $n = 0.25\ when\ T_{surf} < T_{mean}$ $f = (0.790 \ln Re - 1.64)^{-2}$ **First Petukhov equation [25]**	(2-35)	$1 \le \left(\frac{\mu}{\mu_s}\right) \le 40$ $0.5 \le Pr \le 140$ $3000 \le Re \le 5 \times 10^6$ Accounts for variation in fluid properties

2.2 Classical Theory for Concentric Annular Channel

The concentric annular channel is generally quantified by:

$$r^* = \frac{r_i}{r_o} \tag{2-36}$$

In this study, where the 19.4 mm insert is slotted into a 20 mm channel, r^*= 0.97. One limiting case of the annular channel is the flat duct, where r^*= 1. The other is the circular pipe with an infinitesimal core at the centre, where r^*=0. For brevity, the concentric annular channel is henceforth referred to as annular channel.

The hydraulic diameter is 0.6 mm in this study, using Eqn. (2-37):

$$D_h = D_o - D_i \tag{2-37}$$

2.2.1 Hydrodynamic Consideration

Fully developed laminar velocity profile for concentric annular channel is given by [14]:

$$u(r) = -\frac{1}{4\mu}\left(\frac{dp}{dx}\right) {r_o}^2 \left[1 - \left(\frac{r}{r_o}\right)^2 + 2{r_m^*}^2 \ln\left(\frac{r}{r_o}\right)\right] \tag{2-38}$$

$$r_m^* = \frac{r_m}{r_o} = \left(\frac{1 - {r^*}^2}{2\ln(1/r^*)}\right)^{1/2} \tag{2-39}$$

Here, r_m refers to the radius where maximum velocity occurs ($\partial u/\partial r = 0$).
The mean fluid velocity can be found by:

$$u_m = -\frac{1}{8\mu}\left(\frac{dp}{dx}\right) {r_o}^2 (1 + {r^*}^2 - 2{r_m^*}^2) \tag{2-40}$$

The circumferentially averaged fully developed friction factor for laminar flow is:

$$fRe = \frac{64(1-r^*)^2}{1+r^{*2}-2r_m^{*2}} \tag{2-41}$$

Also known as the Poiseuille number, fRe equals to 64 in the case of a circular channel (r*=0).

The circumferentially averaged fully developed friction factor is related by Eqn. (2-42) to fully developed friction factor at the inner and outer wall. The latter are given by Eqn. (2-43) and Eqn. (2-44) respectively.

$$f = \frac{f_i r_i + f_o r_o}{r_i + r_o} \tag{2-42}$$

$$f_i Re = -\frac{4}{\mu}\left(\frac{dp}{dx}\right)\frac{D_h}{u_m}\left(\frac{r_m^2 - r_i^2}{r_i}\right) \tag{2-43}$$

$$f_o Re = -\frac{4}{\mu}\left(\frac{dp}{dx}\right)\frac{D_h}{u_m}\left(\frac{r_o^2 - r_m^2}{r_o}\right) \tag{2-44}$$

The hydrodynamic entrance lengths for laminar flow in annular channels of various r* are reviewed by Shah and London [18]. The dimensionless hydrodynamic entrance length for r* = 0.97 is given by:

$$\left(\frac{x_{fd,h}}{D_h Re}\right)_{lam} \approx 0.0108 \tag{2-45}$$

Reynolds number for annular channel terms of mass flow rate:

$$Re = \frac{\dot{m}\, D_h}{A_c\, \mu} = \frac{4\dot{m}}{\pi(D_o + D_i)\mu} \tag{2-46}$$

$$D_h = D_o - D_i \tag{2-47}$$

$$A_c = \frac{\pi}{4}({D_o}^2 - {D_i}^2) \tag{2-48}$$

The Poiseuille number correlations for concentric annular pipes with $r^* \gtrsim 0.4$ are virtually the same as those for parallel plates even up to $z_{hy}^* = 0.1$ [18]. In the present study, r^* = 0.97 and the largest z_{hy}^* = 0.04. Therefore, Poiseuille number for laminar flow in parallel plates is used as a reference. Table 2-6 shows the friction factor correlation for laminar flow in parallel plates. The critical Reynolds number corresponding to laminar-to-turbulent transition for parallel plates ranges between 2,200 and 3,400 [14].

Table 2-6: Darcy friction factor for laminar flow in parallel plates

Laminar Condition	Correlation		Remarks
Developing and fully developed	$f_{app}Re = \frac{13.76}{\left(z_{hy}^*\right)^{1/2}} + \frac{0.674\left(z_{hy}^*\right)^{-1} + 96 - 13.76\left(z_{hy}^*\right)^{-1/2}}{1 + 0.000029\left(z_{hy}^*\right)^{-2}}$ **Shah and London, 1978 [35]**	(2-49)	$z_{hy}^* = \frac{z}{D_h Re}$ Reference for the annular channel in the present study

2.2.2 Thermal Consideration

The thermal entrance lengths for laminar flow in annular channels of various r^* are also reviewed by Shah and London [18]. The dimensionless thermal entrance length for r^* = 0.97 is given by:

$$\left(\frac{x_{fd,t}}{D_h RePr}\right)_{lam} \approx 0.04101 \tag{2-50}$$

Table 2-7 shows the Nusselt number correlation for laminar flow in parallel plates.

Table 2-7: Average Nusselt number for laminar flow in parallel plates

Laminar Condition	Correlation		Remarks
Thermally developing, constant q_s	$\overline{Nu} = 2.236(RePr\, D_h/L)^{1/3}$ for $RePr\, D_h/L \geq 1000$ $\overline{Nu} = 2.236(RePr\, D_h/L)^{1/3} + 0.9$ for $100 < RePr\, D_h/L < 1000$ $\overline{Nu} = 8.235 + 0.0364 RePr\, D_h/L$ for $RePr\, D_h/L \leq 100$ **Shah and London, 1978 [18]**	(2-51)	$Re < 2{,}200$ Reference for the annular channel in the present study

2.3 Enhanced Heat Transfer in Single-Phase Microchannels

Microscale passages are commonly observed in nature, such as the lungs and kidneys in living beings. The improved efficiency of the transport processes is due to the increased area-to-volume ratio of the microscale passages. Following the advancement of the electronics industry in the 20th century, the scientific community underwent a paradigm shift from macroscale to microscale systems. Tuckerman and Pease [1] ignited interest in this research topic in 1981 when they displayed the capability of microchannels with hydraulic diameter of about 100 μm to remove a heat flux of up to about 790 W/cm^2. Subsequently, the research efforts emphasised on a fundamental understanding of the microscale heat transfer and fluid flow phenomena, as well as the design and implementation of microchannel cooling [36]. The key benefits of microscale cooling include more compact practical devices, as well as low unit costs of microfluidic structures during large-scale production [2].

With the growing interest in miniaturisation, the question of defining it arises. In 2002, Kandlikar [37] proposed that conventional channels scale above 3 mm, minichannel dimensions scale between 200 μm and 3 mm, and microchannel dimensions scale between 10 and 200 μm. Nonetheless, many researchers broadly classify microchannel dimensions between 1 μm and 1 mm [3,4], simply less than 1 mm [5,6]. Hence, the present study adopts the generally-accepted classification of $\leq$ 1 mm as the definition of microchannel dimension.

Microchannel cooling generally involves two-phase flow boiling, as well as single-phase liquid cooling in copper or silicon micro geometry [7]. While two-phase flow boiling appears to be a good choice in fulfilling the projected demand of 1000 W/cm^2 in advanced electronic cooling applications, considering the higher transport efficiency, the primary challenge to the practical implementation of evaporative microscale heat exchangers lies in flow

boiling instabilities [8]. On the other hand, there is great potential for single-phase liquid flow with heat transfer enhancement features to achieve comparable cooling performance to two-phase flow systems, and yet avoids the complexity and high pumping power requirement of the latter [9,38]. The first successful implementation of enhanced heat transfer in microchannels was by Kishimoto and Sasaki [10] in 1987.

2.3.1 Passive Heat Transfer Enhancement Mechanisms

According to Bergles et al. [39] in 1996, the heat transfer enhancement techniques for single-phase liquid flow can be classified into two categories: passive and active. Since the passive techniques do not require any external power, they are preferred in many engineering applications [40]. The passive techniques include flow disruption, secondary flows, channel curvature, surface treatments, and entrance effects. Their applications in conventional channels and microchannels have been summarised by Steinke and Kandlikar [9] in 2004. Other good reviews are by Balaras [41] and Bergles [42]. It is clear that research effort is being directed towards the microscale channels, since Balaras mentioned only 1 paper on microchannel in 1990, while Bergles mentioned at least 4 papers in 2011.

For passive techniques applied in conventional channels, three possible heat transfer enhancement mechanisms have been proposed by Tao et al. [43] in 2002. They include decreasing the thermal boundary layer, increasing flow interruptions, and increasing velocity gradient near the heated surface.

For microscale channels, the re-developing thermal boundary layer concept to enhance heat transfer has been experimentally verified by Xu et al. [44] in 2005. The study was conducted using single-phase deionised water as working fluid, with Reynolds number between 100 and 2,000, and heat flux of up to 100

W/cm^2. The results show that the 155 μm triangular channels can increase Nusselt number by 26% relative to the channel without transverse passages. Furthermore, the study found that enhanced liquid mixing in the transverse microchannels promotes earlier laminar-to-turbulent flow transition, at critical Reynolds number of 1,000–1,100. The same concept was subsequently numerically verified by Xu et al. [45] in 2008.

A similar attempt to re-initialise the boundary layers through the use of oblique fins in microchannels is carried out by Lee et al. [46] in 2015. Using deionised water, with Reynolds number between 180 and 680, the study yielded a maximum heat transfer enhancement of 47% at Reynolds number of 680. In the same year, Deng et al. [47] developed a unique re-entrant microchannel heat sink with a hydraulic diameter of 781 μm. Using deionised water, with Reynolds number between 150 and 1,100, the study concluded that the use of reentrant microchannels can increase Nusselt number by up to 39%, as compared to rectangular microchannels. The heat transfer enhancement is due in part to the disruption of thermal boundary layer development, as well as intensification of fluid mixing in the core section.

In 2010, Sui et al. [48] proposed to use sinusoidal channels instead of straight channels, to improve the performance of the microchannel heat sinks. The core idea is that when liquid flows through curved passages at sufficiently high Reynolds numbers, secondary flows may be generated due to centrifugal forces. Also known as Dean vortices, this form of secondary flow improves fluid mixing, which is essential to achieve significant convective heat transfer. In 2011, Sui et al. [49] experimentally verified this concept using deionised water, with Reynolds number between 300 to 800, using an average heat flux of 50 W/cm^2. The results show that the enhancement in Nusselt number exceeds the increment in friction factor when wavy channels are used over straight channels. This heat transfer enhancement mechanism has also been demonstrated by other researchers [50–53].

2.3.2 Performance Indicators

The enhanced heat transfer offered by microchannels is often accompanied by an undesirable increase in pumping power requirement. Over time as this research topic becomes well-established, there arises the need to devise a performance factor to compare the heat transfer augmentation techniques across the field. In 1971, Webb and Eckert [54] developed a set of equations to define the performance advantage of roughened tubes in heat exchanger design, over smooth tubes of equal diameter. Three design objectives are considered, namely to obtain: 1) reduced heat transfer surface area for equal heat exchange capacity and friction power, 2) increased heat exchange capacity for equal heat transfer surface area and friction power and 3) reduced friction power expenditure for equal heat exchange capacity and heat transfer surface area.

A good example of the procedure to use the three performance equations in heat exchanger applications is demonstrated by Gee and Webb [55]. First, experiments are conducted to determine friction factor and Stanton number data for the smooth tube. Next, the friction factor and Stanton number data for the rough tube are experimentally obtained. Then, the three performance equations can be computed from the aforementioned parameters, since each equation is but an explicit function of these parameters. The results show that the helically rib-roughened tubes using air as working fluid can reduce heat exchange surface area by about 25%, increase heat transfer capacity by about 27%, and reduce pumping power by about 50%.

Of particular interest to many researchers is perhaps the second design objective, which is the increased heat exchange capacity for equal heat transfer surface area and friction power. In 2003, Ligrani, Oliveira and Blaskovich [56] reviewed a series of heat transfer augmentation techniques for internal cooling of turbine airfoils using air as working fluid. They include rib turbulators, pin fins, swirl chambers, dimpled surfaces and surface roughness. The thermo-

hydraulic performance factor was used as a form of performance evaluation over smooth-walled channels. The results show that, for active techniques, the highest thermo-hydraulic performance is achieved by swirl chambers, which can increase heat transfer capacity by up to 150%. For passive techniques, the highest thermo-hydraulic performance is achieved by dimple-smooth arrangements, which can increase heat transfer capacity by up to 140%. On the other hand, the lowest performance is by pin fins, which can perform worse than the smooth channel. There are other similar studies using air as working fluid [57–59].

In 2014, Kathait and Patil [60] conducted a study using water as working fluid, and evaluated the thermo-hydraulic performance of discrete corrugated rib roughened tube relative to smooth tube. The study reported a thermo-hydraulic performance of 95% at Reynolds number of 7,500. Since the study is focused on a macro-scale heat exchanger, the Reynolds number ranges from 7,500 to 50,000.

In 2016, Marschewski et al. [61] investigated the thermo-hydraulic performance of herringbone-grooved microchannels over plain microchannels, with Reynolds number range of 190-510. Using water as working fluid, a thermo-hydraulic performance of about 120% is reported at Reynolds number of 350. The microfluidic test devices consisting of dry etched microchannels are fabricated by a series of microelectromechanical systems (MEMS) and integrated circuit (IC) standard fabrication processes in a class 100/1000 cleanroom.

2.3.3 Overview of Studies on Microchannels

An extensive amount of work has been conducted on single-phase liquid flow in microchannels, and many review papers have been published to date. In 2014, Asadi et al. [62] excellently reviewed 219 articles on both single-phase and two-phase flow in microchannels. The review noted that studies from late 1980s to early 2000s were largely based on experimental approaches, and there were large discrepancies between analytical and experimental results. On the other hand, more recent studies in the past decade used numerical simulations, and correlations were considerably more accurate. Other good reviews are by Sobhan and Garimella [63] in 2001 and Morini [3] in 2004, who reviewed 71 and 90 articles respectively. Notably, Obot [6] quantitatively demonstrated in 2002 that conventional correlations can be used to predict the heat transfer and flow behaviour in microchannels within the accuracy of experimental errors.

In the review by Asadi et al. [62], there is reasonable agreement for friction factor among many studies [64–68] for the laminar flow regime. The studies also show that the experimental friction factor agrees with classical predictions, and microchannel roughness has no effect [64,66,67,69]. In the turbulent regime, however, there is significant deviation between Wu and Little [70] and Yang et al [71], possibly due to the use of different working fluids. In addition, many studies report that the experimental friction factor is lower than the Blasius prediction [64,68,71–75]. In the review by Celata [76] in 2004, the open literature suggests general disagreement among the researchers, with the reported experimental friction factor being higher, lower or similar to classical predictions.

In terms of heat transfer, there is a considerable amount of studies with contradictory conclusions [62]. On one hand, there are studies which found that the experimental Nusselt number is lower than classical predictions [77–82]. On the other hand, there are studies which found that the experimental Nusselt

number is higher than classical predictions [70,74,83–87]. There are also studies which agree with classical predictions for laminar and turbulent flow regimes [88–94].

A summary of selected studies from the early 1990s to early 2000s is presented in Table 2-8. The focus is on comparing the experimental results with classical predictions, using single-phase water as working fluid. The classical predictions include Poiseuille number and Blasius correlation for friction factor, and Hausen and Dittus-Boelter correlations for Nusselt number.

Table 2-8: Selected studies from the 1990s to early 2000s on single-phase flow in microchannels

Study	Year	D_h (µm)	*Re* range	*f*	*Nu*	Critical *Re*
Wang and Peng [81]	1994	311-747	80-3600	NA	<	1000-1500
Peng et al. [95]	1994	133-367	50-4000	>	<	200-700
Yu et al. [72]	1995	19-102	250-20 000	<	>	ID
Harms et al. [91]	1999	404-1923	173-12900	≈	≈	1500
Qu et al. [96]	2000	51-169	6.2-1447	>	NA	ID
Qu et al. [80]	2000	62-169	94-1491	NA	<	ID
Xu et al. [97]	2000	30-344	20-4000	≈	NA	1500
Jiang et al. [98]	2001	300	50-3000	>	>	600
Gao et al. [82]	2002	199-1923	100-8000	≈	<	≈
Qu and Mudawar [89]	2002	349	139-1672	≈	≈	≈
Judy et al. [99]	2002	15-150	8–2300	≈	NA	≈
Bucci et al. [93]	2003	290	2-5272	≈	≈	≈
Liu and Garimella [100]	2004	244-974	230-6500	≈	NA	≈

≈ : Experimental results agree with classical predictions
> : Experimental results are higher than classical predictions
< : Experimental results are lower than classical predictions
NA : Not applicable
ID : Insufficient data

In studies where the experimental results deviate from classical predictions, the researchers proposed correlations for the friction factor and Nusselt number. Table 2-9 presents some proposed correlations from selected studies, with the focus on water as working fluid.

Table 2-9: Proposed correlations from selected studies for single-phase flow in microchannels

Study	Friction factor / Nusselt number correlation
Peng et al. [95]	Laminar: $f = C_{f;l}/Re^{1.98}$ Turbulent: $f = C_{f;t}/Re^{1.72}$ where $C_{f;l}$ and $C_{f;t}$ are constants
Wang and Peng [81]	$Nu = 0.00805Re^{4/5}Pr^{1/3}$ Re>1500
Peng et al. [101]	Laminar: $Nu = C_{h;l}Re^{0.62}Pr^{1/3}$ Turbulent:$Nu = C_{h;t}Re^{0.8}Pr^{1/3}$ where $C_{h;l}$ and $C_{h;t}$ are constants
Adams et al. [86]	$Nu = Nu_{Gn}(1 + F)$ $F = CRe[1 - (D/D_o)^2]$ where C and D_o are constants Nu_{Gn}refers to Gnielinski correlation
Nguyen et al. [102]	Laminar: $Nu = 8.39Re^{0.5} - 1.33Re^{2/3}$ Turbulent: $Nu = 4.73Re^{0.5} - 0.22Re^{2/3}$
Jiang et al. [98]	$Nu = 0.52(X^+)^{-0.62}$ for $X^+ < 0.05$ $Nu = 2.02(X^+)^{-0.31}$ for $X^+ > 0.05$ where $X^+ = RePr\, D_h/L$

In the attempt to resolve the discrepancy among the earlier microchannel studies, Wu and Cheng [90] proposed in 2003 that surface roughness may affect the heat transfer in microchannels. In that same year, Guo and Li [103] suggested surface roughness, axial conduction, and measurement errors as possible reasons. In 2004, Steinke and Kandlikar [104] noted that it is important to apply property correction factors, due to the steep temperature gradient in microchannels. In 2005, Lee et al. [105] noted that careful attention should be given to the boundary conditions applied during the experiments. In 2006, Steinke and Kandlikar [106] proposed entrance region effects, entrance and exit losses, and experimental uncertainties as possible reasons. In summary, the discrepancies among earlier studies have been fairly resolved, and studies from 2002 onwards have presented experimental data verifying the applicability of the continuum theory to microchannel flows.

2.3.4 Laminar-to-turbulent Flow Transition

As indicated in Table 2-8, earlier studies from 1994 to 2001 on microchannels report early laminar-to-turbulent flow transition, at Reynolds number less than 1500 [81,91,95,97,98]. In addition, Mala and Li [107] observed that there is an early laminar-to-turbulent flow transition at $Re \approx 300–900$, and the flow changes to fully developed turbulent flow at $Re \geq 1000–1500$. However, many studies in 2002 and 2003 report no early transition at $Re < 2000$ [73,82,89,93,99,108]. In particular, Sharp and Adrian [109] confirmed in 2004 that the transition to turbulent flow occurs at approximately the same Reynolds numbers as in macroscale channels.

In 2004, Morini [3] reviewed a large number of articles on the laminar-to-turbulent transition in microchannels. For a quick overview, the critical Reynolds number ranges in the review paper are extracted and presented in Figure 2-12. The studies taken as references include the work of Wang and Peng [81], Yu et al. [72], Gui and Scaringe [110], Peng and Peterson [111], Nguyen et al. [102], Harms et al. [91], Mala and Li [107], Ding et al. [112], Celata et al. [108], Yang et al. [71], Pfund et al. [113], Debray et al. [114], Jiang et al. [98], Gao et al. [82], Hegab et al. [115] and Bucci et al. [93].

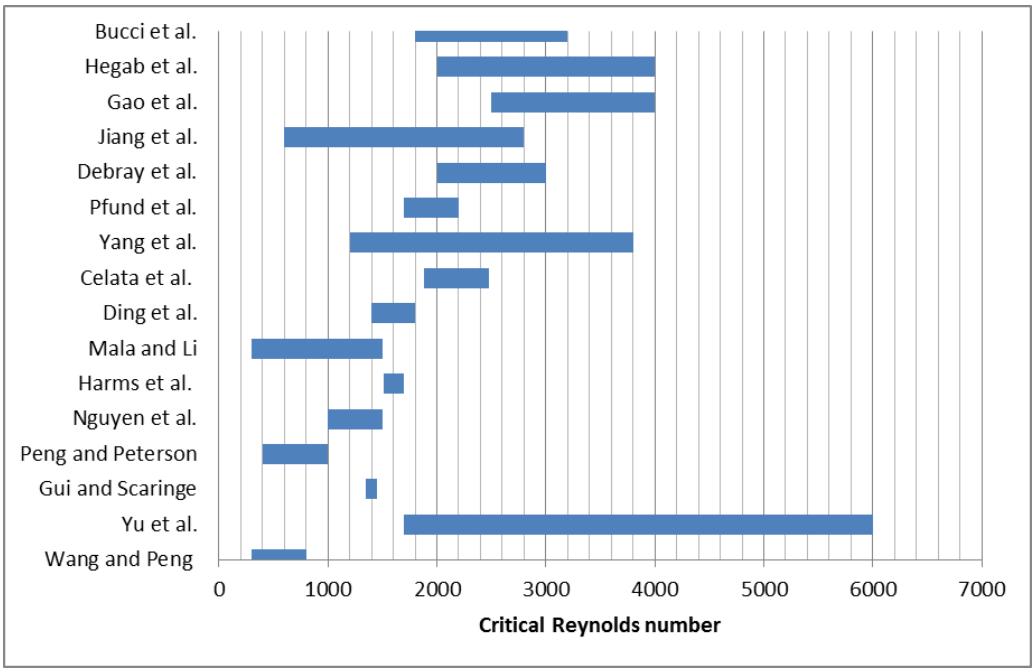

Figure 2-12: Critical Reynolds number ranges for single-phase liquid flow in microchannels

According to Schlichting [116], flow characteristics can be easily observed in the log-log Moody chart. Here, the flow characteristics refer to the laminar, laminar-to-turbulent, and turbulent flow regimes. The laminar-to-turbulent flow transition region is characterised by the indefiniteness of the data when f is plotted against Reynolds number. In his 2004 review, Celata [76] presented two graphs from Bucci et al. [93], which clearly indicates the change in flow and heat transfer behaviour with Reynolds number. The graphs are illustrated in Figure 2-13 and Figure 2-14 respectively. The three flow regimes can then be easily identified from the change in data pattern.

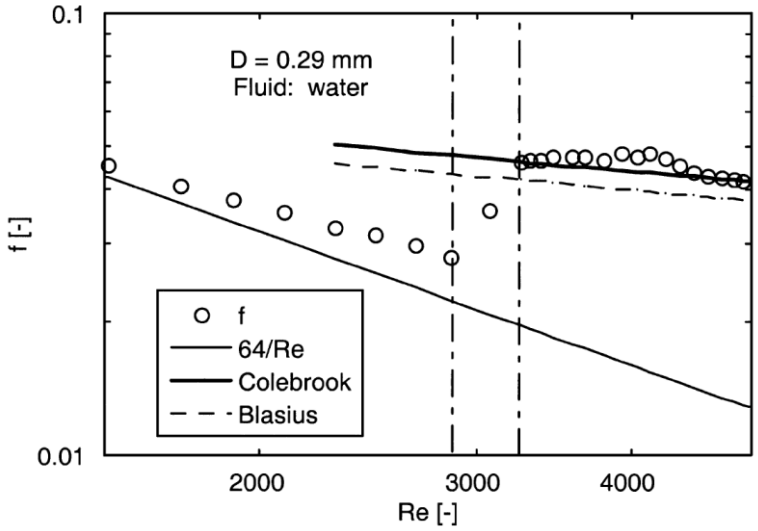

Figure 2-13: Flow regimes observed from friction factor data [93]

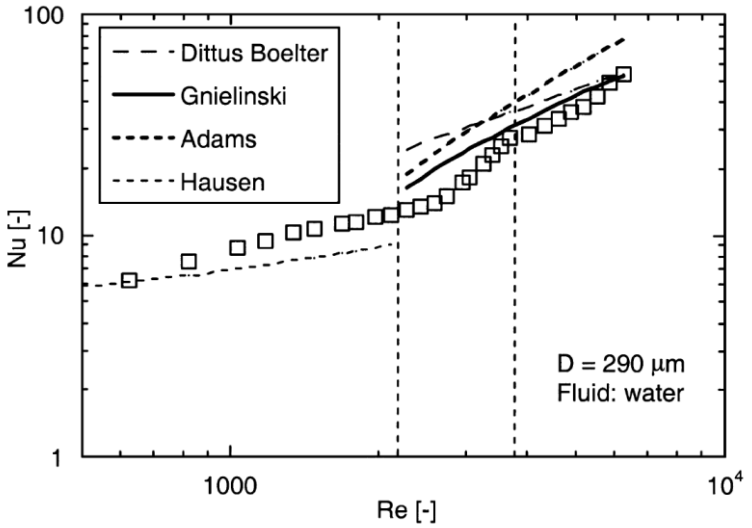

Figure 2-14: Flow regimes observed from Nusselt number data [93]

It is also observed from Figure 2-13 that, for comparison with classical theory, the friction factor is compared with the Hagen-Poiseuille prediction for laminar flow, and the Colebrook and Blasius predictions for turbulent flow. From Figure 2-14, the Nusselt number is compared with the Hausen predictions for laminar flow, and the Dittus Boelter, Gnielinski and Adams predictions for turbulent flow.

In order to accurately determine the Reynolds number range for flow transition, it is useful to compare both the friction factor and Nusselt number data on the same graph. Figure 2-15 shows a sample graph extracted from a study by Celata [108] in 2002. It is clear that both data plots agree on the same Reynolds number range for flow transition.

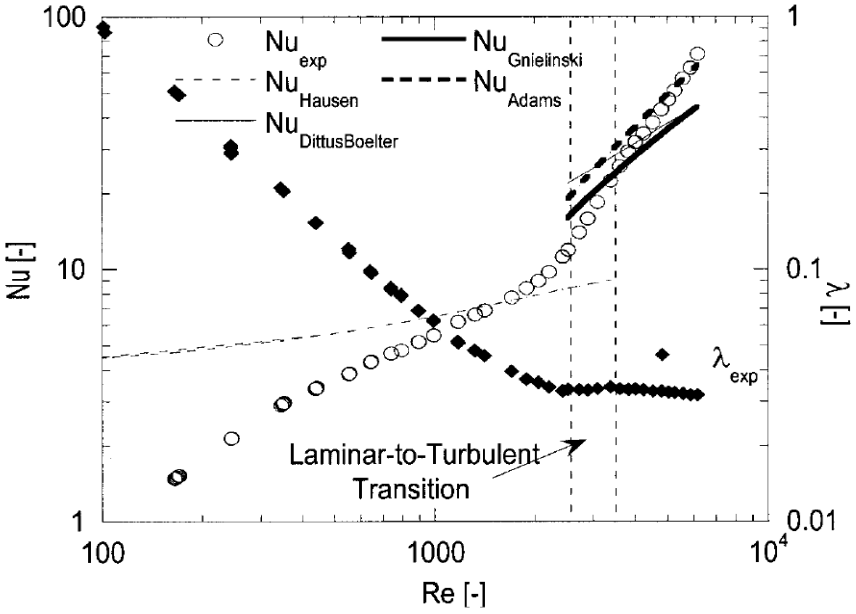

Figure 2-15: Identification of flow transition from the flow and heat transfer behaviour [108]

Interestingly, Bejan [117] showed that the phenomena of laminar-to-turbulent flow transition are manifestations of the Constructal theory [118–120]. The natural choice between laminar and turbulent flow is the one which facilitates the transfer of momentum and heat between the fast and slow fluid layers. In addition, two scaling laws have been proposed to universally characterise laminar-to-turbulent flow transition.

2.4 Biomimicry

Biomimicry can be broadly defined as the process of studying and imitating time-tested systems in nature to solve complex human problems in a sustainable way. The word is derived from two Greek words: bios and mimesis. The former means ‘life’ and the latter means ‘to imitate’. This revolutionary science was first published in 1997 by Benyus [121]. As opposed to Bio-utilisation, such as using natural resources to produce goods for human consumption, and Bio-assisted technology, such as using bacteria to clean water, biomimicry looks to nature as a mentor. In other words, it is based not on extracting from nature, but rather, observing and learning from nature in order to innovate responsibly and sustainably. The core idea is that the most sustainable and efficient systems are found in life forms that have been evolving and adapting to changing conditions for more than 3.8 billion years to date. As the human knowledge reaches a bottleneck, it is humbling to accept that mankind is but a part of nature, and that the only real sustainable model that has passed the test of time is the natural world.

One famous example of biomimicry is Velcro, of which the design was inspired by burrs of the burdock plant. In 1941, the Swiss engineer George de Mestral was removing the burrs his dog picked up on a walk, when he realised how the hooks of the burrs clung to the dog’s fur. His realisation thus led to the invention of Velcro [122]. Another good example is the Shinkansen bullet train in Japan, of which the streamlined forefront is modelled after the kingfisher’s beak, by the engineer Eiji Nakatsu. The train now travels with 30% less noise, 15% less electricity and is 10% faster [123].

In recent years, researchers are becoming increasingly interested in the area of biomimicry. Founded in 2006, the journal ‘Bioinspiration & Biomimetics’ has been publishing interdisciplinary research which connects biology and engineering. The most influential papers include constructing a bio-robotic fin

based on the pectoral fin function in fishes [124], implementing a hydrodynamic imaging system in man-made underwater vehicles that emulate fish sensing [125], constructing a soft-bodied rolling robot that mimics the rolling locomotion of caterpillars [126], as well as increasing the efficiency of thin film solar cells using an anti-reflection coating with surface micro-protuberances similar to those in moth eye facets [127].

In the area of tribology, Greiner and Schäfer [128] developed laser-created textures inspired by scales found on the skin of snakes and certain lizards. Their study showed that this bio-inspired surface morphology is able to reduce dry sliding friction forces by more than 40%. This would have significant impact on all tribological contacts which cannot be lubricated, such as those in a vacuum environment.

In the area of biomaterials, defined as materials used in medical devices, Huebsch and Mooney [129] reviewed the evolution of biomaterials over the past 30 years. In the discussion of future trends, they recognised that understanding the way in which complex dynamic behaviours are achieved in nature may result in the design of new materials which exhibit currently unavailable properties. Furthermore, learning from the cyclic system of plants may significantly diminish the costs and environmental impacts of manufacturing in the chemical and material industries.

In the area of thermal sciences, Chang, Liou and Lu [130] proposed the use of scale-roughened walls as a passive heat transfer enhancement technique. An experimental investigation was conducted, using dry air, on a rectangular channel roughened by scaled surfaces on two opposite walls. The study reported higher thermo-hydraulic performance in the forward flow direction, for Reynolds number above 10,000. The aforementioned “forward flow direction” is analogous to the flow direction for the Inverted Fish Scale profile in the present study.

In 2013, Deshpande, Goh, Goossens and Javdani [131] proposed the use of biomimicry to achieve a carbon-neutral Dover, UK, in the effort to develop coastal eco-cities. This was published as Volume 4 of the LRF Collegium 2013 Series, of which the authors include the present author. As a result of this commitment, the present author has a keen interest in biomimicry, and seeks to employ this revolutionary science to enhance the microscale heat transfer in macro geometry.

2.5 Research Gaps

While exceptional heat transfer rates are well associated with microchannels, microchannel cooling has yet to be implemented on a large-scale basis in the industry. The main challenges lie in the complex and non-economical nature of microfabrication processes, which include microelectromechanical systems (MEMS), photolithographic-based processes and X-ray micromachining [3]. These microfabrication processes, including the tolerances and compatibility of material, have been reviewed [132].

In view of this, Kong and Ooi [11] developed a system for microscale heat transfer in macro geometry in 2013. By securing a conventionally-sized cylindrical insert concentrically within a conventionally-sized circular channel, an annular microchannel can be created. Using water as working fluid, their study reported heat transfer coefficient values of at least 20 $kW/m^2 \cdot K$ at Reynolds number of 5,200, for a microchannel gap of 300 μm. This demonstrates the feasibility of combining two macro geometries to achieve heat transfer effects comparable to that of typical microchannels. This approach is relatively simple and less costly since the macro geometries can be fabricated using conventional machining processes, such as turning, drilling and milling.

Moving forward, the macro geometry readily presents itself as a suitable means of implementing passive heat transfer enhancement techniques. For example, surface modifications can be introduced on the insert to influence the flow pattern, thereby enhancing heat transfer. There currently exists no configuration for enhanced microscale heat transfer in macro geometry, of which the geometrical enhancement profile is completely quantified in the proposed working correlations to evaluate the heat transfer and pressure drop for practical applications.

To address this research gap, the present Ph.D. research study aims to develop a novel nature-inspired configuration to enhance the microscale heat transfer in macro geometry using conventional machining processes, and formulate working correlations for the average Nusselt number and friction factor. The nature-inspired geometrical enhancement profiles are designed to be simple, such that their geometries are mathematically quantifiable in the correlations and can be machined conventionally.

The literature search also shows that the microscale heat exchanger devices are currently still in the initial development stage. There is a growing interest in this area in the past decade, as seen by the emergence of several commercial providers [8]. The main applications include electronics cooling, heat exchanger in offshore facilities and the automotive and aerospace industries. While high heat transfer, compactness and low fluid pressure drop are critical in electronics cooling, the design objectives for offshore heat exchangers are high heat transfer at high pressures and temperatures, along with low susceptibility to fouling and corrosion. In other words, the pressure drop is of less importance. Hence, the design objectives vary according to the practical applications.

In general, microchannels are created directly on the material surfaces, and only come with a rigid pattern for each fabricated microchannel. On the other hand, the proposed configuration for enhanced microscale heat transfer in macro geometry has the potential to offer a one-size-fits-all solution to the different design objectives, since the insert can be easily removed and assembled into the test module. Hence, different insert enhancement profiles can be used to meet the different design objectives, enhancing the versatility of the system.

It is hoped that the present Ph.D. work would eventually result in a large-scale implementation of conventionally-sized heat exchangers employing microscale passages.

Chapter 3 Research Methodology

This chapter explains the research methodology used in the present study. The first section describes how the enhanced microscale heat transfer is achieved in macro geometry. The second and third sections detail the selection of independent and dependent parameters, respectively. The independent variables include the microchannel profile, Reynolds number and heat flux. The dependent variables include both thermal and hydrodynamic considerations. For thermal consideration, convective heat transfer coefficient and Nusselt number are determined. For hydrodynamic consideration, pressure drop and friction factor are determined. More importantly, the thermo-hydraulic performance, which represents the increased heat transfer capacity for equal heat transfer surface area and pumping power, is also computed.

3.1 Model Description

The 300 μm annular microchannel is created by securing a cylindrical insert within a circular channel, as shown in Figure 3-1. Both the insert and the circular channel are of macro scale, where the insert outer diameter and channel inner diameter are 19.4 mm and 20 mm, respectively. While the hydraulic diameter is 600 μm, a gap size of 300 μm is used to describe the annular microchannel. This follows the convention in parallel plates, in view that a sufficiently narrow annular channel exhibits similar flow characteristics to the flow in parallel plates [18].

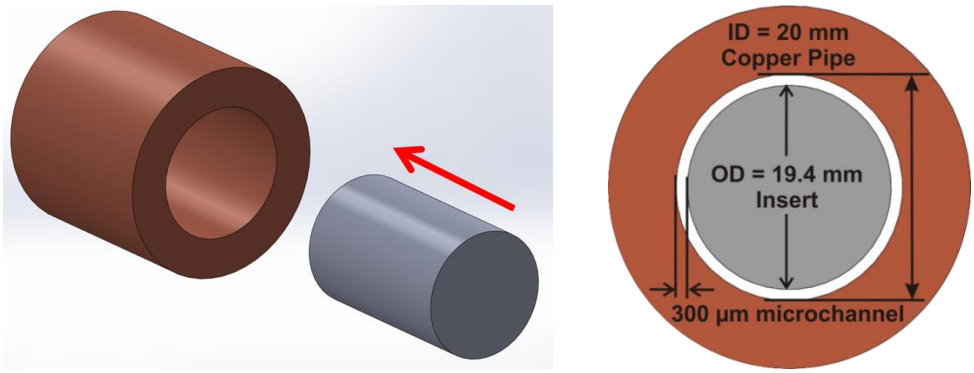

Figure 3-1: Annular microscale passage in macro geometry

In this study, three series of geometrical profiles are introduced on the outer surface of the insert, to investigate their effects on the heat transfer and flow characteristics of the microchannel. The three series are Inverted Fish Scale (IFS), Fish Scale (FS) and Durian (D) profile, respectively. The Plain profile with no protrusion is used as the benchmark for comparison. The insert profiles are shown in Figure 3-2.

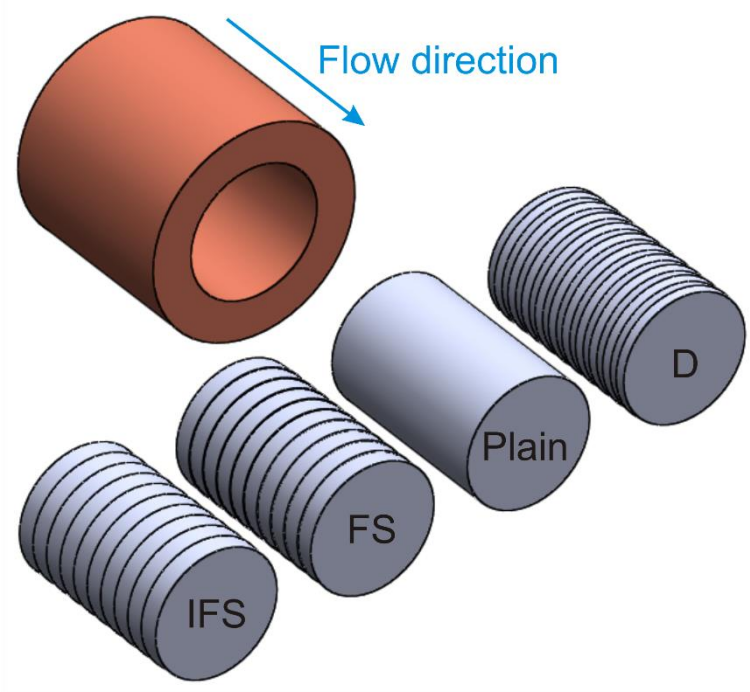

Figure 3-2: Insert profiles for enhancement

The enhancement profiles are designed based on inspiration from nature, as illustrated in Figure 3-3. First, the Inverted Fish Scale profile is conceptualised in view that fishes are naturally streamlined to minimise flow disturbance when they swim forward. However, flow disturbances are imperative to enhance heat transfer. Therefore, the scaly profile is arranged to oppose the flow direction so as to cause maximum flow disruption, hence the name "Inverted" Fish Scale. Second, in view that the penalty for heat transfer enhancement is the accompanying high friction losses, the Fish Scale profile is also investigated for its streamlined flow characteristics. Third, the durian, being regarded as the king of fruits in Southeast Asia, is distinctive for its thorn-covered husk. In fact, its name is derived from 'duri', which means 'thorn' in the Malay and Indonesian languages. The copious pointed protuberances of the durian husk have the potential to cause flow disturbances and enhance the heat transfer.

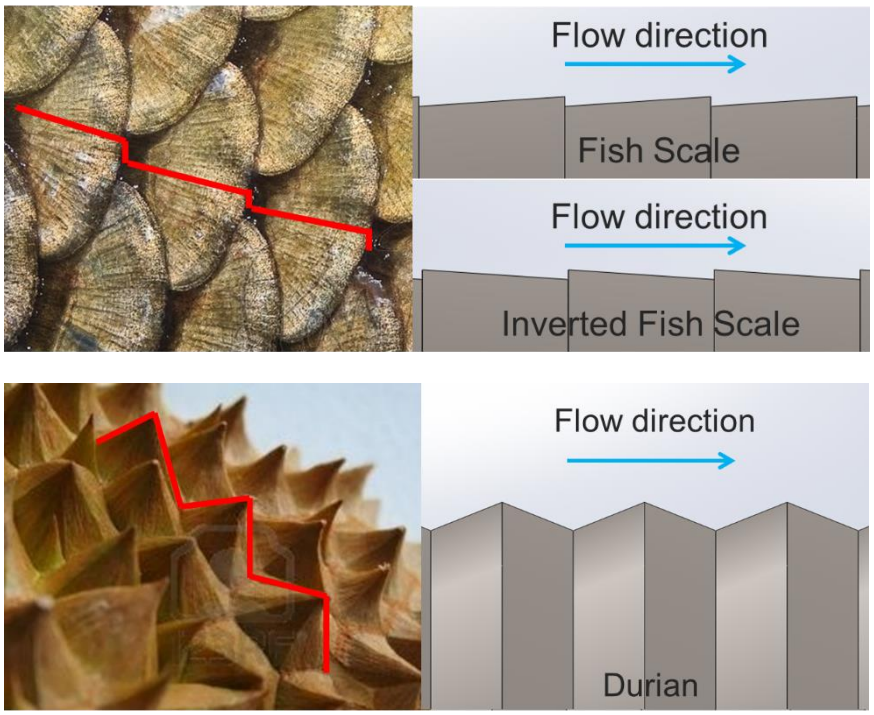

Figure 3-3: Nature-inspired insert profiles

Although the proposed geometries are three-dimensional in their natural forms, the insert profiles adopted in the present study are all designed to have full rotational symmetry about the longitudinal axis. By removing one degree of freedom, the machining process can be significantly simplified. Consequently, the inserts can be fabricated using conventional machining processes, such as Computer Numerical Control (CNC) profile turning.

The insert is secured within the circular channel by means of two insert holders at each end of the insert, as shown in Figure 3-4. Water is driven through the annular microchannel by a pump. Heat is supplied to the water via the inner surface of the circular channel. In other words, the heat transfer surface area is constant. Therefore, by virtue of Newton's law of cooling, the heat transfer rate is improved by increasing the heat transfer coefficient of the fluid flow. This is achieved using the inserts of various enhancement profiles, which influence the flow pattern and cause thinning of the velocity and thermal boundary layers.

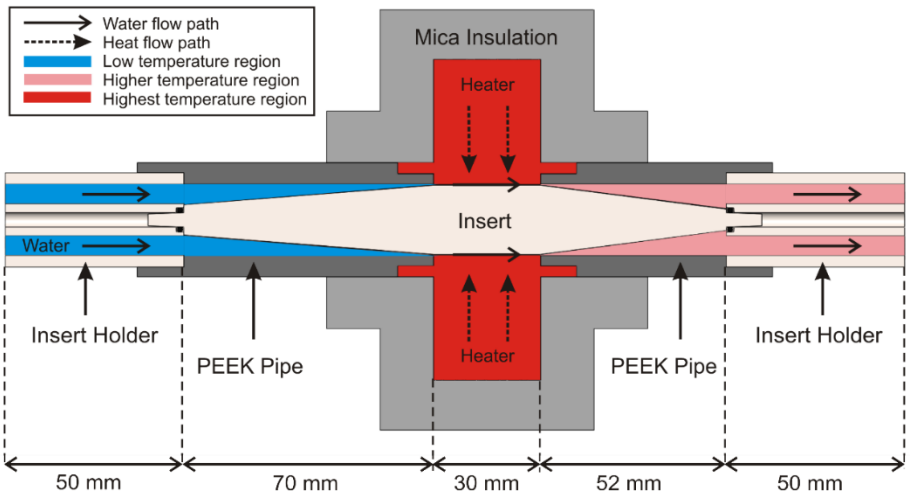

Figure 3-4: Schematic diagram of test module

3.2 Independent Parameters

3.2.1 Microchannel Profile

A total of 22 microchannel profiles are being tested, which include 7 profiles each for the three nature-inspired enhanced Inverted Fish Scale (IFS), Fish Scale (FS) and thorny Durian (D) microchannel series, along with the Plain microchannel. The Plain microchannel with no protrusion is used as the benchmark for comparison. For fair comparison, the insert volume is designed to be the same across all the series, with a mean diameter of 19.4 mm. This means that the mean microchannel gap size of 0.3 mm, and therefore the volume of fluid passing through the microchannel for a particular flow rate, is fixed across all the series throughout the study. The microchannel profiles are illustrated in Figure 3-5 for the ease of understanding.

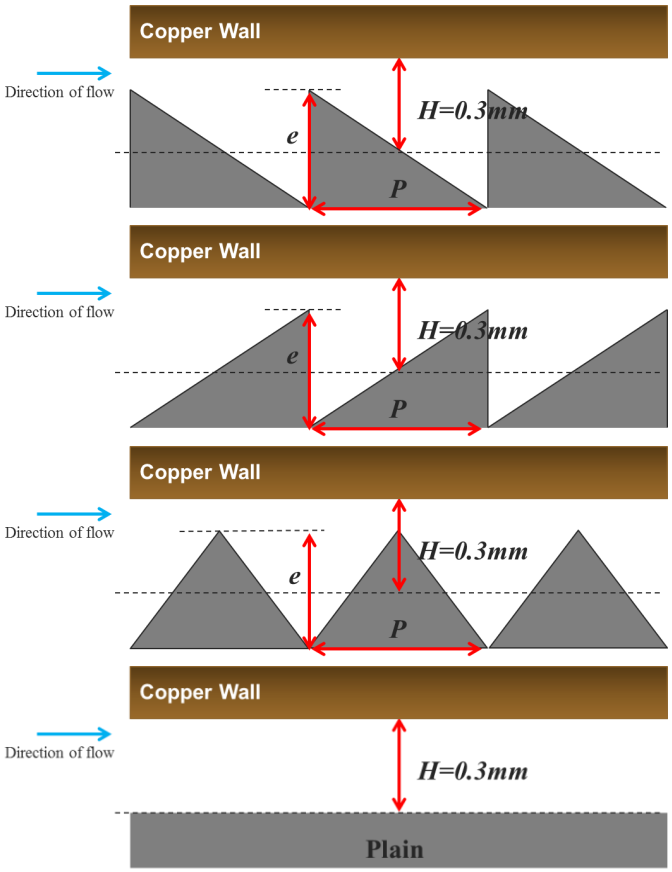

Figure 3-5: Geometrical parameters for the IFS, FS, D and Plain profile (top to bottom)

Within each nature-inspired enhanced microchannel series, the effects of two geometrical ratios are studied. They are the ratio of scale/thorn height (*e*) to mean channel height (*H*), and ratio of scale/thorn pitch (*P*) to scale/thorn height (*e*). The *e*/*H* ratio study includes 0.1, 0.3, 0.5 and 0.7, at constant *P*/*e* ratio of 10. The *P*/*e* ratio study includes 5, 10, 15 and 20, at constant *e*/*H* ratio of 0.5. *H* represents the mean channel height, which is fixed at 0.3mm in the whole study. A total of 22 insert profiles are used, as listed in Table 3-1. The naming convention of the inserts is as follows: (series)_(scale/thorn height in mm)-(scale/thorn pitch in mm).

Table 3-1: 22 microchannel profiles

	IFS Series	FS series	D Series	*e*/*H* Ratio	*P*/*e* Ratio
Plain	IFS_*e*0.03-*P*0.3	FS_*e*0.03-*P*0.3	D_*e*0.03-*P*0.3	0.1	10
	IFS_*e*0.09-*P*0.9	FS_*e*0.09-*P*0.9	D_*e*0.09-*P*0.9	0.3	10
	IFS_*e*0.15-*P*1.5	FS_*e*0.15-*P*1.5	D_*e*0.15-*P*1.5	0.5	10
	IFS_*e*0.21-*P*2.1	FS_*e*0.21-*P*2.1	D_*e*0.21-*P*2.1	0.7	10
	IFS_*e*0.15-*P*0.75	FS_*e*0.15-*P*0.75	D_*e*0.15-*P*0.75	0.5	5
	IFS_*e*0.15-*P*2.25	FS_*e*0.15-*P*2.25	D_*e*0.15-*P*2.25	0.5	15
	IFS_*e*0.15-*P*3.00	FS_*e*0.15-*P*3.00	D_*e*0.15-*P*3.00	0.5	20

In layman terms, the *e*/*H* ratio study varies the scale/thorn height with respect to a fixed mean channel height, while keeping the angle of attack constant. This means that the minimum gap through which the fluid flows decreases as *e*/*H* ratio increases. This is illustrated in Figure 3-6, where the IFS series is used for the purpose of explanation. The figures are drawn to scale, at a length of 3 mm.

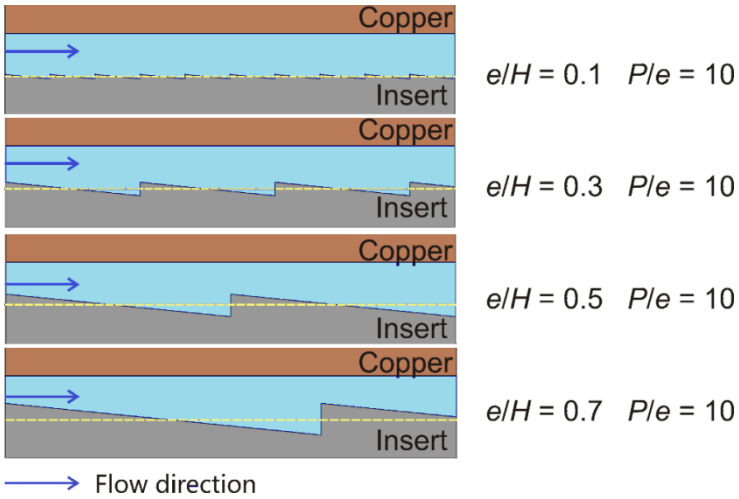

Figure 3-6: *e*/*H* ratio study for IFS series

On the other hand, the *P*/*e* ratio study varies the angle of attack, while keeping the scale/thorn height constant. This means that the slope of each scale/thorn becomes less steep as *P*/*e* ratio increases. Another way to view the *P*/*e* ratio study is in terms of the number of scale/thorn protrusions. As the *P*/*e* ratio decreases, the number of scale/thorn protrusions of the same height increases, resulting in more flow disruptions. This is illustrated in Figure 3-7, where the IFS series is used for the purpose of explanation. Similarly, the figures are drawn to scale, at a length of 3 mm.

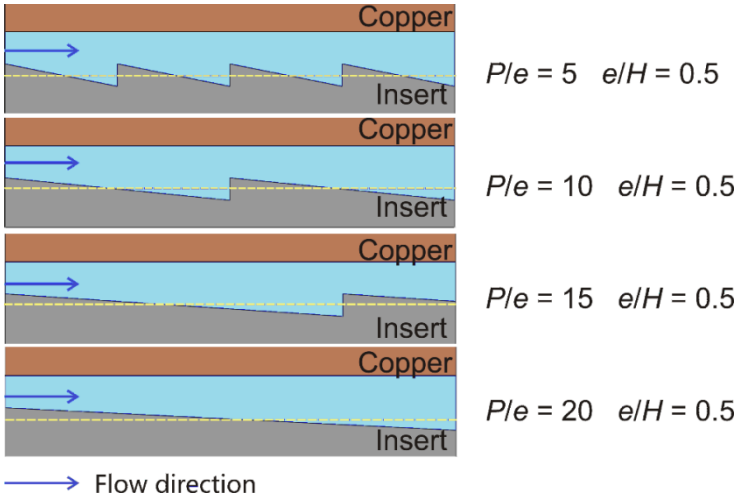

Figure 3-7: *P*/*e* ratio study for IFS series

3.2.2 Reynolds Number

Based on the literature review in Chapter 2, the Reynolds number range in microchannels generally falls between 500 and 3,000. This is generally lower than that of a conventional macro-scale flow passage, considering that the hydraulic diameter is smaller and the flow rate is lower in microchannels. As a guideline, the laminar-to-turbulent flow transition in parallel plates occurs at $2{,}200<Re<3{,}400$.

In the present study, the Reynolds number range was initially selected to be between 1,300 and 4,600. Assuming that the continuum mechanics theory for conventionally-sized channels is applicable to microchannel flow, this would cover both laminar and non-laminar flows. Correspondingly, the flow rates at which the experiments are conducted are between 2.0 and 7.0 L/min. While this Reynolds number range is suitable for the study of the plain microchannel, preliminary results for the enhanced microchannels show signs of early laminar-to-turbulent flow transition. To further investigate this, the Reynolds number range was extended to be $350<Re<4{,}600$. This corresponds to a flow rate range between 0.5 and 7.0 L/min. For a detailed investigation, the data is collected at an interval of 0.25 L/min.

3.2.3 Heat Flux

A removal of heat flux in excess of 100 W/cm^2 is often required in the microelectronics and power electronics industries [113]. Specifically, the heat flux target is 300 W/cm^2 in 2007, according to a review by Agostini et al. [7]. Among the researchers, a wide range of heat fluxes has been experimentally tested, as listed in Table 3-2.

Table 3-2: Heat flux tested by selected studies

Study	Heat flux (W/cm^2)
Koşar and Peles, [133]	3.8 to 167
Dominic et al. [134]	4.5 and 6.5
Kong and Ooi [11]	5.3 to 37.1
Deng et al. [47]	13.3, 20 and 26.7
Sio-Ho et al. [135]	50 and 100
Qu and Mudawar [89]	100 and 200

As mentioned in Section 1.2, the present study focuses on single-phase liquid flow. Hence, the heat flux must be carefully controlled to avoid boiling of the water. The temperature of the heated copper wall, which is in contact with the flowing water, is set to assume an upper limit of 80°C. This safety factor is incorporated in view that any localised hot spot along the imperfect copper surface could possibly induce localised boiling.

A preliminary test was conducted to determine a suitable heat flux for higher flow rates ranging from 2.0 to 7.0 L/min. The highest possible heat input for 2.0 L/min is 1000 W, as the copper wall temperature rises to about 75°C. Hence, a constant heat input of 1000 W, which is equivalent to a heat flux of 53 W/cm^2, is used. On the other hand, a constant heat input of 250 W, which is equivalent to a heat flux of 13.3 W/cm^2, is used for lower flow rates ranging from 0.5 to 2.0 L/min.

In addition, careful attention has been given to the design of the test module, such that the flow channel is subjected to a constant and uniformly distributed heat flux during the experiments. The description of the experimental test module is detailed in Section 5.4.

3.3 Dependent Parameters

3.3.1 Thermal Consideration

3.3.1.1 Convective Heat Transfer Coefficient

As mentioned in Section 2.1.1, any gain in the average convective heat transfer coefficient h results in an improvement in the total heat transfer rate, by virtue of Newton's law of cooling. As a guideline, the typical h values are at most 10 kW/m^2·K, for single-phase liquid water in conventionally-sized channels. The h results in the present study should exceed the aforementioned value, if

microscale heat transfer effects are to be successfully achieved in macro geometry. Furthermore, the *h* results ought to be much higher for the enhanced microchannels, should the enhancement profiles be advantageous. For example, Koşar and Peles [133] studied water flow in enhanced microchannel using pin fins, and obtained a maximum heat transfer coefficient of around 55 $kW/m^2 \cdot K$ at $Re \approx 112$.

In order to accurately determine the average convective heat transfer coefficient, as many thermocouples as possible should be used to measure the wall temperature in the measurement system. However, the intrinsically short length of microchannels makes it challenging to install a large number of thermocouples along the flow direction. In some studies, the average heat transfer coefficient values were calculated from as few as three thermocouples readings [49,136]. In the previous study by Kong [12], six thermocouples were used over a microchannel length of 30 mm. As an improvement over previous studies, ten thermocouples are installed across the same length of 30 mm in the present study.

3.3.1.2 Nusselt Number

The average Nusselt number is computed based on the average convective heat transfer coefficient and other measured key parameters. The average Nusselt number values for the Plain microchannel are used to compare with classical predictions, for validation purpose. On the other hand, the values obtained for the enhanced microchannels are processed using a non-linear least-squares curve-fitting approach to yield a Nusselt number correlation. A Nusselt number correlation is proposed for each of the IFS, FS and D series, respectively. For the purpose of this study, the Nusselt number refers to the average Nusselt number, unless otherwise stated.

The normalised Nusselt number is the ratio of Nusselt number of the enhanced microchannel to that of the Plain microchannel. It is computed to understand the extent of improvement in Nusselt number, when the enhanced microchannel is used over the Plain microchannel. It is also used to compute the thermo-hydraulic performance.

3.3.2 Hydrodynamic Consideration

3.3.2.1 Pressure Drop

The improvement in convective heat transfer coefficient in microchannels is often accompanied by an increase in pressure drop. As the flow channel becomes smaller, the wall surface area to volume ratio increases, thereby introducing higher frictional resistance to the flow. This parameter is measured and monitored, in order to ensure that the pumping requirement is realistic and can be readily met by a commercially available pump.

3.3.2.2 Friction Factor

The average Darcy friction factor is computed based on the pressure drop and other measured key parameters. It is the dimensionless form of pressure drop in internal flow. The average friction factor values for the Plain microchannel are used to compare with classical predictions, for validation purpose. On the other hand, the values obtained for the enhanced microchannels are processed using a non-linear least-squares curve-fitting approach to yield a friction factor correlation. A friction factor correlation is proposed for each of the IFS, FS and D series, respectively. For the purpose of this study, the friction factor refers to the average friction factor, unless otherwise stated.

The normalised friction factor is the ratio of friction factor of the enhanced microchannel to that of the Plain microchannel. It is computed to understand the extent of increase in friction factor, when the enhanced microchannel is used over the Plain microchannel. It is also used to compute the thermo-hydraulic performance.

3.3.3 Performance Indicator

As discussed in Section 2.3.2, there are three performance indicators to define the performance advantage of enhanced tubes in heat exchanger design, over smooth tubes of equal diameter [54]. In the present study, the focus is on the increased heat exchange capacity for equal heat transfer surface area and friction power requirement. A higher heat transfer capacity may be advantageous in obtaining an increased heat duty, or securing a reduced mean temperature difference. Also known as the thermo-hydraulic performance, this performance indicator is widely used by researchers to compare heat transfer augmentation techniques across the field [55,56,130].

The thermo-hydraulic performance is computed based on the normalised Nusselt number and the normalised friction factor, using the equation provided by Eqn. (5-18) in Section 5.9.3.

3.4 Scope of Investigation

The present work focuses on the internal flow of single-phase liquid in an annular microscale passage created in macro-scale geometry. The forced convective steady-state flow of a constant-property incompressible Newtonian fluid through a stationary, nonporous channel is considered. Similar to other studies involving single-phase liquid flow in microchannels [89,105,106], the compressibility effect and slip boundary condition are not considered, and the continuum mechanics theory is assumed to be valid when the hydraulic diameter is larger than 1 μm.

Both physical measurements and numerical simulations are carried out, using distilled water as working fluid. With a Reynolds number range of 350-4600, the laminar, transitional and turbulent flow regimes are studied. For the purpose of fair comparison between the enhanced and plain microchannel, the mean channel gap size is fixed at 300 μm for the whole study. The effect of roughness is not considered, for the reasons detailed in Section 5.4.6.1.

The effects of axial conduction along the wall are not considered. According to Lu and Wang [137], when the Reynolds number is lower than 150, axial heat conduction has a significant influence on the overall heat transfer, and the heat transfer deteriorates. However, the Reynolds number range in the present study is well above the stated value. To further verify this, the axial temperature distribution across both the outer and inner wall of the flow passage is monitored. From all the 600 steady-state measurements, the maximum temperature difference between the two ends of the insert is only 7 K, and that across the copper wall is only 4 K. Therefore, the effect of axial heat conduction is not considered to be of critical importance to the results.

Chapter 4 Numerical Model

This chapter describes the three-dimensional numerical conjugate heat transfer model used in the present study. The numerical model provides useful insight into the flow field, which cannot be directly and completely observed from the measurement system. These insights are valuable in explaining the physics behind the measured results. The discussion in this chapter includes the Computational Fluid Dynamics code, governing equations, model simplification, turbulence model, mesh settings, boundary conditions and convergence criteria. The numerical model is validated through the comparison of its predictions with the measurements, which will be discussed in Section 7.2, Section 8.2 and Section 9.2.

4.1 Computational Fluid Dynamics

Computational Fluid Dynamics (CFD) is a computer-based tool for simulating the behaviour of systems involving fluid flow, heat transfer, and other related physical processes. It solves the Navier-Stokes equations numerically over a particular region of interest, with user-specified boundary conditions. There are two commercially available CFD simulation codes by ANSYS, namely Fluent and CFX. The latter is employed because thermophysical variation of the working fluid based on the International Association for the Properties of Water and Steam (IAPWS) [138] database can be conveniently employed.

Liu and Garimella [100] confirmed that a conventional CFD analysis approach can be employed to offer reliable predictions for the flow characteristics in microchannels with hydraulic diameters from 244 to 974 μm at Reynolds numbers ranging from 230 to 6,500. In the present study, the hydraulic diameter is 600 μm, and the Reynolds number ranges from 350 to 4,600.

4.2 Governing Equations

The three-dimensional unsteady form of Navier-Stokes equations consists of five partial differential equations: one time-dependent continuity equation for conservation of mass, three time-dependent conservation of momentum equations and one time-dependent conservation of energy equation. Derived by Navier and Stokes in the early 1800's [139], these five equations describe how the velocity, pressure, temperature, and density of a moving fluid are related. Table 4-1 lists the four independent variables and six dependent variables in the problem. All the dependent variables are functions of all four independent variables.

Table 4-1: Independent and dependent variables in Navier-Stokes equations

Independent variables	Dependent variables
x spatial coordinate of some domain	*u* component of velocity vector in the *x* direction
y spatial coordinate of some domain	*v* component of velocity vector in the *y* direction
z spatial coordinate of some domain	*w* component of velocity vector in the *z* direction
Time *t*	Pressure *p*
	Temperature *T* in the energy equation
	Density ρ

In the present study, the scope is limited to steady-state conditions. The mass, momentum, and energy conservation equations under steady-state conditions are listed in the following sections.

4.2.1 Mass Conservation Equation

Eqn. (4-1) shows the mass conservation equation [140]. It is valid for both incompressible and compressible flows.

$$\nabla \cdot \left(\rho_f \, \boldsymbol{U}_f\right) = 0 \tag{4-1}$$

The term on the left describes the net flow of mass out of the element across its boundaries and is called the convective term.

4.2.2 Momentum Conservation Equations

Eqn. (4-2) shows the momentum conservation equation in a stationary reference frame [140].

$$\nabla \cdot \left(\rho_f \, \boldsymbol{U}_f \otimes \boldsymbol{U}_f\right) = -\nabla p + \nabla \cdot (\bar{\bar{\tau}}) + \rho \vec{g} + \vec{F} \tag{4-2}$$

where p is the static pressure, $\bar{\bar{\tau}}$ is the stress tensor, and $\rho \vec{g}$ is the gravitational body force. $\vec{F}$ includes external body forces and other model-dependent source terms such as porous-media and user-defined sources. The stress tensor is defined as:

$$\bar{\bar{\tau}} = \mu \left[\left(\nabla \boldsymbol{U}_f + \nabla {\boldsymbol{U}_f}^T\right) - \frac{2}{3} \nabla \cdot \boldsymbol{U}_f I\right] \tag{4-3}$$

where μ is the molecular viscosity and I is the unit tensor. The second term on the right represents effect of volume dilation.

The momentum conservation equation is simply another form of Newton's second law, which states that the rate of change of momentum of a fluid particle equals the sum of the forces on the particle. The terms on the left represent the rate of increase of momentum per unit volume of a fluid particle, whereas the terms on the right represent the sum of forces on the fluid particle, due to pressure, viscous, gravity and external body forces respectively.

4.2.3 Energy Conservation Equation

The 3D conjugate heat transfer model accounts for convection in the fluid regions, as well as thermal conduction in the solid regions. Eqn. (4-4) shows the energy conservation equation for the fluid domain.

$$\nabla \cdot \left(\, \rho_f \, \boldsymbol{U}_f \, h_{e,f}\right) = \nabla \cdot \left(k_f \, \nabla T_f\right) + S_{E,f} \tag{4-4}$$

Eqn. (4-5) shows the energy conservation equation for the solid domain.

$$0 = \nabla \cdot (k_S \, \nabla T_S) + S_{E,S} \tag{4-5}$$

The Navier-Stokes equations are solved numerically to obtain the flow field and heat transfer solutions for the test module.

4.3 Model Simplification

The simulation model is simplified to some extent in order to ease the computational load. They include the simplifications from the fabricated test module, symmetry modelling, and some assumptions.

4.3.1 Simplification from Practical Case

In the simplification from the practical case, some features are removed to obtain a clean geometry. The removal of these localised non-critical features would not affect the results for the microchannel zone. They include the protruding ends of the insert, the thermocouple holes in the copper block, the flat surface for wrenching purposes of the insulation pipes and insert holders, the threaded section of the insulation pipe for assembly purpose, as well as the hole in the insert holder that is used to secure the insert. The fillet edges of the insert holder are also removed to improve the mesh quality. In addition, a circular pipe of length 10 mm is extended from the insert holder that is connected to the rest of the piping system. This is so that uniform velocity boundary condition may be applied at the inlet of the test module, and pressure losses may be better approximated.

Figure 4-1 shows the difference between the fabricated and simplified test module, where the insulation cover is partly removed to reveal the internal components. On the other hand, Figure 4-2 shows the cross-section of the whole test module.

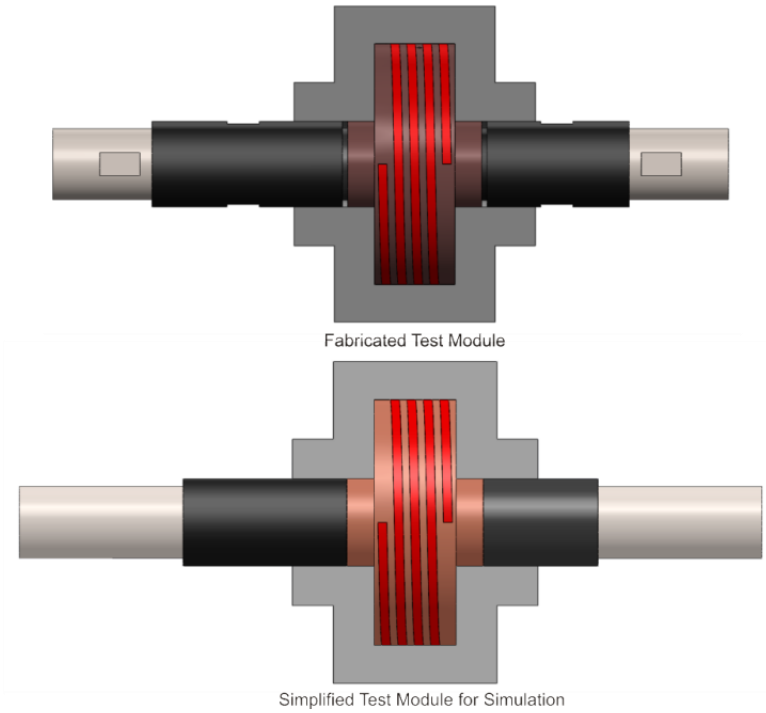

Figure 4-1: Fabricated and simplified test module, showing only the cross-section of insulation cover

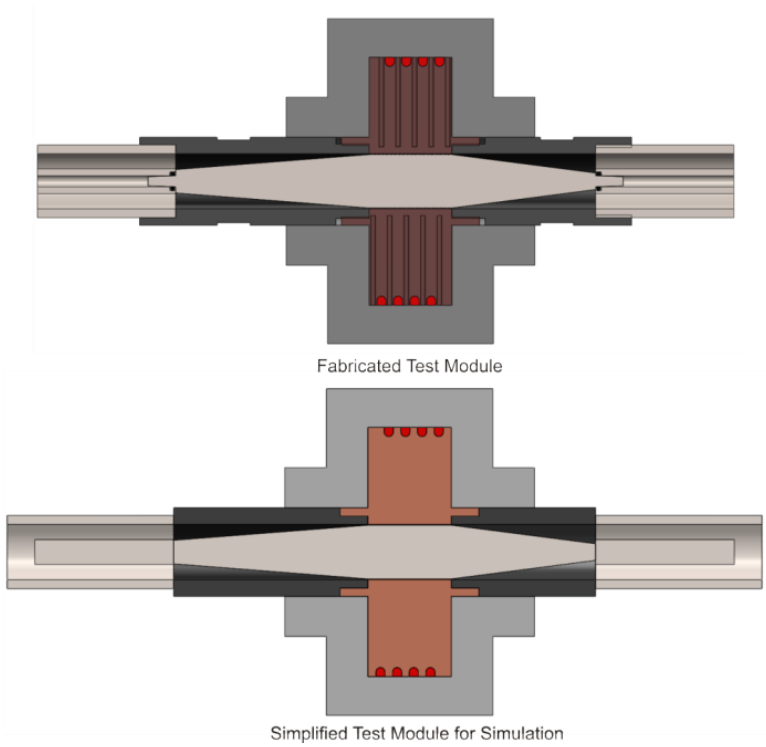

Figure 4-2: Fabricated and simplified test module, showing the full cross-section

4.3.2 Symmetry Modelling

Due to the symmetrical nature of the test module, a quarter-symmetry model can be employed instead of the full model. This helps to save computational resources and time. To do so, the spiral heating coil is modelled as four cylindrical coils. This modification does not affect the computational results, since the coils are modelled as uniform volumetric heat sources, and the total heat rate generated is still the same. Next, two planes of symmetry are introduced to transform the full model into the quarter-symmetry model, as illustrated in Figure 4-3.

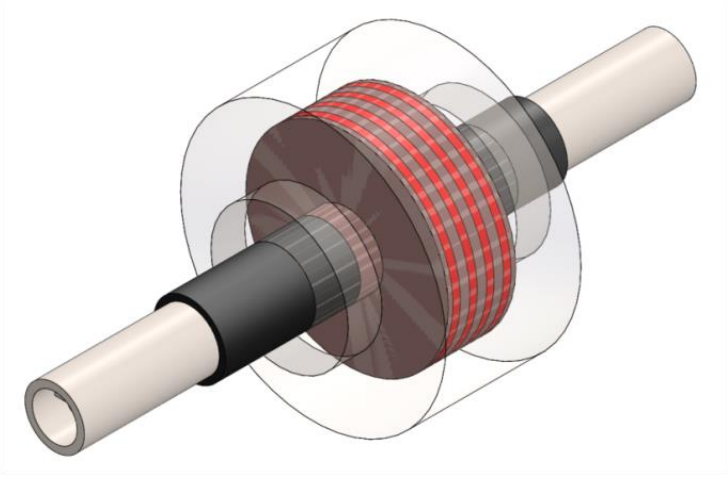

Figure 4-3: Full model versus quarter-symmetry model

In addition, the quarter-symmetry model is checked for its solution accuracy. A comparison between the quarter-symmetry and full model shows a discrepancy of 0.12% and -0.10% for the heat transfer coefficient and pressure drop respectively, using the Plain microchannel at 7 L/min. This implies that the quarter-symmetry model is a good approximation of the full model, with a minimal compromise on the solution accuracy.

4.3.3 Model Scope

First, the variation of the fluid properties with temperature is considered, as the temperature gradients are considerably steep near the wall for a microchannel. Therefore, the International Association for the Properties of Water and Steam (IAPWS) [138] database in ANSYS-CFX is activated. On the other hand, all solid properties are assumed to be constant, using the reference state at atmospheric pressure and room temperature 28°C. Specifically, the solid materials are copper, stainless steel insert and insert holders, PEEK insulation pipes and GL-P insulation cover. The solid properties do not change significantly for the temperature range occurred in this study. For example, the thermal conductivity of copper decreases by about 1.5%, while the specific heat increases by about 2.5%, when the temperature increases from 30°C to 100°C. The solid properties used in the numerical model are listed in Table 4-2.

Table 4-2: Solid properties at standard temperature and pressure

Solid material	Density (kg/m^3)	Thermal conductivity (W/m·K)	Specific heat (J/kg·K)
Copper	8,933	401	385
Stainless steel	7,854	60.5	434
PEEK insulation pipes	1,400	0.92	1,800
GL-P insulation cover	2,100	0.31	500

Second, thermal contact resistance at solid-solid interfaces, such as the interface between the heating coil and the copper block, is not considered. By assuming a perfect contact in the simulation model, the computed temperature values of the heating coil are lower than those in the actual case. For example, the simulation predicts a maximum heating coil temperature of 80 °C, while the measured value is 91 °C. This means that there is a possibility of overheating in the measurement system, due to the higher-than-expected temperature of the heating coil. However, a high level of safety factor has been incorporated in the design of the measurement system. The selected material for the insulation cover, which is in contact with the heater, can withstand a temperature of up to 500 °C under long-term operation. Hence, this does not pose any problem at all.

Third, thermal expansion of the solid components is not considered. To prevent boiling, the copper wall temperature is kept below 80 °C. At best, the copper wall temperature ranges from 28 °C to 39 °C for the IFS_*e*0.21-*P*2.1 microchannel at 6.5 L/min and 1000 W. For this temperature change, the expansion of the copper wall diameter is about 4 µm, from an initial value of 20 mm. This corresponds to 0.7% expansion of the nominal microchannel gap at 300 µm. At worst, the copper wall temperature ranges from 28 °C to 75 °C for the Plain microchannel at 2 L/min and 1000 W. The expansion of the copper wall diameter is about 15 µm, which corresponds to 2.5% of the nominal microchannel gap.

4.4 Turbulence Model

4.4.1 Overview of Computational Approaches

In general, there are three approaches to solving the Navier-Stokes equations numerically. They are Direct Numerical Simulation (DNS), Large Eddy Simulation (LES), and Reynolds Averaged Navier-Stokes Simulation (RANS). Table 4-3 [140] summarises the advantages and disadvantages of the three

approaches. For a turbulence model to be useful, it has to be accurate, simple and economical to run, with wide applicability. In the present study, RANS is employed as it is computationally efficient and generally sufficient to predict the averaged quantities in turbulent flow.

Table 4-3: Overview of computational approaches to turbulence modelling [140]

Simulation	Computational Approach	Computational requirement
DNS	• Full Navier-Stokes equations are numerically solved. • All laminar, transition and turbulent flows are simulated. • No modelling is required, since the whole spectrum from the dissipative Kolmogorov scales to the mean flow scales is resolved.	• The massive amount of computational resources required makes it unpractical for industrial flows. It is feasible only for simple geometries at low Reynolds number.
LES	• The spatially averaged Navier-Stokes equations are solved. • Large eddies are directly resolved, while eddies smaller than the mesh are modelled.	• Albeit less expensive than DNS, the costs are still too high for most practical applications.
RANS	• The time-averaged Navier-Stokes equations are solved. • All turbulent length scales are modelled.	• Computationally efficient and generally sufficient to predict flow for most industrial applications.

4.4.2 Reynolds Averaged Navier-Stokes Simulation

In 1895, Reynolds [141] modified the Navier-Stokes equations to include fluctuations of the velocity components. The modification introduced six additional unknowns called Reynolds stresses, which cannot be solved by analytical means alone. This is known as the turbulence closure problem. Turbulence modelling is therefore the implementation of various closing assumptions to evaluate the Reynolds stresses. The RANS turbulence models can be classified into two groups: Reynolds Stress Models (RSM) and Eddy Viscosity Models (EVM). Table 4-4 summarises their features and applications. In the present study, EVM is used, since the Boussinesq hypothesis is sufficient for channel flows involving the boundary layers.

Table 4-4: RANS turbulence models

RANS Model	Additional Transport Equations	Application
RSM	• Solves the transport equations for each of the six terms in the Reynolds stress tensor. An additional scale-determining equation, for ε or ω, is also required. This means that five and seven additional transport equations are required in 2D and 3D flows, respectively.	• The additional computational expense makes them less useful for practical applications. • However, they are useful in situations where turbulence anisotropy has a strong effect on the mean flow, i.e. when the Boussinesq hypothesis is invalid. • Such cases include highly swirling flows and stress-driven secondary flows
EVM	• Employs the Boussinesq hypothesis. Under this hypothesis, the Reynolds stresses are modelled using an isotropic scalar quantity known as eddy viscosity, μ_T. The complex evaluation of Reynolds stresses are therefore simplified to solving for μ_T. Furthermore, by expressing μ_T as a function of two variables, a maximum of two additional transport equations are to be solved.	• The Boussinesq assumption is sufficient for simple turbulent shear flows, including boundary layers and channel flows.

4.4.3 Eddy Viscosity Model

In 1877, Boussinesq [142] hypothesised eddy viscosity as: $\mu_T = \rho v_T l$, where v_T and l are the characteristic velocity and length scale of the turbulence. The turbulence models which employ the Boussinesq hypothesis seek to compute μ_T by finding ways to reasonably evaluate v_T and l. They can be classified according to the number of additional transport equations required to be solved, in order to compute the eddy viscosity. They include zero, one and two additional transport equation(s). Table 4-5 summarises the features and applicability of the turbulence models. In the present study, the two-equation model is used, since it offers a good balance between numerical effort and computational accuracy.

Table 4-5: Eddy viscosity models

Eddy Viscosity Model	Features	Applicability
Zero-equation model - Prandtl mixing length model	• Employs an algebraic approach to compute the eddy viscosity and hence requires no extra equation	• More useful as a rough estimate of turbulence.
One-equation model - Spalart-Allmaras model [143]	• An additional transport equation for turbulent kinetic energy, *k*, is used to calculate the velocity scale, v_T. The length scale, l, is still algebraically determined based on the mean flow.	• Increasingly popular for turbomachinery applications. • Economical and accurate for wall-bounded flows and flows with mild separation and recirculation. • Not as useful for massively separated flows and free shear flows.
Two-equation model - *k*-ε - *k*-ω	• Two additional transport equations are solved to obtain v_T and l. The first equation solves for turbulent kinetic energy. The second equation uses different transport variables, ε [144] or ω [145], depending on the model.	• Offers a good compromise between numerical effort and computational accuracy. • Generally recommended for flows in industrial applications.

4.4.3.1 k-ε Model

Table 4-6 summarises the advantages and disadvantages of the *k*-ε models. Developed in the early 1970s, the standard *k*-ε model expresses eddy viscosity as: $\mu_T = \rho C_\mu \frac{k^2}{\varepsilon}$, where C_μ is a constant. *k* is the turbulent kinetic energy and is defined as the variance of the fluctuations in velocity. ε is the turbulence eddy dissipation, and is defined as the rate at which the velocity fluctuations dissipate per unit mass. In other words, it describes the dissipation of *k* because of the work done by the smallest eddies against the viscous stresses. *k* and ε are solved using two additional transport equations. Efforts to improve the standard *k*-ε model led to the development of RNG *k*-ε and realizable *k*-ε model.

The RNG *k*-ε model is based on the renormalisation group analysis of the Navier-Stokes equations. The equations are similar in form to the standard *k*-ε equations, except that the ε transport equation includes an additional term which describes the interaction between turbulence dissipation and mean shear. The effect of swirl on turbulence, an analytical formula for turbulent Prandtl number and a differential formula for effective viscosity are also accounted for.

The realizable *k*-ε model expresses eddy viscosity as: $\mu_T = \rho C_\mu \frac{k^2}{\varepsilon}$, where C_μ is a variable. While the same *k* transport equation as the standard *k*-ε model is solved, the ε transport equation is improved.

Table 4-6: *k*-ε models

***k*-ε Model**	**Advantages**	**Disadvantages**
Standard *k*-ε	• Relatively simple to implement. • Leads to stable calculations that converge relatively easily. • Reasonable predictions for many flows.	• Poor predictions for: - swirling and rotating flows, - flows with strong separation, - axisymmetric jets, - certain unconfined flows, and - fully developed flows in non-circular ducts. • Valid only for fully turbulent flows. • Simplistic ε equation.
RNG *k*-ε	• Improved predictions for: - High streamline curvature and strain rate. - Transitional flows. - Wall heat and mass transfer.	• Still does not predict the spreading of a round jet correctly.
Realizable *k*-ε	• Improved performance for flows involving: - Planar and round jets (predicts round jet spreading correctly). - Boundary layers under strong adverse pressure gradients or separation. - Rotation, recirculation. - Strong streamline curvature.	

4.4.3.2 k-ω Model

The *k*-ω based model is more accurate and numerically stable than the *k*-ε model, due to its ability to predict the viscous sublayer in the boundary layer, without additional viscous modifications or complex nonlinear damping functions [140,146]. The *k*-ω model expresses eddy viscosity as: $\mu_T = \rho \frac{k}{\omega}$, where ω is the specific dissipation rate, and is related to turbulence eddy dissipation by: $\omega \sim \frac{\varepsilon}{k}$.

The standard *k*-ω model used in ANSYS CFX is developed by Wilcox in 1988 [147,148]. The main issue with this model is its severe dependency on freestream conditions [149]. This means that the results are strongly sensitive to the user input. Therefore, it is not recommended for general industrial flow simulations. This led to the development of the zonal baseline (BSL) and Shear-Stress Transport (SST) models [150,151].

The BSL model integrates the advantages of both the standard *k*-ω model and the *k*-ε model [151]. It retains the accuracy and robustness of the standard *k*-ω model in the near wall region, and employs the freestream independence of the *k*-ε model in the outer part of the boundary layer. As a result, the BSL model is as accurate as the standard *k*-ω model, along with significant reduction in the freestream dependency. However, it generally over-predicts the eddy viscosity in flow separation.

The SST model takes the BSL model one step further, by introducing a limiter in the eddy viscosity definition in the latter model [151]. This modification accounts for the transport of the principal turbulent shear stress, which is critical in predicting severe adverse pressure gradient flows. As a result, the SST model is the only available two-equation model that can accurately predict pressure-induced separation and the resulting viscous-inviscid interaction. The numerical

stability of both the BSL and SST models even in complex applications has been demonstrated as well [152]. Therefore, the RANS EVM two-equation SST turbulence model is employed in the present study.

4.5 Meshing

In order to numerically solve the continuous medium in the simplified quarter-symmetry model, the model is discretised into a finite number of elements. This process is known as meshing. Both global and local mesh settings are applied to the quarter-symmetry model. Thereafter, the mesh is checked for its quality, and mesh independence test is carried out.

4.5.1 Global Mesh Settings

Global mesh settings are used to make general adjustments to the whole model. They are useful to resolve important features of the model with minimal inputs. The controls of interest are Advanced Size Function, Relevance and Relevance Centre. Table 4-7 summarises the global mesh settings used for the quarter-symmetry model. Although the settings increase computational time, they are deemed necessary in order to obtain fine mesh for accurate results.

Table 4-7: Global mesh settings for quarter-symmetry model

Global Mesh Controls	Settings
Advanced Size Function	Curvature
Relevance Centre	Fine
Relevance	0

4.5.2 Local Mesh Settings

Local mesh settings are used to further refine the mesh for individual components, particularly in the critical regions. The settings include element sizing and inflation.

4.5.2.1 Element Sizing

Table 4-8 summarises the local mesh settings for the quarter-symmetry model. Different method and element sizing are applied to the various components according to the geometry and domain.

Table 4-8: Local mesh settings for quarter-symmetry model

Component	Method	Element sizing (mm)
MICA Insulation Cover	Sweep	1
PEEK Insulation Pipes	Sweep	0.5
Heating Coil	Sweep	0.5
Copper block	Sweep	0.5
	Tetrahedral (Patch Conforming)	Multi-scale meshing
Insert	Tetrahedral (Patch Conforming)	0.5
Insert Holders	Tetrahedral (Patch Conforming)	0.5
Fluid	Tetrahedral (Patch Conforming)	0.1 for microchannel 0.5 for the rest of fluid domain

4.5.2.2 Inflation Settings

Inflation extrudes faces normal to a boundary to increase the mesh resolution. The mesh refinement is critical to resolve the velocity and thermal boundary layers, where the fluid interacts with the solid boundary. As such, inflation is applied to the fluid body at all fluid-solid interfaces. Table 4-9 summarises the inflation settings applied to the fluid body.

Table 4-9: Inflation settings for fluid body

Inflation Controls	Settings
Inflation Option	Smooth Transition
Transition Ratio	Default (0.77)
Maximum Layers	10
Growth Rate	1.5

Smooth transition option maintains smooth volumetric growth between each adjacent layer. The maximum layers and growth rate are set as 10 and 1.5, respectively. This ensures that there are sufficient layers to accurately resolve the boundary layers, as well as to achieve $y^+ \sim 1$. The importance of y^+ will be explained in Section 4.5.3.

Figure 4-4 shows the mesh in three-dimensional view after the meshing is completed. Figure 4-5 illustrates the detailed mesh for the different components due to the local mesh settings, while Figure 4-6 shows the inflation layers for the fluid body.

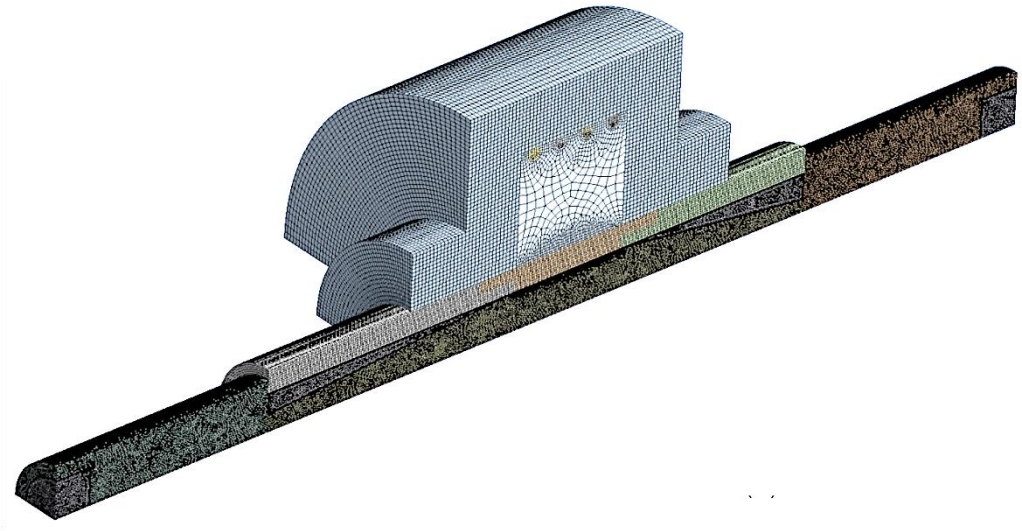

Figure 4-4: Three-dimensional view of mesh

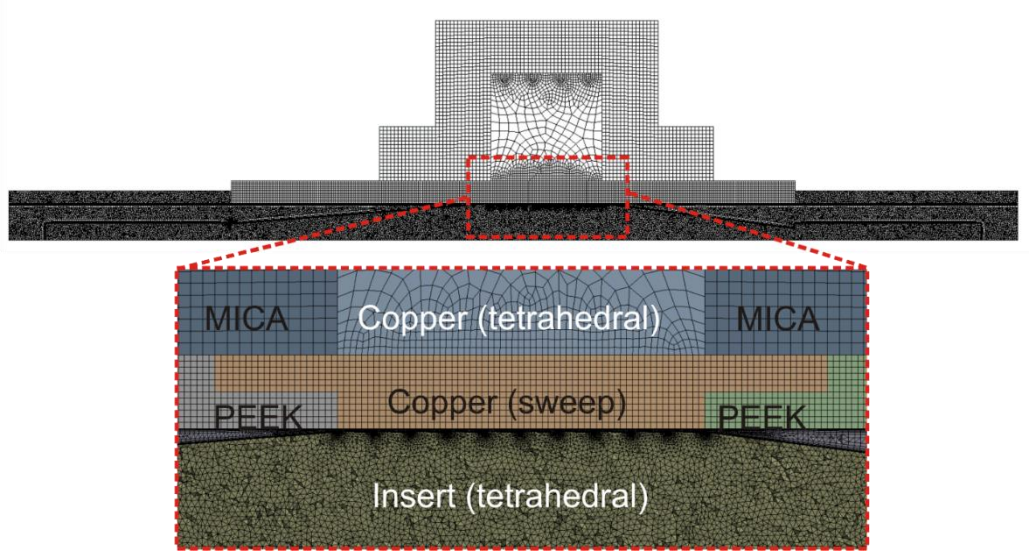

Figure 4-5: Local mesh for the different components

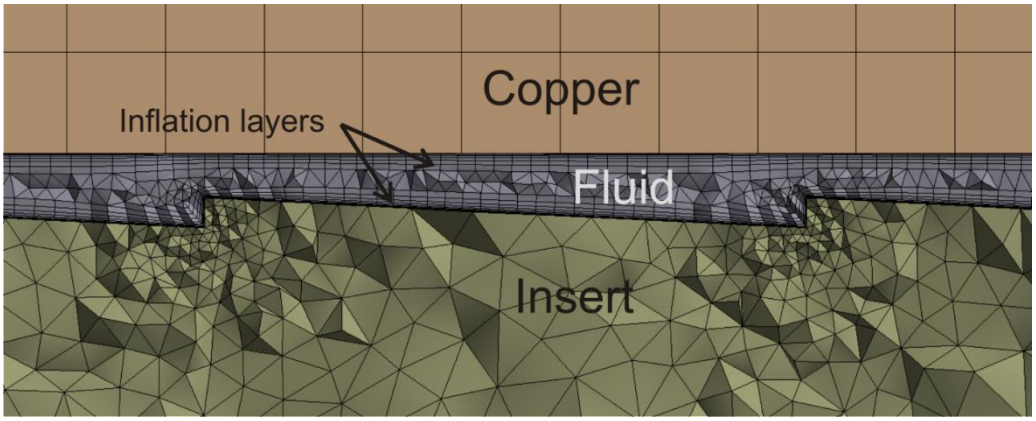

Figure 4-6: Inflation layers for the fluid body

4.5.3 Mesh Quality Check

There are two important factors to consider when checking the mesh quality, namely orthogonal quality and y^+ value.

Orthogonal quality relates to the selection of meshing method and element sizing. As a general guideline, high orthogonal quality values are favourable, and the minimum orthogonal quality should be larger than 0.1 [153]. After

every mesh is completed, a graph of number of elements versus orthogonal quality is plotted. A typical graph is illustrated in Figure 4-7. It is observed and verified that the majority of the elements falls in the region of high orthogonal quality values.

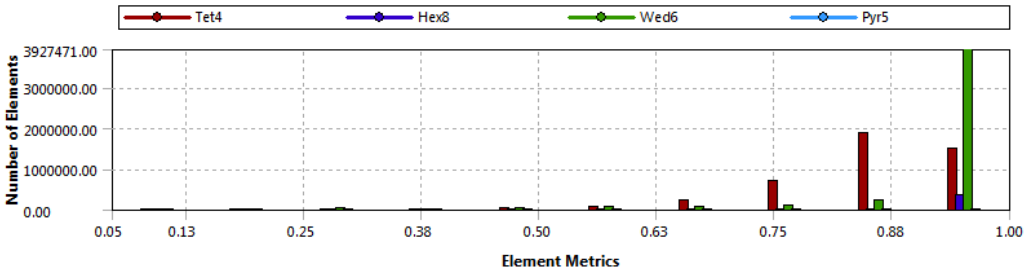

Figure 4-7: Orthogonal quality check

On the other hand, the y^+ value relates to the selection of inflation settings. As a general guideline, a y^+ value of approximately 1 indicates that the mesh resolution is sufficiently fine to accurately resolve the boundary layers for a near-wall analysis [140]. Figure 4-8 shows the typical y^+ plots for the fluid-solid interfaces, namely the fluid-copper interface and the fluid-insert interface. A y^+ value of approximately 1, or in the same order of magnitude as 1, is observed for both the outer and inner walls along the channel of interest.

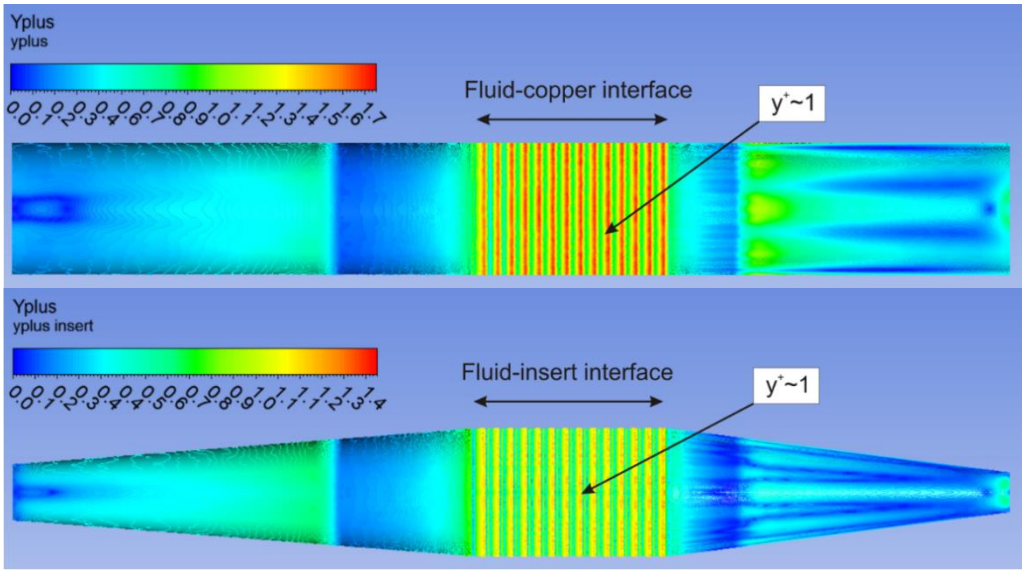

Figure 4-8: The y^+ plots at the fluid-copper interface and fluid-insert interface

4.5.4 Mesh Independence Test

Mesh independence tests are carried out to ensure that the simulation results are independent of the element sizes selected, which are listed in Section 4.5.2.1. The mesh independence tests in this study only focus on the most important region, which is the flow channel of interest within the fluid domain. The element sizing for all the solid domains is chosen based on the finalised work of Kong [12], who has previously conducted similar mesh independence tests for the solid domains.

The mesh independence test is first conducted for the Plain microchannel at 4 L/min and 1000 W. Three mesh sizes are tested, and the respective computational resources required are listed in Table 4-10.

Table 4-10: Required computational resources for different mesh sizes

Mesh	Element size (mm)	Number of elements (million)	Computational time (min)
Coarse	0.20	3.6	143
Standard	0.10	9.0	240
Fine	0.05	45.7	941

Two key parameters of the converged solutions are monitored, namely the convective heat transfer coefficient and pressure drop across the test module. The parameters are normalised with respect to the values obtained using the fine mesh. Figure 4-9 shows the variation of the normalised parameters with the number of mesh elements. It is observed that using the fine mesh instead of the standard mesh only improves the heat transfer coefficient and pressure drop solutions by 1% and 2% respectively, while the computational resources rise about fivefold, from 9 million to 45 million elements. Therefore, the standard mesh of element size 0.1 mm is chosen. Similar mesh independence tests are conducted for the IFS, FS and D microchannel series, yielding the same conclusion.

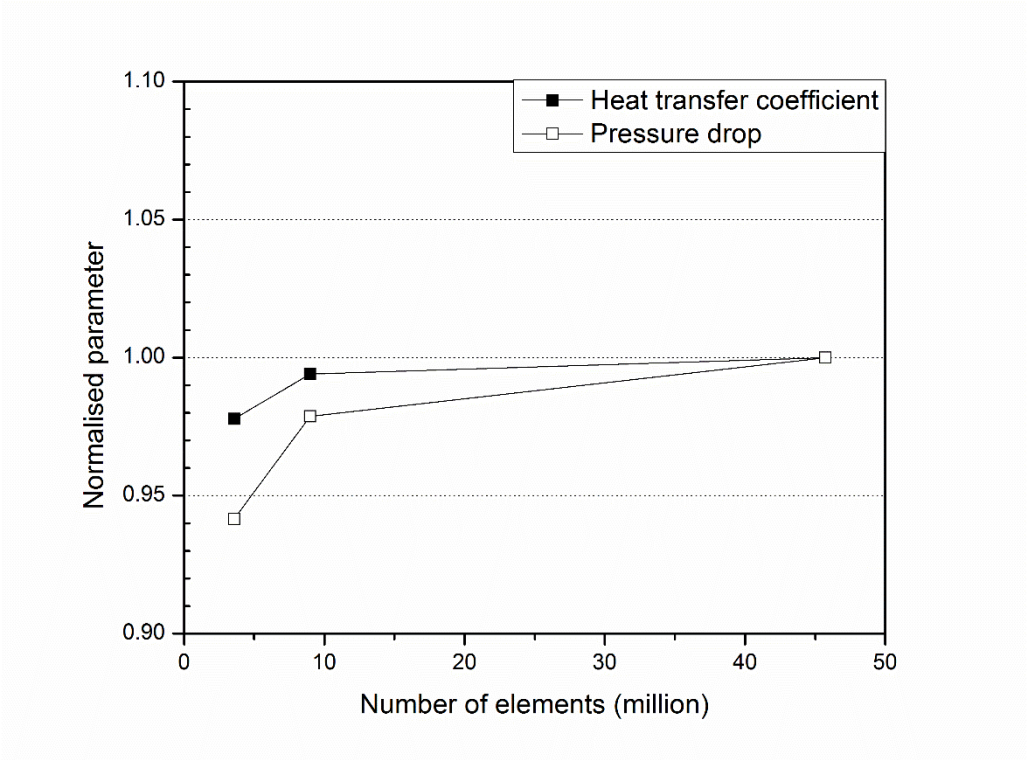

Figure 4-9: Mesh independence test for Plain microchannel

For uniform reporting of grid refinement studies, Roache [154] proposed the use of a Grid Convergence Index (GCI). The method provides an objective asymptotic approach to the quantification of uncertainty of grid convergence. In other words, the GCI provides an estimated error band within which the numerically converged solution at zero grid spacing will likely lie. The GCI for the fine grid solution is given as:

$$\mathrm{GCI[fine\ grid]} = \frac{3|\varepsilon|}{r^p - 1} \tag{4-6}$$

In most practical applications, however, the coarse grid solution is used for majority of the computations. The GCI for the coarse grid solution is given as:

$$\mathrm{GCI[coarse\ grid]} = r^p \times \mathrm{GCI[fine\ grid]} \tag{4-7}$$

The coefficient of 3 is chosen such that grid doubling (r=2) with second-order methods (p=2) can be used as the standard of comparison. On the other hand, a coefficient of 1 would make the GCI equal to the error estimator obtained from

the Richardson Extrapolation. As concurred by Roache [154], a coefficient of 3 is possibly too conservative, and the coefficient could arguably be between 1 and 3. A search of literature reveals that most studies use a safety factor of 1.25 [146,155,156]. Hence, the same is employed in the present study.

Table 4-11 shows the coarse grid solution GCI for the Plain and FS_*e*0.21-*P*2.1 microchannel profiles, using a safety factor of 1.25. It is observed that while the GCI for pressure drop remains relatively constant at about 6.3%, the GCI for heat transfer coefficient can vary from 1.2% to 79.3%. This is likely due to more complicating factors affecting the heat transfer coefficient. The pressure drop prediction, on the other hand, is relatively straightforward.

Table 4-11: Grid Convergence Index for coarse grid solution, using safety factor of 1.25

Microchannel profile	GCI for h (%)	GCI for Δp (%)
Plain	1.19	6.35
FS_*e*0.21-*P*2.1	79.34	6.31

4.6 Boundary Conditions

Figure 4-10 shows the quarter-symmetry model after the fluid domain is generated. At the inlet, the flow is defined to have a uniform velocity distribution. The volumetric flow rate is set to range from 2.0 to 7.0 L/min, while the fluid temperature is set at 28 °C. At the outlet, the fluid pressure is set at atmospheric temperature of 101 kPa. The heating coil is modelled as a uniform volumetric heat source, generating a total heat rate of 1,000 W. At all solid-solid and solid-fluid interfaces, the temperature and heat flux are set to be continuous. The heat loss from the assembly is modelled by setting free convection at the outermost surfaces of the MICA insulation cover, with the surrounding air temperature set at 28 °C and heat transfer coefficient set at 8 $W/m^2 \cdot K$.

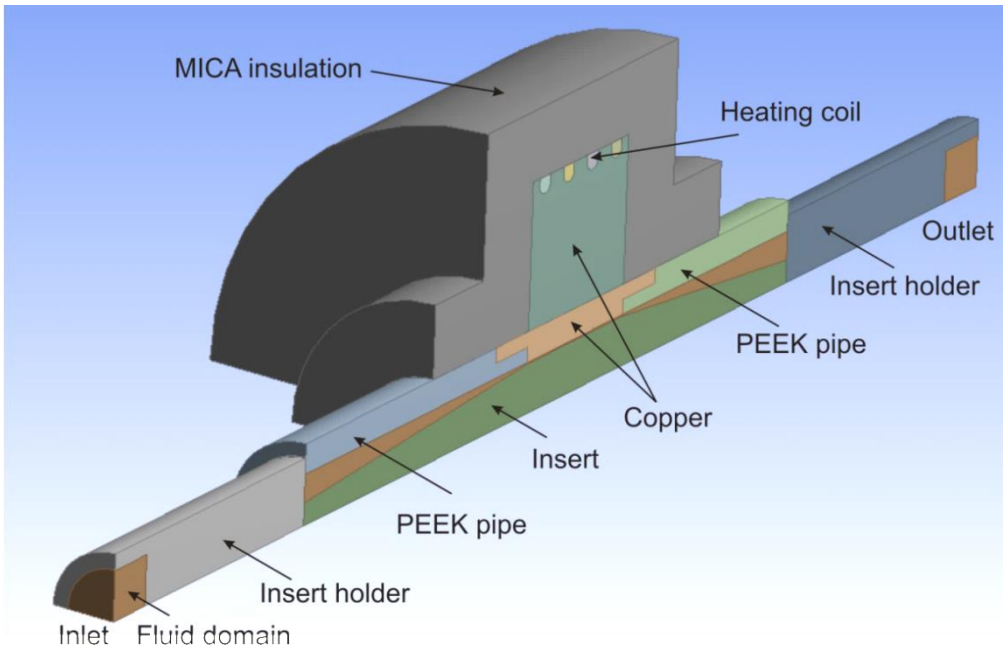

Figure 4-10: Quarter-symmetry model with fluid domain

4.7 Convergence Criteria

Convergence of the solution is measured based on the normalised Root Mean Square (RMS) residual level, as listed in Table 4-12 [153]. In the current study, the convergence criterion is set at 10^{-6}, with a maximum of 500 iterations. This means that the CFX-Solver run will be stopped automatically when either the residual levels fall below 10^{-6}, or when 500 iterations have been executed.

Table 4-12: Guide on the usefulness of the numerical modelling results [153]

RMS Residual Level	Usefulness of model
Above 10^{-4}	Loose convergence. Sufficient for qualitative understanding of flow field.
Between 10^{-5} and 10^{-4}	Relatively loose convergence. May be sufficient for many engineering applications.
Between 10^{-6} and 10^{-5}	Good convergence. Sufficient for most engineering applications.
Below 10^{-6}	Very tight convergence. Useful but may be difficult to achieve, especially when a single precision solver is used.

Figure 4-11 shows the typical convergence history for the results of the momentum equations, energy equations and turbulence model. The normalised residuals generally stabilise at a value below 10^{-5}, indicating good convergence. This is expected in the current study, since a single precision solver is used to ease the computational load.

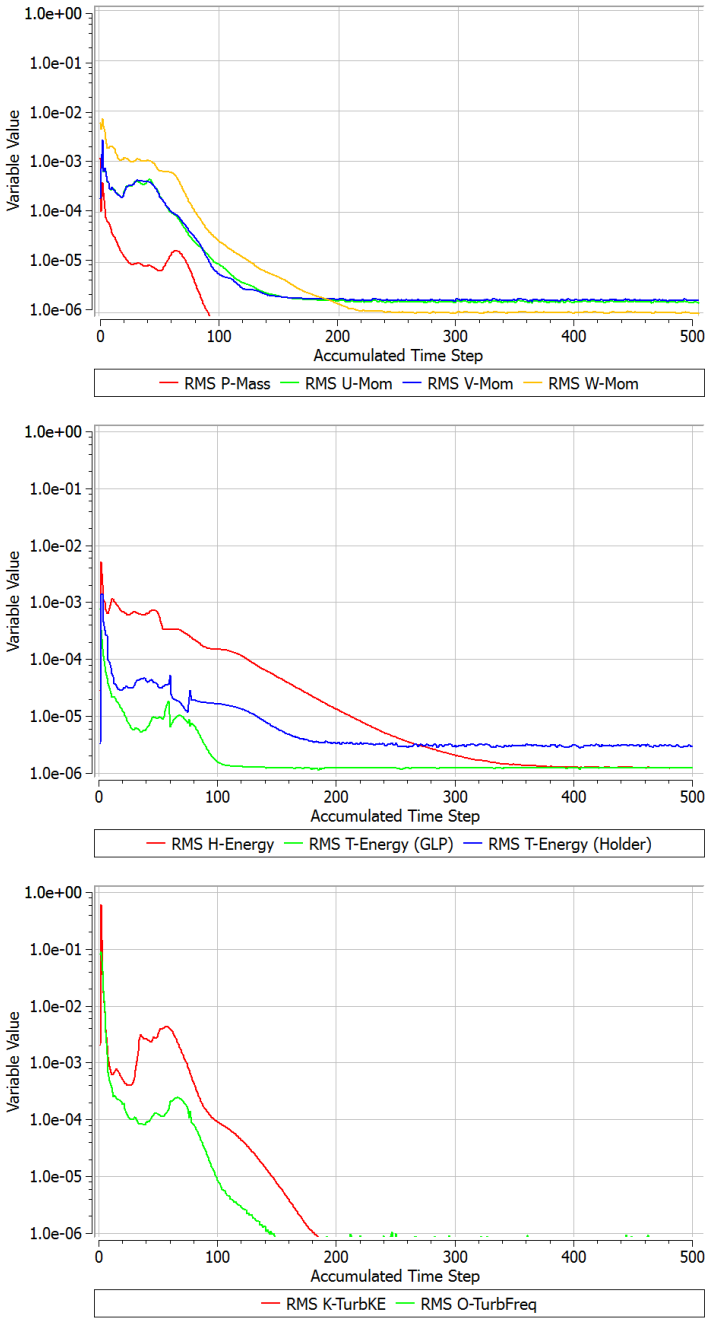

Figure 4-11: Typical convergence history for (a) momentum equations (b) energy equations (c) turbulence model

Chapter 5 Measurement System

This chapter describes the measurement system used in the present study, which was entirely designed, fabricated and commissioned by the author. The flow loop which connects all the components is first outlined, followed by the detailed specifications of each component. The main components include the chiller, filter, test module, heat supply system, measuring devices and data acquisition system. Calibration of the critical measuring devices and dimension inspection of the critical components is presented. The operational limits of the measurement system are also summarised. Next, the data reduction procedure is presented, along with the uncertainty analysis. Lastly, validation of the measurement system is carried out to demonstrate that the pressure and heat transfer measurements are accurate and consistent.

5.1 Flow Loop

The measurement system was designed after reviewing the work of several researchers [11,89,105]. Figure 5-1 shows the schematic of the flow loop.

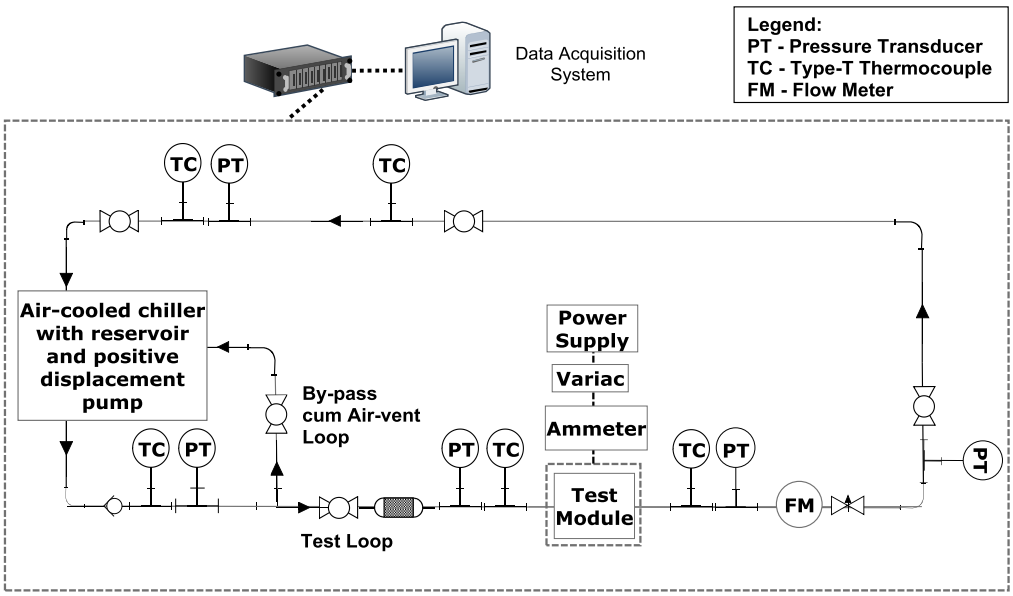

Figure 5-1: Schematic diagram of the flow loop

The flow loop consists of the test loop, as well as the by-pass cum air-vent loop. Distilled water is circulated through the flow loop by a positive displacement pump, which is integrated into a chiller unit. The latter also serves to cool the water to the desired inlet temperature of the test module. Upon exiting the chiller at a fixed temperature, a controlled amount of water is channelled to the test loop by means of a needle valve, while the remaining water flows back to the reservoir through the by-pass loop. The air-vent loop serves to remove air bubbles in the flow, in view that higher friction factors can be resulted from the increased flow resistance due to small bubbles forming on the walls [36].

In the test loop, water is first channelled through a 40 µm filter to remove solid particles. It then flows through the microchannel in the test module and removes the electrically-generated heat from the test module. The flow rate through the test module is measured by the Coriolis flow meter. Temperature and pressure sensors are located at the entrance and exit of the test module to measure the key parameters. Finally, the test loop flow is channelled back to the chiller to be cooled and re-circulated. Figure 5-2 shows the actual measurement system in the laboratory.

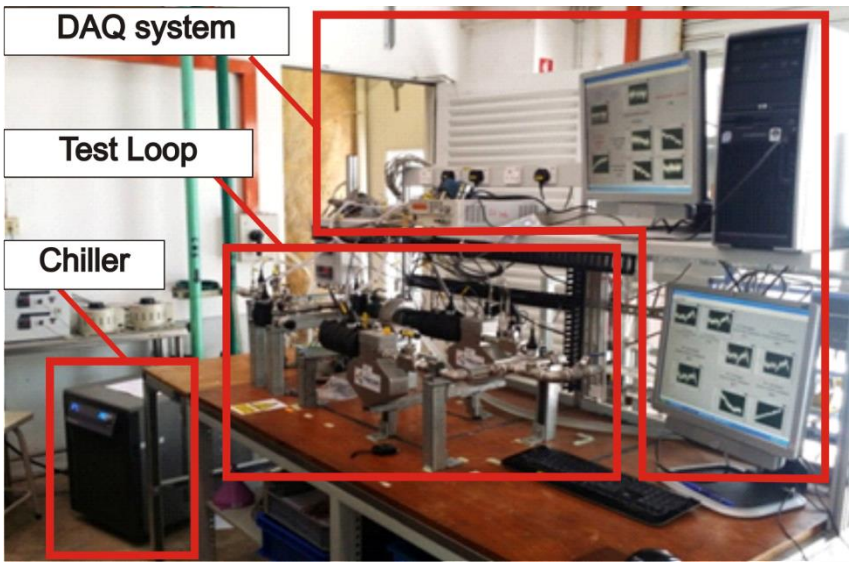

Figure 5-2: Actual measurement system

5.2 Integrated Chiller Unit

The integrated chiller unit serves three main purposes: to store, pump and cool the working fluid, which is water in this case. Polyscience DuraChill Air-Cooled 1.5 HP Chiller, model 6850P66A270E, is used in this study. A positive displacement rotary vane pump with stainless steel body supplies flow of up to 13 L/min at a maximum pressure of 6.8 bar(g). A positive displacement pump is chosen because it supplies a relatively constant flow rate regardless of the system pressure requirement. It is best suited for this study since it entails the variation of Reynolds number and hence flow rate, which in turn necessitates a constant flow rate at different pressure requirements. The cooling capacity of the chiller is 4576 W at 20 °C, with process output temperature range of 5 °C to 35 °C. In addition, the chiller has an in-built mechanical pressure relief valve. This safety feature eliminates the need for a pressure relief loop, which is included in Kong's measurement system [11].

5.3 Filter

A 40 µm filter is installed to remove solid particles from the water before it flows into the test modules. Swagelok tee-type filter of stainless steel 316 is chosen, since the filter element can be easily replaced and cleaned without having to remove the whole filter from the piping system. Figure 5-3 shows the internal construction of the filter and the actual filter.

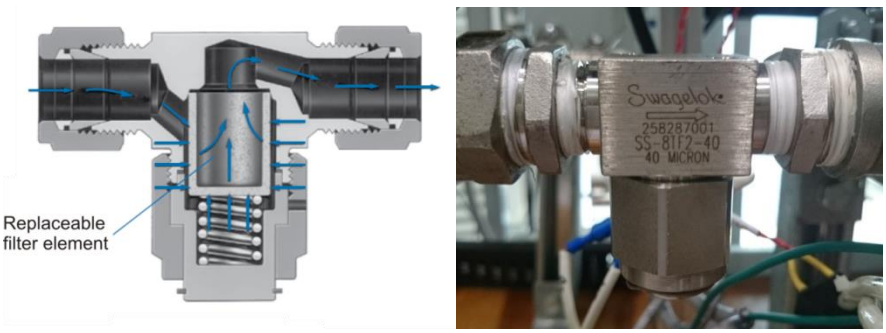

Figure 5-3: Swagelok tee-type 40-micron filter

5.4 Test Module

The microchannel test module is the most important component of the measurement system. It comprises of two insert holders, two insulation pipes, one copper block with heater, one insulation cover and one insert. Figure 5-4 presents the assembled test module, while Figure 5-5 presents the test module with the insulation cover removed, to show the copper block with heater.

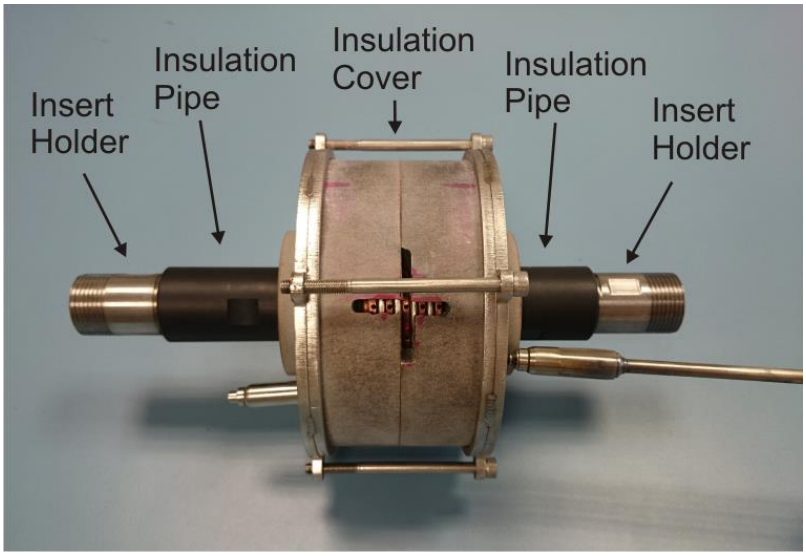

Figure 5-4: Assembled test module

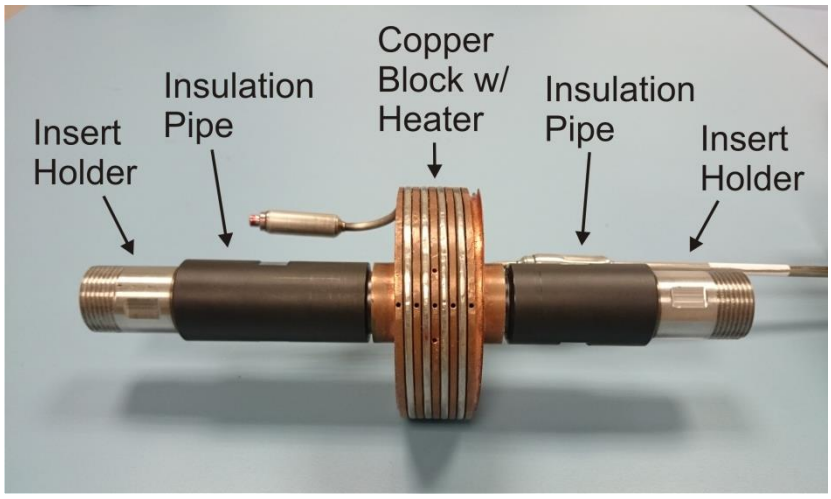

Figure 5-5: Test module without insulation cover

5.4.1 Insert Holders

The stainless steel 316 insert holders are designed to secure the insert concentrically within the copper block, and also connect the test module to the external pipelines. The tolerance of the hole, into which the insert is slotted, is tightly controlled at ± 0.010 mm to ensure concentricity. In addition, a groove is created on the insert holder, as shown in Figure 5-6, to house the ISO3601 A0035 O-ring which ensures that the insert fits snugly into the insert holder. A flat surface is also created on the insert holder for assembling purposes.

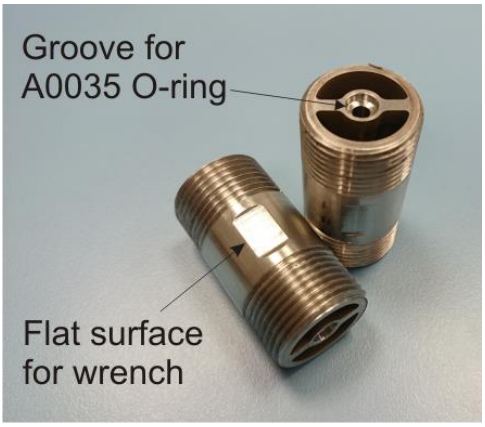

Figure 5-6: Insert holders

5.4.2 Insulation Pipes

The insulation pipes are located between each insert holder and the copper block. As the asymmetric insert holder inevitably disturbs the flow, a calming section is introduced. The length of the front insulation pipe is determined to be 70 mm [11], so that the flow velocity profile becomes evenly distributed in the circumferential direction before it enters the microchannel heat transfer section., The insulation pipes are made of 30% carbon fibre-reinforced polyether ether ketone, also known as PEEK CA 30. They have a thermal conductivity of 0.92 W/m·K at room temperature, and are able to withstand a temperature of up to 250°C under continuous operation.

5.4.3 Copper Block with Heater

The copper block with heater serves as the heat source in the test module. A spiral groove is created at the outer cylindrical surface of the copper block to house the pressed-on heater. The mineral insulated heating cable of diameter 3.3 mm and length 1100 mm is rated at 3000W/230 V. Copper is chosen for its high thermal conductivity at 401 W/m·K at 27 °C. This property, along with a thickness of 35 mm, ensures uniform heat distribution at the heat transfer area. The inner cylindrical surface of the copper block, which is in contact with the flowing water, forms the heat transfer surface area. Since the copper inner diameter is 20 mm and length is 30 mm, the heat transfer area is 1885 mm^2.

In addition, a total of 12 holes of diameter 1.7 mm are drilled radially into the copper block, by means of Electric Discharge Machining, to house 12 Type-J thermocouples. Figure 5-7 shows the 10 thermocouple holes which are evenly spaced over the 30 mm heat transfer section, with 5 on each opposite side. Located at a radial distance of 2.5 mm from the copper inner surface, these 10 thermocouples are used to obtain, through extrapolation, the temperature of the copper surface in contact with the flow.

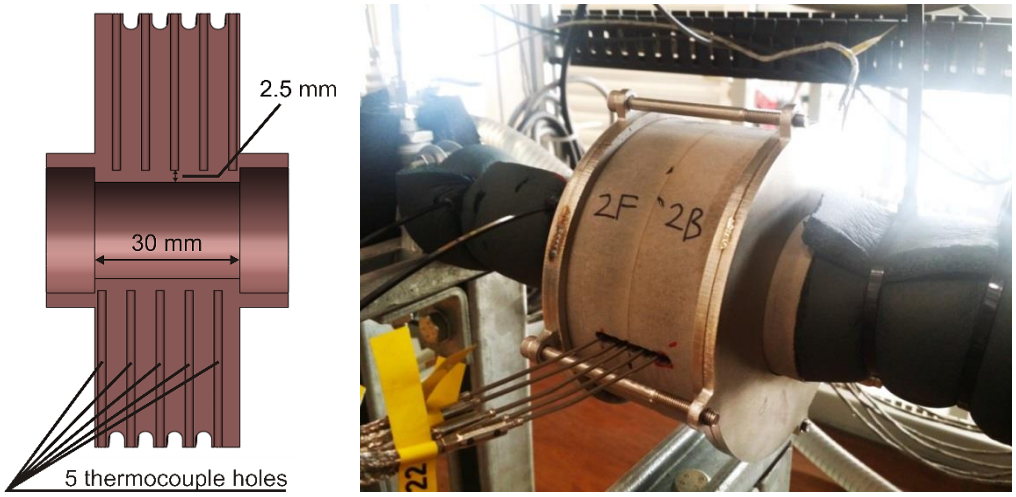

Figure 5-7: 10 Type-J thermocouples slotted into test module

The other 2 thermocouples are located at a depth of 5 mm from the copper outer surface, as shown in Figure 5-8. They are used to measure temperature of the heating cable region. One is connected to the data acquisition system for monitoring purpose, and the other is connected to a circuit-cut-off panel for safety purposes.

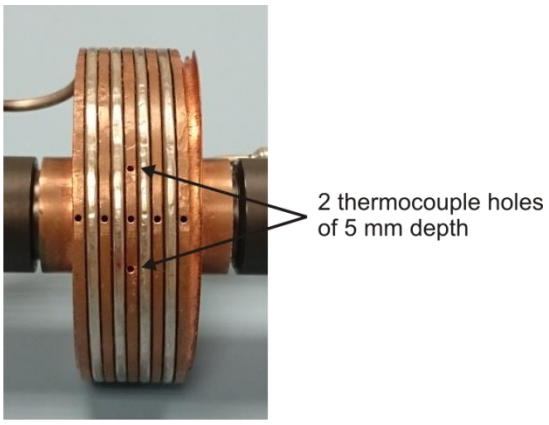

Figure 5-8: 2 Type-J thermocouples at heating cable region

5.4.4 Insulation Cover

An insulation cover is placed over the cylindrical copper block with heater to prevent heat loss to the surroundings. GL-P material, comprising of high-quality mica fractions impregnated with silicon resin, is chosen for its extremely high heat resistant property. With thermal conductivity of 0.37 W/m·K at 200 °C, this material can withstand a temperature of up to 500 °C under long-term operation.

The presence of the insulation cover keeps the percentage heat loss to surroundings within 12% of the heat supplied to the test module. Nonetheless, this heat loss does not affect the accuracy of the results, since the heat transferred to the water is computed based on the measured fluid temperature at the entrance and exit of the test module, instead of the heat supplied to the test module. The detailed data reduction is presented in Section 5.9.

5.4.5 Insert

The stainless steel insert is slotted into the circular copper channel to reduce the flow path to an annular microchannel. The 21 nature-inspired enhancement profiles are introduced on the insert surface, as shown by the box in Figure 5-9. For the purpose of illustration, Figure 5-10 shows a representative profile for each of the Inverted Fish Scale (IFS), Fish Scale (FS) and Durian (D) series.

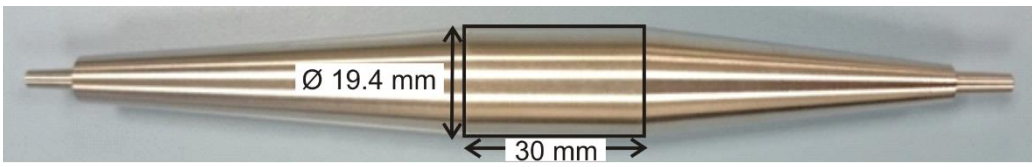

Figure 5-9: Plain insert

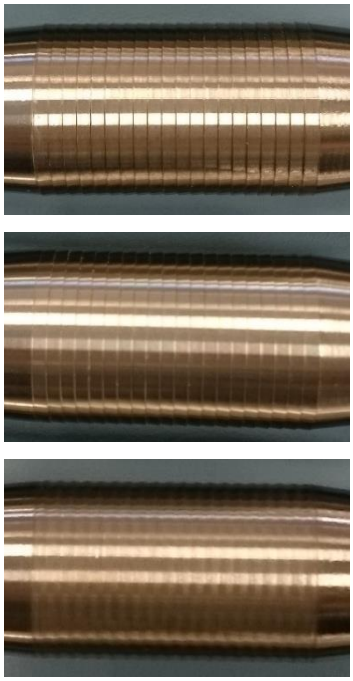

Figure 5-10: IFS, FS and D enhancement profiles for 30 mm length

The insert profiles are visually inspected to check if they are machined as per the drawing specifications, using the AxioCam Microscope STEMI 2000C. The microscopic pictures, for a 3 mm section length, for all the IFS, FS and D insert profiles are shown in Figures 5-11 to 5-16 respectively.

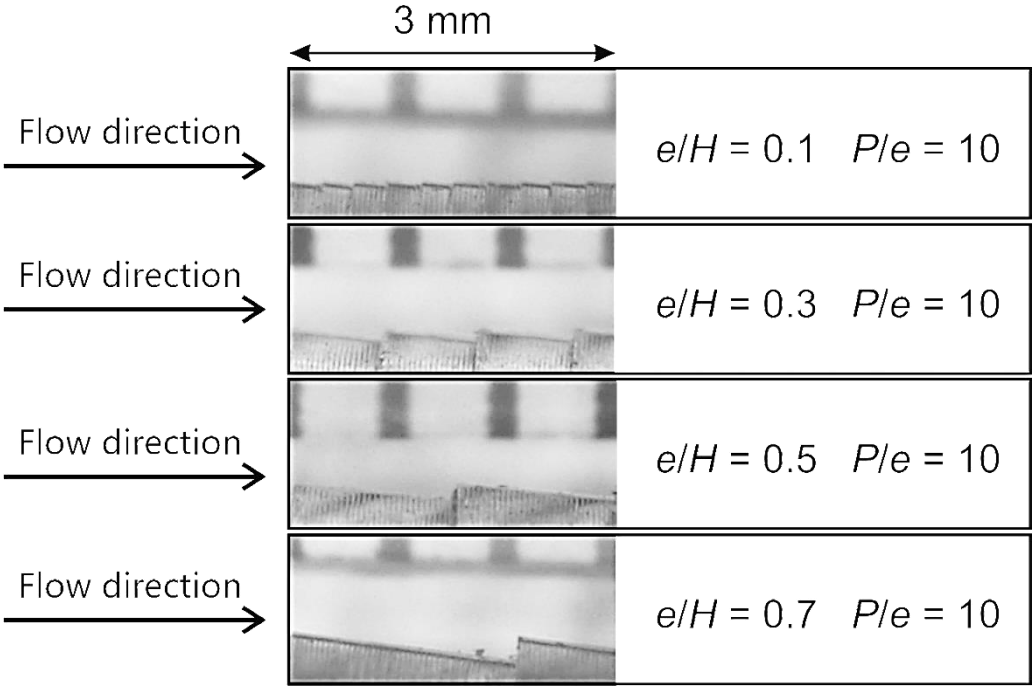

Figure 5-11: IFS insert profiles for the *e*/*H* ratio study

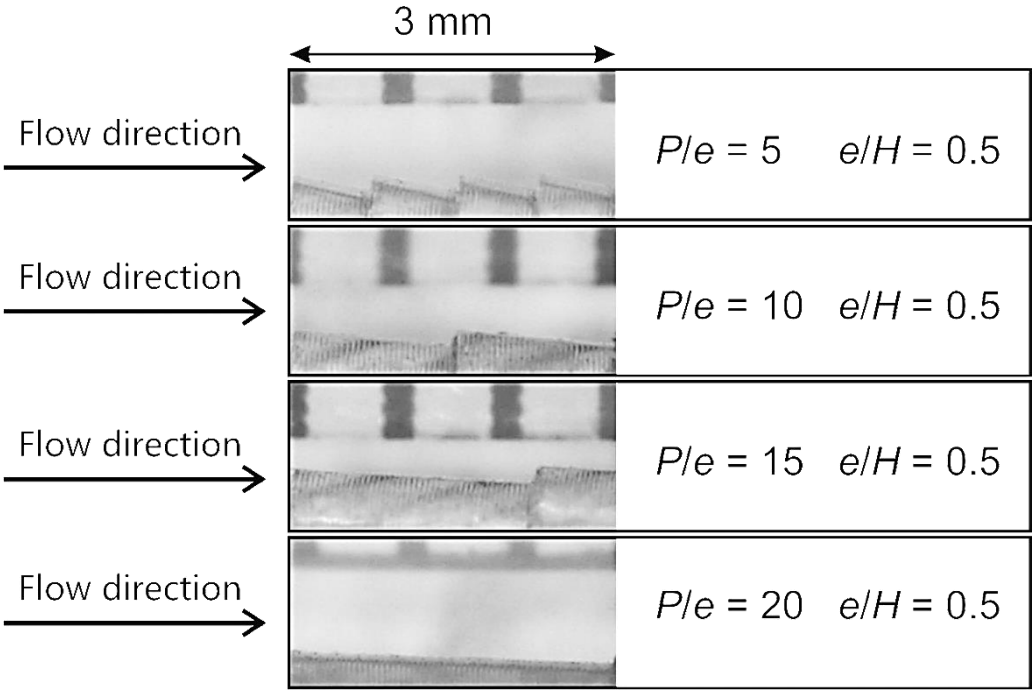

Figure 5-12: IFS insert profiles for the *P*/*e* ratio study

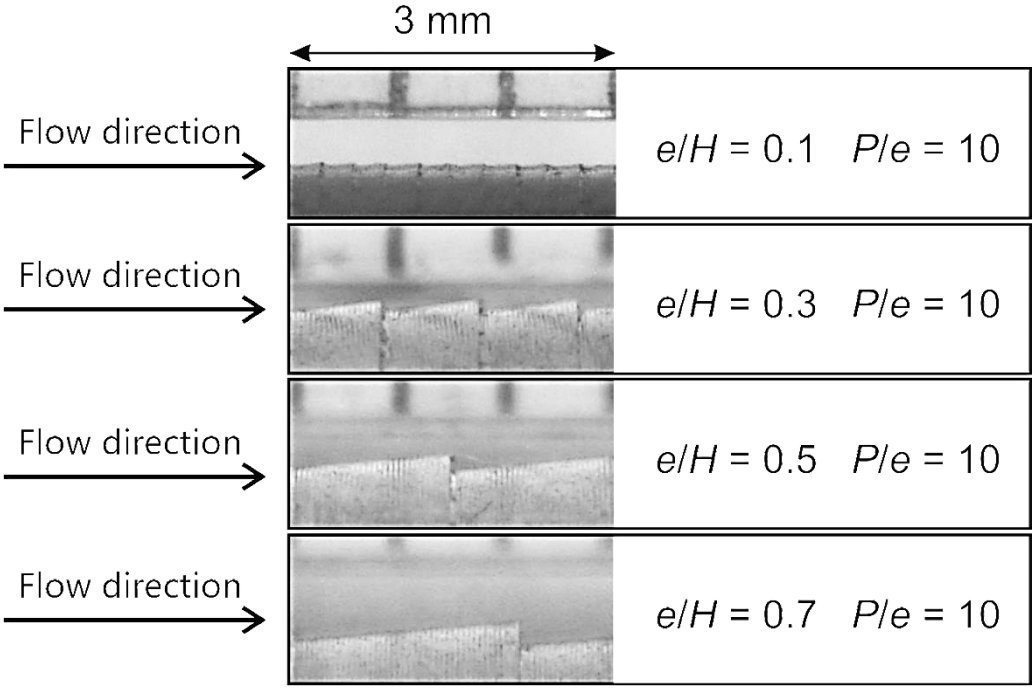

Figure 5-13: FS insert profiles for the *e*/*H* ratio study

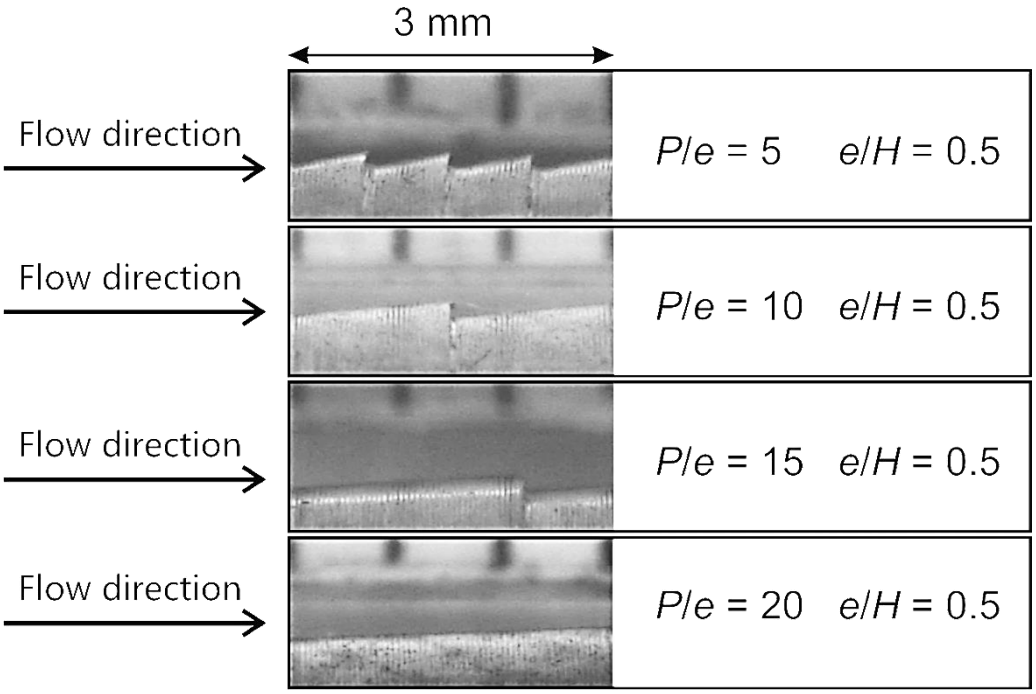

Figure 5-14: FS insert profiles for the *P*/*e* ratio study

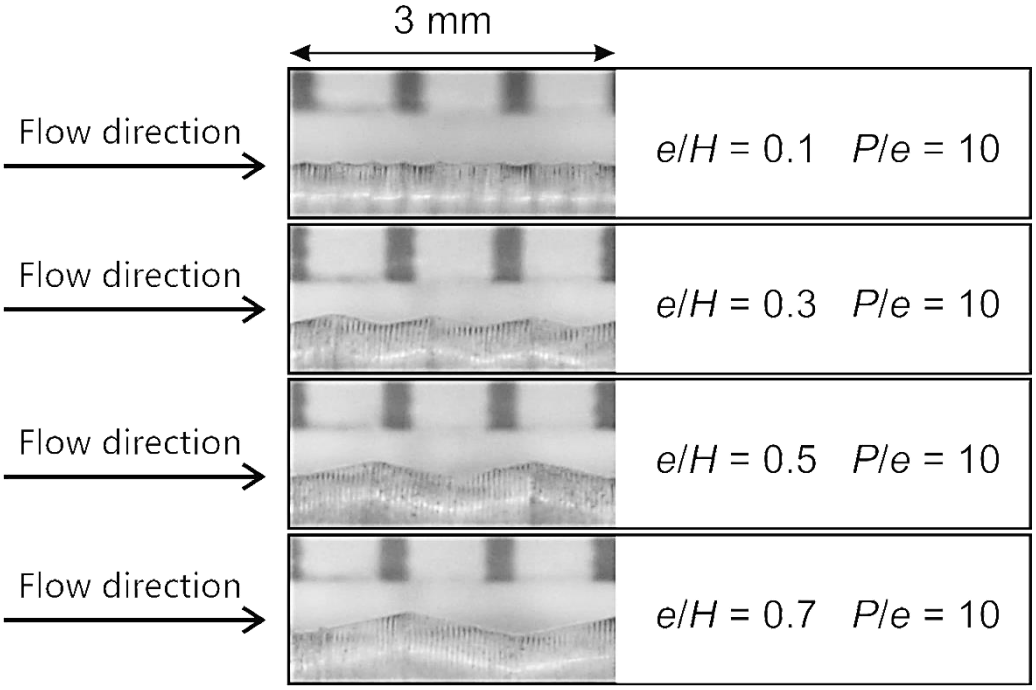

Figure 5-15: D insert profiles for the *e*/*H* ratio study

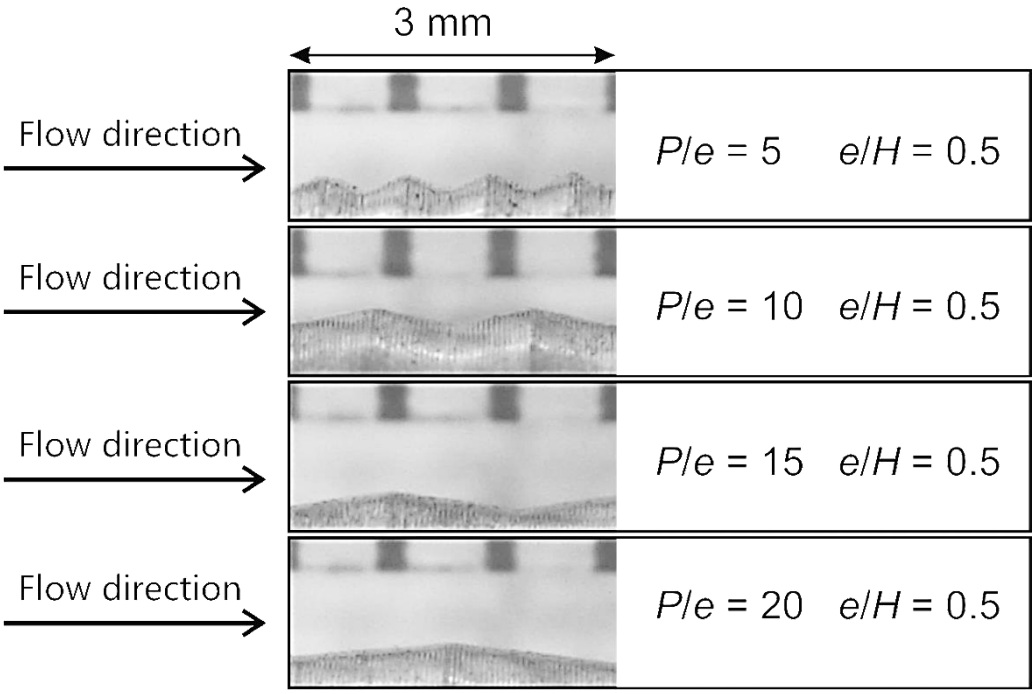

Figure 5-16: D insert profiles for the *P*/*e* ratio study

5.4.6 Dimension Inspection

5.4.6.1 Surface Roughness

As illustrated using Figure 2-6 in Section 2.1.2.2, there are three regimes of turbulent pipe flow: hydraulically smooth, transitional rough and hydraulically rough. In order to find out which regime the flow lies in, the knowledge of the microchannel surface roughness is important.

Surface roughness of all the critical components is measured using Mitutoyo Surftest 301, of resolution 0.01 μm. For mean surface roughness, 5 measurements are taken at five different randomly chosen locations and then averaged. The results are summarised in Table 5-1 and Table 5-2.

Table 5-1: Mean surface roughness of Copper wall and PEEK pipes

Test Module	Mean surface roughness, R_a (μm)
Copper block	1.58
PEEK 2F	1.83
PEEK 2B	1.56
Plain	0.38

Table 5-2: Mean surface roughness of IFS, FS and D insert series

Insert Profile		Mean surface roughness, R_a (μm)		
e (mm)	P (mm)	IFS Series	FS Series	D Series
0.03	0.3	0.95	0.64	0.87
0.09	0.9	0.86	0.36	0.66
0.15	1.5	0.93	0.55	0.89
0.21	2.1	1.28	0.64	0.56
0.15	0.75	0.95	0.56	0.79
0.15	2.25	0.94	0.18	0.91
0.15	3.0	1.04	0.38	0.80

For the microchannel to be considered as hydraulically smooth, the following condition applies:

$$0 \leq \varepsilon^* \leq 5 \tag{5-1}$$

The dimensionless surface roughness ε^* is calculated from the measured roughness value ε:

$$\varepsilon^* = \varepsilon \frac{u_\tau}{\upsilon} \tag{5-2}$$

The friction velocity u_τ is given by [14,20]:

$$u_\tau = \left(\frac{\tau_w}{\rho}\right)^{0.5} = \left(\frac{f}{8}\right)^{0.5} u_m = \left(\frac{f}{8}\right)^{0.5} \frac{4\dot{m}}{\rho\pi({D_o}^2 - {D_i}^2)} \tag{5-3}$$

In the entire study, the largest mean surface roughness of 1.83 µm occurs at the front PEEK insulation pipe. The highest pressure drop of 3.3 bars occurs at the highest Reynolds number using IFS_*e*0.15-*P*0.75 insert. Correspondingly, the largest dimensionless surface roughness ε^* is calculated to be 2.87. This value falls within the regime where the microchannel wall is considered hydraulically smooth. Therefore, the effect of wall surface roughness is not considered in the present study.

5.4.6.2 Microchannel Size

Since this study involves dimensions in the range of hundreds of microns, the accuracy and precision of the fabricated channel is important. As the test module components are fabricated using conventional machining methods, the results may be affected significantly if the actual dimensions deviate from the designed dimensions by a large percentage. Hence, inspection of the microchannel size is carried out.

Inspection of the copper inner diameter is carried out using Intec 468-106 electronic 3 point internal micrometer, of resolution 0.001 mm. 3 measurements are taken at random locations along the circumferential direction, at the front, middle and rear section of the copper inner surface respectively. The 9 measurements are then averaged to give a final value. On the other hand, inspection of the microchannel length is carried out using the Intec IM-EC1-071132 electronic calliper, of resolution 0.01 mm. Similarly, 9 measurements are taken at random locations along the circumferential direction and averaged.

The mean diameter at the 30 mm microchannel length of interest of each insert is determined in two steps. First, the maximum diameter of the insert is measured using the Intec IM-EC1-071132 electronic calliper, of resolution 0.01 mm. 5 measurements are taken at random circumferential and axial locations and averaged. Second, the scale/thorn height of each insert enhancement profile is measured using Talyscan 150 Hobson Precision 3D scanning instrument, of resolution 0.06 μm. The mean diameter is computed as the difference between the maximum diameter and the scale/thorn height.

After the copper inner diameter and the mean diameter of each insert have been determined, the mean microchannel gap size for each channel profile is computed. The measured dimensions are presented in Table 5-3 and Table 5-4.

Table 5-3: Measured key dimensions

	Nominal value	**Actual value**	**Unit**
Inner diameter of copper block	20.00	19.969	mm
Microchannel length	30.00	30.00	mm
Mean gap size for Plain microchannel	300	285	μm

Table 5-4: Measured mean gap size for IFS, FS and D microchannel series

Insert Profile		Actual mean microchannel gap size (μm)		
e **(mm)**	***P*** **(mm)**	**IFS Series**	**FS Series**	**D Series**
0.03	0.3	286	283	286
0.09	0.9	282	285	285
0.15	1.5	280	275	283
0.21	2.1	276	273	283
0.15	0.75	277	279	279
0.15	2.25	284	274	287
0.15	3.0	285	278	289

5.5 Heat Supply System

In this study, different heat flux is used with different mass flow rate. Variable heat flux is achieved through a meticulous design of the electrical power supply system, as shown in Figure 5-17. The system consists of three components: the incoming power supply distribution panel, variac and heater.

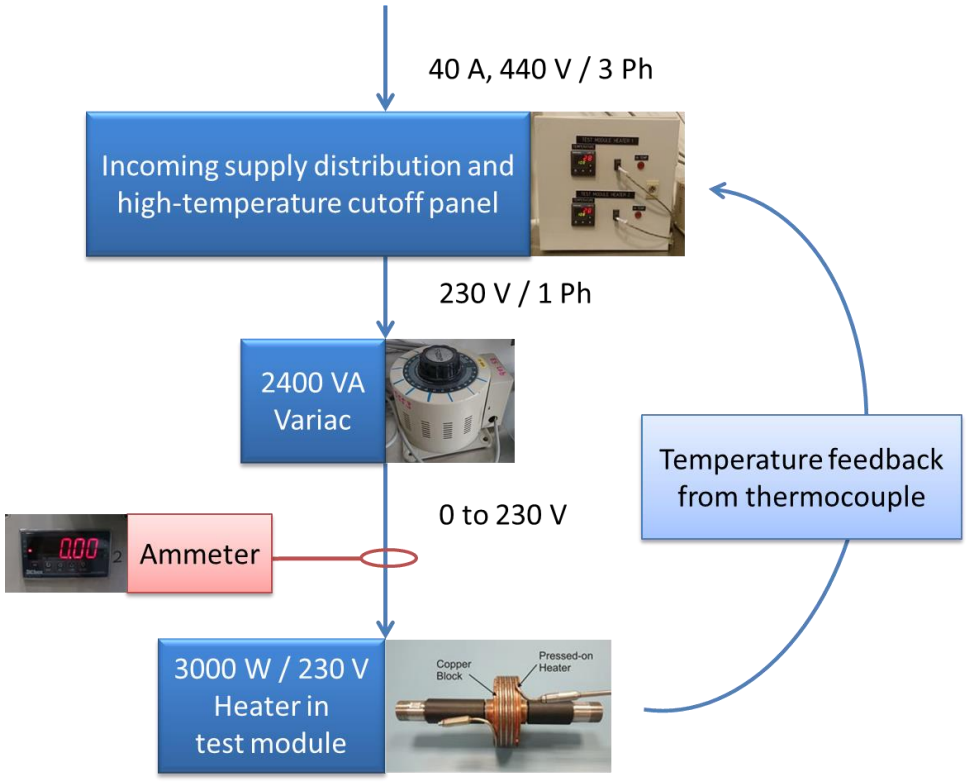

Figure 5-17: Schematic diagram of the heat supply system

The incoming power supply distribution panel, which is connected to a 3-phase industrial wall socket, is first used to convert the 3-phase power supply to a 230V / 1 Ph power supply. The single-phase power supply is then connected to a variac, which is used to step down the voltage so as to vary the power supply to the heater in the test module. As a result, the heat flux supplied to the water may be varied. Furthermore, an ammeter is positioned before the heater to measure the current, and therefore the power, supplied to the heater.

The incoming power supply distribution panel also incorporates a high-temperature cut-off safety feature. The panel takes signals from the Type-J thermocouple embedded in the test module. Once a pre-set high temperature is detected, the circuit breaker will be activated to cut off the power supply to the test module. A red warning light will be activated to warn the user as well.

5.6 Measuring Devices

5.6.1 Type-J Thermocouple

As shown in Figure 5-18, mineral insulated Type-J thermocouple probes, according to DIN EN 60584 standard, are used to measure localised temperature at various locations of the copper block. These thermocouples come with sensor surface as small as 1.5 mm, which is important since 10 thermocouples are required to be evenly spaced within 30 mm. The temperature range of a Type-J thermocouple is -40 °C to 750 °C, which well covers the required measurement range of 25 °C to 500 °C.

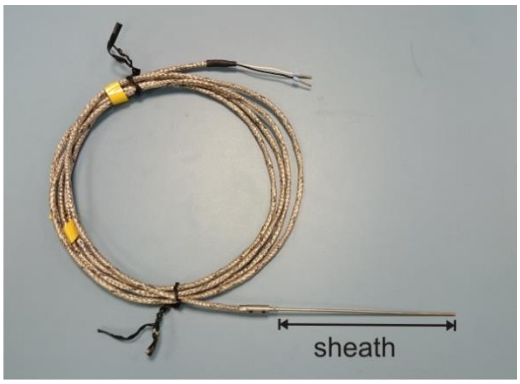

Figure 5-18: Type-J thermocouple

The 12 Type-J thermocouples are calibrated using the Industrial grade Fluke Calibration 7103 micro-bath with a range of -30 to 125 °C. The thermometer probe used is the Fluke Calibration 5628 platinum resistance thermometer probe with a range of -200 to 661 °C and accuracy of ± 0.006 °C at 0 °C. For data logging purposes, the Fluke Calibration 1529 Chub-E4 Thermometer along with MET/TEMP II software is used. Table 5-5 presents the calibration results for all the 12 Type-J thermocouples. The standard error of estimate (S.E.E.) represents the uncertainty of the measured temperature values obtained from using the calibration results.

Table 5-5: Calibration results for Type-J thermocouples

Thermocouple	Best Fit Equation	R^2 value	Standard Error of Estimate (S.E.E.)
TC-J-01	y = 1.0085x + 0.3513	1.000	0.114
TC-J-02	y = 1.0073x + 0.3685	1.000	0.0870
TC-J-03	y = 1.0071x + 0.3930	1.000	0.0522
TC-J-04	y = 1.0068x + 0.3806	1.000	0.0487
TC-J-05	y = 1.0083x + 0.3005	1.000	0.0662
TC-J-06	y = 1.0078x + 0.3670	1.000	0.0503
TC-J-07	y = 1.0105x + 0.2771	1.000	0.0608
TC-J-08	y = 1.0085x + 0.4073	1.000	0.0444
TC-J-09	y = 1.0084x + 0.3912	1.000	0.0401
TC-J-10	y = 1.0091x + 0.3869	1.000	0.0416
TC-J-11	y = 1.0095x + 0.3632	1.000	0.0424
TC-J-12	y = 1.0092x + 0.4107	1.000	0.0531

After calibration, a verification check is conducted to ensure that the temperature readings provided by the thermocouples are accurate. The details of the calibration procedure are provided in Appendix A.

5.6.2 Type-T Thermocouple

As previously illustrated in Figure 5-1, a total of 5 Type-T thermocouples are used to measure localised flow temperature at various positions of interest along the flow loop. Most importantly, two thermocouples are positioned before and after the test module, in order to compute heat transferred from the heater in the test module to the water. The other three thermocouples are spread out over the flow loop for monitoring purposes. The temperature range of the Type-T thermocouple, as shown in Figure 5-19, is -40 °C to 350 °C, which well covers the required measurement range of 25 °C to 85 °C.

Figure 5-19: Type-T thermocouple

Similarly, the Type-T thermocouples are calibrated using the same temperature calibration system, of which the procedure is detailed in Appendix A. Table 5-6 presents the calibration results for all the 5 Type-T thermocouples.

Table 5-6: Calibration results for Type-T thermocouples

Thermocouple	Best Fit Equation	R^2 value	Standard Error of Estimate (S.E.E.)
TC-T-01	y = 1.0032x + 0.2620	1.000	0.0611
TC-T-02	y = 1.0043x + 0.2324	1.000	0.0573
TC-T-03	y = 1.0003x + 0.2712	1.000	0.0541
TC-T-2F	y = 1.0019x + 0.3888	1.000	0.0468
TC-T-2B	y = 1.0006x + 0.3582	1.000	0.0523

5.6.3 Pressure Transducer

As previously illustrated in Figure 5-1, a total of 5 pressure transducers are used to measure localised flow pressure at various positions of interest. Most importantly, two pressure transducers are positioned before and after the test module, in order to compute the pressure drop across the test module. The other three pressure transducers are spread out over the flow loop for monitoring purposes.

In this study, WIKA pressure transmitters of model A-10 are used, as shown in Figure 5-20(a). Since the maximum pressure of the chiller is set at 6.0 bar(g), the measuring range of the pressure transducers is chosen at 0 to 6 bar(g), which corresponds to a current output of 4-20 mA. During operation, the pressure transmitters are powered at 24 V DC by Agilent power supply unit, as shown in Figure 5-20(b).

Figure 5-20: (a) WIKA pressure transmitter and (b) Agilent DC power supply unit

The 5 pressure transducers are calibrated using DRUCK 452 pneumatic dead weight tester. The equipment is designed for a calibration range of 0 to 7 bar(g), which covers the pressure transducer range of 0 to 6 bar(g). The calibration is carried out for the full range of the pressure transducer, at an interval of 0.5 bar(g). A complete run consists of both increasing and decreasing pressure points, so as to account for any hysteresis related errors.

Table 5-7 presents the calibration results for all the five pressure transducers. The standard error of estimate (S.E.E.) represents the uncertainty of the measured pressure values obtained from using the calibration results.

Table 5-7: Calibration results for pressure transducers

Pressure transducer	Best Fit Equation	R^2 value	Standard Error of Estimate (S.E.E.)
PT-01	y =0.376x - 1.495	1.000	0.00162
PT-02	y = 0.375x - 1.494	1.000	0.00224
PT-03	y = 0.376x - 1.497	1.000	0.00138
PT-2F	y = 0.376x - 1.503	1.000	0.00196
PT-2B	y = 0.376x - 1.497	1.000	0.00100

5.6.4 Flow Meter

As previously illustrated in Figure 5-1, a flow meter is positioned after the test module to measure the flow rate in the test loop. Since the study involves the variation of Reynolds number, accurate and repeatable measurements of the flow rate is an important consideration. The selected Tricor TCM 0650 Coriolis flow meter, as shown in Figure 5-21, supports a flow rate measurement range of 0.1 to 10 L/min and offers an uncertainty of ± 0.1 % of reading. The flow meter comes with a TCE 6000 transmitter, which provides two 4-20 mA current output signals for data acquisition. During operation, the flow meter is powered at 24 V DC by Agilent power supply unit.

Figure 5-21: Tricor TCM 0650 Coriolis flow meter

While calibration is not required due to the high accuracy of the Coriolis flow meter, validation is carried out to ensure that it is working as expected. Using the primary standard of mass and time, the amount of water collected is measured using a mass balance with a range of 0–30 kg, while the time taken is measured using a stopwatch. The flow rate is then calculated and compared against the value obtained using the flow meter. The process is repeated for six flow rates, and the results of the validation process are tabulated in Table 5-8. The results show that the flow meter is functioning well.

Table 5-8: Validation results for Coriolis flow meter

DAQ Flow Rate (L/min)	Primary Flow Rate (L/min)	Difference (L/min)
1.01	1.02	-0.01
2.06	2.07	-0.01
3.07	3.07	+0.00
4.01	4.00	+0.01
5.98	5.98	+0.00
6.00	5.97	+0.03

5.6.5 Ammeter

The ammeter, as shown in Figure 5-22, is used to measure the current supplied to the heater in the test module. Combined with the known resistance of the heater, the current reading can be used to compute the electrical power supplied to the test module using $P = I^2R$.

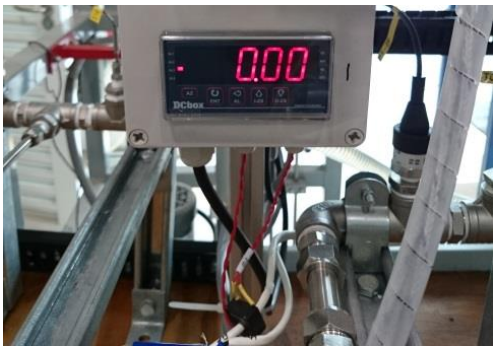

Figure 5-22: Ammeter to measure current

Since calibration is not critical for the ammeter, validation is carried out to ensure that it is functioning. The values obtained by the ammeter are compared against those measured by a digital current probe. The results of the validation process are tabulated in Table 5-9. It is verified that the ammeter is working as expected.

Table 5-9: Validation results for ammeter

Current probe (A)	Ammeter (A)	Difference (A)
0.01	0.01	+0.00
2.00	2.00	+0.00
4.03	4.01	+0.02
6.02	6.00	+0.02
7.99	7.98	+0.01
10.01	10.01	+0.00

5.7 Data Acquisition System

A data acquisition (DAQ) system is set up to acquire the output signals of all the measuring devices, convert these signals into their corresponding measurement values, and display the values on-screen for monitoring purposes. The measured parameters are temperature, pressure, flow rate and electrical current. As illustrated in Figure 5-23, the DAQ system comprises of three main components: measuring devices, corresponding modules and computer software.

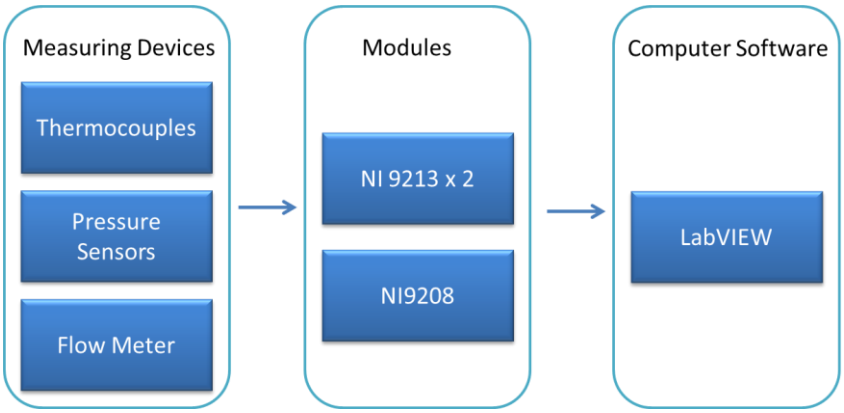

Figure 5-23: Schematic diagram of data acquisition system

The measuring devices, which have been covered in the preceding section, are connected to a total of three modules from National Instruments (NI). The Type-T and Type-J thermocouples are connected to a total of two NI 9213 modules, while the pressure transducers and Coriolis flow meter are connected to the NI 9208 module. The three modules are housed in a 4-slot chassis NI cDAQ-9174, which connects the modules to the computer through a USB cable.

The NI LabVIEW software is used to convert the signals obtained from the modules into their corresponding measurement values. During the software execution, the measurements are written into an excel file for data reduction purposes. The software is also programmed to display the measurement values on-screen for monitoring purposes. As shown in Figure 5-24, the interface is designed to be user-friendly, with critical parameters highlighted in red.

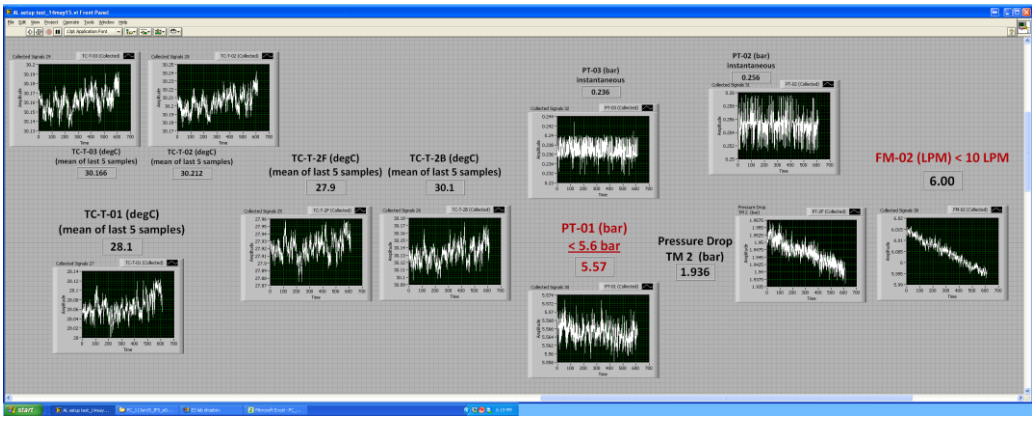

Figure 5-24: NI LabVIEW software user interface

5.8 Limits of the Current Measurement System

The measurement system is designed to function within a certain range of operating conditions. To ensure that all the equipment is used within their intended range, it is important to take note of their respective limits and avoid going beyond these limits when running the experiments. Table 5-10 summarises the limits of the measurement system.

Table 5-10: Limits of the measurement system

Key Parameters	Maximum limit	Consequences of exceeding the limit
Fluid pressure	6.0 bar(g)	Chiller will stop functioning and pressure transducers will spoil
Fluid flow rate	10 L/min	Flow meter will spoil
Heat flux	2000 W	Variac will spoil, although heater is rated at 3000 W

The copper wall temperature is kept at a maximum of 80 °C. This is to prevent the occurrence of hot spots, which may lead to localised boiling regions. As such, tests were conducted to compute the maximum heat flux that can be supplied at each flow rate, in order to prevent boiling. The findings are summarised in Table 5-11.

Table 5-11: Heat flux cap for single-phase flow at each flow rate

Flow Rate L/min	Highest Heat Flux (W)
1.00	700
2.00	1000
3.00	1200
4.00	1400
5.00	1600
6.00	1800
7.00	2000

5.9 Data Reduction

The data reduction method is adopted after reviewing the work of several researchers [11,44,105,157]. Each steady-state measurement is computed as an average of 600 data points logged at 1 Hz. The steady-state condition is deemed to be achieved when all the temperature measurements fluctuate within 0.3 °C, all the pressure measurements within 0.04 bar(g), and the flow measurement within 0.05 L/min. The measurements are then used in the data reduction.

The fluid properties include density, dynamic viscosity, thermal conductivity and specific heat. They are all evaluated at the mean fluid temperature and pressure.

$$T_{f,m} = \frac{T_o + T_i}{2} \tag{5-4}$$

$$p_{f,m} = \frac{p_o + p_i}{2} \tag{5-5}$$

The fluid properties are computed using the REFPROP software, which is developed by the National Institute of Standards and Technology [158]. The software is based on the Helmholtz-free-energy formulations from the International Association for the Properties of Water and Steam (IAPWS) [138].

5.9.1 Thermal Consideration

The steady-state sensible heat gain by the water is determined by the energy balance equation:

$$q = \rho c_p Q(T_o - T_i) \tag{5-6}$$

The outlet and inlet temperatures are measured by the two Type-T thermocouples positioned before and after the test module. The volumetric flow rate is measured using the Coriolis flow meter.

The mean wall temperature, $T_{w,m}$, is obtained by averaging ten local wall temperature measurements. Each local wall temperature, $T_{w,i}$, is determined by extrapolating the reading of the Type-J thermocouple embedded in the copper block, as in Eqn. (5-8).

$$T_{w,m} = \sum_{i=1}^{10} T_{w,i}/10 \tag{5-7}$$

$$T_{w,i} = T_{r=2.5mm,i} - q\frac{\ln(D_r/D_w)}{2\,\pi\,L\,k_c} \tag{5-8}$$

The average heat transfer coefficient is then evaluated using Newton's law of cooling:

$$h = \frac{q}{A(T_{w,m} - T_{f,m})} \tag{5-9}$$

The heat transfer area, A, is the area of the copper inner surface which is in contact with the flow. It is calculated by $\pi D_o L$, and is therefore fixed at 18.85 cm^2 in the present study.

The average Nusselt number is calculated from the average heat transfer coefficient:

$$Nu = \frac{h\,D_h}{k_f} \tag{5-10}$$

The normalised Nusselt number is quantified by:

$$E_{Nu} = \frac{Nu}{Nu_{Plain}} \tag{5-11}$$

5.9.2 Hydrodynamic Consideration

The pressure drop across the entire test module is the difference between inlet and outlet fluid pressure. They are measured by the two pressure transducers positioned before and after the test module.

$$\Delta p_{module} = p_o - p_i \tag{5-12}$$

For best accuracy, the pressure drop across the 30-mm microchannel should be obtained by subtracting $\Delta p_{entrance}$ and Δp_{exit} from Δp_{module}.

$$\Delta p_{microchannel} = \Delta p_{module} - (\Delta p_{entrance} + \Delta p_{exit}) \tag{5-13}$$

However, simulation results obtained from the numerical model indicate that $\Delta p_{microchannel}$ can be well approximated by Δp_{module}, as shown in Table 5-12. Furthermore, using this data reduction method is not only more convenient, but it also reduces the overall uncertainty of friction factor, since the uncertainty of the numerical data can be excluded from the calculations.

Table 5-12: Simulation results for Δp_{module} and $\Delta p_{microchannel}$

Insert profile	Flow rate (L/min)	Δp_{module} (Pa)	$\Delta p_{microchannel}$ (Pa)	$\frac{\Delta p_{microchannel}}{\Delta p_{module}}$
Plain	6	45347.8	40978.9	0.90
IFS_*e*0.15-*P*0.75	5.5	185347.0	177748.0	0.96
FS_*e*0.15-*P*1.5	2	18731.7	18453.6	0.99
D_*e*0.21-*P*2.1	4	75422.8	73265.7	0.97

Hence, the pressure drop across the 30-mm microchannel is obtained by:

$$\Delta p_{microchannel} \approx \Delta p_{module} \tag{5-14}$$

The Darcy friction factor f in the present study is determined by:

$$f = \frac{\Delta p_{microchannel}}{\frac{1}{2}\,\rho\, u_m^2}\frac{D_h}{L} = \frac{\Delta p_{microchannel}}{Re^2}\left(\frac{2\,{D_h}^3}{L}\times\frac{\rho}{\mu^2}\right) \quad (5\text{-}15)$$

Reynolds number for the annular microchannel is calculated by:

$$Re = \frac{\dot{m}\,D_h}{A_c\,\mu} = \frac{4\dot{m}}{\pi(D_o + D_i)\mu} = \frac{4\rho Q}{\pi(D_o + D_i)\mu} \quad (5\text{-}16)$$

The normalised friction factor is quantified by:

$$E_f = \frac{f}{f_{Plain}} \quad (5\text{-}17)$$

5.9.3 Thermo-hydraulic Performance

As explained in Section 3.3.3, the thermo-hydraulic performance is quantified by:

$$\eta = \left(\frac{Nu}{Nu_{Plain}}\right)\Big/\left(\frac{f}{f_{Plain}}\right)^{\frac{1}{3}} \quad (5\text{-}18)$$

5.10 Uncertainty Analysis

The uncertainty analysis is carried out after reviewing several guidelines on reporting measurements, including the National Physical Laboratory guide [159], United Kingdom Accreditation Service (UKAS) guide [160], the Joint Committee for Guides in Metrology (JCGM) guide [161], the National Institute of Standards and Technology (NIST) guide [162] and Journal of Heat Transfer Policy [163].

Measurement is the "process of experimentally obtaining one or more quantity values that can reasonably be attributed to a quantity" [164]. The purpose of measurement is to assign a quantitative value to the measurand. There are four

parts to reporting a measurement: the nominal value, the units of measurement, the uncertainty and the confidence level.

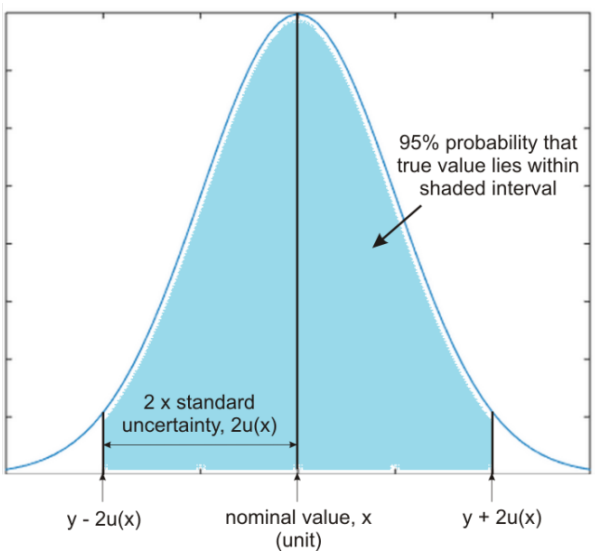

Figure 5-25: Parameters for reporting measurements

As illustrated in Figure 5-25, the nominal value is the best estimate of the (unknown) true quantity value. The uncertainty of a measurement provides an interval, of limits less and more than the nominal value, within which the true quantity value is believed to lie. The confidence level refers to the statistical probability that the true quantity value indeed lies within the reported interval. The Journal of Heat Transfer suggests that all uncertainty evaluation is to be performed with a 95% confidence interval [163].

Uncertainty in measurement is largely due to two effects: random and systematic. Random effects occur when several consecutive measurements give randomly different results; whereas systematic effects occur when the measured quantity is, on average, consistently higher/lower than the true quantity value. Uncertainty due to random effects may be reduced by increasing the number of measurements; whereas uncertainty due to systematic effects may be reduced by applying a correction relation determined from calibration. However, due to

the lack of complete knowledge of the measurement process, uncertainty can only be minimised but never eliminated.

In this study, the uncertainty of a measurement is evaluated by first computing standard uncertainty, followed by combined standard uncertainty and expanded uncertainty.

The standard uncertainty due to systematic effects may be attributed mainly to the uncertainty of the estimation of the nominal value based on the best fit equation from the calibration, which is the standard error of estimate (S.E.E.).

The standard uncertainty due to random effects is computed through statistical analysis of a large number of samples, where a normal distribution may be assumed. This is commonly known as Type A evaluation, and can be quantified by:

$$\bar{x} = \frac{1}{n}\sum_{i=1}^{n} x_i$$

$$u(x) = s(\bar{x}) = \sqrt{\frac{1}{n(n-1)}\sum_{i=1}^{n}(x_i - \bar{x})^2} \quad (5\text{-}19)$$

where $\bar{x}$ is the mean of the measurements
x_i is the value of each measurement
n is the number of independent measurements taken
$u(x)$ is the standard uncertainty
$s(\bar{x})$ is the standard deviation of the mean

Combined standard uncertainty of an individual measurement is therefore [163]:

$$u_c(x) = \sqrt{{u_{random}}^2 + {u_{systematic}}^2} \quad (5\text{-}20)$$

For a normal distribution, 1 standard uncertainty, u_c, corresponds to 68% confidence that true value lies within the stated interval. Expanded uncertainty,

U, increases the level of confidence by including a coverage factor, *k*, as in Eqn. (5-21). For 95% confidence, *k* = 2.

$$U = k\, u_c(x) \tag{5-21}$$

The final result of a measurement would then be $\bar{x} \pm U$, with 95% confidence.

The uncertainty calculations for the Type-J and Type-T thermocouples, as well as the pressure transducer and flow meter are presented in Appendix B.

5.10.1 Uncertainty of Dimensions

To evaluate the standard uncertainty of numeric rounding caused by finite resolution of the measuring instruments, the rectangular probability distribution is considered. As shown in Figure 5-26, there is equal probability of the value of x_i being anywhere within the range $x_i - a$ to $x_i + a$, and zero probability of it being outside these limits. Half-width a is simply half of the instrument resolution. This method is classified as Type B evaluation.

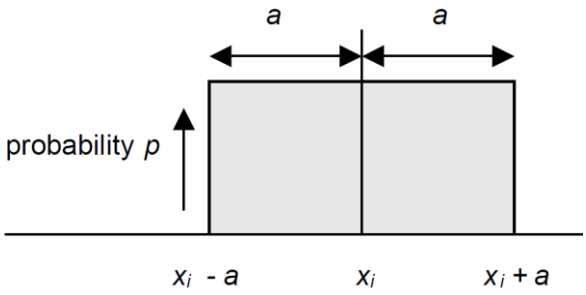

Figure 5-26: Rectangular probability distribution [160]

The standard uncertainty corresponding to the rectangular probability distribution can be estimated as a function of half-width, *a*:

$$u(x) = \frac{a}{\sqrt{3}} \tag{5-22}$$

The uncertainty calculation for the key dimensions is shown in Appendix B.

5.10.2 Uncertainty of Derived Parameters

The individual measurements, such as pressure, temperature and flow rate, are subsequently used to derive certain parameters of interest. In this study, these parameters include convective heat transfer coefficient, pressure drop, Nusselt number, Reynolds number, friction factor, normalised Nusselt number, normalised friction factor and thermo-hydraulic performance.

The uncertainty for the derived parameters are computed using the law of propagation [162]:

Given that $y = f\ (x_1, x_2, \dots, x_N)$

$$U_{derived}(y) \approx \sqrt{\sum_{i=1}^{N} \left(\frac{\partial f}{\partial x_i}\right)^2 U^2(x_i)} \tag{5-23}$$

where $\frac{\partial f}{\partial x_i}$ is sensitivity coefficient and $U(x_i)$ is the expanded uncertainty of each measurement.

The calculated uncertainty values for the derived parameters are tabulated in Table 5-13. The expanded uncertainty of all fluid properties, such as density, specific heat, thermal conductivity and kinematic viscosity are taken to be 0.5 %. The measurement system was initially designed for flow rates ranging from 2.0 to 7.0 L/min. Hence, the uncertainty values are low. However, preliminary results for the enhanced microchannels show signs of early laminar-to-turbulent flow transition. To further investigate this, the flow rate range was extended to be from 0.5 to 7.0 L/min. The maximum uncertainty values for flow rates from 0.5 to 2.0 L/min are computed as well. While the uncertainty values are high, the measured values exhibit a well-behaved trend even at low flow rates, as can be observed from all the results in Chapters 6 to 9. This provides confidence that the measured values are accurate despite the high maximum uncertainty values.

Table 5-13: Uncertainty of key parameters

Parameter	Range of uncertainty for 2 to 7 L/min	Maximum uncertainty for 0.5 to 2 L/min
h	2.8 – 10.3%	36.9%
Δp	0.3 – 10.2%	43.3%
Nu	3.1 – 10.4%	36.9%
Re	0.5 %	0.5 %
f	1.3 – 10.3%	43.3%
E_{Nu}	4.3 – 14.7%	52.1%
E_f	1.8 – 14.5%	61.2%
η	4.4 – 15.5%	56.0%

5.11 Validation of Measurement System

5.11.1 Comparison of Measured Values with Classical Theory

The measured friction factor for the Plain microchannel is validated through the comparison with classical correlations. For Reynolds number less than 2,200, the parallel plate formula for laminar flow by Shah in 1978 [35] is used. This is reasonable since the Poiseuille number correlations for concentric annular pipes with $r^* \gtrsim 0.4$ are virtually the same as those for parallel plates even up to z_{hy}^*=0.1 [18]. In the present study, r^*=0.97 and the largest z_{hy}^*=0.04. For Reynolds number above 3,400, the circular pipe formula for turbulent flow by Phillips in 1987 [22] is considered, with the circular diameter replaced by hydraulic diameter. After accounting for the variation in fluid properties due to the large temperature difference between the wall and the bulk fluid, the measured and predicted values of friction factor have a maximum discrepancy of 9.2%, as shown in Table 5-14. The overall mean discrepancy is 7.8%.

Table 5-14. Validation of friction factor for Plain microchannel

Reynolds number	Measured f	Predicted f	Discrepancy
350	0.3127	0.2878	-8.0 %
1,700	0.0741	0.0692	-6.6 %
3,472	0.0523	0.0484	-7.5 %
4,591	0.0493	0.0448	-9.2 %

The measured Nusselt number for the Plain microchannel is also validated through the comparison with classical correlations. For Reynolds number less than 2,200, the circular pipe formula by Shah and London for laminar flow under constant heat flux condition [18] is used. For Reynolds number above 3,400, the Gnielinski's equation [34] for turbulent flow is considered. After accounting for the variation in fluid properties due to the large temperature difference between the wall and the bulk fluid, the measured and predicted values of Nusselt number have a maximum discrepancy of 19.6%, as shown in Table 5-15. The overall mean discrepancy is 13.4%.

Table 5-15. Validation of Nusselt number for Plain microchannel

Reynolds number	Measured *Nu*	Predicted *Nu*	Discrepancy
350	6.85	6.50	-5.1 %
1,700	12.47	11.07	-11.2 %
3,472	21.10	24.80	17.6 %
4,591	28.44	34.02	19.6 %

According to classical heat transfer theory for developing flow, Nusselt number for a fixed geometry remains constant for the same Reynolds number and Prandtl number [13]. Table 5-16 shows that the measured Nusselt number varies within 3.3%, when the Reynolds number and Prandtl number are maintained within 0.2%. This is in good agreement with the classical theory. In addition, it is validated that the Nusselt number measurements are independent of the heat supplied to the test module, also shown in Table 5-16.

Table 5-16: Validation of Nusselt number

	Re	*Pr*	*Nu*	Heat Input (W)
IFS_*e*0.21-p2.1	3798	5.53	46.21	1000
	3791	5.53	47.72	250
Discrepancy	-0.2%	0.0%	3.3%	

5.11.2 Repeatability Test

The repeatability test is conducted at five randomly selected cases, using different IFS inserts and flow rates. The measurement is performed twice for each case, and the key parameters are computed and compared. As shown in Table 5-17, the maximum discrepancy in pressure drop and Nusselt number measurements are 0.57% and 0.39% respectively, indicating an excellent repeatability.

Table 5-17. Repeatability test

IFS insert		Flow Rate	Heat Flux	Discrepancy in Pressure Drop	Discrepancy in Nusselt number
e (mm)	***P*** (mm)	(L/min)	(W/cm^2)	(%)	(%)
0.21	2.1	2.00	53.0	0.36	-0.17
0.15	2.25	3.00	53.0	0.57	-0.39
0.15	0.75	4.00	53.0	0.05	0.16
0.15	1.5	6.00	53.0	0.46	0.36
0.15	3.0	7.00	53.0	-0.16	-0.12

Chapter 6 Results for the Plain Microchannel

This chapter presents the measured results for the Plain annular microchannel, with a gap size of 300 μm. The first section demonstrates that high heat transfer coefficient values, which are comparable to those in a typical microchannel, can be achieved in macro geometry without involving complex and costly manufacturing methods. The second and third sections compare the measured results with predictions from the classical theory, and discuss the possible reasons for any deviation. The fourth section identifies the laminar-to-turbulent flow transition regime in the present study based on the flow and heat transfer behaviour, and compares it with those from the classical theory. The fifth section distinguishes the flow regime based on the hydrodynamic and thermal entrance lengths.

6.1 Overview of Measured Results for the Plain Microchannel

Figure 6-1 shows the variation of convective heat transfer coefficient h with flow rate for the Plain microchannel. For single-phase liquid water in conventionally-sized channels, the typical h values are at most 10 $kW/m^2 \cdot K$ [14,27]. In the present study, the heat transfer coefficient for the Plain microchannel ranges from 10.9 to 27.1 $kW/m^2 \cdot K$, for flow rates between 2 and 7 L/min. This confirms the feasibility of achieving microscale heat transfer effects in macro geometry.

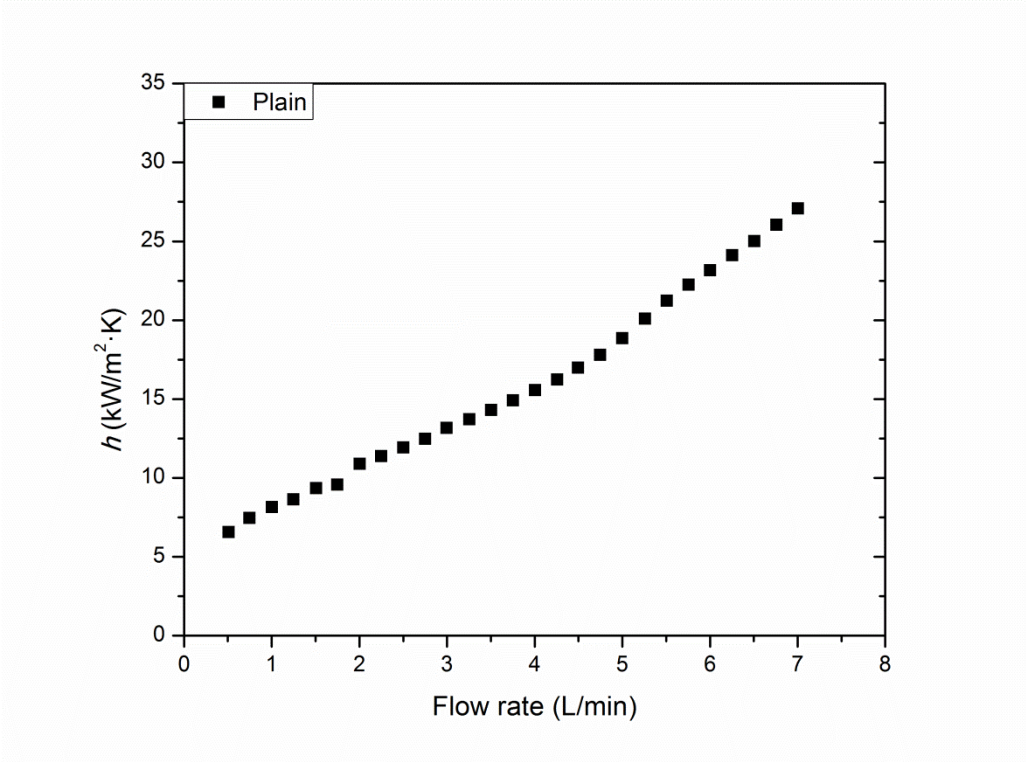

Figure 6-1: Heat transfer coefficient against flow rate for Plain microchannel

6.2 Comparison of Friction Factor with Classical Theory

For hydrodynamic considerations, Figure 6-2 compares the measured friction factor with the values predicted by classical theory. For laminar flow, friction factor predictions from Shah and London for circular pipes (Eqn. 2-11) and parallel plates (Eqn. 2-49) are used. They are valid for both developing and fully developed flow. The Hagen–Poiseuille theory (Eqn. 2-12) is not used as it is applicable to fully developed flow, and therefore does not consider the entrance effect which is significant in the present study. For turbulent flow, the Phillips correlation (Eqn. 2-13) is used, as it is applicable to both developing and fully developed flow, and for smooth pipes.

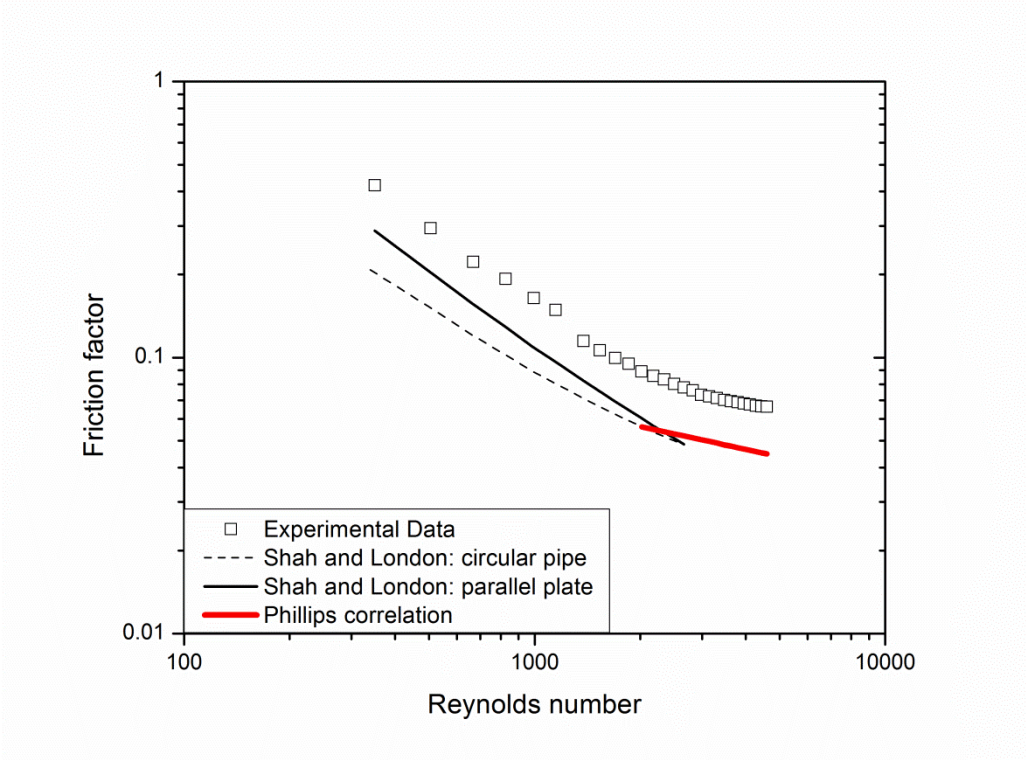

Figure 6-2: Comparison of measured friction factor with classical correlations

It is observed that the measured friction factor values are higher than those predicted by classical theory, for both laminar and turbulent flow. Upon closer scrutiny, the friction factor in the present study is derived by evaluating all the fluid properties at the mean fluid temperature, using the data reduction procedure in Section 5.9. However, when there is a large temperature difference between the wall and the bulk fluid, the variation in fluid properties becomes important. Specifically, the viscosity of the fluid next to the heated wall is lower than that of the bulk fluid. Hence, the average friction factor of the microchannel would be lower.

Kakaç et al. [14] proposed a property correction factor for dynamic viscosity: $f_{adjusted} = f(\mu_b/\mu_w)^{-0.58}$, where the subscripts b and w stand for bulk and wall, respectively. Using the aforementioned equation, the adjusted friction factor is approximated to be 74% of the original data. As shown in Figure 6-3,

the adjusted friction factor values agree with the correlations by Shah and London for laminar flow in parallel plates, and by Phillips for turbulent flow. This suggests that it is important to consider property correction factors in microchannel flows, and that this could be a factor for the discrepancies among earlier studies regarding the deviation from classical theory.

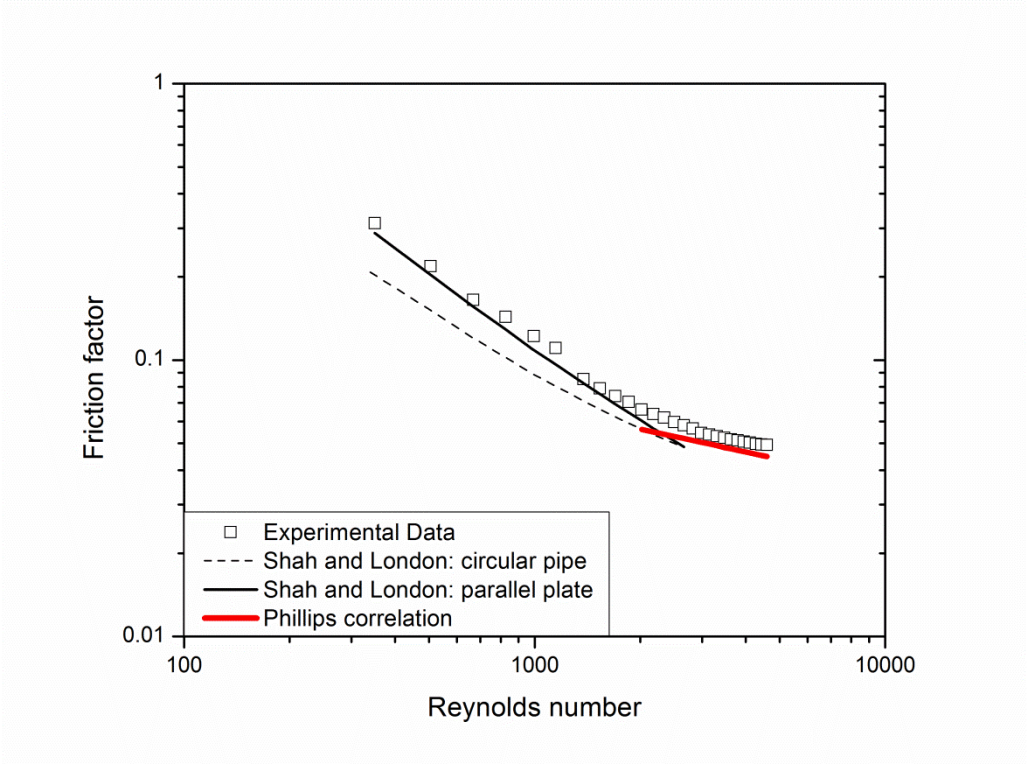

Figure 6-3: Comparison of adjusted measured friction factor with classical correlations

6.3 Comparison of Nusselt Number with Classical Theory

For thermal considerations, Figure 6-4 compares the measured Nusselt number with the values predicted by classical theory. For laminar flow, Nusselt number correlations by Shah and London for circular pipes (Eqn. 2-28) and parallel plates (Eqn. 2-51) are used. They are applicable to thermally developing flow, subject to constant wall heat flux conditions. Although the Hausen prediction (Eqn. 2-25) is commonly used by many researchers as highlighted in Chapter 2, it is only applicable for constant wall temperature conditions. Hence, it is not

applicable in the present study, where the flow is subjected to constant heat flux conditions.

For turbulent flow, the Gnielinski's correlation (Eqn. 2-34) is used. This correlation is applicable to fully developed flow in smooth pipes, and hold for both constant wall temperature and heat flux boundary conditions. Although it is proposed for fully developed flow, it is sufficient as an approximation in the present study. This is because the entrance effects are less significant in turbulent flow, due to the fact that the hydrodynamic and thermal entrance lengths are much shorter. The detailed calculation is presented in Section 6.5.

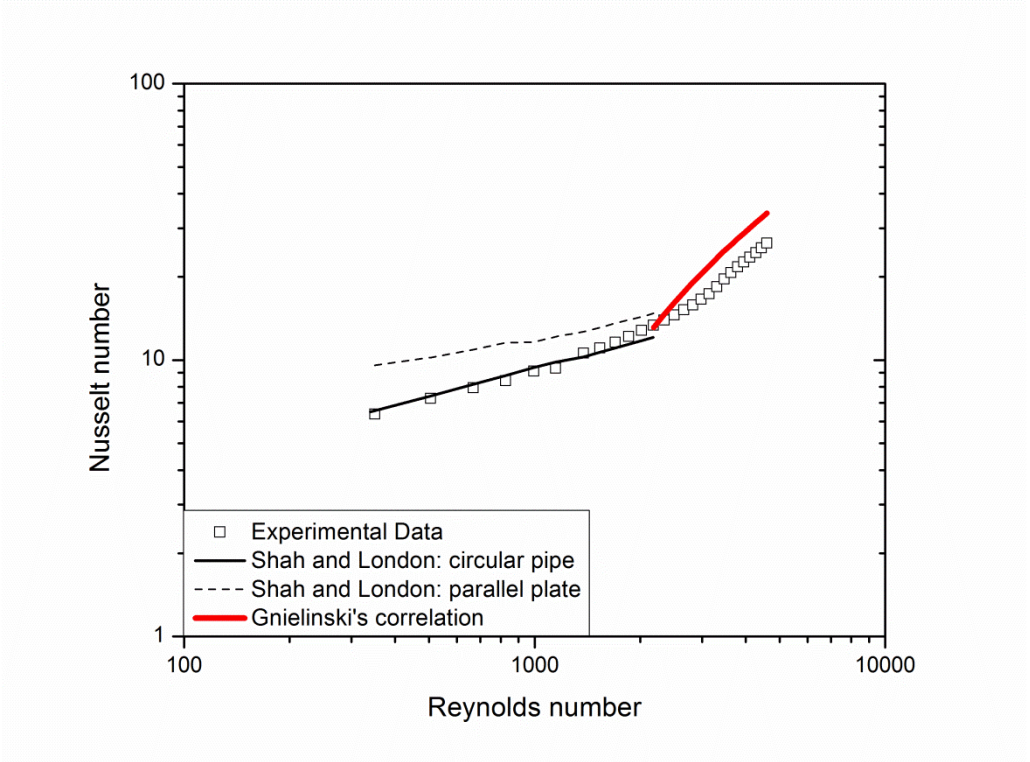

Figure 6-4: Comparison of measured Nusselt number with classical correlations

It is observed that the correlation by Shah and London for circular pipes is in good agreement with the measured Nusselt number, while the Gnielinski's correlation is slightly higher than the measured data. Similarly, the Nusselt number in the present study is derived by evaluating all the fluid properties at

the mean fluid temperature. If the large temperature difference between the wall and the bulk fluid were considered, the fluid near the wall would be less viscous than the bulk fluid. This means that the velocity gradient at the wall would be greater, leading to higher local Nusselt number near the wall. Hence, the average Nusselt number of the microchannel would be higher.

Sider and Tate [31] provided a property correction factor for dynamic viscosity: $Nu_{adjusted} = Nu(\mu_b/\mu_w)^{0.14}$, where the subscripts b and w stand for bulk and wall, respectively. Using the aforementioned equation, the adjusted Nusselt number is approximated to be 7% higher than the original data. As shown in Figure 6-5, the adjusted Nusselt number values agree with the correlations by Shah and London for laminar flow, and Gnielinski's correlation for turbulent flow. This again suggests that property correction factors are important in microchannel flows.

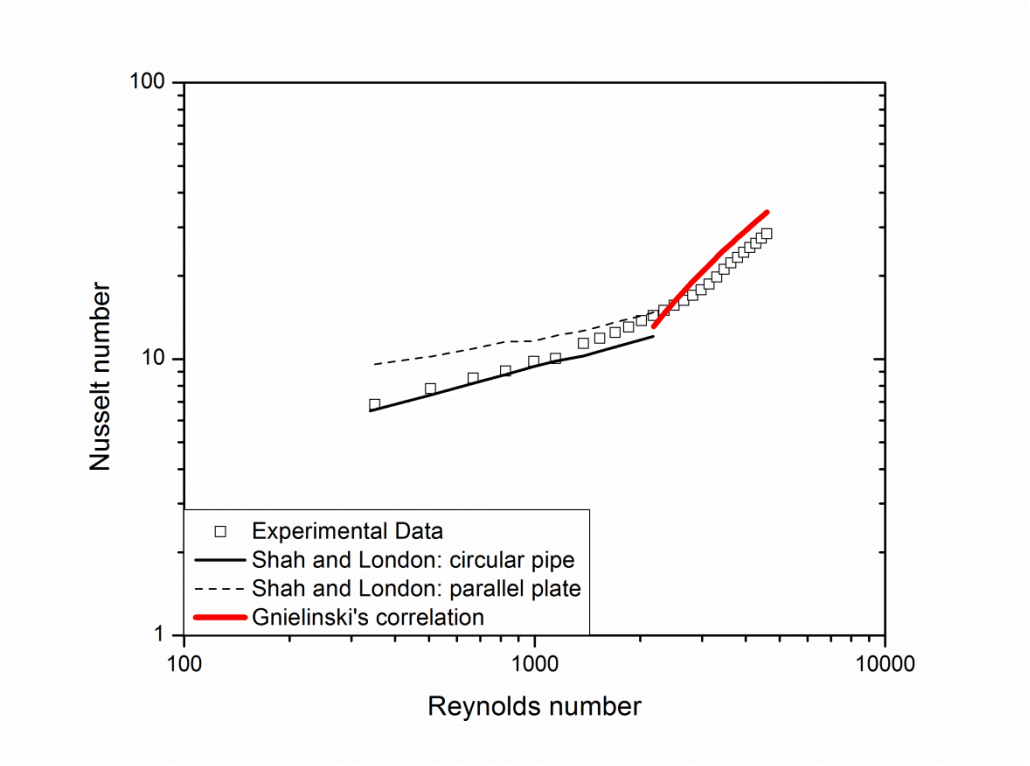

Figure 6-5: Comparison of adjusted measured Nusselt number with classical correlations

6.4 Laminar-to-turbulent Transition

Figure 6-6 presents both the variation of measured friction factor and Nusselt number with Reynolds number in the same figure, in order to accurately determine the Reynolds number range for flow transition. As discussed in Sections 2.1 and 2.2, the critical Reynolds number corresponding to laminar-to-turbulent flow transition for parallel plates ranges between 2,200 and 3,400 [14,165], while that in circular pipes is approximately 2,300 [13]. It is clear that both the friction factor and Nusselt number data agree on the same critical Reynolds number range for the Plain microchannel in the present study, and that this range agrees with those for the conventionally-sized macro-scale channels.

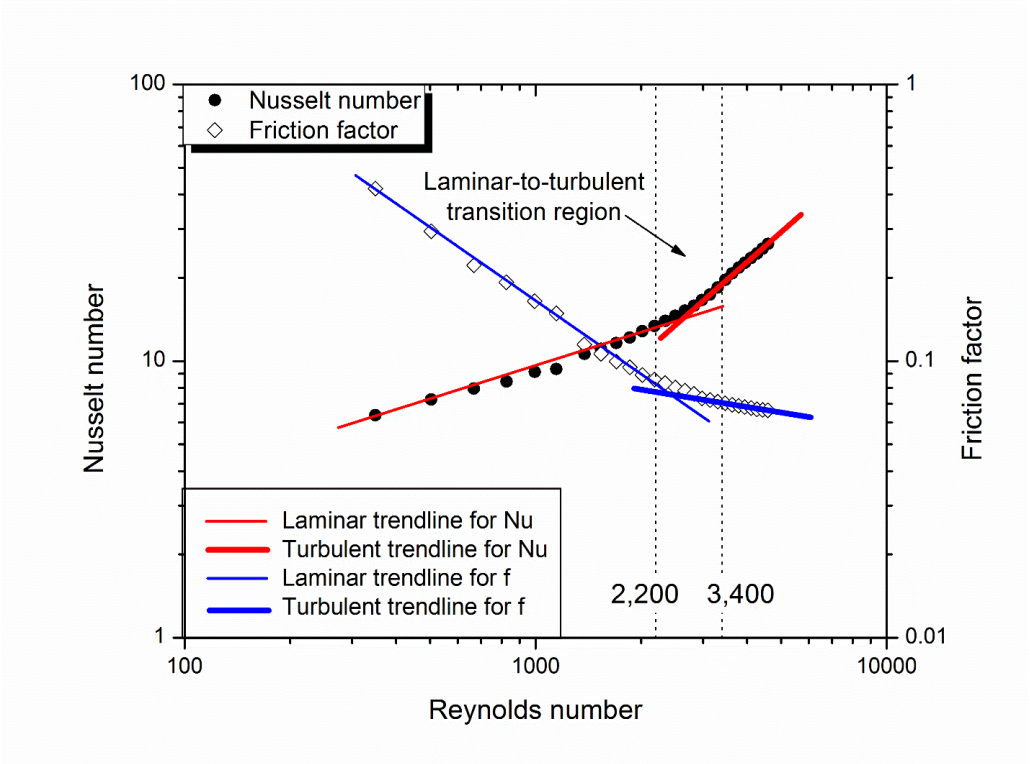

Figure 6-6: Identification of flow transition from the flow and heat transfer behaviour

6.5 Classification of Flow Regime

In order to understand whether the flow is developing or fully developed, the hydrodynamic and thermal entrance lengths are computed. For the laminar flow regime, Shah and London [18] proposed that the dimensionless hydrodynamic and thermal entrance lengths for an annular channel are 0.0108 and 0.04101, respectively. The equations to determine the corresponding dimensional lengths are provided by Eqns. (2-45) and (2-50) in Section 2.2. Since the flow condition has been determined to be laminar up to a Reynolds number of 2,200 in the present study, the entrance lengths are computed accordingly.

Figure 6-7 shows the estimated hydrodynamic and thermal entrance lengths under laminar conditions. At the lowest Reynolds number of 350, the hydrodynamic and thermal entrance lengths are approximately 2 and 45 mm, respectively. Given that the microchannel length is 30 mm in the present study, it implies that 8% of the microchannel length is occupied by the hydrodynamic entrance region, and the flow is thermally developing for the entire microchannel length. On the other hand, at the highest Reynolds number of about 2,200, the hydrodynamic and thermal entrance lengths are approximately 14 and 292 mm, respectively. This implies that 47% of the microchannel length is occupied by the hydrodynamic entrance region, and the flow is thermally developing for the entire microchannel length. In other words, the laminar flow for the Plain microchannel in the present study falls largely in the thermally developing region with fully developed velocity boundary layer.

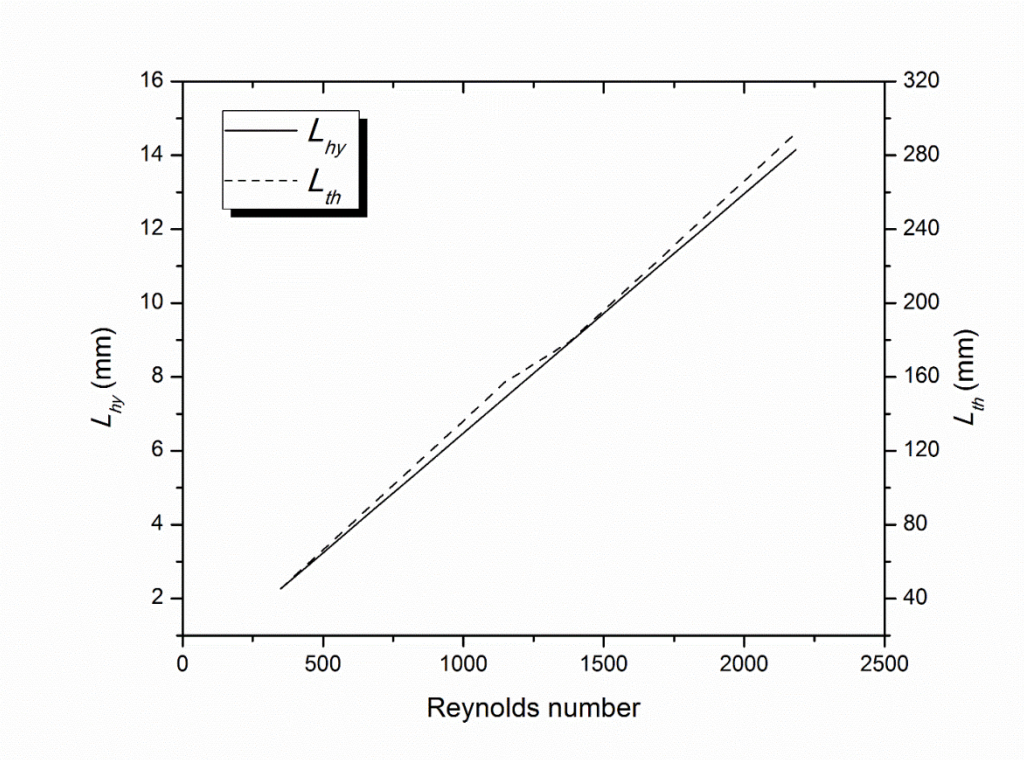

Figure 6-7: Estimated hydrodynamic and thermal entrance lengths under laminar conditions

For turbulent flow, the boundary layers develop much faster, at approximately 10 times the hydraulic diameter of the flow channels [13,17]. In the present study, the hydrodynamic and thermal entrance lengths are therefore 6 mm, implying that 20% of the microchannel length is in the entrance region. In other words, the turbulent flow for the Plain microchannel in the present study falls largely in the fully developed regime, both hydrodynamically and thermally.

Chapter 7 Results for the Inverted Fish Scale Microchannels

The Inverted Fish Scale profile was conceptualised in view that fishes are naturally streamlined to minimise flow disturbance when they swim forward. However, flow disturbances are crucial to enhance heat transfer. Therefore, the scaly profile is designed to oppose the flow direction, as shown in Figure 7-1, so as to cause maximum flow disruption, hence the name "Inverted" Fish Scale. The IFS geometrical profile is quantified by the scale height (e) and scale pitch (P). For a fair comparison with the Plain microchannel, the mean flow gap (H) is kept constant at 300 µm. The results suggest that the IFS profile would be useful for heat transfer applications, where a high heat transfer coefficient is warranted, with less stringent pressure drop restrictions.

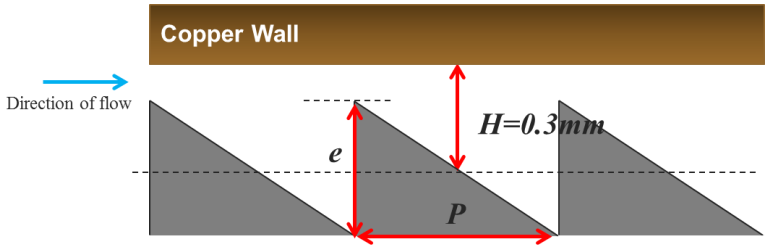

Figure 7-1: Inverted Fish Scale profile

This chapter presents the results for the Inverted Fish Scale (IFS) microchannel series. First, the measured heat transfer coefficient and pressure drop for all the IFS microchannels is presented. Second, a comparison between the measured and numerical results is presented. Third, the effects of e/H ratio and P/e ratio on Nusselt number, friction factor and thermo-hydraulic performance are studied. The physical mechanisms behind the heat transfer and flow phenomena are examined using the flow field, as well as velocity and temperature distributions, from the numerical results.

7.1 Overview of Measured Results for the IFS Microchannels

Figure 7-2 shows the variation of convective heat transfer coefficient *h* with flow rate, for all the IFS and Plain microchannels. The measured data indicates that the IFS profiles generally enhance heat transfer. For flow rates above 3.5 L/min, all the IFS microchannels yield heat transfer coefficient values higher than those of the Plain microchannel. The highest heat transfer coefficient achieved in the present study is 52.8 kW/m^2·K, at 6.5 L/min using the IFS_*e*0.21-*P*2.1 insert. This is 2.1 times the value of 25.0 kW/m^2·K, achieved with the Plain microchannel at the same flow rate. This demonstrates the effectiveness of the IFS profile in enhancing heat transfer performance. Furthermore, with a convective heat transfer coefficient of 52.8 kW/m^2·K, the system is able to remove heat flux of up to 375 W/cm^2 for a temperature difference of 71 K.

As the subsequent analysis focuses on two parts, namely the effects of the scale height (*e*) to mean channel height (*H*) ratio and scale pitch (*P*) to scale height (*e*) ratio, the data points are symbolised accordingly to enhance the visual understanding. This is so that the effects of *e*/*H* ratio and *P*/*e* ratio can be obvious at a glance. For the *e*/*H* ratio study, the IFS_*e*0.03-*P*0.3, IFS_*e*0.09-*P*0.9, and IFS_*e*0.21-*P*2.1 profiles are represented by hollow symbols. They correspond to an *e*/*H* ratio of 0.1, 0.3 and 0.7, respectively, with a *P*/*e* ratio of 10. For the *P*/*e* ratio study, the IFS_*e*0.15-*P*3.00, IFS_*e*0.15-*P*2.25 and IFS_*e*0.15-*P*0.75 profiles are represented by solid symbols. They correspond to a *P*/*e* ratio of 20, 15 and 5, respectively, with an *e*/*H* ratio of 0.5. The IFS_*e*0.15-*P*1.5 profile, being involved in both studies, is represented by a hollow symbol with a cross. It corresponds to an *e*/*H* ratio of 0.5 and a *P*/*e* ratio of 10.

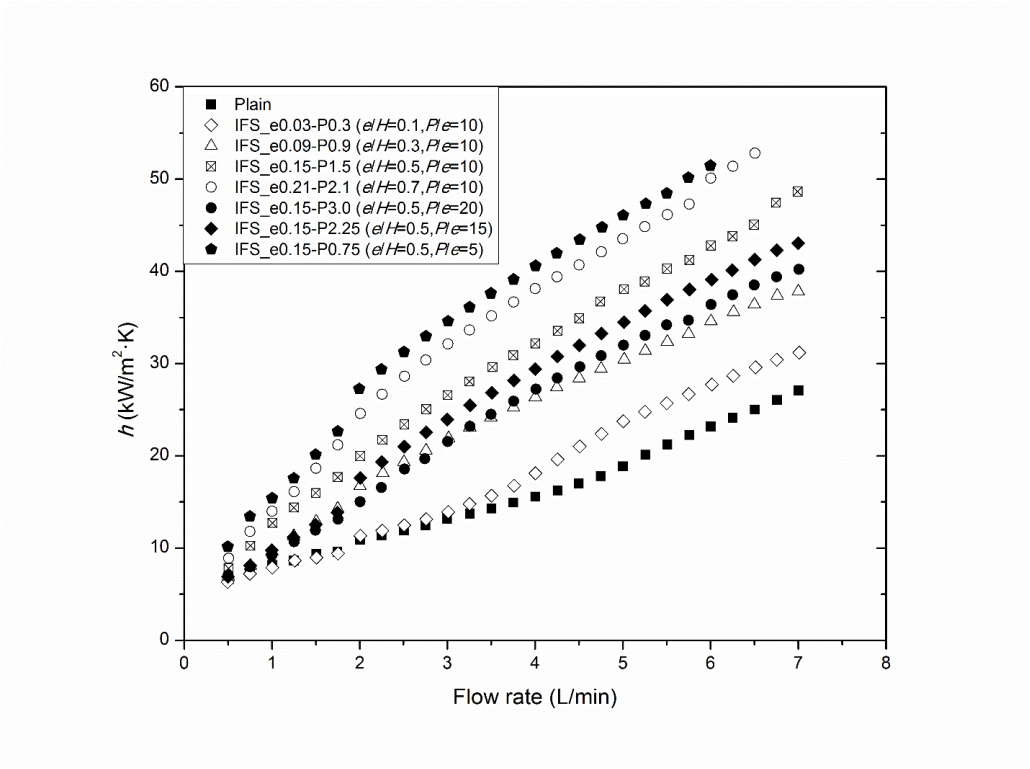

Figure 7-2: Heat transfer coefficient against flow rate for all IFS and Plain microchannels

Figure 7-3 shows the variation of pressure drop across the microchannel with flow rate, for all the IFS and Plain microchannels. It is observed that the maximum pressure drop for the IFS microchannel series is 3.3 bars. This value is also the maximum pressure drop in the whole study. The pressure drop of 3.3 bars does not present itself to be a practical issue at all, since it can be easily overcome by a commercially available pump, which is readily available in the market for use in a macro system.

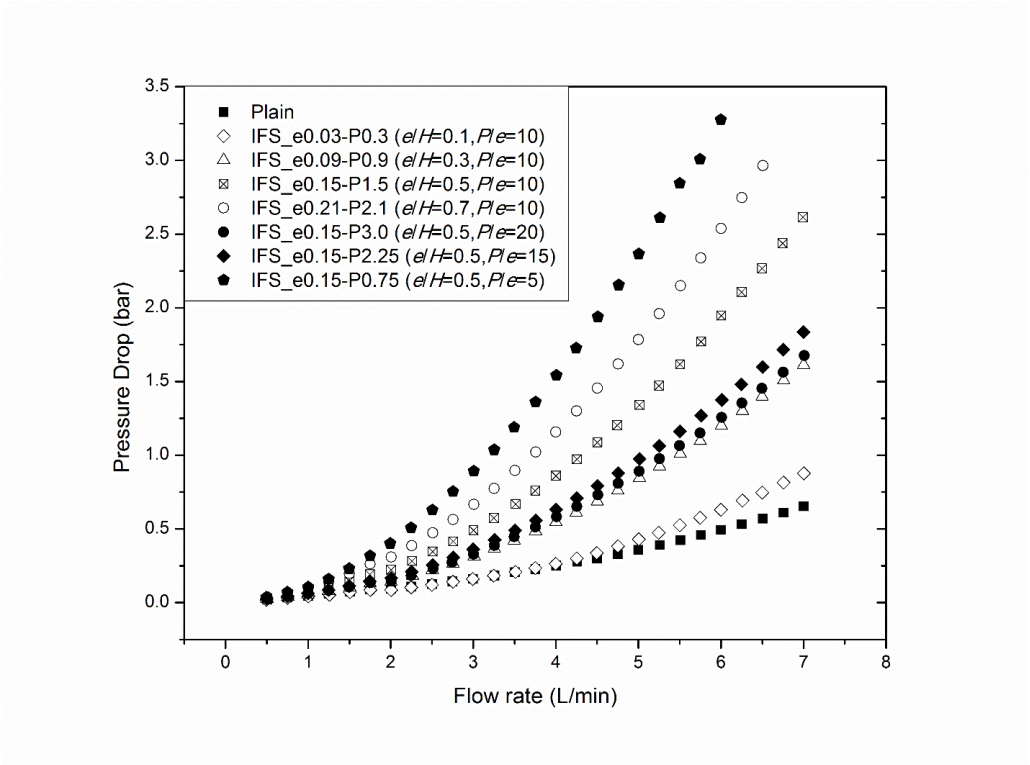

Figure 7-3: Pressure drop against flow rate for all IFS and Plain microchannels

7.2 Comparison between Measured and Numerical Results

Figure 7-4 compares the measured and predicted pressure drop, for various insert profiles at flow rates between 2 and 7 L/min. It is observed that about 80% of the predictions agree well with the measurements, with the deviations falling within the ±10% band. This demonstrates that the classical momentum and continuity equations are capable of predicting single-phase microscale flow in the IFS microchannels. Nonetheless, the numerical model generally under-predicts the pressure drop.

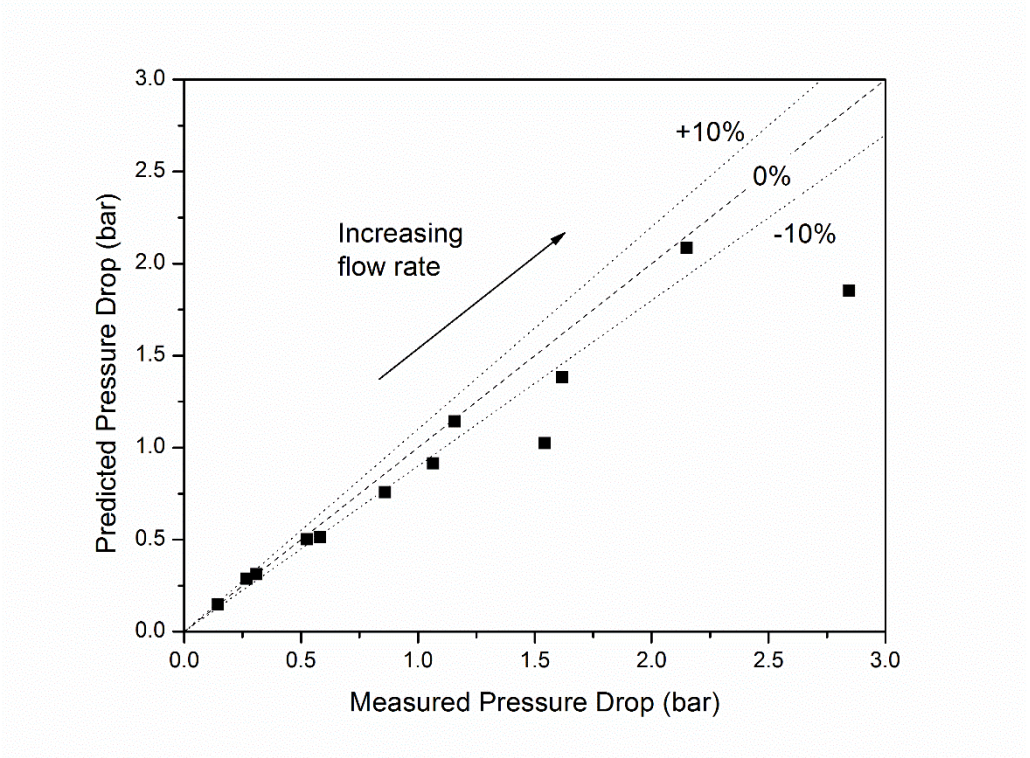

Figure 7-4: Predicted pressure drop against measured pressure drop (IFS series)

Similarly, Figure 7-5 compares the measured and predicted Nusselt number, for various insert profiles at Reynolds numbers approximately between 1,300 and 4,600. It is observed that about 80% of the predictions agree with the measurements within the ±30% deviation band. For heat transfer predictions in single-phase microscale flow, the deviation band is generally expected to be larger than that for pressure drop. As concurred by Kong and Ooi [11], the classical governing equations employed in numerical analyses may be less adequate in predicting the heat transfer behaviour of single-phase flow in microscale channels. Overall, the numerical model generally over-predicts the Nusselt number.

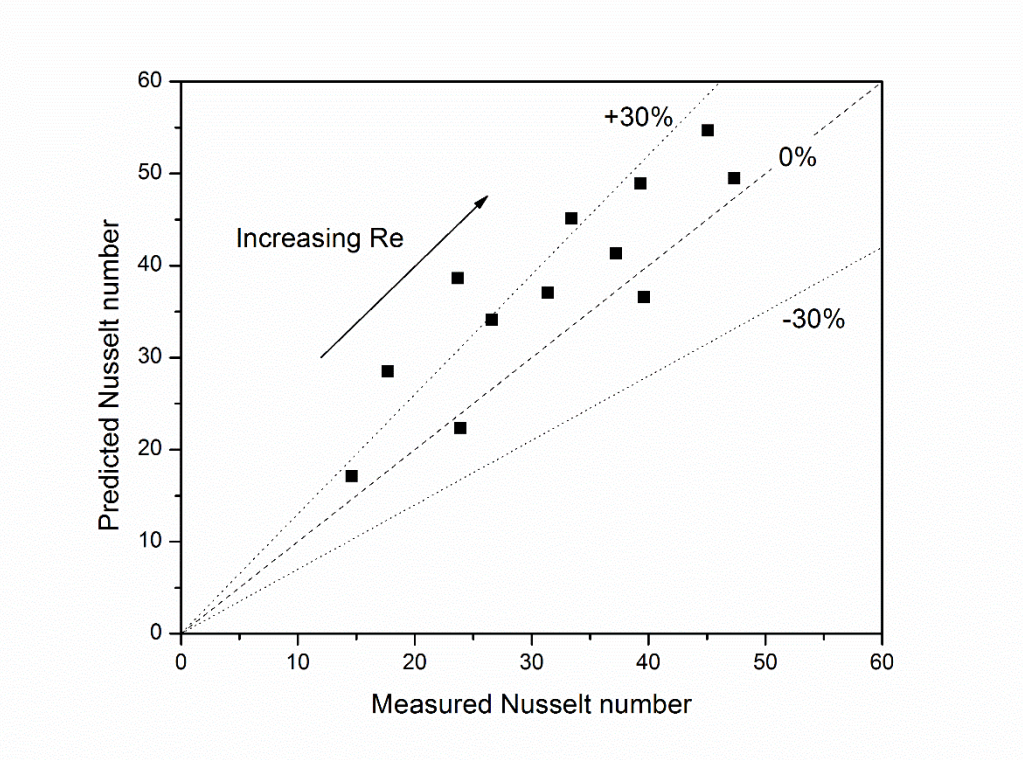

Figure 7-5: Predicted Nusselt number against measured Nusselt number (IFS series)

7.3 Scale Height (*e*) to Mean Channel Height (*H*) Ratio Study

In order to investigate the effect of the scale protrusion height on the heat transfer and flow characteristics, the scale height (*e*) to mean channel height (*H*) ratio is varied, where *H* is fixed at 0.3 mm. In this parametric study, four *e*/*H* ratios of 0.1, 0.3, 0.5 and 0.7 are studied, with a fixed scale pitch (*P*) to scale height (*e*) ratio of 10. A larger *e*/*H* ratio corresponds to a narrower minimum gap through which the fluid flows. The schematic diagram explaining these terminologies can be found in Section 3.2.1.

7.3.1 Thermal Considerations

Figure 7-6 shows the variation of Nusselt number with Reynolds number, for different *e*/*H* ratio. It is observed that Nusselt number increases with Reynolds number and *e*/*H* ratio. This will be considered in the formulation of the Nusselt number correlation. The maximum Nusselt number achieved is 52, at Reynolds number of 4,280 using the IFS profile with *e*/*H* ratio of 0.7. This is also the maximum Nusselt number achieved in the whole study, due to the imposed pressure drop limit of 3.5 bars.

The Nusselt number is plotted with a y-axis range of 0 to 60 throughout the thesis. This is useful for a meaningful comparison across the three different microchannel series.

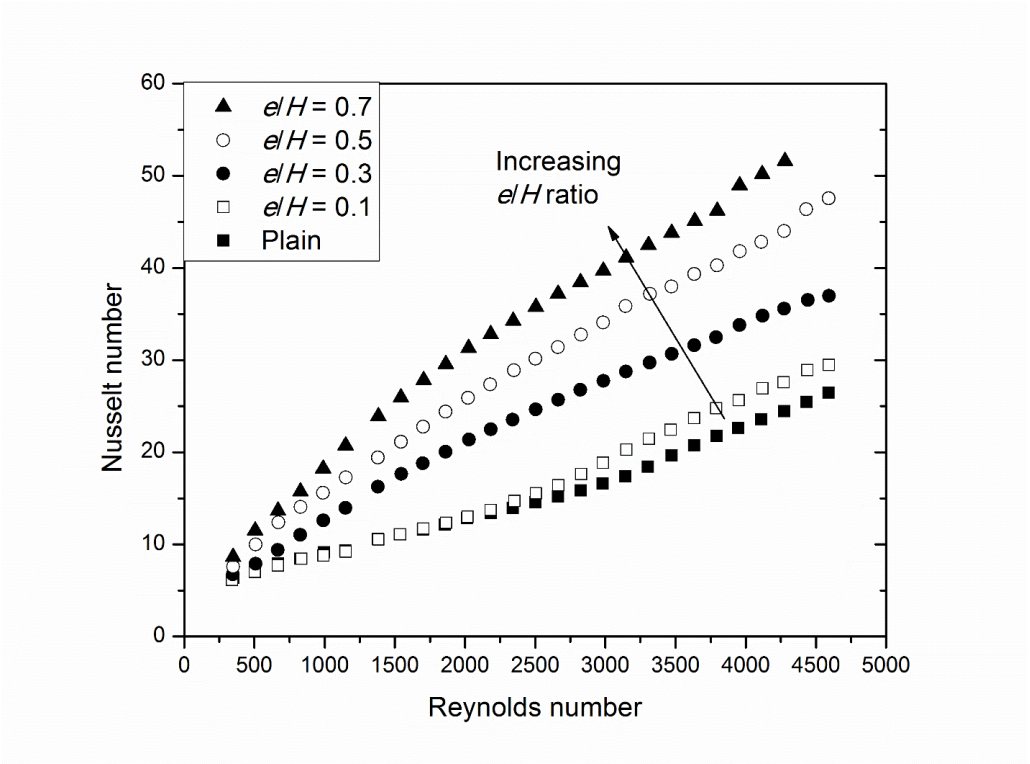

Figure 7-6: Nusselt number against Reynolds number, for different *e*/*H* ratio (IFS series)

Figure 7-7 shows the variation of normalised Nusselt number with Reynolds number, for different *e*/*H* ratio. The Nusselt number is normalised with respect to that of the Plain microchannel. The IFS profile with *e*/*H* ratio of 0.7 is observed to achieve a Nusselt number of nearly 2.5 times that of the Plain microchannel. For the IFS profiles with *e*/*H* ratio of 0.3, 0.5 and 0.7, the heat transfer enhancement starts to become significant when Reynolds number exceeds 600. This is likely due to the onset of turbulence, since the corresponding friction factor to be presented in Figure 7-15 also exhibits a change in flow behaviour at Reynolds number of 600. In other words, the presence of a sufficiently high scale height in the IFS microchannel promotes early laminar-to-turbulent flow transition, thereby enhancing heat transfer.

Another interesting observation is that the normalised Nusselt number declines beyond a Reynolds number of 3,400. This is due to the fact that the Nusselt number of the Plain microchannel increases more rapidly with Reynolds number upon reaching a turbulent flow state. Based on Figure 7-6, the absolute difference between the Nusselt number values for the IFS microchannel and the Plain microchannel appears to be relatively constant. Given that the normalised Nusselt number is defined as Nu/Nu_{Plain}, it would logically decrease when Nu_{Plain} increases, while $Nu - Nu_{Plain}$ remains relatively constant. This implies that when both the IFS and Plain microchannels have reached a turbulent flow state, the IFS profile becomes less effective in improving the heat transfer relative to the Plain microchannel. In other words, the IFS profile is most effective in improving the heat transfer if it promotes early laminar-to-turbulent flow transition at a Reynolds number lower than 3,400.

For a meaningful comparison across the three different microchannel series, the normalised Nusselt number is plotted with a y-axis range of 0.8 to 3.0 throughout the thesis.

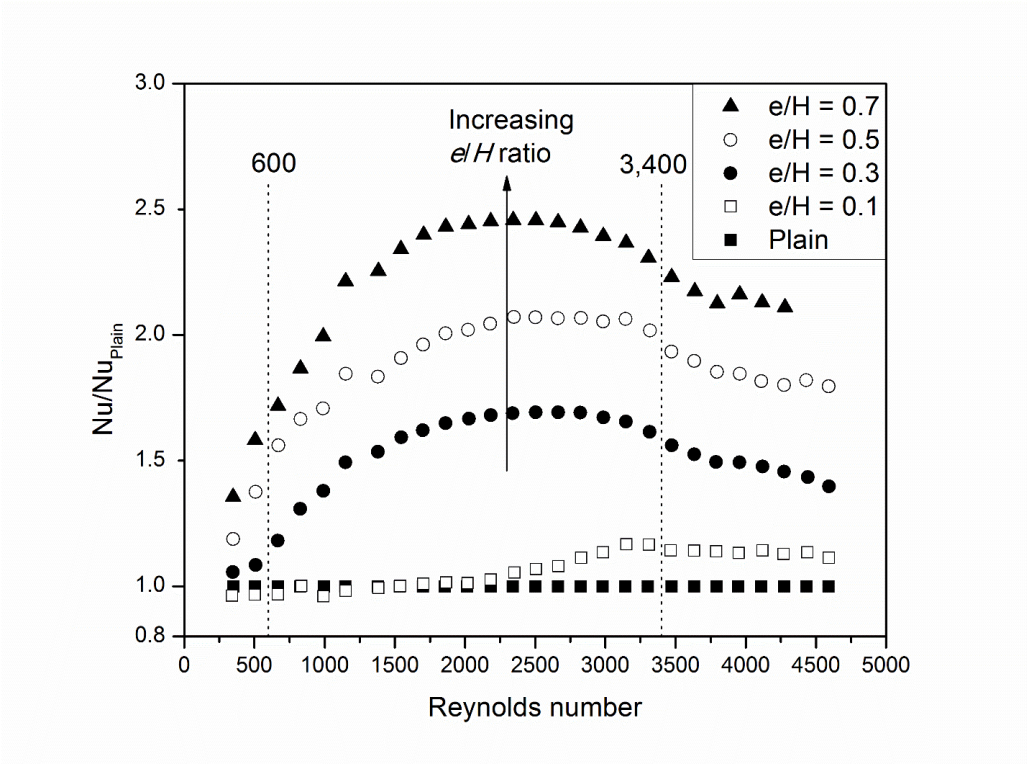

Figure 7-7: Normalised Nusselt number against Reynolds number, for different *e*/*H* ratio (IFS series)

Figure 7-8 presents the same data from Figure 7-6 in a different manner to show the variation of Nusselt number with *e*/*H* ratio. Nusselt number is observed to increase with *e*/*H* ratio, for the same *P*/*e* ratio and Reynolds number. For *e*/*H* ratio=0, which is the Plain microchannel, the Nusselt number is 15 at *Re*≈2,664. As the *e*/*H* ratio increases to 0.1 and 0.7, the Nusselt number increases to 16 and 37 respectively, at the same Reynolds number.

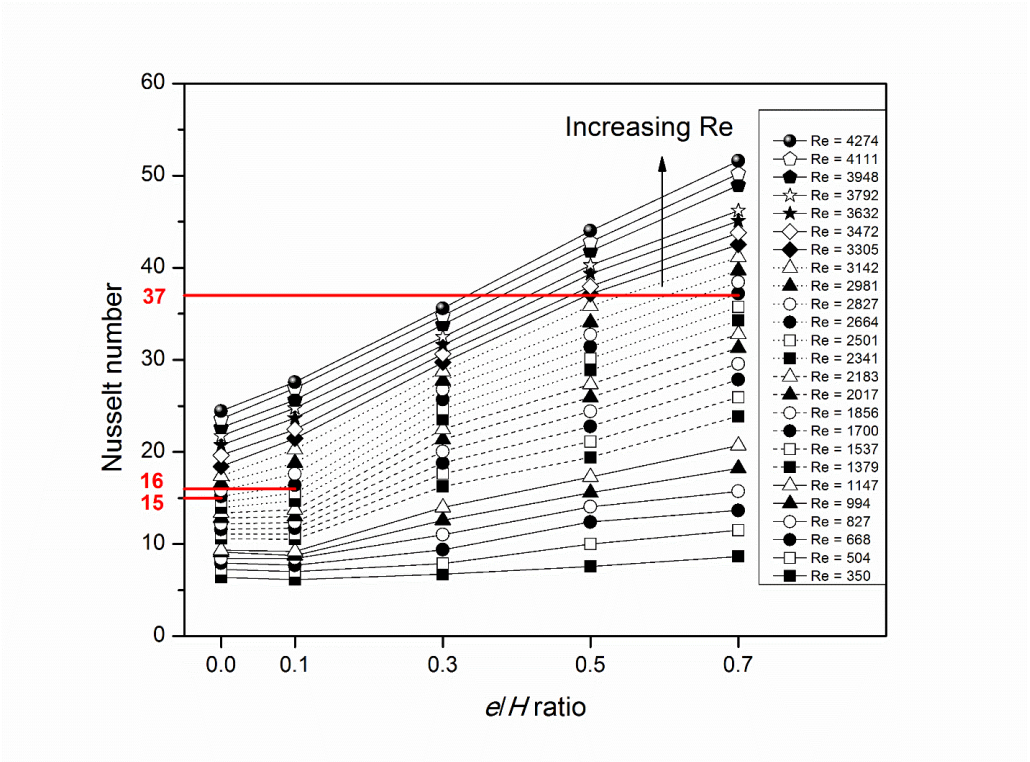

Figure 7-8: Nusselt number against *e*/*H* ratio, at different Reynolds number (IFS series)

The increase of Nusselt number with *e*/*H* ratio is caused by the narrowing of the minimum gap through which the fluid flows. As the incompressible fluid is forced through a narrower gap at the same flow rate, the local fluid velocity becomes higher by virtue of mass conservation. As illustrated in Figure 7-9, when the *e*/*H* ratio=0, which is the Plain microchannel, the channel height is constant at 0.3 mm, and the maximum fluid velocity is about 4.9 m/s. When the *e*/*H* ratio increases slightly to 0.1, the minimum channel height reduces slightly to 0.285 mm, and the maximum fluid velocity remains close to 4.9 m/s, as illustrated in Figure 7-10. However, when the *e*/*H* ratio increases further to 0.7, the minimum channel height reduces significantly to 0.195 mm, and the maximum fluid velocity increases to about 7.5 m/s, as illustrated in Figure 7-11. This maximum fluid velocity occurs slightly downstream of the minimum channel height. The mean channel height, as denoted by the horizontal red dotted line, is fixed at 0.3 mm in the whole study.

For a meaningful comparison, the range for the fluid velocity in the figures is set to be from 0 to 7.5 m/s throughout the thesis. This is so that the fluid velocities can be easily distinguished from the changes in the colour contours. The figures are drawn to scale, at a section length of 3 mm. They are a good representation of the whole microchannel length of 30 mm.

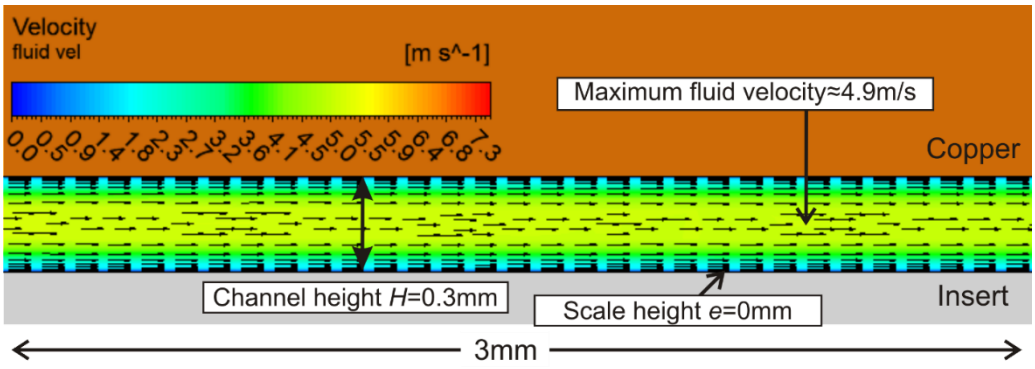

Figure 7-9: Flow field of Plain microchannel at *Re* ≈ 2,664

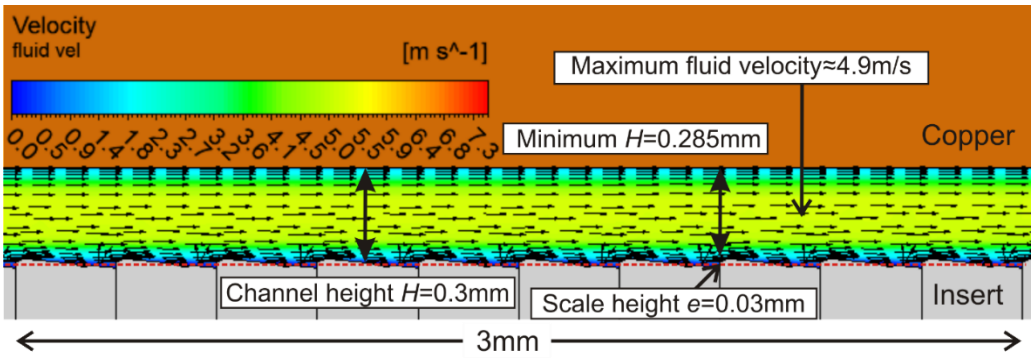

Figure 7-10: Flow field of IFS microchannel with *e*/*H* ratio of 0.1 at *Re* ≈ 2,664

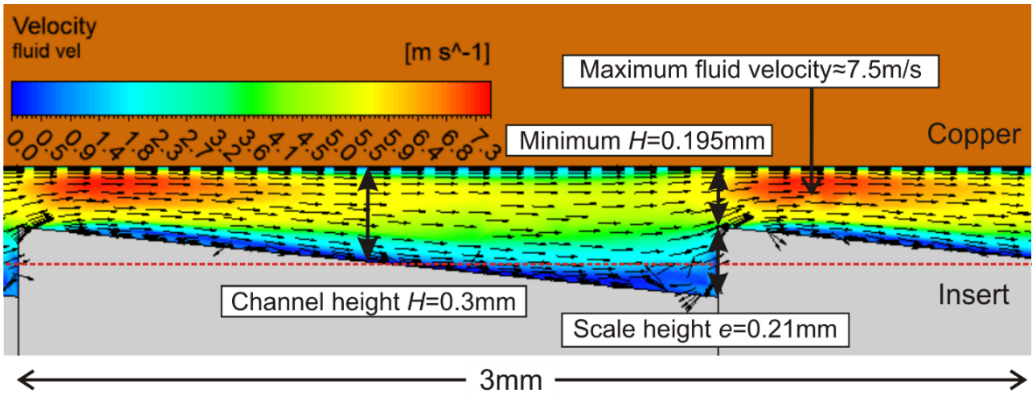

Figure 7-11: Flow field of IFS microchannel with *e*/*H* ratio of 0.7 at *Re* ≈ 2,664

The high local fluid velocity causes the thermal boundary layer near the heated copper wall to become very thin. In accordance with classical theory, for a channel of constant height, the thermal boundary layer keeps developing along the channel until it reaches a fully developed state. At some point, it develops into a thick layer, as illustrated in Figure 7-12. The constant development of thermal boundary layer in the Plain microchannel results in a low Nusselt number of 15. When the e/H ratio increases slightly to 0.1, the low scale height is insufficient to cause significant thinning of the thermal boundary layer, as illustrated in Figure 7-13. Thus the Nusselt number remains low at 16. However, when the e/H ratio increases further to 0.7, significant thinning of the thermal boundary layer near the heated copper wall occurs slightly downstream of the scale tip, as illustrated in Figure 7-14. Hence, the near wall fluid temperature gradient, and therefore the local Nusselt number, becomes high. Since there are 14 scale tips over the entire microchannel length for e/H ratio of 0.7, this repeated thinning effect results in a high average Nusselt number of 37.

For a meaningful comparison, the range for the fluid temperature in the figures is set to be from 301 to 320 K throughout the thesis. This is so that the fluid temperatures can be easily compared by observing the changes in the colour contours. The figures are drawn to scale at a section length of 3 mm, and all of them are located 6 mm downstream of the microchannel entrance. They are a good representation of the whole microchannel length of 30 mm.

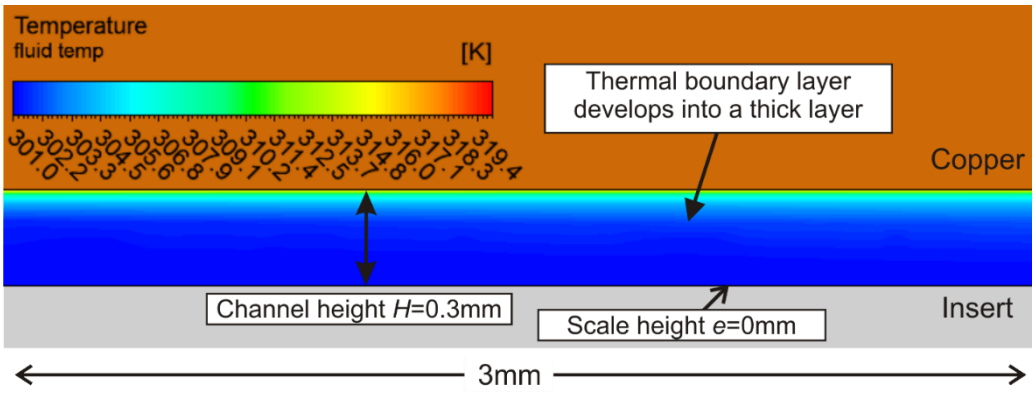

Figure 7-12: Temperature distribution of Plain microchannel at *Re* ≈ 2,664

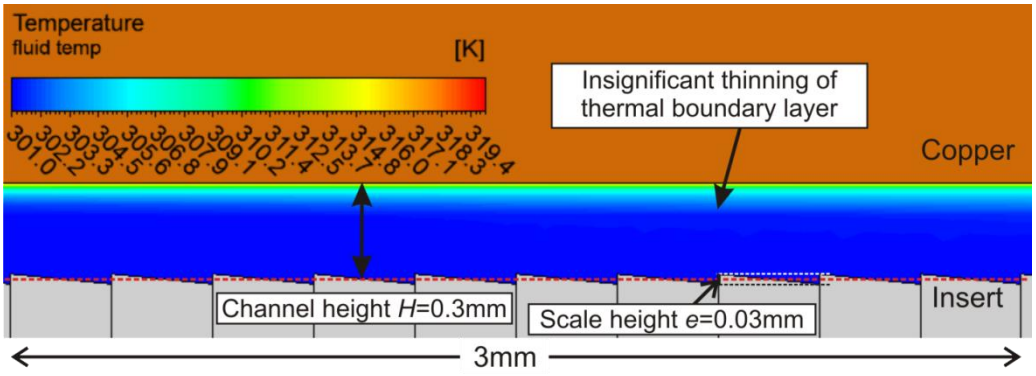

Figure 7-13: Temperature distribution of IFS microchannel with *e*/*H* ratio of 0.1, at *Re* ≈ 2,664

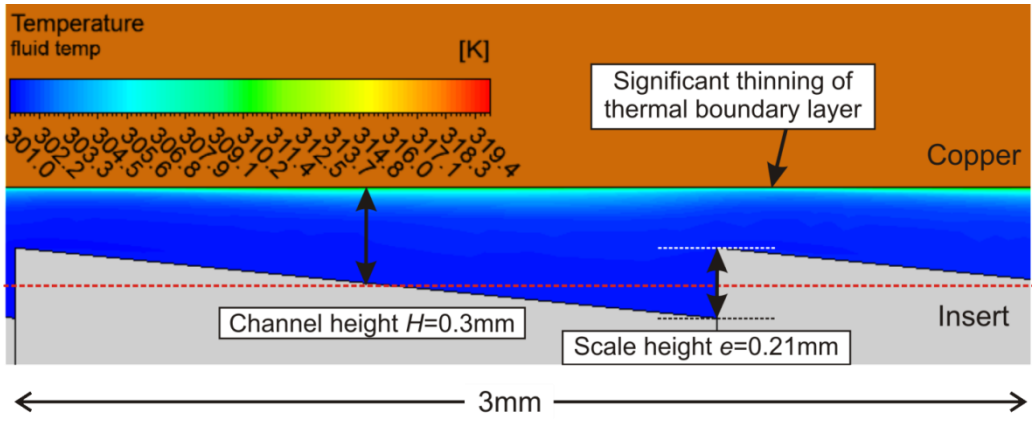

Figure 7-14: Temperature distribution of IFS microchannel with *e*/*H* ratio of 0.7, at *Re* ≈ 2,664

7.3.2 Hydrodynamic Considerations

Figure 7-15 shows the variation of friction factor with Reynolds number, for different *e*/*H* ratio. It is observed that the friction factor decreases with Reynolds number and increases with *e*/*H* ratio. This will be considered in the formulation of the friction factor correlation. The maximum friction factor of 0.73 occurs at Reynolds number of 350, using the IFS_*e*0.21-*P*2.1 insert. The friction factor is plotted using logarithmic scales with the y-axis ranging from 0.05 to 1 throughout the thesis. This is useful for identifying the laminar, transition and turbulent flow regimes. The same y-axis range also allows for a meaningful comparison across the three different microchannel series.

As mentioned in Section 7.3.1, the heat transfer enhancement starts to become significant when Reynolds number exceeds 600, for the IFS profile with *e*/*H* ratio of 0.3, 0.5 and 0.7. This corresponds to the change in flow behaviour as displayed in Figure 7-15. At lower Reynolds numbers, the trend line for the friction factor has a gradient similar to that of the laminar trend line for the Plain microchannel. At Reynolds number of approximately 600, the gradient of the friction factor values starts to deviate from that of the laminar trend line, indicating the onset of turbulence. Furthermore, there is another distinct trend line at higher Reynolds numbers, which has a gradient similar to the turbulent trend line of the Plain microchannel. This confirms that the presence of a sufficiently high scale height in the IFS microchannel promotes early laminar-to-turbulent flow transition.

On the other hand, a lower scale height with *e*/*H* ratio of 0.1 is insufficient to promote early transition. Hence the flow transition occurs at a Reynolds number close to that of the Plain microchannel. The flow remains laminar at lower Reynolds numbers, because the disturbances caused by the low scale height are dissipated by the dominant viscous forces, and the friction factor is similar to that of the Plain microchannel. At higher Reynolds numbers, however, the

inertia forces become sufficiently large to amplify the flow disturbances caused by the tip of the low scale height. This results in higher turbulence such that the friction factor is higher than that of the Plain microchannel.

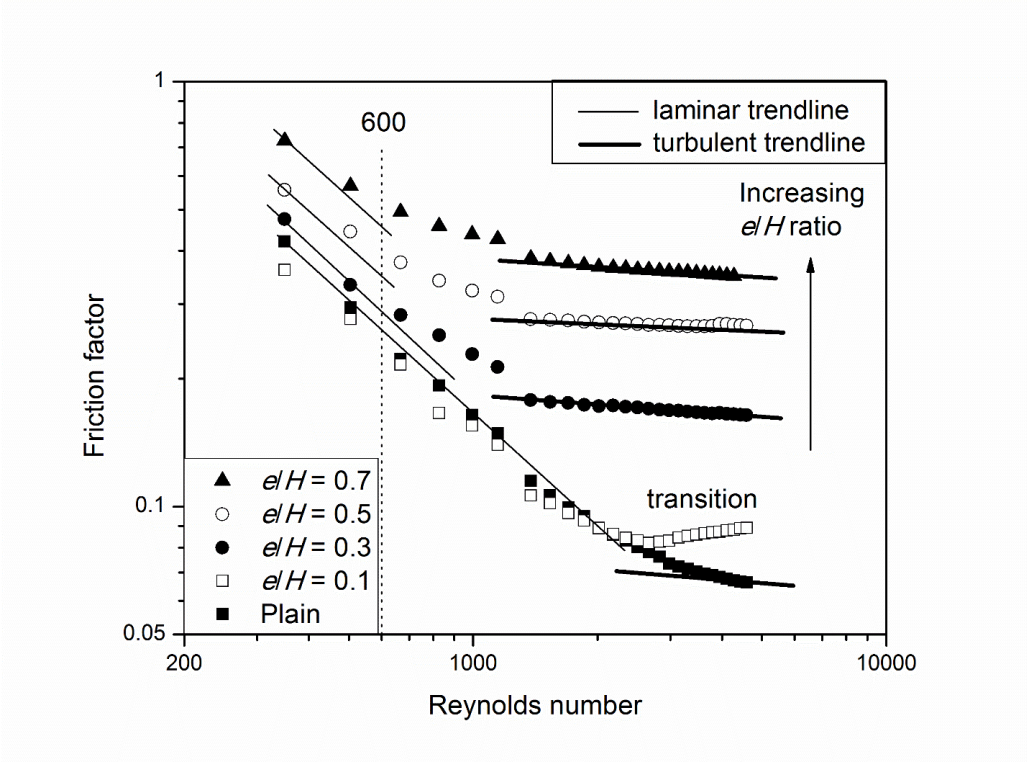

Figure 7-15: Friction factor against Reynolds number, for different *e*/*H* ratio (IFS series)

Figure 7-16 shows the variation of normalised friction factor with Reynolds number, for different *e*/*H* ratio. It is observed that the normalised friction factor increases with Reynolds number. For $350 \lesssim Re \lesssim 2{,}200$, the increase is relatively steep. This is due to the steep decline of friction factor with Reynolds number for the Plain microchannel in the laminar flow regime, while the friction factor of the IFS microchannels decreases at a slower rate upon the early transition to turbulent flow. For $Re \gtrsim 3{,}400$ when the Plain microchannel also transits to turbulent flow, the corresponding friction factor decreases at a slower rate with Reynolds number. Hence, the normalised friction factor increases gradually with Reynolds number.

The normalised friction factor is plotted with a y-axis range of 0 to 8 throughout the thesis, so as to facilitate comparison across the different microchannels.

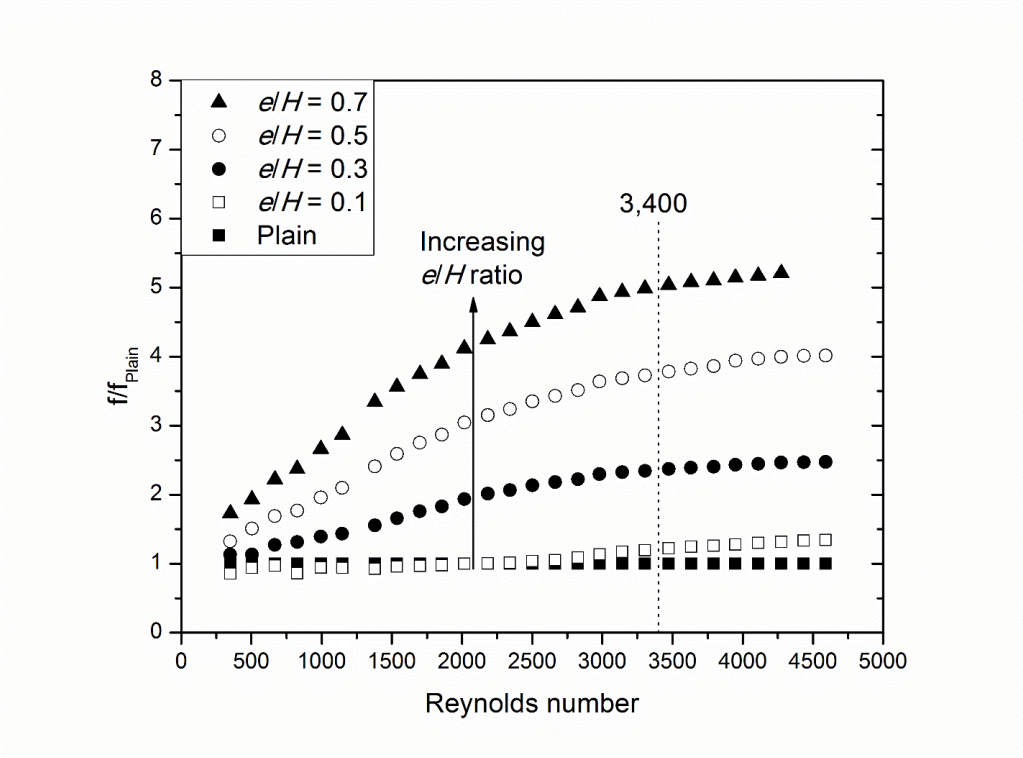

Figure 7-16: Normalised Friction factor against Reynolds number, for different *e*/*H* ratio (IFS series)

Figure 7-17 presents the same data from Figure 7-15 in a different manner to show the variation of friction factor with *e*/*H* ratio. The friction factor is observed to increase with *e*/*H* ratio, for the same *P*/*e* ratio and Reynolds number. For *e*/*H* ratio=0, which is the Plain microchannel, the friction factor is 0.08 at *Re*≈2,664. When the *e*/*H* ratio increases slightly to 0.1, the friction factor remains close to 0.08. When the *e*/*H* ratio increases further to 0.7, the friction factor increases to 0.36 at the same Reynolds number.

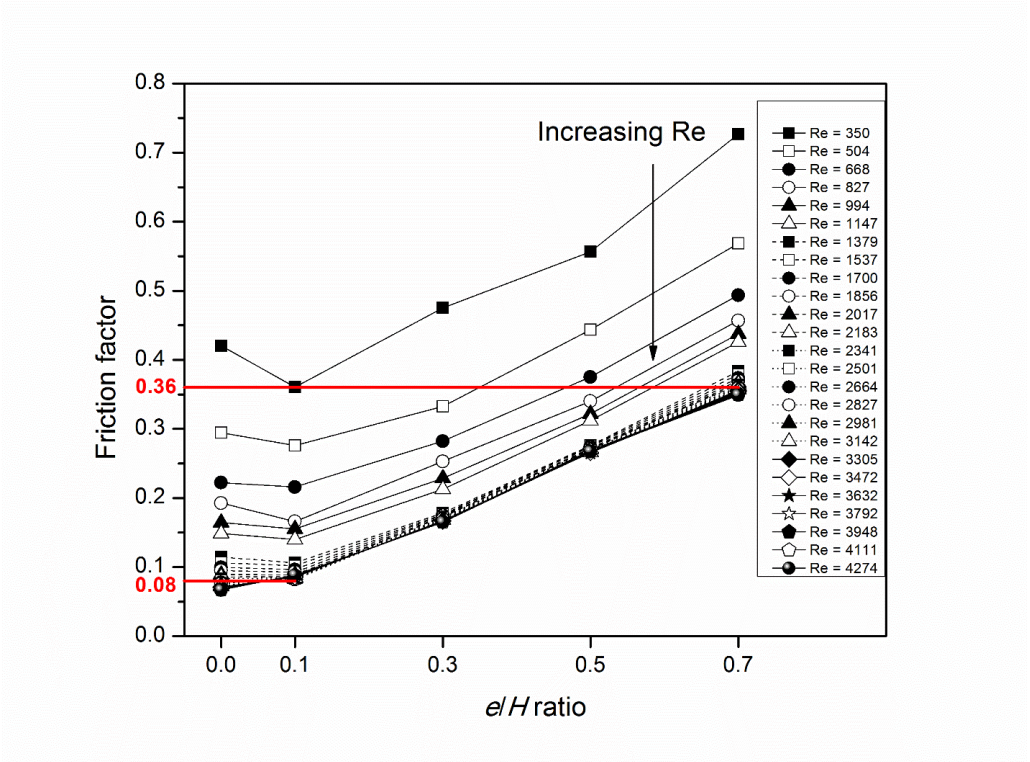

Figure 7-17: Friction factor against *e*/*H* ratio, at different Reynolds number (IFS series)

The increase of friction factor with *e*/*H* ratio is physically reasonable, considering that the minimum gap through which the fluid flows decreases and the local fluid velocity increases as *e*/*H* ratio increases, as explained earlier using Figures 7-9 to 7-11. The high local fluid velocity causes the velocity boundary layer near the copper wall to become very thin. As a result, the near wall fluid velocity gradient, and therefore the local friction factor, becomes significant.

In accordance with classical theory, for a channel of constant height, the velocity boundary layer keeps developing along the channel until it reaches a fully developed state. The thick velocity boundary layer in the Plain microchannel, as illustrated in Figure 7-18, results in a relatively low friction factor of 0.08. When the *e*/*H* ratio increases slightly to 0.1, the low scale height is insufficient to cause significant thinning of the velocity boundary layer, as illustrated in Figure 7-19. Thus the friction factor remains close to 0.08.

However, when the *e*/*H* ratio increases further to 0.7, significant thinning of the velocity boundary layer near the copper wall occurs slightly downstream of the scale tip, as illustrated in Figure 7-20. Since there are 14 scale tips over the microchannel length for *e*/*H* ratio of 0.7, this repeated thinning effect results in a higher friction factor of 0.37.

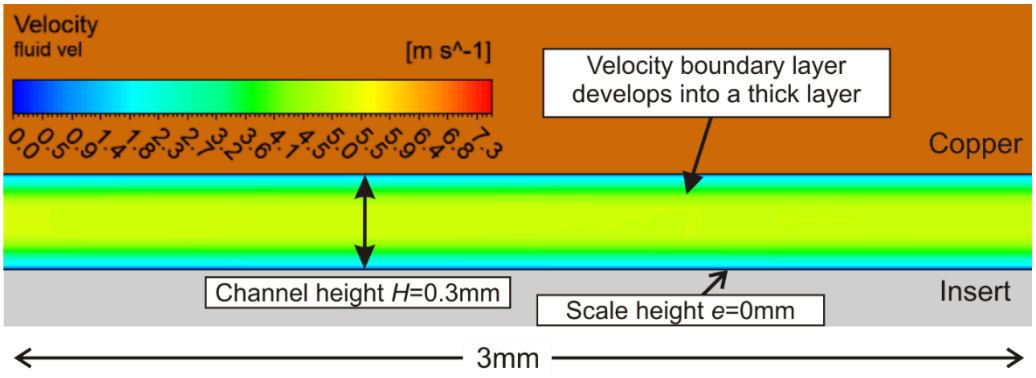

Figure 7-18: Velocity distribution of Plain microchannel at *Re* ≈ 2,664

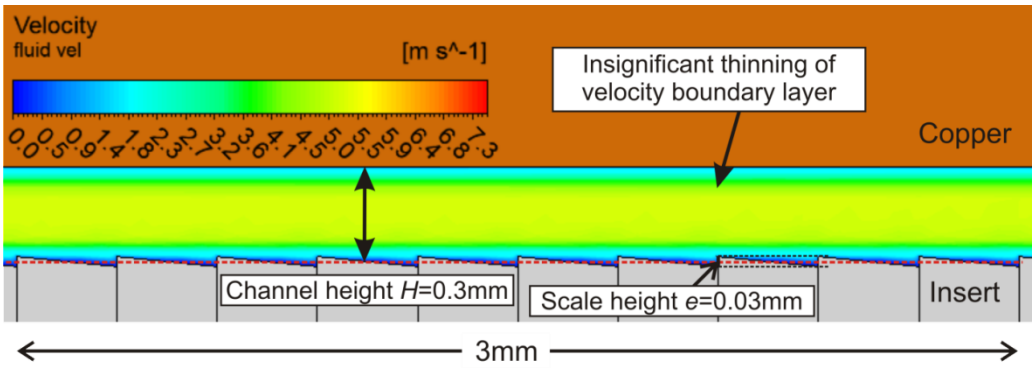

Figure 7-19: Velocity distribution of IFS microchannel with *e*/*H* ratio of 0.1 at *Re* ≈ 2,664

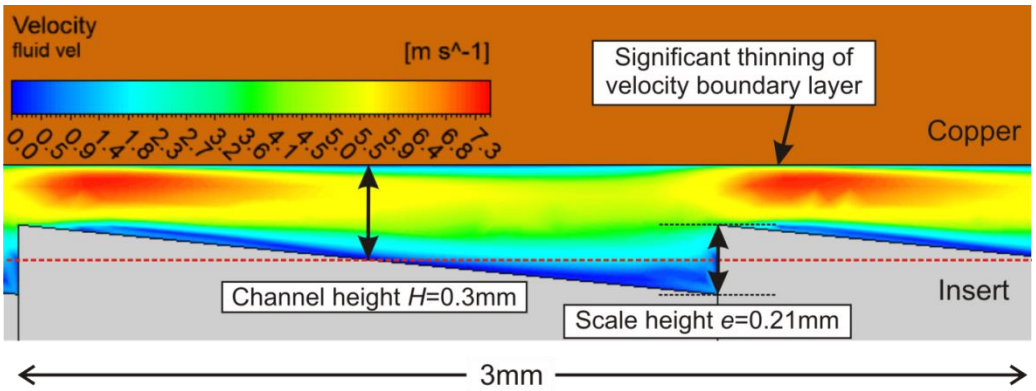

Figure 7-20: Velocity distribution of IFS microchannel with *e*/*H* ratio of 0.7 at *Re* ≈ 2,664

7.3.3 Thermo-hydraulic Performance

Figure 7-21 shows the variation of thermo-hydraulic performance factor with Reynolds number, for different *e*/*H* ratio. In the design of practical heat exchangers, the thermo-hydraulic performance factor represents the increased heat transfer capacity for equal heat transfer surface area and pumping power.

It is observed that the IFS microchannels perform significantly better than the Plain microchannel when the critical Reynolds number is exceeded, due to the onset of turbulence as discussed earlier in Sections 7.3.1 and 7.3.2. This is because the Inverted Fish Scale profile promotes early laminar-to-turbulent flow transition, thereby enhancing the thermo-hydraulic performance. However, when the flow in the Plain microchannel becomes more turbulent at higher Reynolds numbers, the Inverted Fish Scale profile becomes less effective in improving the thermo-hydraulic performance relative to the Plain microchannel. This accounts for the decrease in thermo-hydraulic performance at higher Reynolds numbers.

In this parametric study, a larger *e*/*H* ratio generally exhibits higher thermo-hydraulic performance, and the IFS profile with the largest *e*/*H* ratio of 0.7 performs the best. Given a fixed heat transfer surface area and pumping power, this IFS profile improves the heat transfer capacity by 54% relative to the Plain profile, at Reynolds number of 1,800.

The thermo-hydraulic performance is plotted with a y-axis range of 0.8 to 1.8 throughout the thesis, to facilitate the comparison across the three different microchannel series.

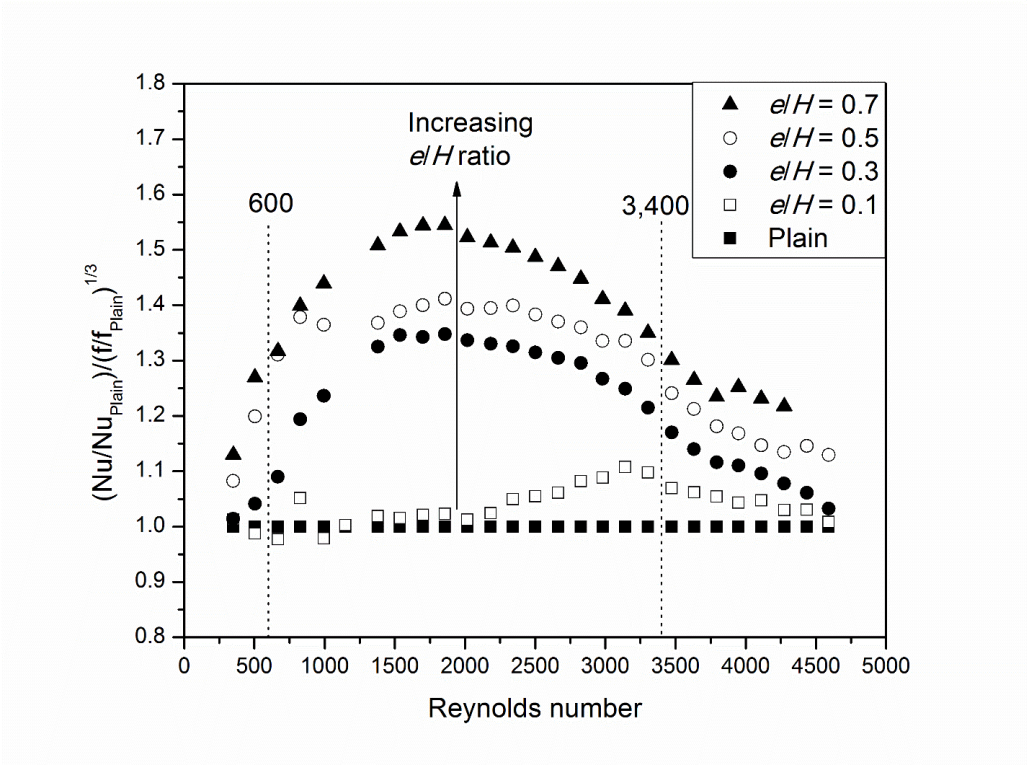

Figure 7-21: Thermo-hydraulic performance against Reynolds number, for different *e*/*H* ratio (IFS series)

7.4 Scale Pitch (*P*) to Scale Height (*e*) Ratio Study

In order to investigate the effect of the number of scale protrusions on the heat transfer and flow characteristics, the scale pitch (*P*) to scale height (*e*) ratio is varied. Four *P*/*e* ratios of 5, 10, 15 and 20 are studied, with a fixed scale height (*e*) to mean channel height (*H*) ratio of 0.5. A lower *P*/*e* ratio corresponds to a larger number of scale protrusions of the same height and therefore implies more flow disruptions within a fixed channel length (*L*) of 30 mm. The schematic diagram explaining these terminologies can be found in Section 3.2.1.

7.4.1 Thermal Considerations

Figure 7-22 shows the variation of Nusselt number with Reynolds number for different *P*/*e* ratio. The maximum Nusselt number achieved is 50, at Reynolds number of about 4,000 using the IFS profile with *P*/*e* ratio of 5.

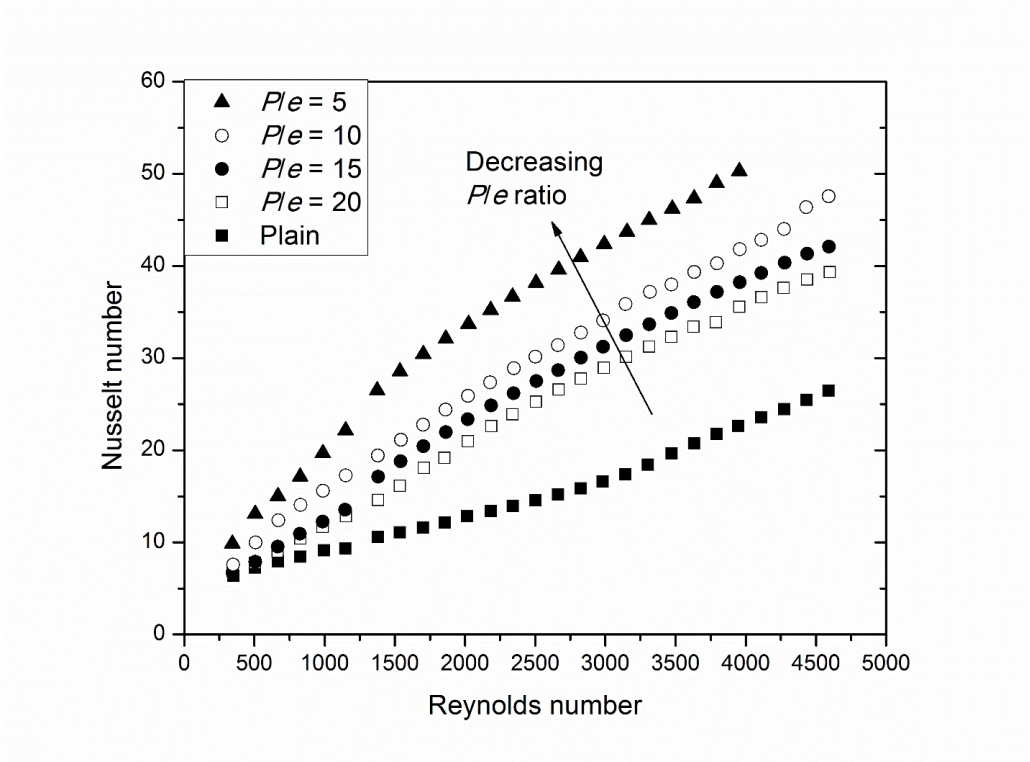

Figure 7-22: Nusselt number against Reynolds number, for different *P*/*e* ratio (IFS series)

Figure 7-23 shows the variation of normalised Nusselt number with Reynolds number, for different *P*/*e* ratio. The IFS profile with *P*/*e* ratio of 5 is able to achieve a Nusselt number of about 2.6 times that of the Plain profile. For all the IFS profiles, the heat transfer enhancement starts to become significant when Reynolds number exceeds 600. This is likely due to the onset of turbulence, which can be seen from the change in flow behaviour at Re≈600, using the friction factor variation in Figure 7-29. Once again, this confirms the postulation that the IFS profile promotes early laminar-to-turbulent flow transition, thereby enhancing heat transfer.

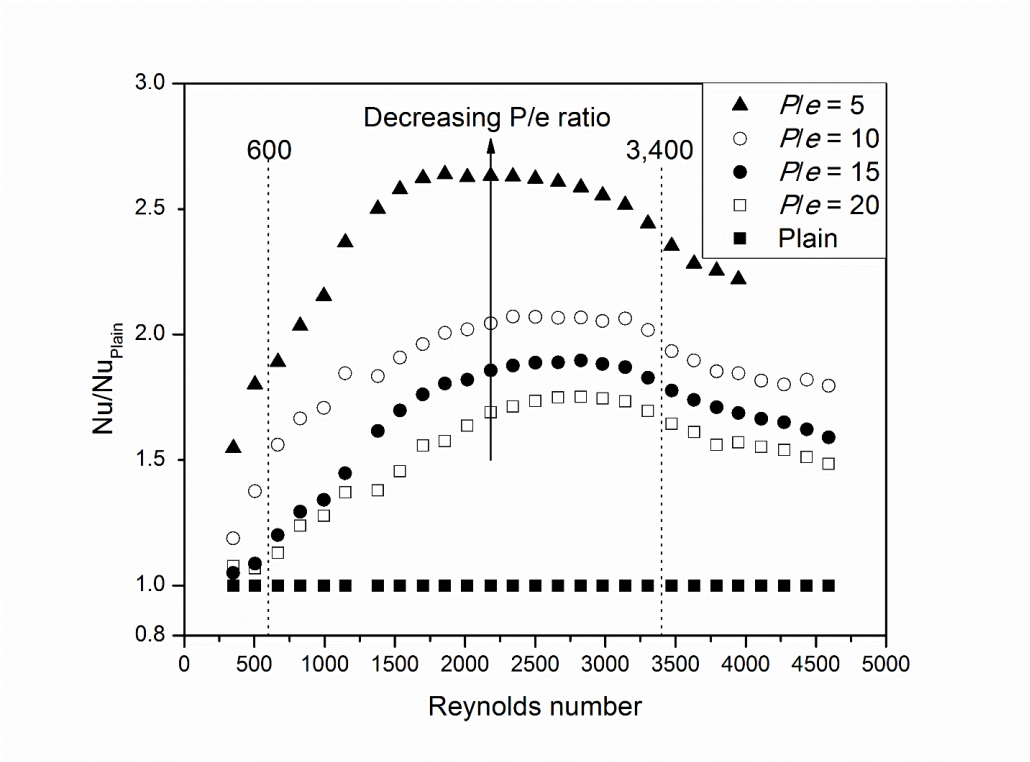

Figure 7-23: Normalised Nusselt number against Reynolds number, for different *P*/*e* ratio (IFS series)

Figure 7-24 presents the same data from Figure 7-22 in a different manner to show the variation of Nusselt number with *P*/*e* ratio. The Nusselt number is observed to increase when *P*/*e* ratio decreases, for the same *e*/*H* ratio and Reynolds number. For example, the Nusselt number increases from 27 to 40, when the *P*/*e* ratio decreases from 20 to 5, at Reynolds number≈2,664. This will also be considered in the formulation of the Nusselt number correlation.

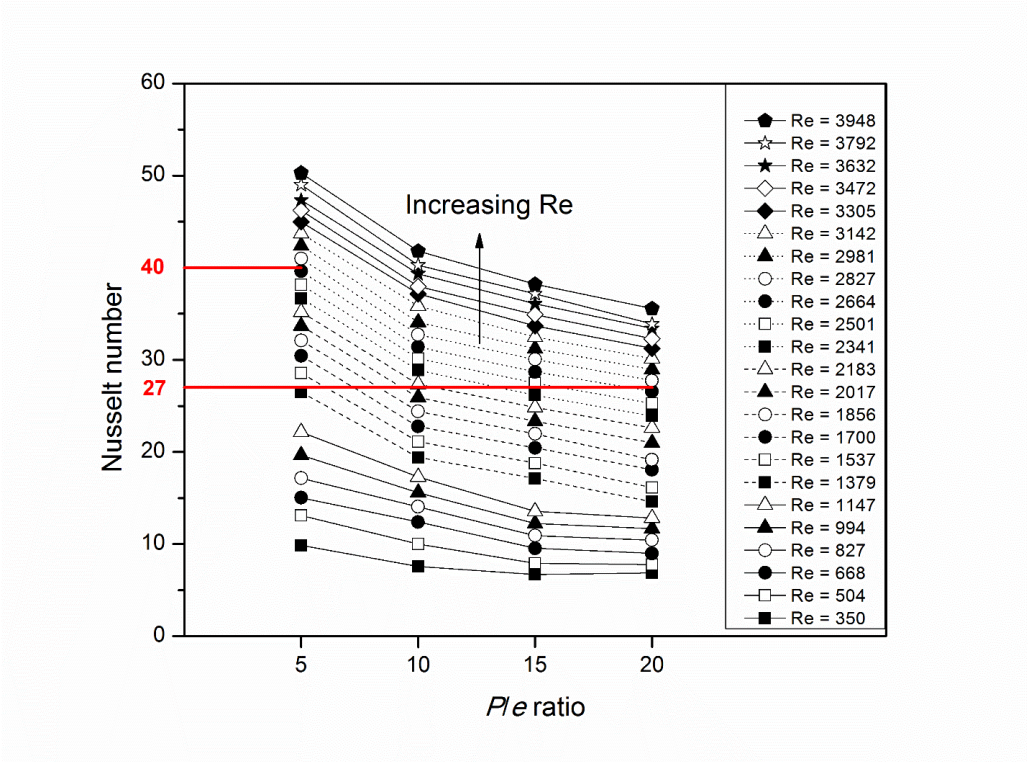

Figure 7-24: Nusselt number against *P*/*e* ratio, at different Reynolds number (IFS series)

The increase in Nusselt number with decreasing *P*/*e* ratio is physically reasonable, considering that the number of scales of the same height increases for the same channel length. As illustrated in Figure 7-25 and Figure 7-26, the number of scales increases from 1 to 4 for a section length of 3 mm, as the *P*/*e* ratio decreases from 20 to 5. Since the scale height is fixed at 0.15 mm and the minimum channel height is fixed at 0.225 mm, the maximum fluid velocity is comparable at about 6.2 m/s for both *P*/*e* ratio of 5 and 20.

However, for a larger *P*/*e* ratio of 20, there is insignificant flow recirculation, as illustrated in Figure 7-25. Hence, the fluid flows through the microchannel at high and low bulk fluid velocities based on the small and large flow area, by virtue of mass conservation. Consequently, the thermal boundary layer near the heated copper wall becomes thicker at the region of low bulk fluid velocity, as illustrated in Figure 7-27. This results in a low Nusselt number of 27.

On the other hand, for a smaller *P*/*e* ratio of 5, significant flow recirculation occurs on the non-heated insert surface between the scale tips, as illustrated in Figure 7-26. Due to these regions of flow recirculation, the fluid path effectively narrows and the incompressible fluid is constantly accelerated through the microchannel at a high bulk fluid velocity. Consequently, the thermal boundary layer near the heated copper wall is constantly kept thin, as illustrated in Figure 7-28. This results in a high Nusselt number of 40.

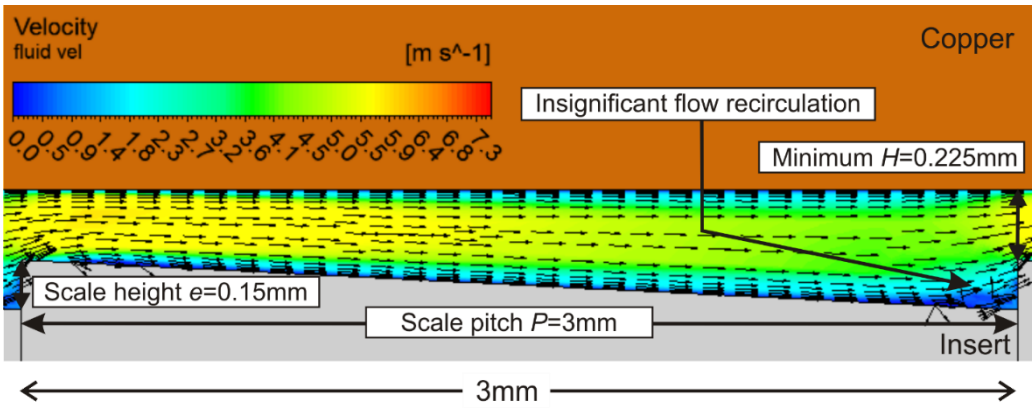

Figure 7-25: Flow field of IFS microchannel with *P*/*e* ratio of 20, at *Re* ≈ 2,664

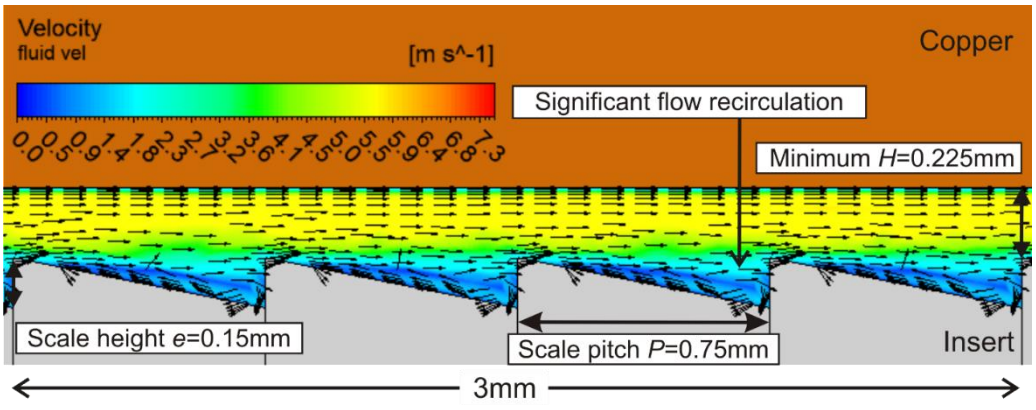

Figure 7-26: Flow field of IFS microchannel with *P*/*e* ratio of 5, at *Re* ≈ 2,664

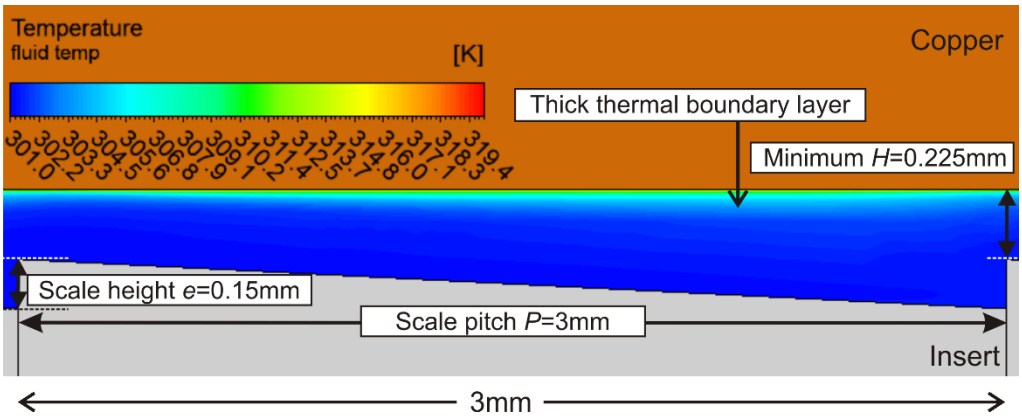

Figure 7-27: Temperature distribution of IFS microchannel with *P*/*e* ratio of 20, at *Re* ≈ 2,664

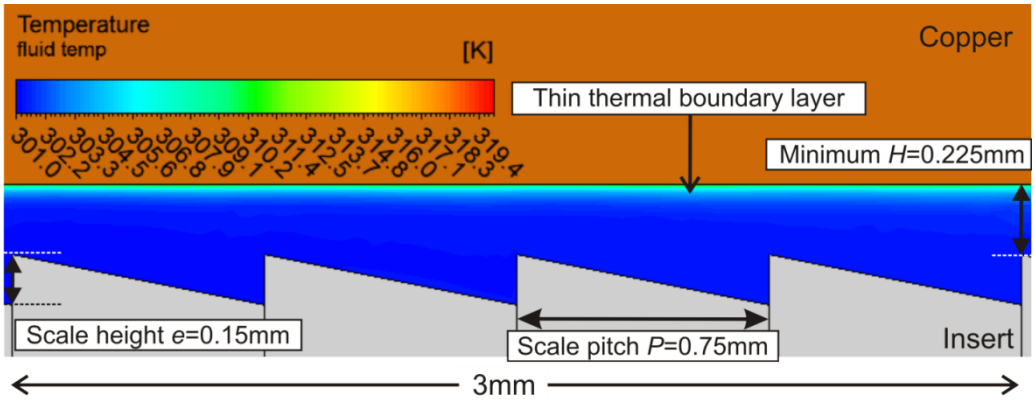

Figure 7-28: Temperature distribution of IFS microchannel with *P*/*e* ratio of 5, at *Re* ≈ 2,664

7.4.2 Hydrodynamic Considerations

Figure 7-29 shows the variation of friction factor with Reynolds number, for different *P*/*e* ratio. As discussed in Section 7.4.1, the heat transfer enhancement starts to become significant when Reynolds number exceeds 600. Correspondingly, the friction data values starts to deviate from the laminar trend line at Reynolds number of approximately 600, indicating the onset of turbulence. The turbulent flow regime is characterised by another distinct trend line of a lower gradient.

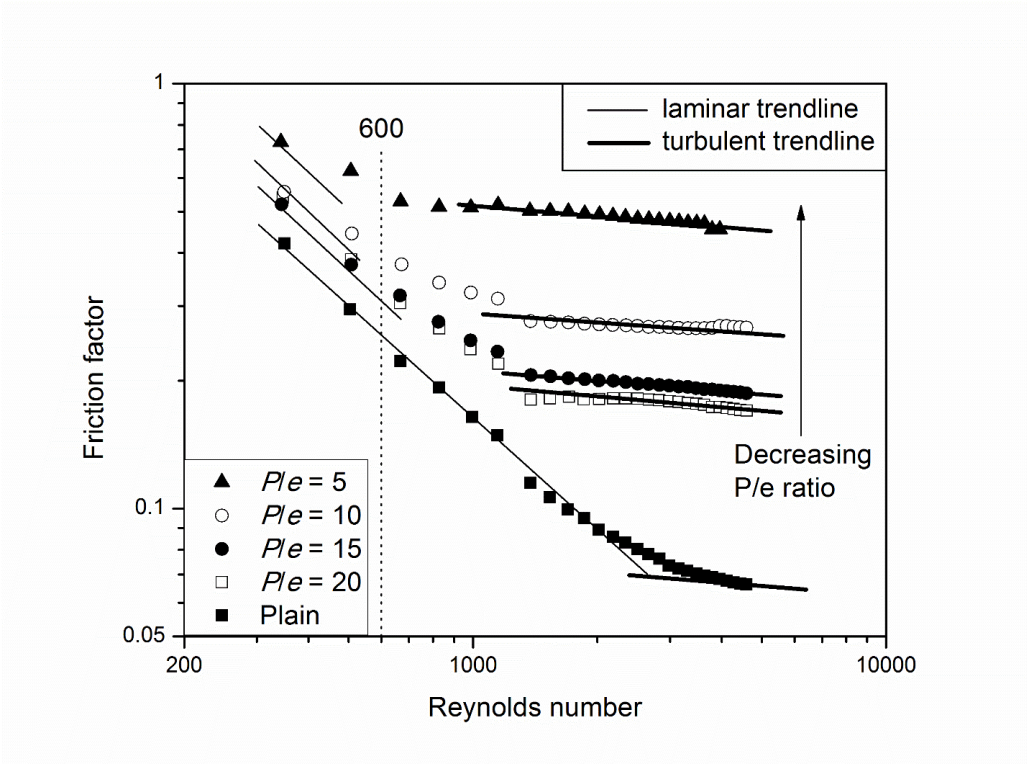

Figure 7-29: Friction factor against Reynolds number, for different *P*/*e* ratio (IFS series)

Figure 7-30 shows the variation of normalised friction factor with Reynolds number, for different *P*/*e* ratio. The normalised friction factor is observed to increase with Reynolds number, with the increase being relatively steep for $350 \lesssim Re \lesssim 2{,}200$ and gradual for $Re \gtrsim 3{,}400$. The reason for this has been explained earlier in Section 7.3.2.

Additionally, it is observed that the IFS profile induces high friction losses. In particular, the normalised friction factor can reach a value of 6.7 for the IFS microchannel with a *P*/*e* ratio of 5 at $Re \approx 3{,}953$.

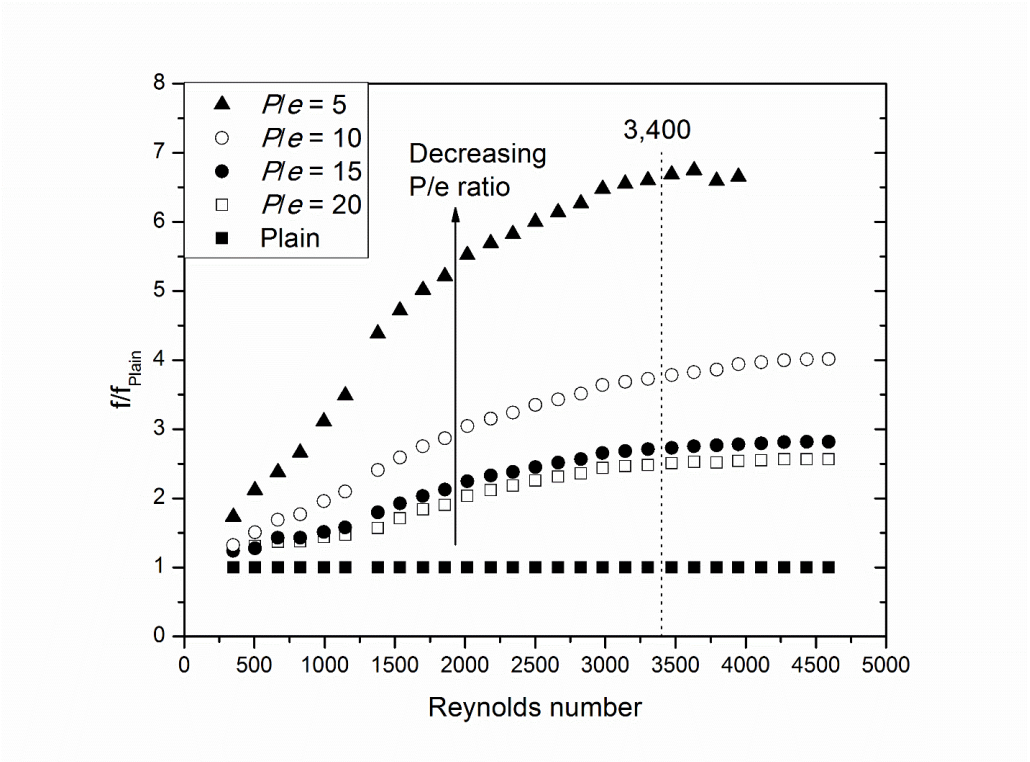

Figure 7-30: Normalised friction factor against Reynolds number, for different *P*/*e* ratio (IFS series)

Figure 7-31 presents the same data from Figure 7-29 in a different manner to show the variation of friction factor with *P*/*e* ratio. The friction factor is observed to increase when *P*/*e* ratio decreases, for the same *e*/*H* ratio and Reynolds number. For example, the friction factor increases from 0.16 to 0.47, when the *P*/*e* ratio decreases from 20 to 5, at Reynolds number≈2,664. This will also be considered in the formulation of the friction factor correlation.

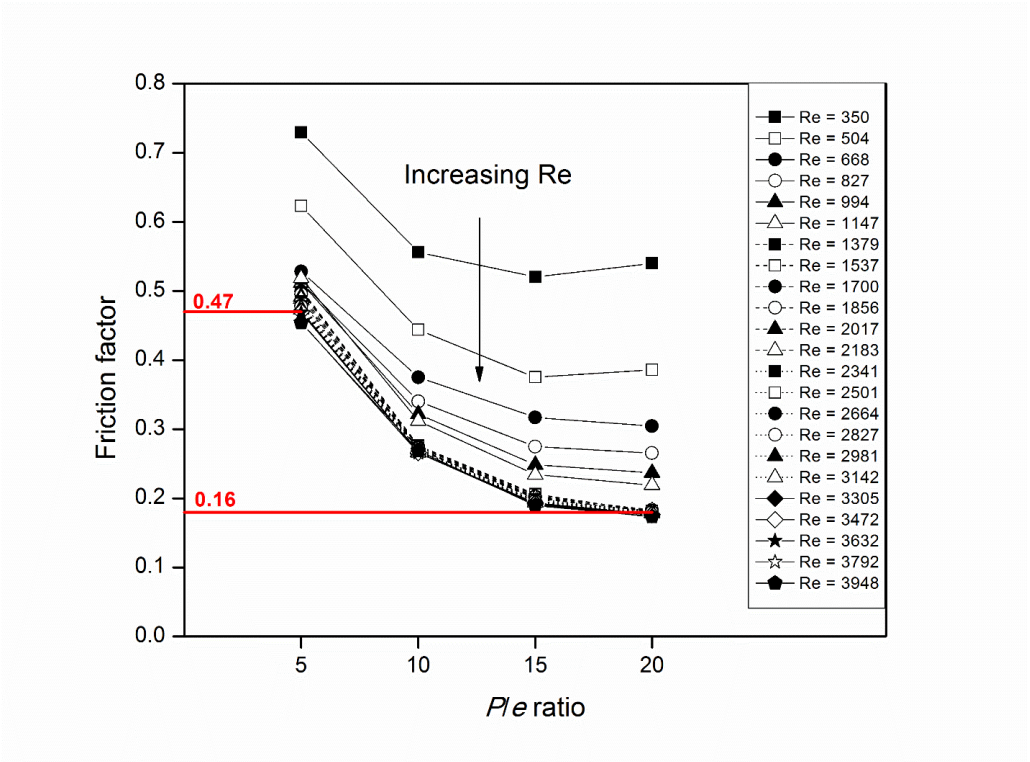

Figure 7-31: Friction factor against *P*/*e* ratio, at different Reynolds number (IFS series)

The increase in friction factor with decreasing *P*/*e* ratio can be explained by looking at the corresponding velocity distributions. As illustrated in Figure 7-32, the velocity boundary layer becomes thicker at the region of low bulk fluid velocity, resulting in a low friction factor of 0.16 for a larger *P*/*e* ratio of 20. On the other hand, for a smaller *P*/*e* ratio of 5, the velocity boundary layer is constantly kept thin due to the high bulk fluid velocity, as characterised by the yellow region in Figure 7-33. This results in a high friction factor of 0.47.

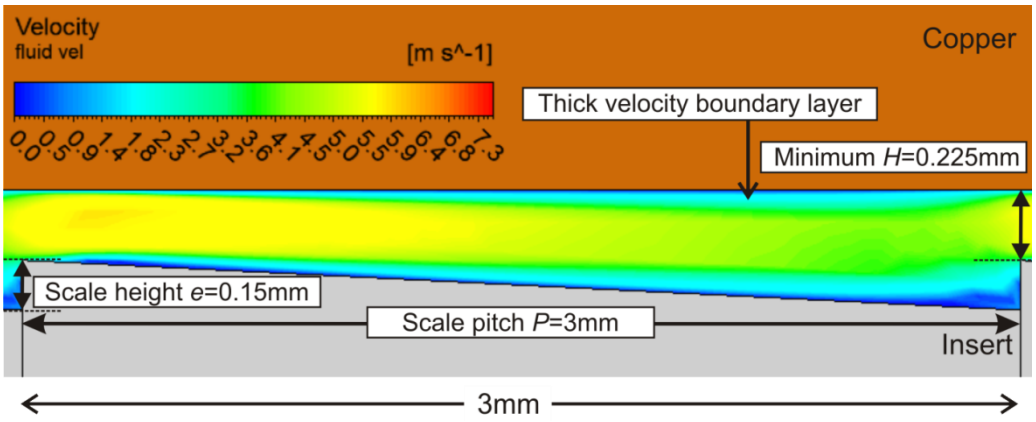

Figure 7-32: Velocity distribution of IFS microchannel with *P*/*e* ratio of 20, at *Re* ≈ 2,664

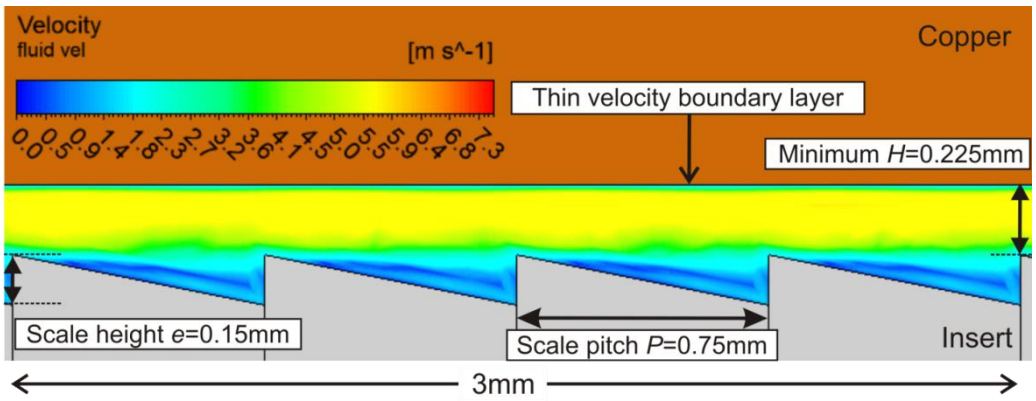

Figure 7-33: Velocity distribution of IFS microchannel with *P*/*e* ratio of 5, at *Re* ≈ 2,664

7.4.3 Thermo-hydraulic Performance

Figure 7-34 shows the variation of thermo-hydraulic performance with Reynolds number, for different *P*/*e* ratio. In general, a smaller *P*/*e* ratio exhibits higher thermo-hydraulic performance, and the IFS profile with the smallest *P*/*e* ratio of 5 performs the best. Given a fixed heat transfer surface area and pumping power, this IFS profile improves the heat transfer capacity by 54% relative to the Plain profile, at Reynolds number of 1,500.

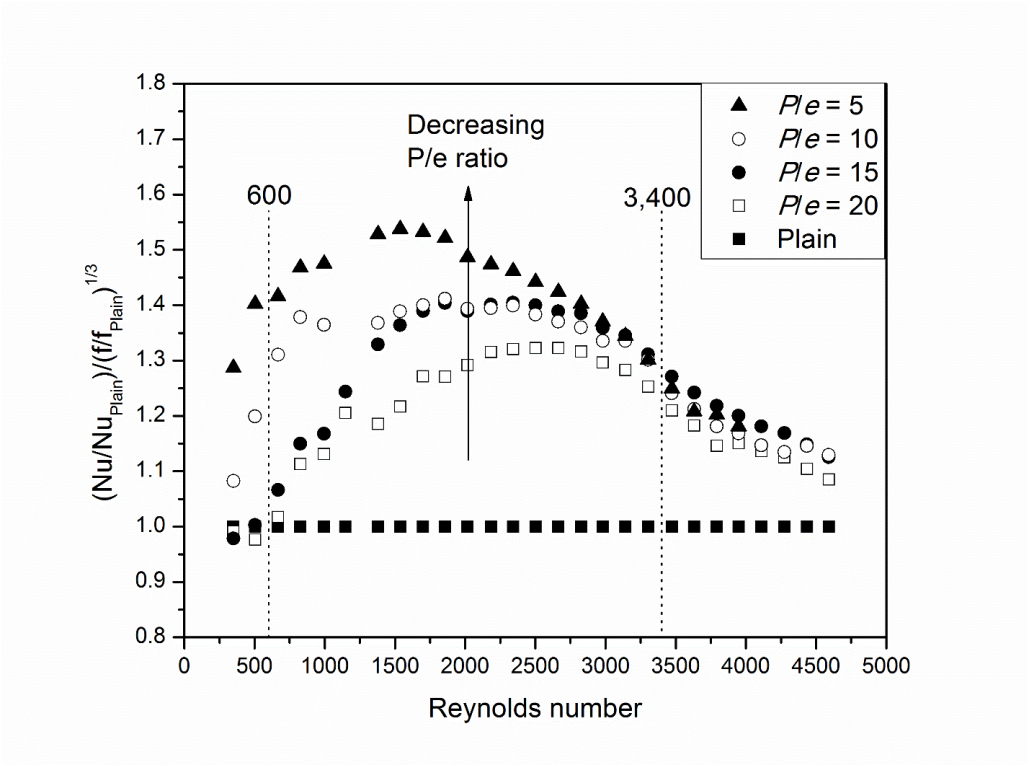

Figure 7-34: Thermo-hydraulic performance against Reynolds number, for different *P*/*e* ratio (IFS series)

It is also observed that increasing the number of scale protrusions by decreasing the *P*/*e* ratio is more effective in improving the thermo-hydraulic performance at lower Reynolds numbers. This can be explained by studying the variation of normalised Nusselt number and friction factor with Reynolds number in Figures 7-23 and 7-30, respectively. While a decrease in *P*/*e* ratio consistently increases Nu/Nu_{Plain} at all Reynolds numbers, the increase in f/f_{Plain} varies with the Reynolds number. At lower Reynolds numbers, the flow disturbances caused by the increase in number of scale protrusions are partially dissipated by the dominant viscous forces, resulting in a smaller increase in friction losses. On the other hand, at higher Reynolds numbers, the flow disturbances are amplified by the dominant inertia forces, leading to a larger increase in friction losses. Consequently, the improvement in Nusselt number is outweighed by the surge in friction factor, such that the decrease in *P*/*e* ratio has a minimal effect on the thermo-hydraulic performance at higher Reynolds numbers.

Chapter 8 Results for the Fish Scale Microchannels

In Chapter 7, the friction factor of the Inverted Fish Scale (IFS) microchannel can reach 6.7 times higher than that of the Plain microchannel. In view of the high friction losses incurred when the scaly IFS profile opposes the flow direction, the Fish Scale (FS) profile is designed to mimic the natural forward swimming direction of fishes, as shown in Figure 8-1, to investigate its streamlined flow characteristics. The results suggest that the FS profile would be useful for heat transfer applications where low pressure drop is of higher importance.

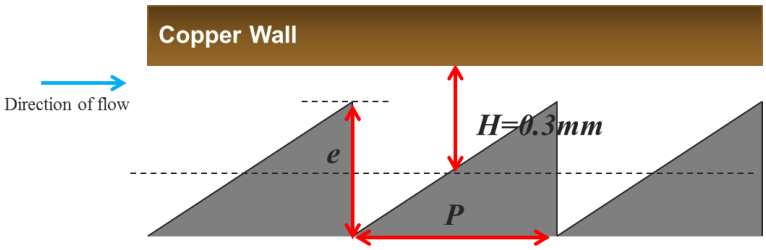

Figure 8-1: Fish Scale profile

This chapter focuses on the results for the Fish Scale (FS) microchannel series. While the organisation of this chapter is similar to that of the preceding chapter, the differences between the results for the IFS and FS microchannels are also highlighted.

8.1 Overview of Measured Results for the FS Microchannels

Figure 8-2 shows the variation of convective heat transfer coefficient *h* with flow rate, for the Fish Scale (FS) and Plain microchannels. Similar to the IFS profiles, the FS profiles also enhance heat transfer. For flow rates above 3 L/min, all the FS profiles, with the exception of FS_*e*0.03-*P*0.3, yield higher *h* values than those of the Plain microchannel. The highest heat transfer coefficient achieved is 47.9 kW/m^2·K, at 6.75 L/min using FS_*e*0.21-*P*2.1 profile.

On the other hand, the maximum *h* achieved for the IFS series is 52.8 kW/m^2·K, at 6.5 L/min using the IFS_*e*0.21-*P*2.1 profile. At the flow rate 6.5 L/min, the FS_*e*0.21-*P*2.1 profile only attains a *h* value of 46.8 kW/m^2·K. This verifies the postulation that the disruptive IFS profile causes more flow disturbances, thereby enhancing heat transfer.

Within the FS series, the effect of scale height (*e*) to mean channel height (*H*) ratio is significant, while the effect of scale pitch (*P*) to scale height (*e*) ratio is considerably less significant, especially at higher flow rates. This is unlike the phenomena with the IFS series, as illustrated in Figure 7-2, where both ratios have a significant effect on the convective heat transfer coefficient. In addition, the FS_*e*0.03-*P*0.3 profile exhibits the same heat transfer behaviour as the Plain profile, while the IFS_*e*0.03-*P*0.3 profile yields higher *h* than the Plain profile at flow rates above 3.5 L/min. This implies that for the same scale height and scale pitch, the IFS profile is able to disrupt the flow and enhance heat transfer more significantly than the FS profile, particularly at high flow rates.

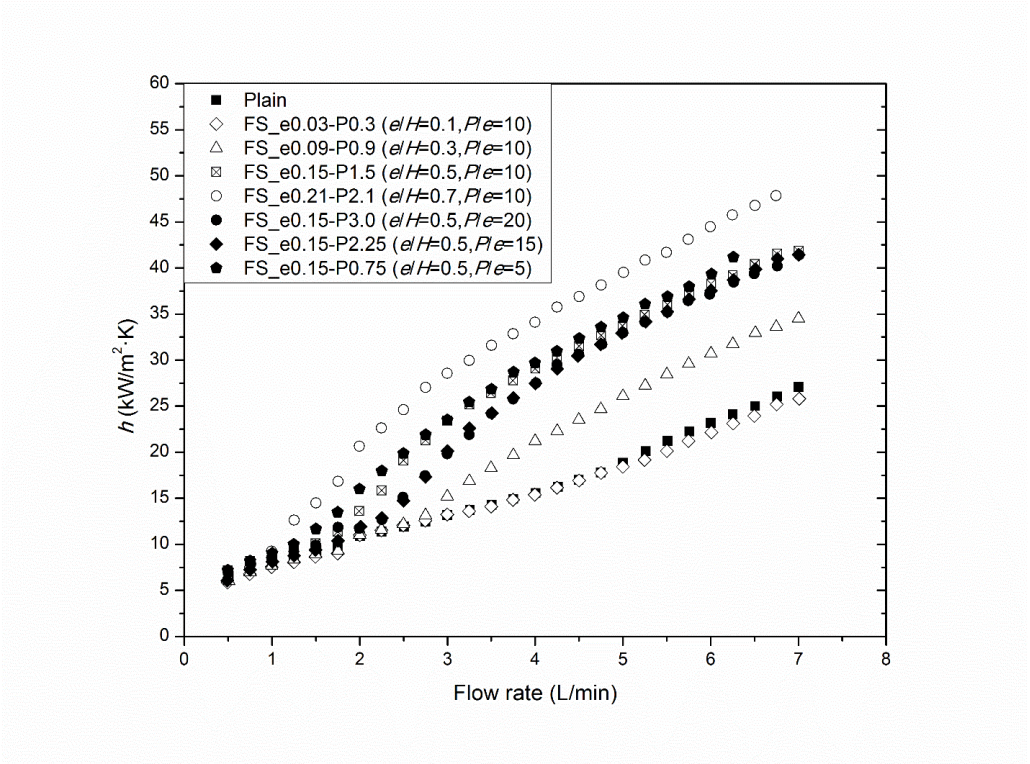

Figure 8-2: Heat transfer coefficient against flow rate for all FS and Plain microchannels

Figure 8-3 shows that the maximum pressure drop for the FS series is only 2.6 bars, which is well below the imposed pressure drop limit of 3.5 bars. On the other hand, the maximum pressure drop for the IFS microchannel series is 3.3 bars, at 6.0 L/min using the IFS_*e*0.15-*P*0.75 profile. At the same flow rate, the FS_*e*0.15-*P*0.75 profile incurs a pressure drop of only 2.1 bars. This demonstrates that the FS profile is indeed better suited for heat transfer applications where a low pressure drop is desired.

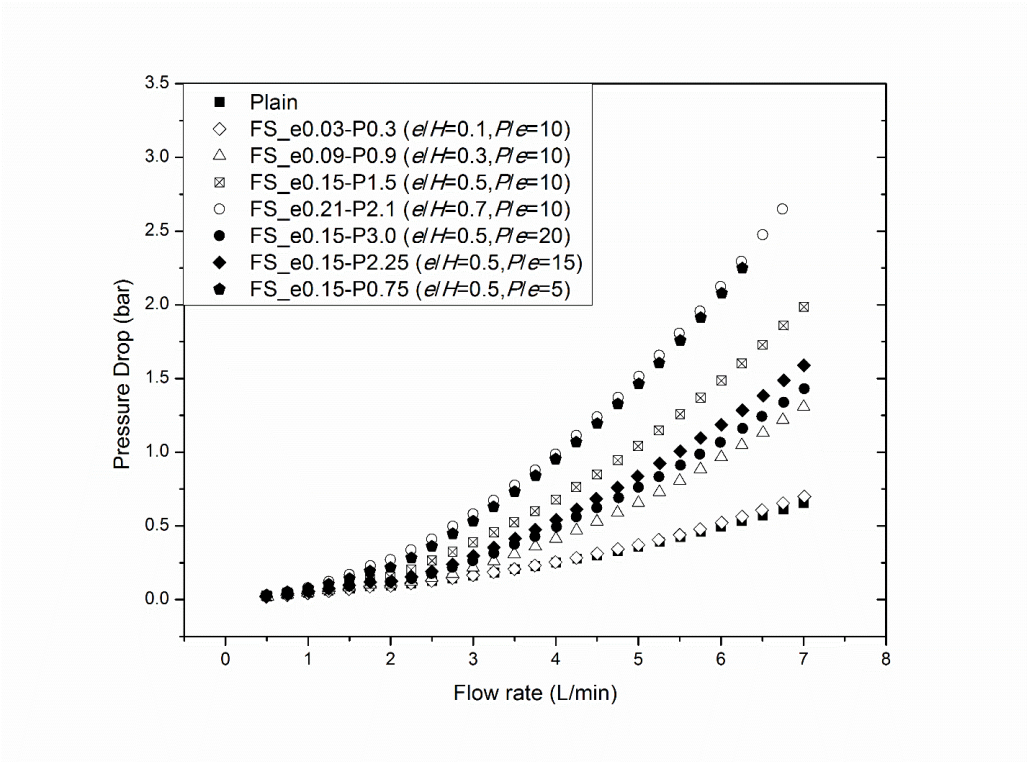

Figure 8-3: Pressure drop against flow rate for all FS and Plain microchannels

8.2 Comparison between Measured and Numerical Results

Figure 8-4 compares the measured and predicted pressure drop, for various insert profiles at flow rates between 2 and 7 L/min. It is observed that all the predictions agree well with the measurements, with the deviations falling within the ±10% band. Once again, the numerical model generally under-predicts the pressure drop.

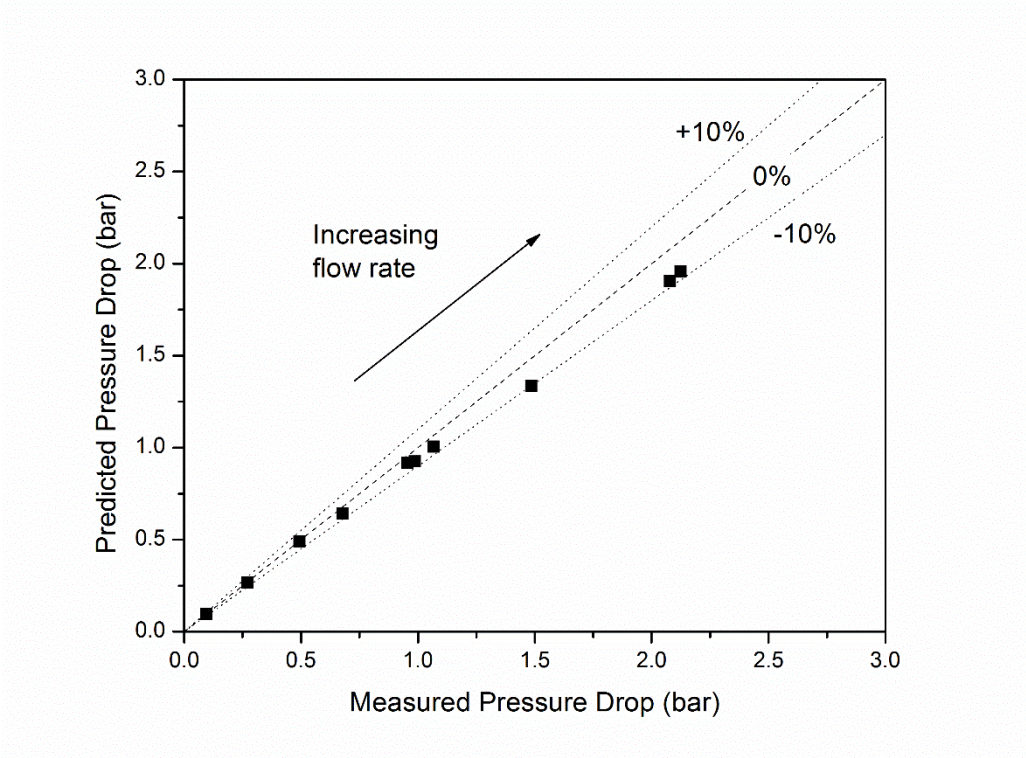

Figure 8-4: Predicted pressure drop against measured pressure drop (FS series)

Figure 8-5 compares the measured and predicted Nusselt number, for various insert profiles at Reynolds numbers approximately between 1,300 and 4,600. It is observed that all the predictions agree with the measurements, within the ±30% deviation band. Once again, the numerical model generally over-predicts the Nusselt number.

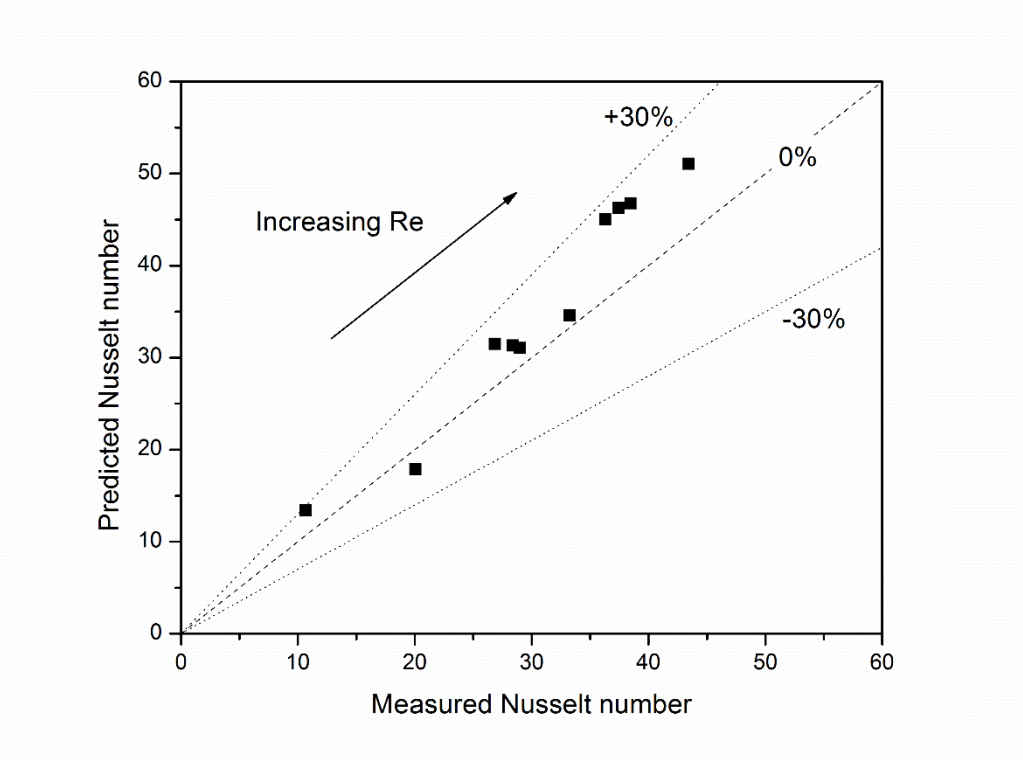

Figure 8-5: Predicted Nusselt number against measured Nusselt number (FS series)

8.3 Scale Height (*e*) to Mean Channel Height (*H*) Ratio Study

8.3.1 Thermal Considerations

Figure 8-6 shows the variation of Nusselt number with Reynolds number, for different *e*/*H* ratio, using the FS microchannel series. Similar to the phenomena with the IFS series, Nusselt number increases with Reynolds number and *e*/*H* ratio. The maximum Nusselt number achieved is 47, at Reynolds number of about 4,430 using the FS profile with *e*/*H* ratio of 0.7.

In addition, the FS profile with *e*/*H* ratio of 0.1 is observed to resemble the heat transfer behaviour of the Plain microchannel for the Reynolds number range investigated. On the other hand, the FS profile with *e*/*H* ratio of 0.3 assumes the

heat transfer behaviour of the Plain microchannel at lower Reynolds numbers up to 1,850, after which the Nusselt number becomes significantly higher than that of the Plain microchannel. Similarly, the FS profile with *e*/*H* ratio of 0.5 and 0.7 exhibits a change in heat transfer behaviour at Reynolds number of 1,300 and 700, respectively.

The aforementioned Reynolds number values match those representing the onset of transition, as shown in the friction factor variation to be presented in Figure 8-13. Clearly, the critical Reynolds number reduces as the *e*/*H* ratio increases. It can thus be inferred that an increase in scale height relative to mean channel height promotes early laminar-to-turbulent flow transition, thereby enhancing the heat transfer. This agrees well with the conclusions of other studies [69,70].

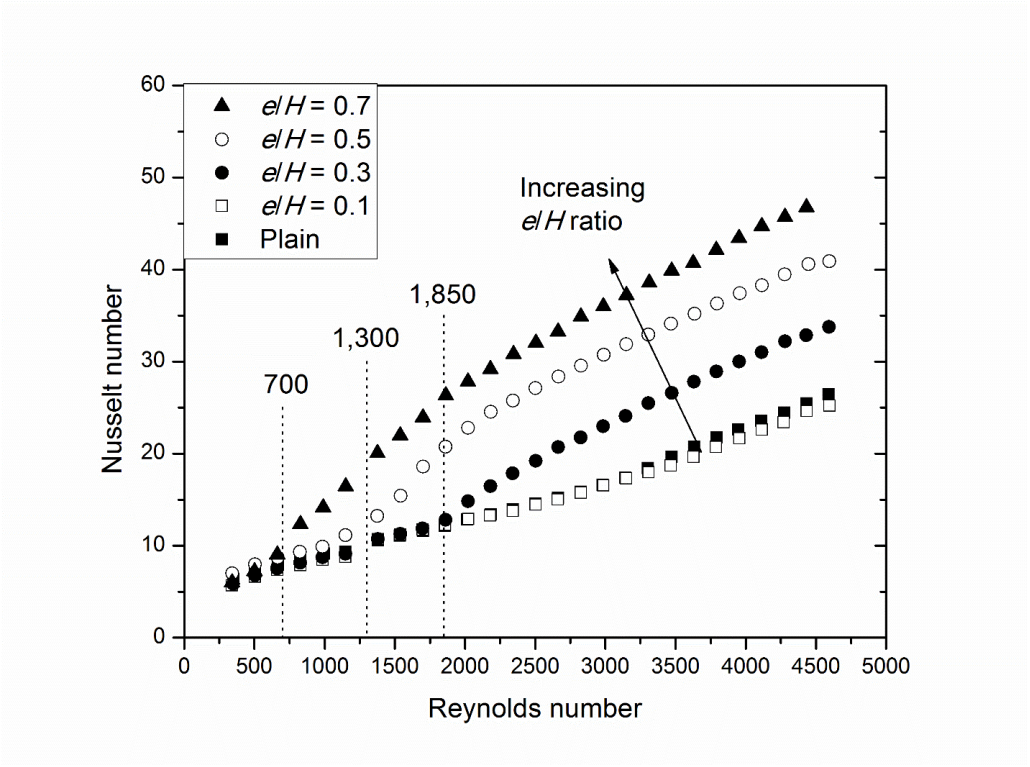

Figure 8-6: Nusselt number against Reynolds number, for different *e*/*H* ratio (FS series)

Figure 8-7 shows the variation of normalised Nusselt number with Reynolds number, for different *e*/*H* ratio, using the FS microchannel series. The FS profile with *e*/*H* ratio of 0.7 is observed to achieve a Nusselt number of at most 2.2 times that of the Plain profile. This is lower than the maximum value of 2.5 achieved by the IFS profile with the same *e*/*H* ratio, within the same range of Reynolds number from 350 to 4,280.

In addition, the normalised Nusselt number for the FS microchannels with *e*/*H* ratio of 0.3, 0.5 and 0.7 increases rapidly after their respective critical Reynolds number, after which it begins to flatten and then decrease after the Reynolds number exceeds 3,400. As discussed in Section 7.3.1 for the IFS microchannel series, the decrease of Nu/Nu_{Plain} is caused by the rapid growth in Nusselt number of the Plain microchannel upon entering a turbulent flow state.

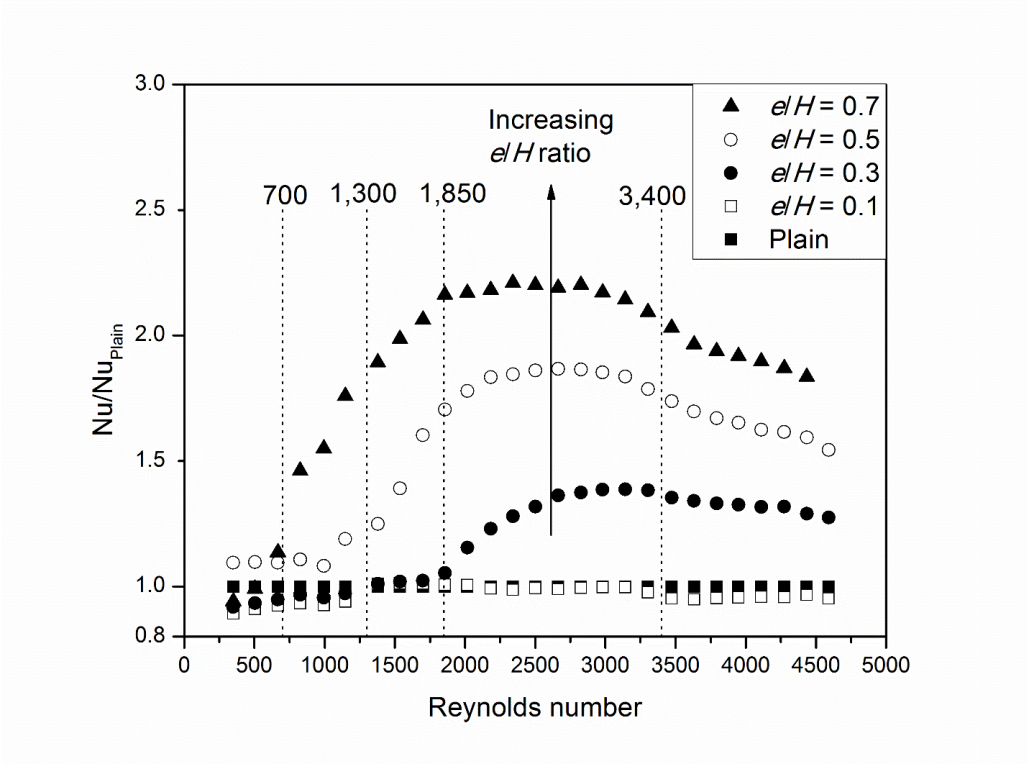

Figure 8-7: Normalised Nusselt number against Reynolds number, for different *e*/*H* ratio (FS series)

Figure 8-8 shows the variation of Nusselt number with *e*/*H* ratio for the FS microchannel series. Nusselt number is again observed to increase with *e*/*H* ratio, for the same *P*/*e* ratio and Reynolds number, albeit to a less extent as compared to the IFS microchannel series. For example, when the *e*/*H* ratio increases from 0.1 to 0.7 at *Re*≈2,664, the Nusselt number increases from 15 to 33 for the FS series, while it increases from 16 to 37 for the IFS series.

An analysis of the flow field and temperature distribution for the Plain microchannel and FS microchannels with *e*/*H* ratio of 0.1 and 0.7 suggests that the heat transfer enhancement mechanisms are the same as that for the IFS microchannel series, which has been discussed in Section 7.3.1. For completeness, the numerical results are presented in Figures C-1 to C-6 in Appendix C.

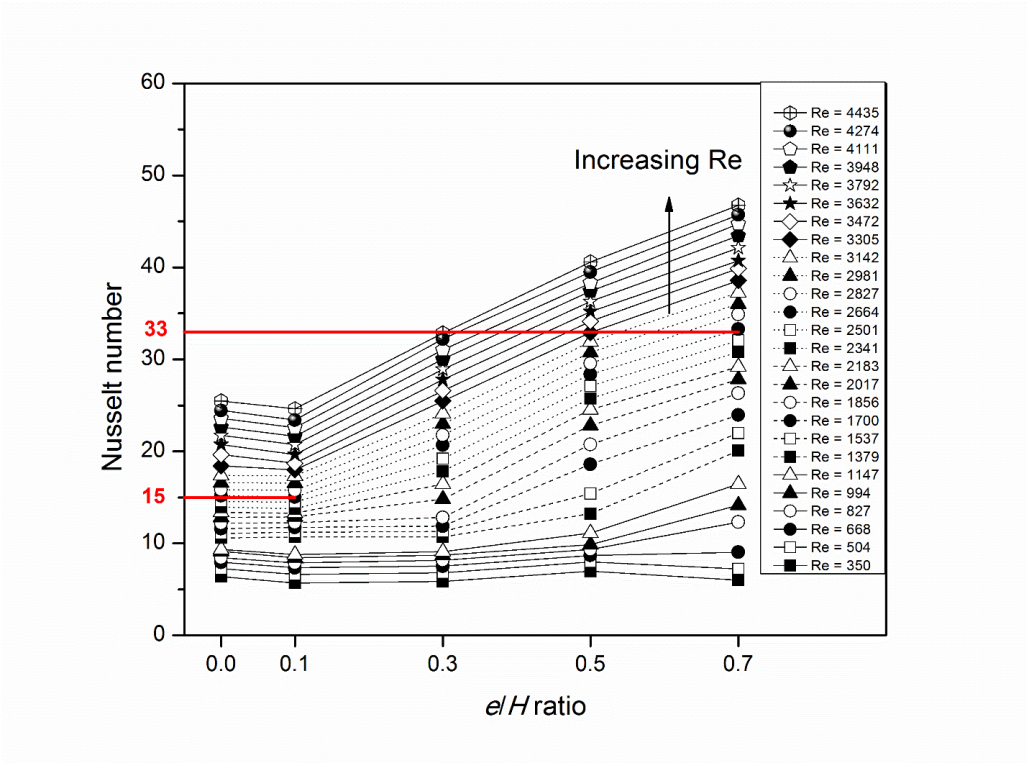

Figure 8-8: Nusselt number against *e*/*H* ratio, at different Reynolds number (FS series)

It is also observed that the IFS profile is able to achieve a higher Nusselt number than the FS profile. Using an *e*/*H* ratio of 0.7 at *Re*≈2,664, the Nusselt number is 37 and 33, respectively, for the IFS and FS series. This can be explained by comparing the corresponding flow field and temperature distribution for the IFS and FS microchannels. For the purpose of comparison, Figures 7-11 and 7-14 are re-presented in this section as Figures 8-9 and 8-11, respectively. Figures 8-9 and 8-10 show that the IFS profile induces a higher maximum local fluid velocity than the FS profile. With the same *e*/*H* ratio of 0.7 at *Re*≈2,664, the maximum fluid velocity is 7.5 and 6.7 m/s, respectively, for the IFS and FS microchannel. This is because there is a sudden constriction of the flow channel at the minimum channel gap in the IFS microchannel, whereas there is a sudden expansion of the flow channel at the same location in the FS microchannel.

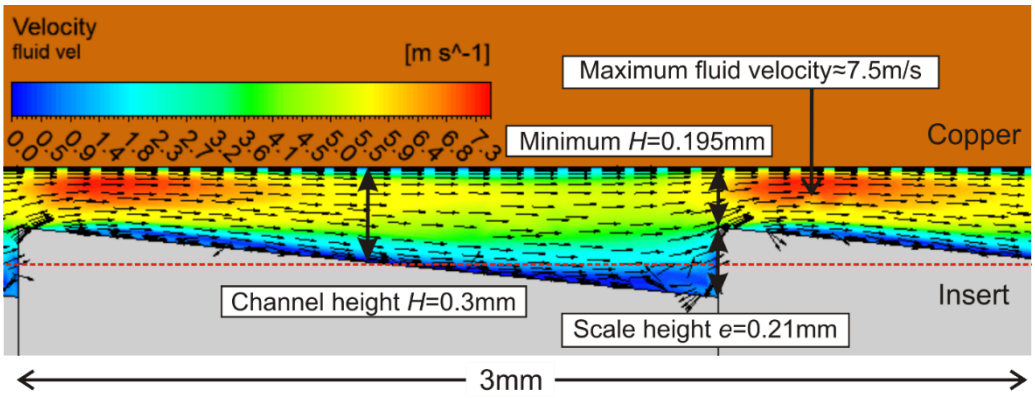

Figure 8-9: Flow field of IFS microchannel with *e*/*H* ratio of 0.7 at *Re* ≈ 2,664

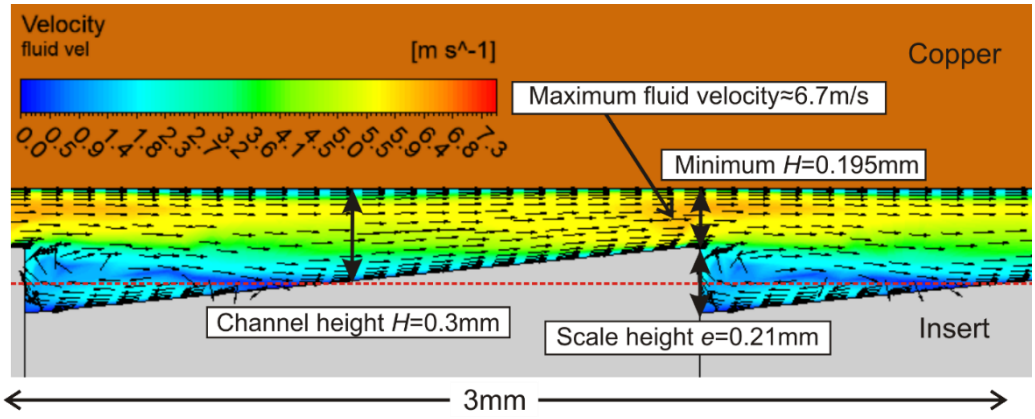

Figure 8-10: Flow field of FS microchannel with *e*/*H* ratio of 0.7, at *Re* ≈ 2,664

A higher local fluid velocity results in thinner thermal boundary layer for the IFS profile as compared to the FS profile, as shown in Figures 8-11 and 8-12. This accounts for the higher Nusselt number for the IFS profile.

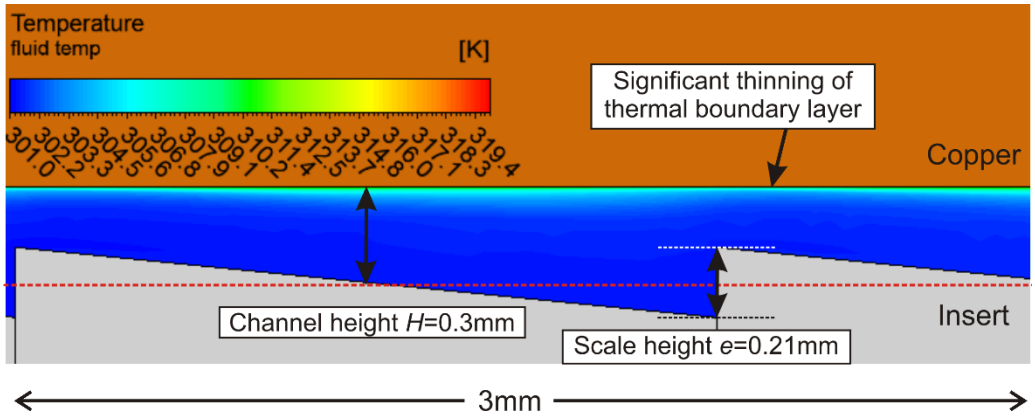

Figure 8-11: Temperature distribution of IFS microchannel with *e*/*H* ratio of 0.7, at *Re* ≈ 2,664

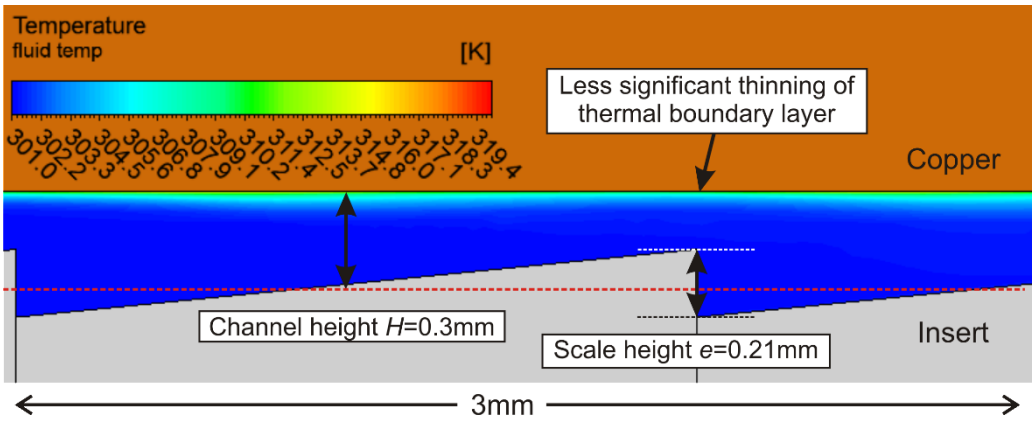

Figure 8-12: Temperature distribution of FS microchannel with *e*/*H* ratio of 0.7, at *Re* ≈ 2,664

8.3.2 Hydrodynamic Considerations

Figure 8-13 shows the variation of friction factor with Reynolds number, for different *e*/*H* ratio, using the FS microchannel series. Similar to the phenomena with the IFS microchannel series, the friction factor is observed to decrease with Reynolds number and increase with *e*/*H* ratio. The maximum friction factor is 0.58 at Reynolds number of 350 using FS_*e*0.21-*P*2.1 profile. This value is lower than the value of 0.73 at the same flow condition, when IFS_*e*0.21-*P*2.1 profile is used. This proves that the more streamlined FS profile causes less flow disturbances and thus incurs lower friction losses, as compared to the disruptive IFS profile.

The FS profile with *e*/*H* ratio of 0.1 is observed to resemble the hydrodynamic behaviour of the Plain microchannel for the Reynolds number range investigated. In other words, the Reynolds number corresponding to the onset of transition is 2,200. For the FS profiles with *e*/*H* ratio of 0.3, 0.5, and 0.7, the critical Reynolds number is 1,850, 1,300 and 700, respectively. The transition is characterised by a region where the friction factor data can be described by neither the laminar nor turbulent trend line. Once again, this verifies the postulation that an increase in scale height relative to mean channel height promotes early laminar-to-turbulent flow transition.

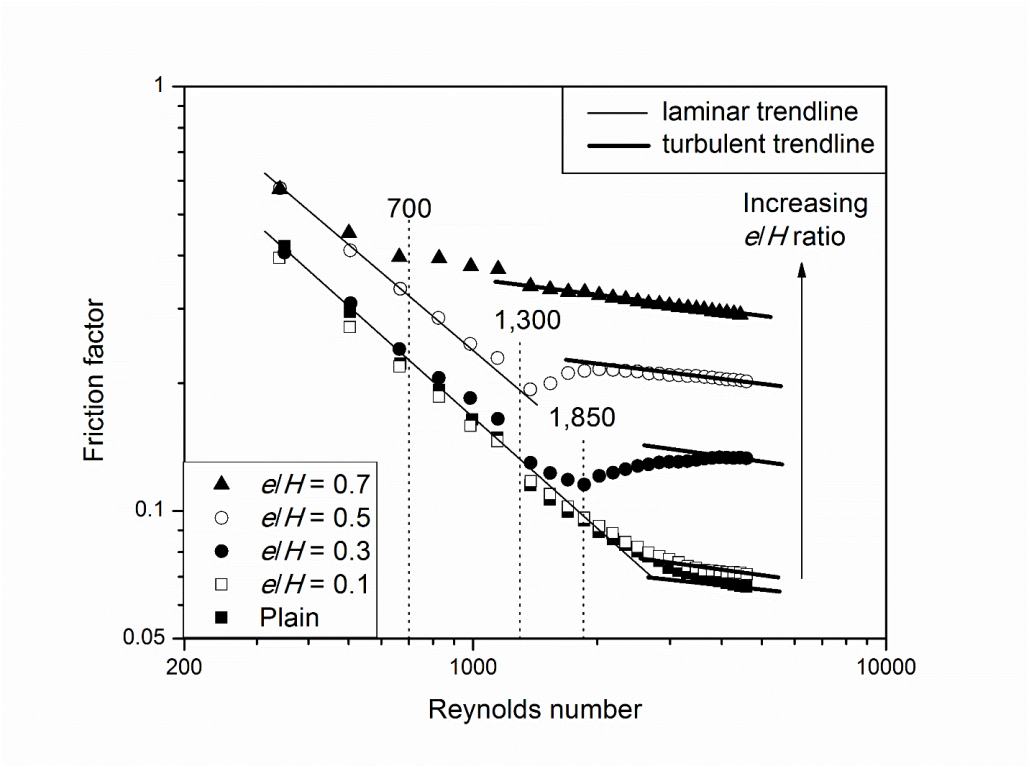

Figure 8-13: Friction factor against Reynolds number, for different *e*/*H* ratio (FS series)

Figure 8-14 shows that the normalised friction factor for the FS microchannel series increases with Reynolds number. Similar observations have been made using the IFS microchannel series. With the same y-axis range of 0 to 8 across the three microchannel series, it can be seen that the normalised friction factor is relatively low for the FS microchannel series. The maximum normalised friction factor for the FS series is 4.4, with an *e*/*H* ratio of 0.7.

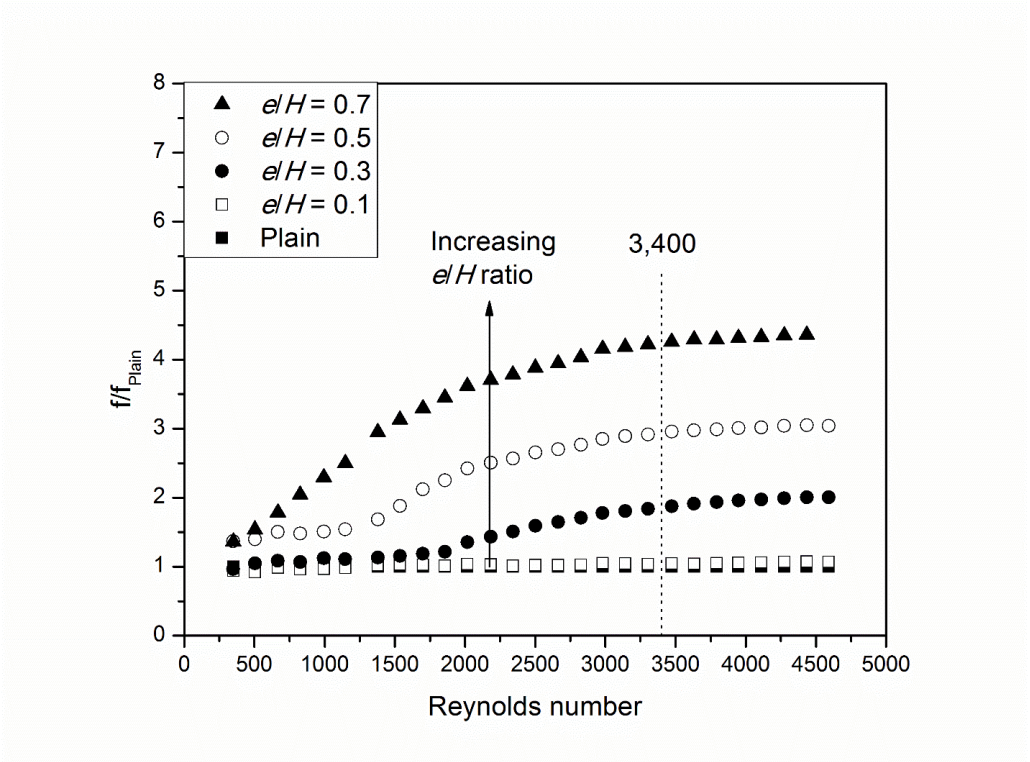

Figure 8-14: Normalised Friction factor against Reynolds number, for different *e*/*H* ratio (FS series)

Figure 8-15 shows the variation of friction factor with *e*/*H* ratio for the FS microchannel series. The friction factor is again observed to increase with *e*/*H* ratio, for the same *P*/*e* ratio and Reynolds number, but to a less extent as compared to the IFS microchannel series. For example, when the *e*/*H* ratio increases from 0.1 to 0.7 at *Re*≈2,664, the friction factor increases from 0.08 to 0.31 for the FS series, while it increases from 0.08 to 0.36 for the IFS series.

The explanation for the increase in friction factor with *e*/*H* ratio is the same as that with the IFS microchannel series, which has been discussed in Section 7.3.2. The corresponding velocity distributions are presented in Figures C-7 to C-9 in Appendix C for completeness.

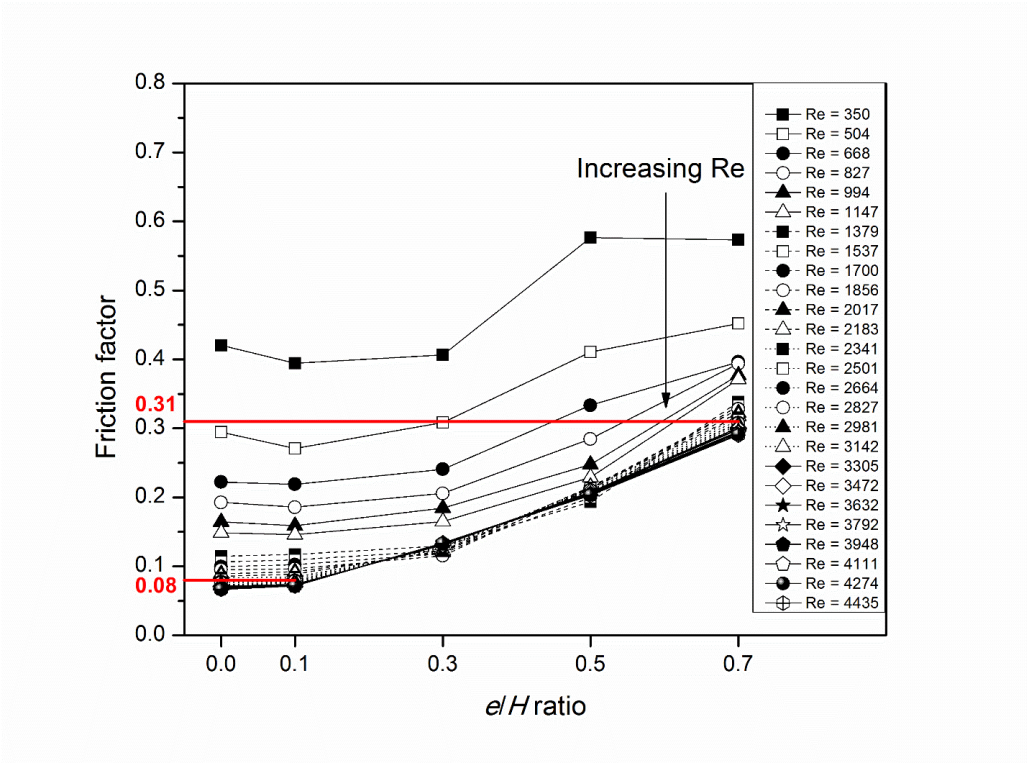

Figure 8-15: Friction factor against *e*/*H* ratio, at different Reynolds number (FS series)

Similarly, the higher friction factor of the IFS profile can be explained by Figure 8-16, where there is significant thinning of the velocity boundary layer. On the other hand, the lower friction factor of the FS profile can be explained by Figure 8-17, where there is less significant thinning of the velocity boundary layer.

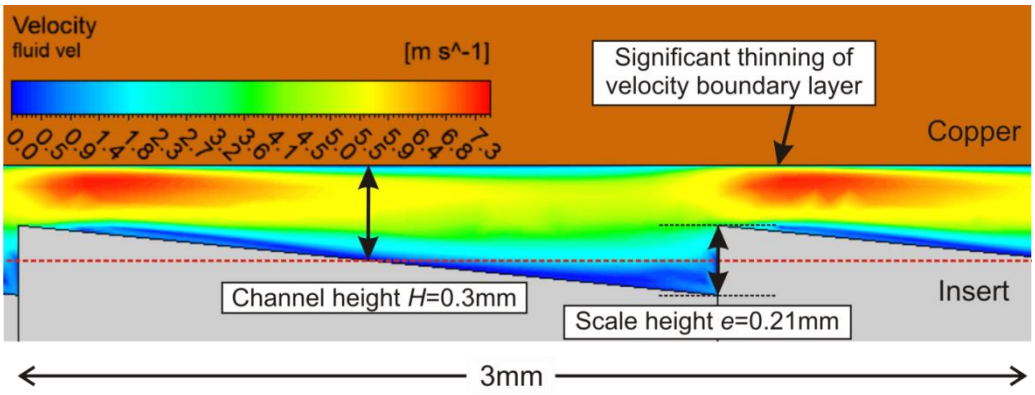

Figure 8-16: Velocity distribution of IFS microchannel with *e*/*H* ratio of 0.7 at *Re* ≈ 2,664

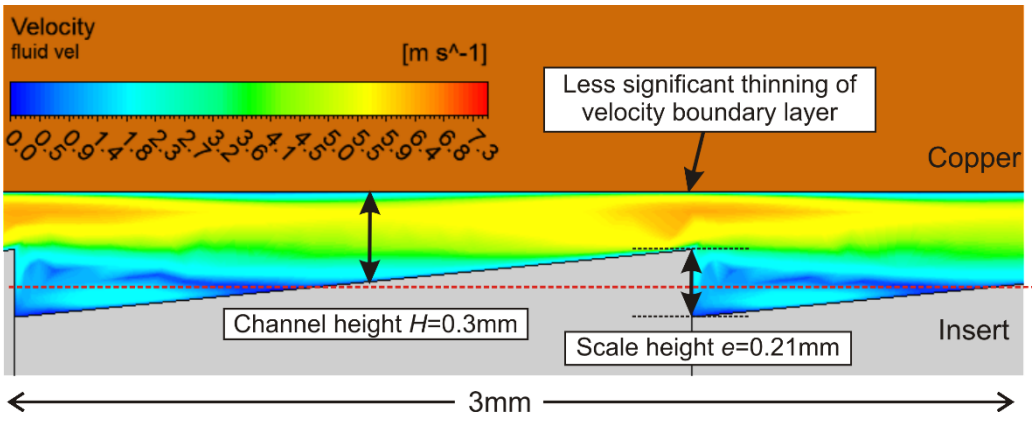

Figure 8-17: Velocity distribution of FS microchannel with *e*/*H* ratio 0.7, at *Re* ≈ 2,664

8.3.3 Thermo-hydraulic Performance

Figure 8-18 shows the variation of thermo-hydraulic performance with Reynolds number, for different *e*/*H* ratio. As expected, the FS microchannels perform better than the Plain microchannel after the critical Reynolds number, due to the early transition to turbulent flow. It decreases at higher Reynolds number, particularly after 3,400.

Once again, this parametric study concludes that the largest *e*/*H* ratio of 0.7 exhibits the highest thermo-hydraulic performance. Given a fixed heat transfer surface area and pumping power, this FS profile improves the heat transfer capacity by 43% relative to the Plain profile, at Reynolds number of 1,850.

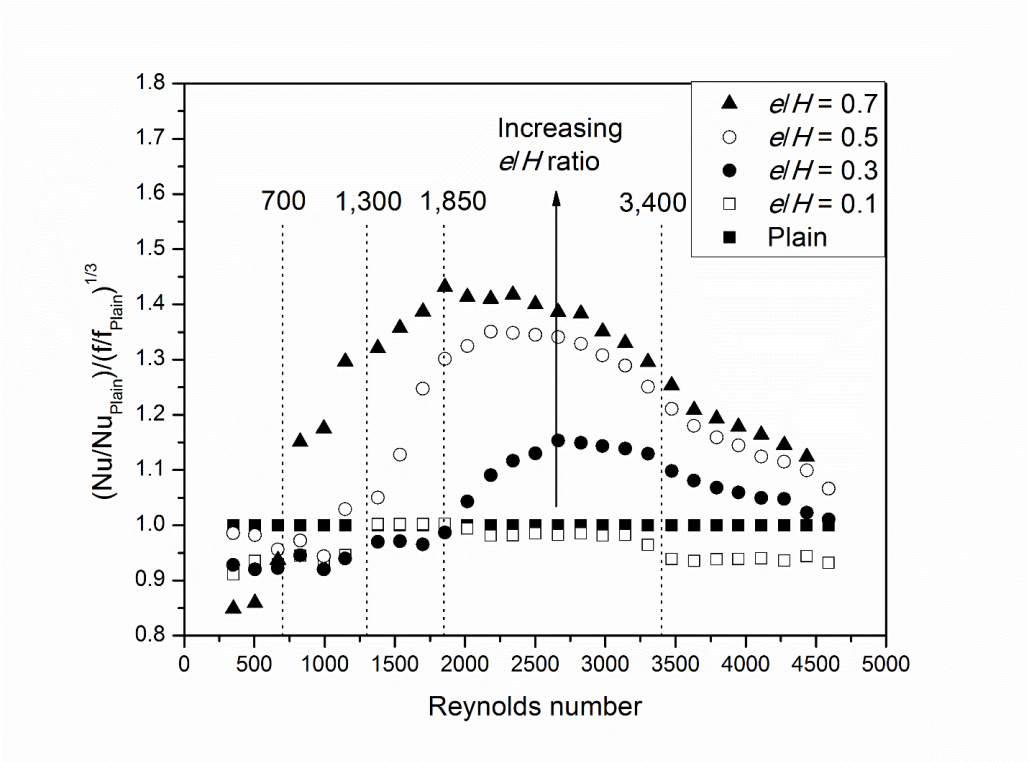

Figure 8-18: Thermo-hydraulic performance against Reynolds number, for different *e*/*H* ratio (FS series)

8.4 Scale Pitch (*P*) to Scale Height (*e*) Ratio Study

8.4.1 Thermal Considerations

Figure 8-19 shows the variation of Nusselt number with Reynolds number for different *P*/*e* ratio. The maximum Nusselt number achieved is 41, at Reynolds number of 4,430 using the FS profile with *P*/*e* ratio of 5.

There is again a visible change in heat transfer behaviour at a particular Reynolds number. The critical Reynolds number is 800, 1,300, 1,600 and 1,600, respectively, for the FS microchannels with *P*/*e* ratio of 5, 10, 15 and 20. In other words, as the *P*/*e* ratio decreases, the critical Reynolds number reduces.

This means that increasing the number of scale protrusions for a fixed microchannel length by decreasing the *P*/*e* ratio helps to promote early laminar-to-turbulent flow transition. This postulation is also supported by the flow characteristics, as will be discussed using Figure 8-26 in Section 8.4.2.

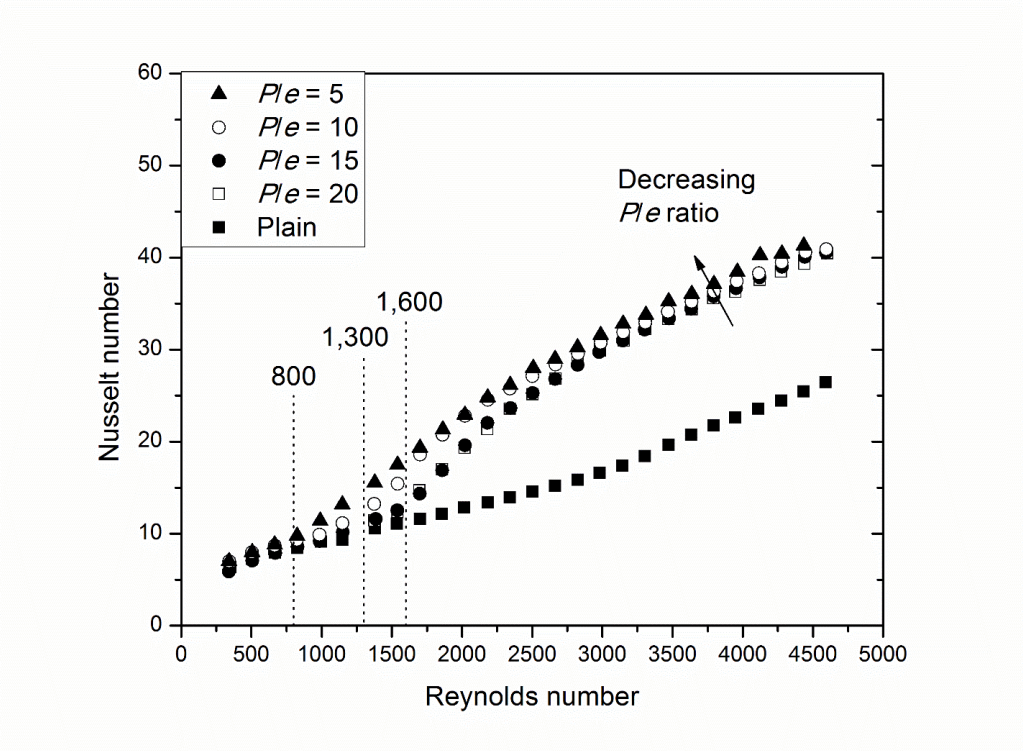

Figure 8-19: Nusselt number against Reynolds number, for different *P*/*e* ratio (FS series)

Figure 8-20 shows the variation of normalised Nusselt number with Reynolds number, for different *P*/*e* ratio, using the FS microchannel series. Using the same y-axis range of 0.8 to 3.0 across the three microchannel series, the normalised Nusselt number is visibly lower for the FS series in the *P*/*e* ratio study. The FS profile with *P*/*e* ratio of 5 is observed to achieve a Nusselt number of at most 1.9 times that of the Plain profile. For the same *P*/*e* ratio, the IFS profile can improve the Nusselt number by 2.6 times, within the same range of Reynolds number from 350 to 3,948.

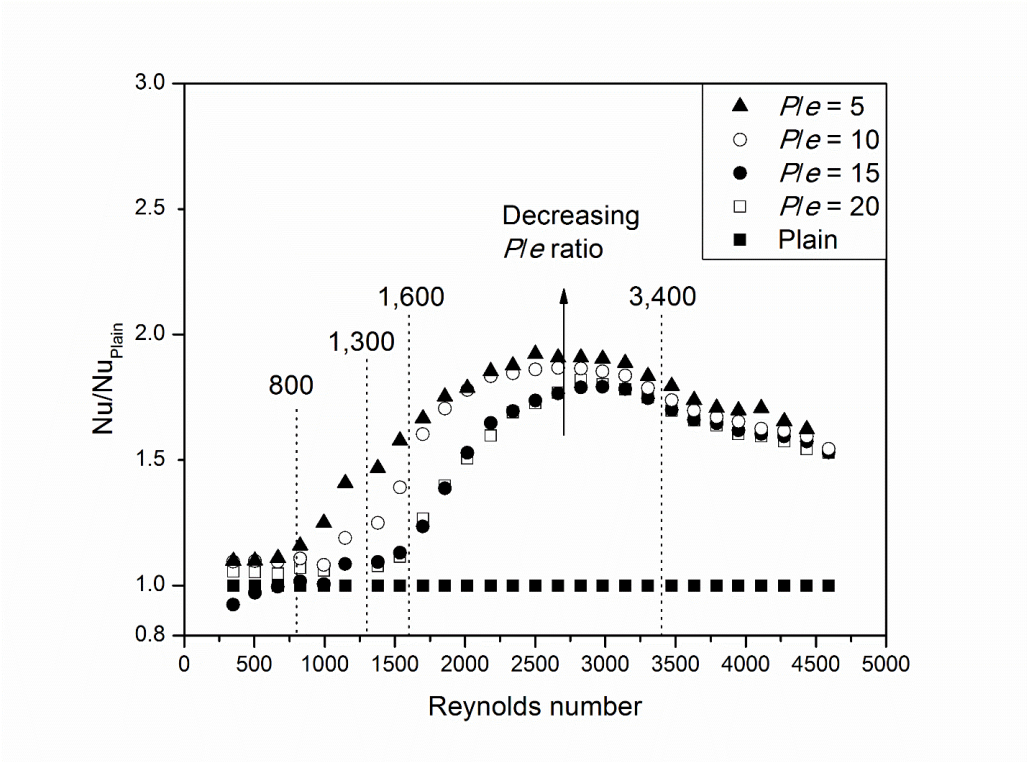

Figure 8-20: Normalised Nusselt number against Reynolds number, for different *P*/*e* ratio (FS series)

Within the FS microchannel series, Figure 8-21 again shows that Nusselt number increases when *P*/*e* ratio decreases, for the same *e*/*H* ratio and Reynolds number. For example, the Nusselt number increases from 27 to 29, when the *P*/*e* ratio decreases from 20 to 5, at Reynolds number≈2,664. Interestingly, however, the effect of *P*/*e* ratio on Nusselt number for the FS microchannel series is considerably less.

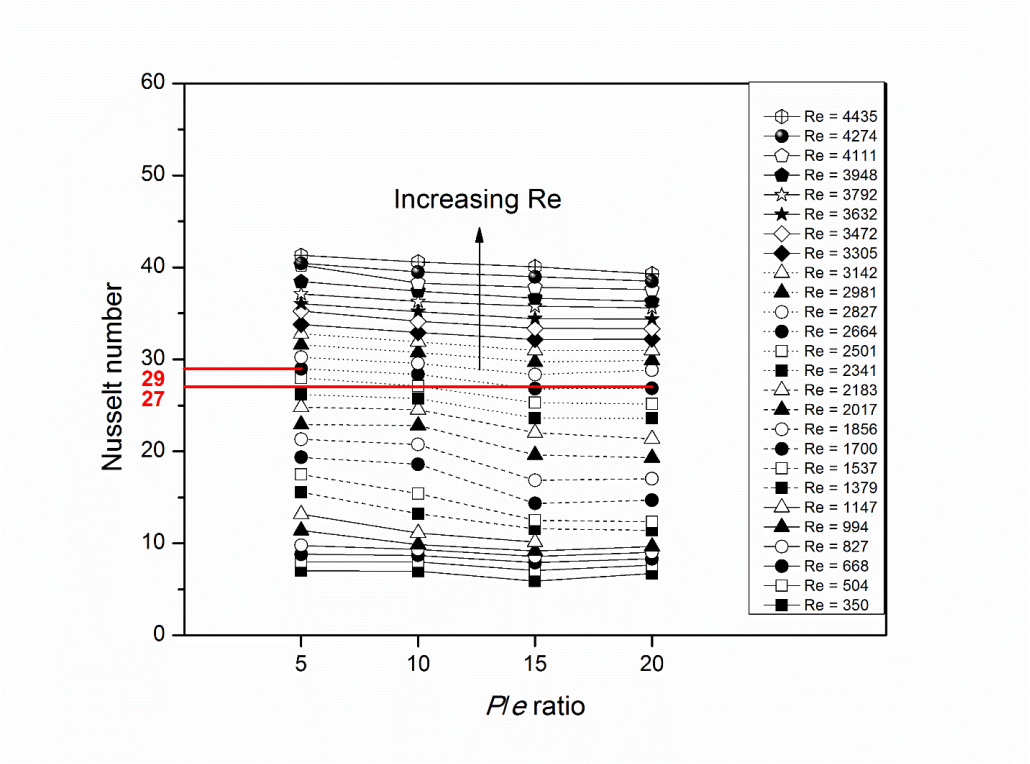

Figure 8-21: Nusselt number against *P*/*e* ratio, at different Reynolds number (FS series)

To understand the reason behind, the respective flow field and temperature distribution are analysed. Due to the geometrical configuration of the Fish Scale profile, there is a sudden expansion of the flow channel immediately after the scale tip. The flow channel then narrows gradually until the next sudden expansion. The sudden flow channel expansion results in a localised region of flow recirculation. For a larger *P*/*e* ratio of 20, there is only one region of flow recirculation, as illustrated in Figure 8-22. The fluid then flows at low and high bulk fluid velocities through the large and small channel flow paths, by virtue of mass conservation. At the region of low bulk fluid velocity, the thermal boundary layer near the heated copper wall develops rapidly into a thick layer, as illustrated in Figure 8-24. This results in a low Nusselt number of 27.

On the other hand, there are four regions of flow recirculation for a smaller *P*/*e* ratio of 5, as illustrated in Figure 8-23. These localised regions of flow recirculation narrow the bulk flow path, such that the incompressible fluid is constantly accelerated through the microchannel at a higher bulk fluid velocity. However, due to the flow channel expansion immediately after the scale tip, the fluid flows at a moderate bulk fluid velocity in between the scale tips, as characterised by the green region in Figure 8-23. This results in a moderately thin thermal boundary layer, as illustrated in Figure 8-25. Hence, the Nusselt number increases only slightly to 29.

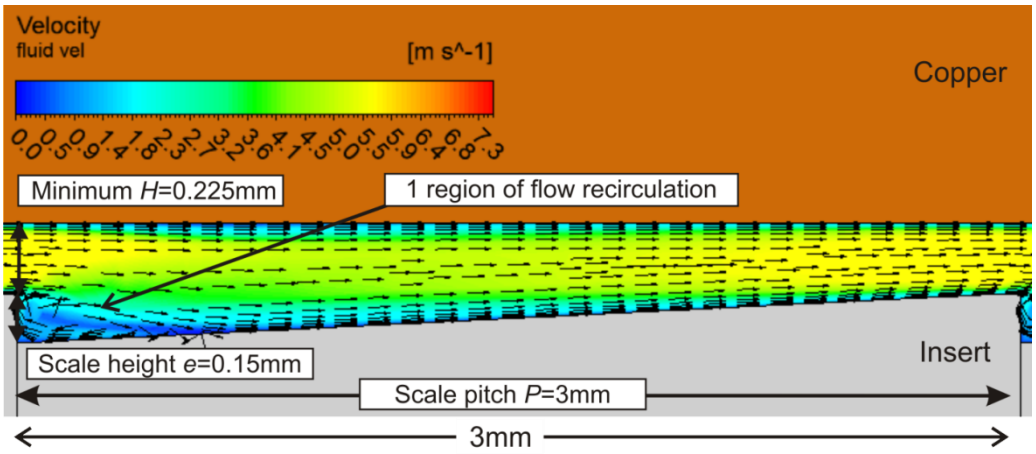

Figure 8-22: Flow field of FS microchannel with *P*/*e* ratio of 20, at *Re* ≈ 2,664

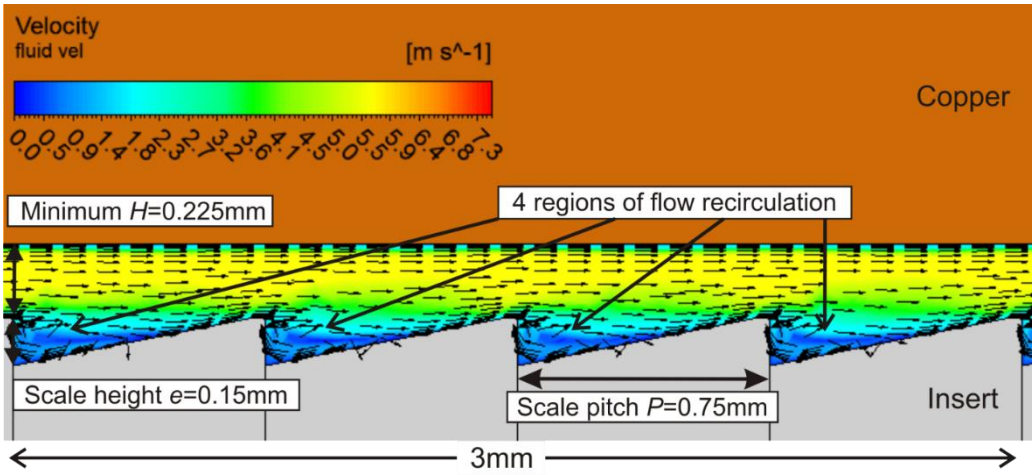

Figure 8-23: Flow field of FS microchannel with *P*/*e* ratio of 5, at *Re* ≈ 2,664

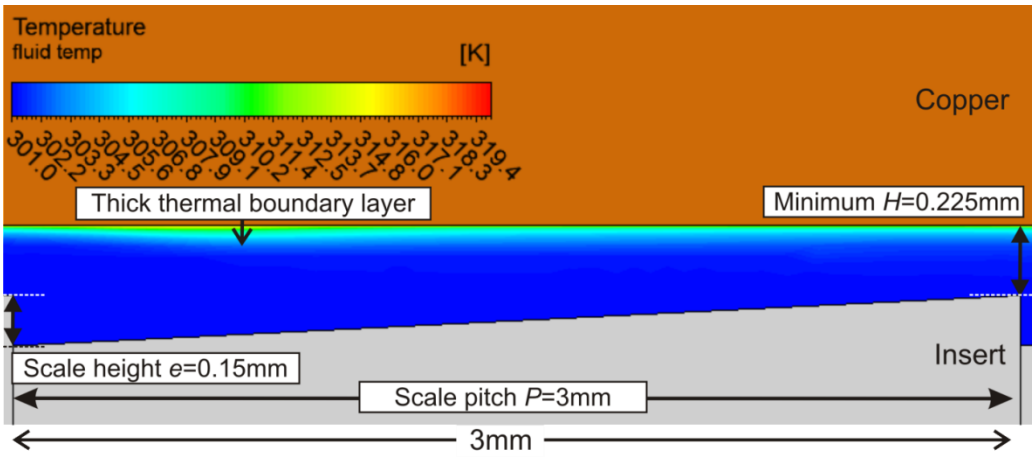

Figure 8-24: Temperature distribution of FS microchannel with *P*/*e* ratio of 20, at *Re* ≈ 2,664

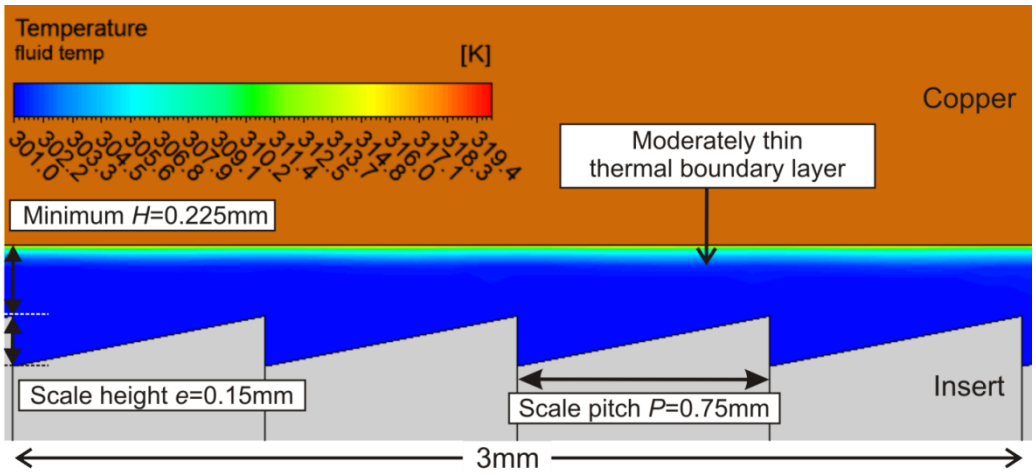

Figure 8-25: Temperature distribution of FS microchannel with *P*/*e* ratio of 5, at *Re* ≈ 2,664

8.4.2 Hydrodynamic Considerations

Figure 8-26 shows the variation of friction factor with Reynolds number, for different *P*/*e* ratio, using the FS microchannel series. As expected, the critical Reynolds number for each profile matches those listed in Section 8.4.1. The maximum friction factor is 0.63 at *Re*≈350 using the FS_*e*0.15-*P*0.75 profile. Conversely, the IFS_*e*0.15-*P*0.75 profile incurs a friction factor of 0.73 at the same flow condition. This implies that the more streamlined FS profile is able to reduce friction losses by 14%, as compared to the disruptive IFS profile.

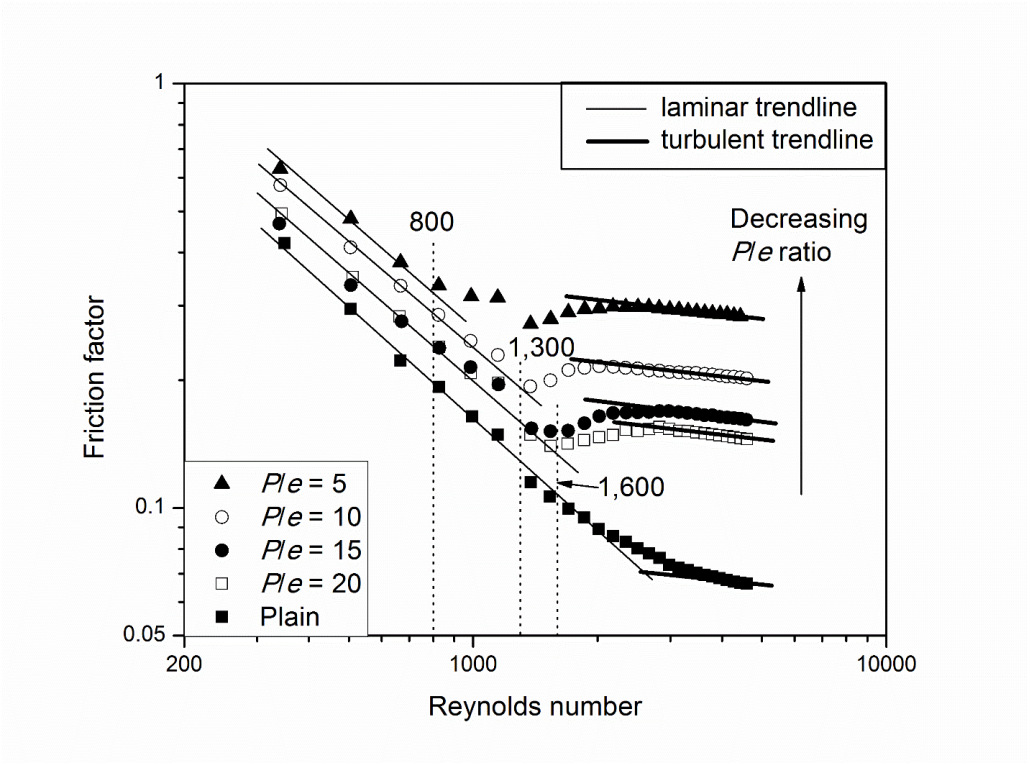

Figure 8-26: Friction factor against Reynolds number, for different *P*/*e* ratio (FS series)

As mentioned in the beginning of this chapter, the FS profile is investigated in view of the high friction losses incurred with the IFS profile. In particular, the maximum normalised friction factor for the IFS profile is 6.7 with a *P*/*e* ratio of 5 at *Re*≈3,953. Conversely, the normalised friction factor for the FS profile is only 4.2 for the same conditions, as shown in Figure 8-27. Hence, the more streamlined FS profile has been demonstrated to incur lower friction losses than those for the disruptive IFS profile.

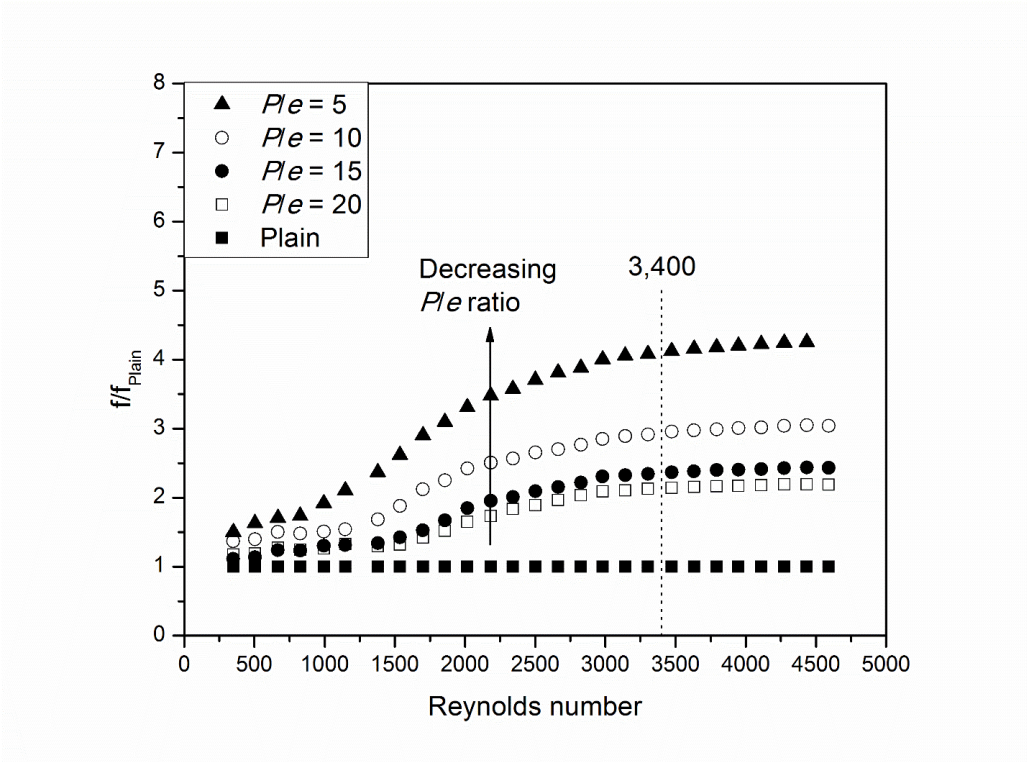

Figure 8-27: Normalised Friction factor against Reynolds number, for different *P*/*e* ratio (FS series)

Within the FS microchannel series, the friction factor is also observed to increase when *P*/*e* ratio decreases, as shown in Figure 8-28. For example, the friction factor doubles from 0.15 to 0.3, when the *P*/*e* ratio decreases from 20 to 5, at *Re*≈2,664. Since the explanation is similar to that for the IFS microchannel series, the velocity distributions for the FS microchannels with *P*/*e* ratio of 20 and 5 are presented in Figures C-10 and C-11 in Appendix C instead.

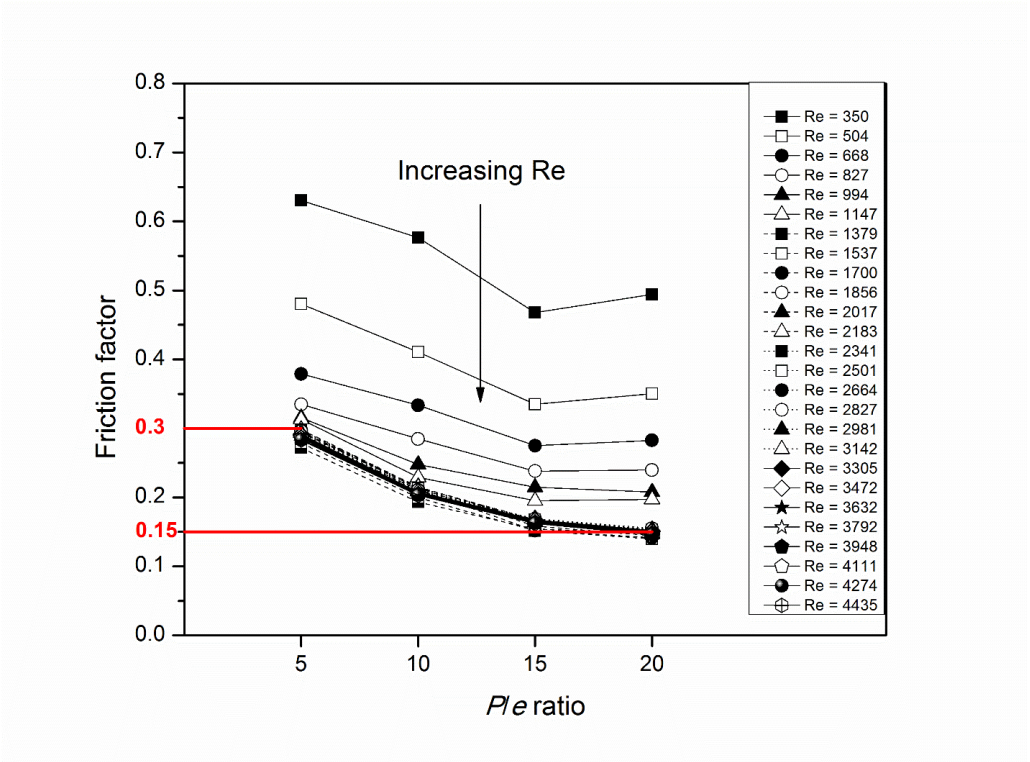

Figure 8-28: Friction factor against *P*/*e* ratio, at different Reynolds number (FS series)

It is again observed that the effect of *P*/*e* ratio on friction factor for the FS microchannel series is considerably less as compared to that for the IFS microchannel series. For example, the friction factor increases by two times from 0.15 to 0.3 for the FS microchannel series, while it increases by about three times from 0.16 to 0.47 for the IFS microchannel series, when the *P*/*e* ratio decreases from 20 to 5 at Reynolds number≈2,664. This is likely due to the different flow patterns induced by the IFS and FS profiles. As mentioned earlier, there is a sudden constriction of the flow channel at the minimum channel gap in the IFS microchannel, whereas there is a sudden expansion of the flow channel at the same location in the FS microchannel.

8.4.3 Thermo-hydraulic Performance

Figure 8-29 shows the variation of thermo-hydraulic performance with Reynolds number, for different *P*/*e* ratio. As expected, the performance of the each FS microchannel surpasses that of the Plain microchannel after the respective critical Reynolds number is exceeded, when the flow transits to the non-laminar region. This reinforces the postulation that the FS profile promotes early laminar-to-turbulent flow transition, thereby enhancing the thermo-hydraulic performance. The thermo-hydraulic performance consistently decreases with Reynolds number for $Re \gtrsim 3{,}400$.

In this parametric study, the effect of *P*/*e* ratio on the thermo-hydraulic performance is unclear at lower Reynolds numbers. At higher Reynolds numbers, a larger *P*/*e* ratio exhibits higher thermo-hydraulic performance, and the FS profile with the largest *P*/*e* ratio of 20 performs the best. Given a fixed heat transfer surface area and pumping power, this FS profile improves the heat transfer capacity by 44% relative to the Plain profile, at Reynolds number of 2,800. This is because the decreasing the *P*/*e* ratio improves the Nusselt number minimally, and yet increases the friction factor considerably. This means that increasing the number of scale protrusions by decreasing the *P*/*e* ratio has a detrimental effect on the thermo-hydraulic performance at higher Reynolds numbers, for the FS microchannel series.

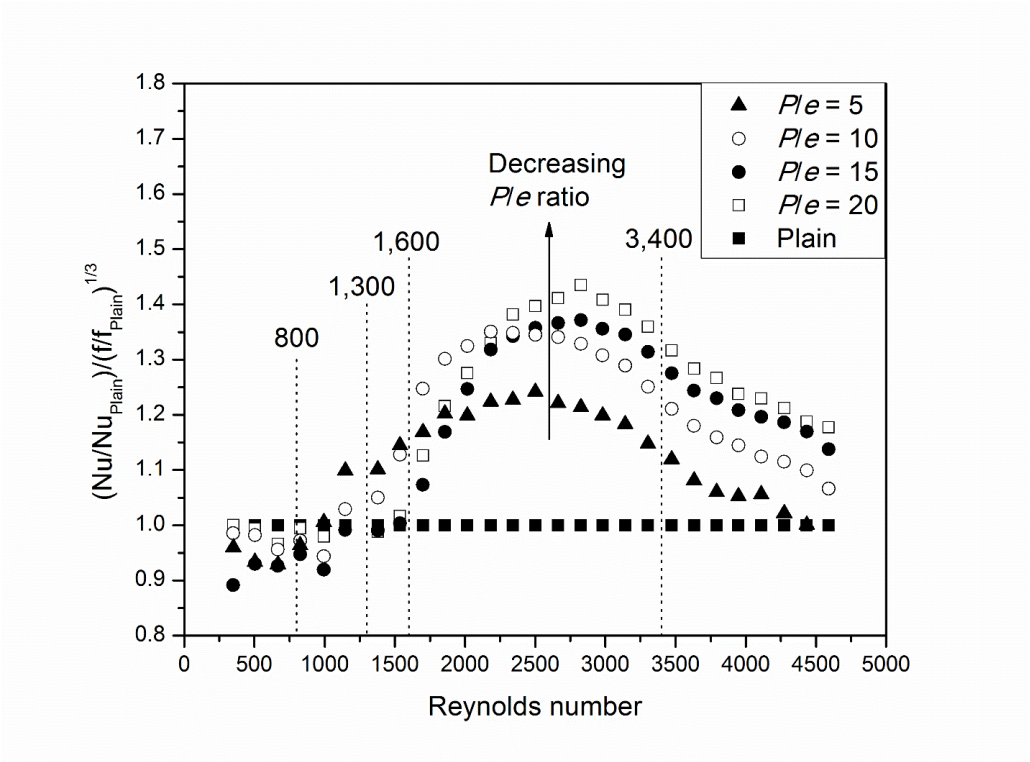

Figure 8-29: Thermo-hydraulic performance against Reynolds number, for different *P*/*e* ratio (FS series)

This finding seems to contradict the results from the IFS microchannel series, where a smaller *P*/*e* ratio exhibits a higher thermo-hydraulic performance. However, a closer scrutiny reveals that the aforementioned effect is only applicable for $Re \lesssim 1{,}400$. In fact, the effect of *P*/*e* ratio on performance diminishes with an increase in Reynolds number. For $Re \gtrsim 3{,}400$, the *P*/*e* ratio has an insignificant effect on the performance. The observations from both the IFS and FS microchannel series point to the fact that, at higher Reynolds number above 3,400, increasing the number of scale protrusions does not improve the thermo-hydraulic performance, since it has at best an insignificant effect, if not a detrimental one.

Chapter 9 Results for the Thorny Durian Microchannels

While the IFS profile is able to achieve high heat transfer coefficients, the accompanying friction losses are high. Conversely, lower friction losses are incurred by the FS profile, along with lower heat transfer coefficients. In view that that there is either a sudden constriction or expansion of the flow area for the scale-inspired microchannel series, which results in flow recirculation and possibly unnecessary friction losses, another new configuration is considered.

Inspired by the thorn-covered husk of a tropical fruit, which is regarded as the king of fruits in Southeast Asia, the thorny Durian (D) microchannel shows potential to create flow disturbances and enhance heat transfer, while keeping the friction losses low due to the wavy flow path, as shown in Figure 9-1. The results suggest that the D profile is the best candidate for heat exchanger applications where the aim is to achieve a significant increase in heat transfer capacity for a fixed heat transfer surface area and pumping power.

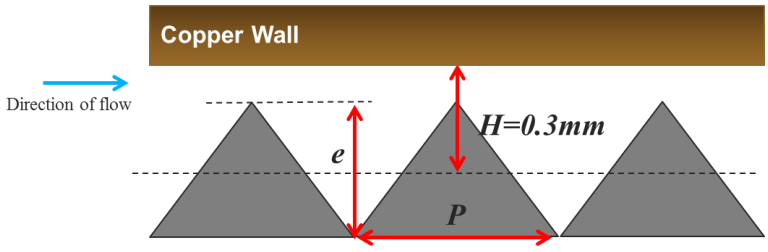

Figure 9-1: Thorny Durian (D) profile

This chapter presents the results for the thorny Durian (D) microchannel series. While the organisation of this chapter is similar to that of the two preceding chapters, the differences between the results for the durian-inspired D microchannels and the scale-inspired IFS and FS microchannels are also highlighted.

9.1 Overview of Measured Results for the D Microchannels

Similar to the scale-inspired IFS and FS profiles, the thorny D profiles enhance heat transfer as well. As shown in Figure 9-2, for flow rates above 3 L/min, all the D microchannels, with the exception of D_*e*0.03-*P*0.3, yield higher heat transfer coefficients than the Plain microchannel. The highest heat transfer coefficient achieved for the D series is 51 kW/m^2·K, at 7 L/min using the D_*e*0.21-*P*2.1 profile.

Within the D microchannel series, the effect of *e*/*H* ratio on the heat transfer is visibly significant, with reference to the hollow symbols. However, the effect of *P*/*e* ratio, as represented by the solid symbols, is less significant especially at higher flow rates. In comparison with the scale-inspired microchannel series, the effect of *e*/*H* ratio is generally significant for all the three different microchannel series. On the other hand, the effect of *P*/*e* ratio on the heat transfer for the D microchannel series lies in between that of the IFS and FS microchannel series, where the effect is significant for the IFS microchannel series and considerably less significant for the FS microchannel series, particularly at higher flow rates.

The maximum pressure drop for the D series is 2.7 bars, as shown in Figure 9-3. This is well below the imposed pressure drop limit of 3.5 bars.

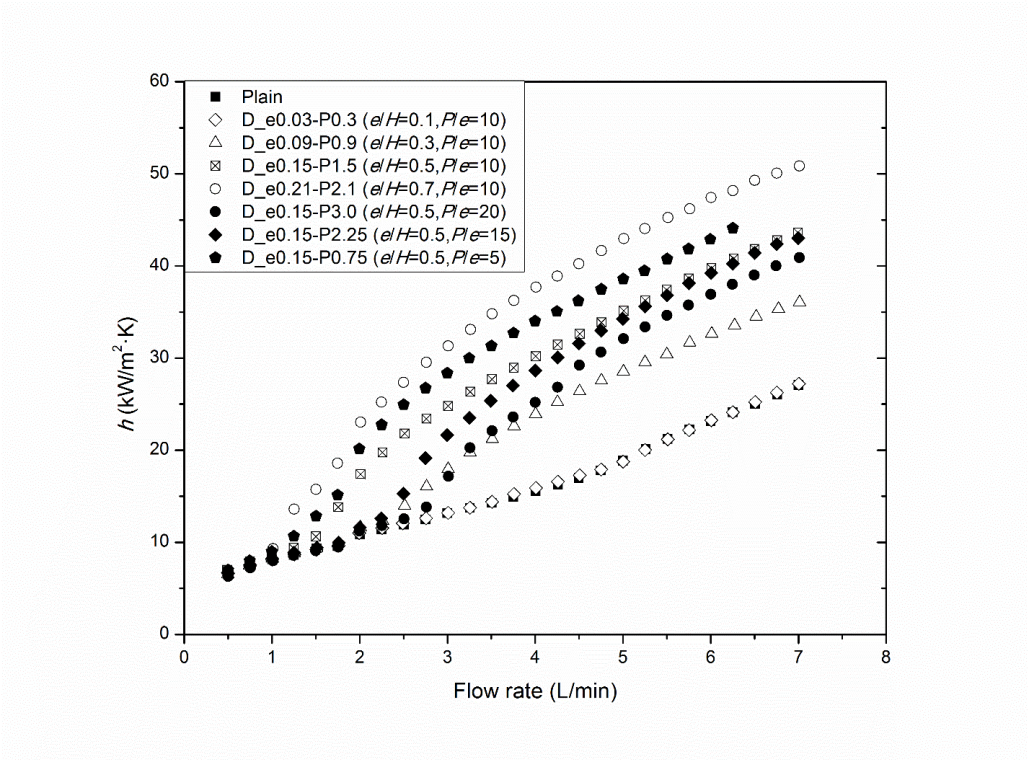

Figure 9-2: Heat transfer coefficient against flow rate for all D and Plain microchannels

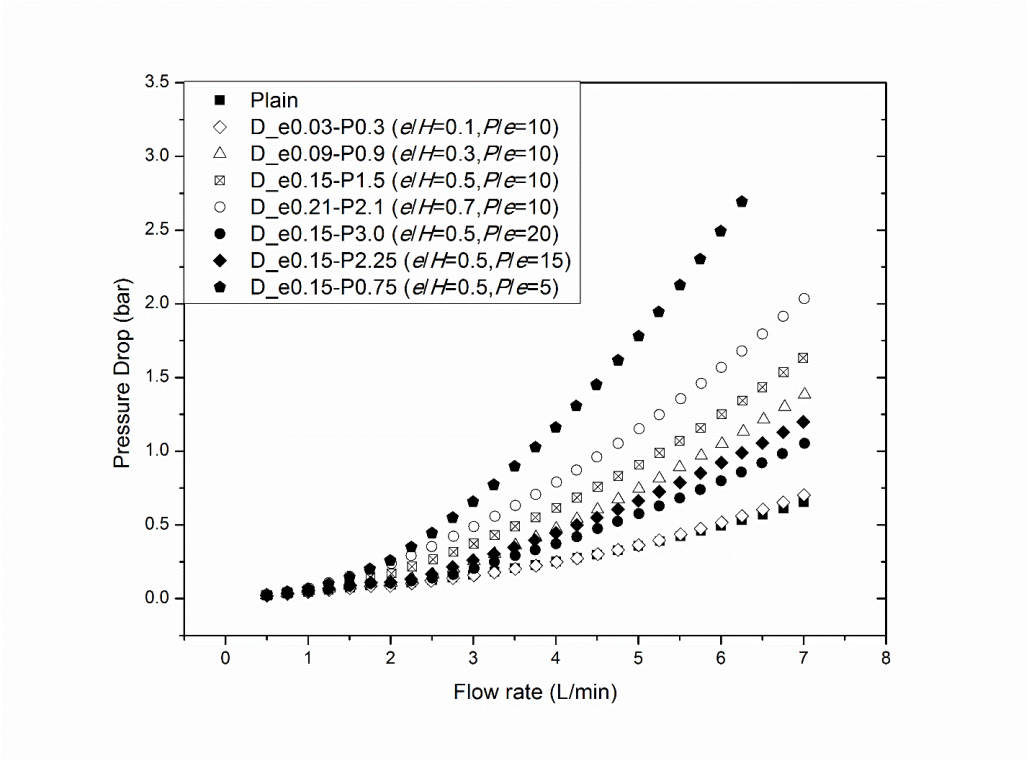

Figure 9-3: Pressure Drop against flow rate for all D and Plain microchannels

9.2 Comparison between Measured and Numerical Results

Figure 9-4 compares the measured and predicted pressure drop, for various insert profiles at flow rates between 2 and 7 L/min. It is observed that about 90% of the predictions agree well with the measurements, with the deviations falling within the ±10% band. Once again, the numerical model generally under-predicts the pressure drop.

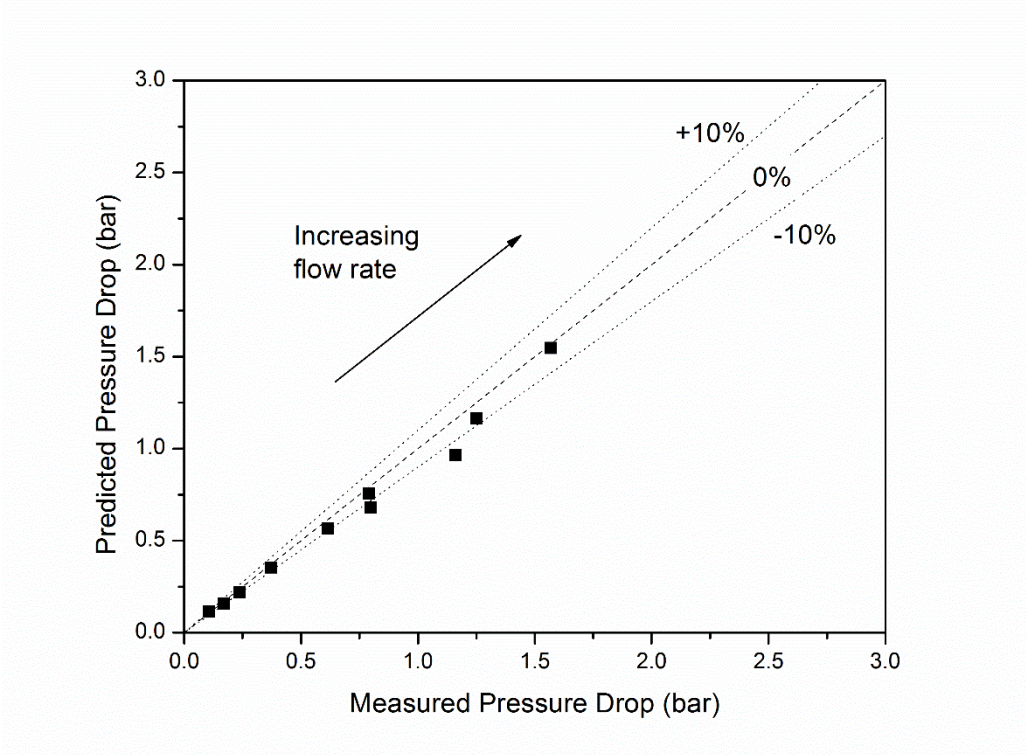

Figure 9-4: Predicted pressure drop against measured pressure drop (D series)

Figure 9-5 compares the measured and predicted Nusselt number, for various insert profiles at Reynolds numbers approximately between 1,300 and 4,600. It is observed that about 90% of the predictions agree with the measurements, with the deviations falling within the ±30% band. Once again, the numerical model generally over-predicts Nusselt number.

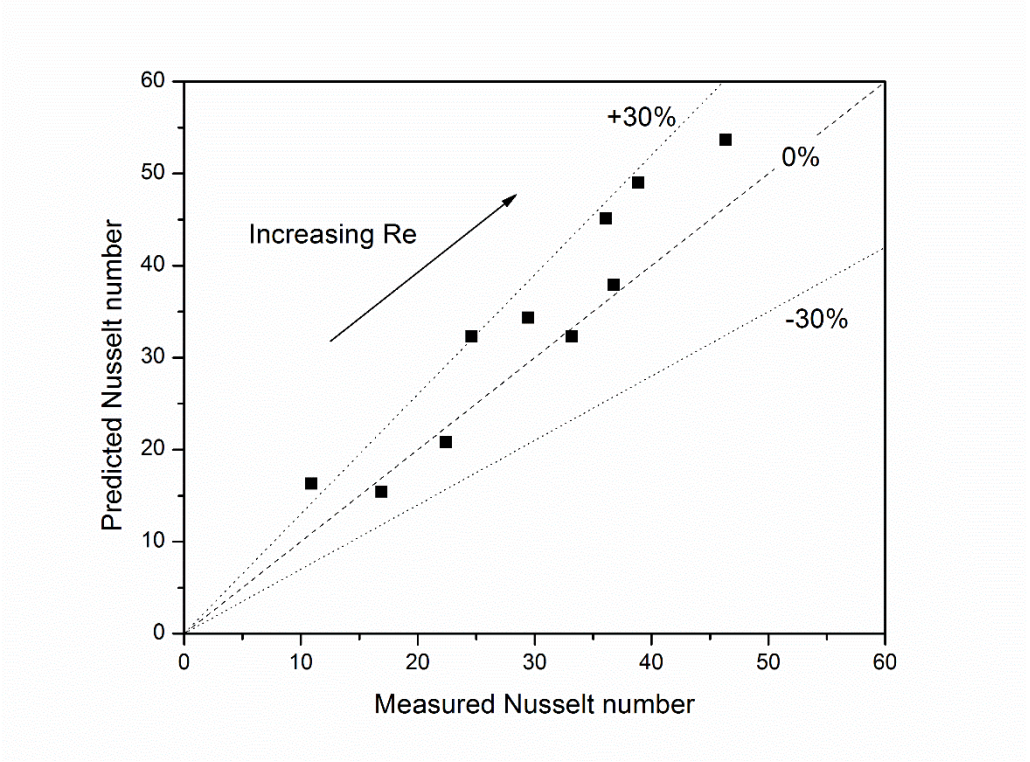

Figure 9-5: Predicted Nusselt number against measured Nusselt number (D series)

9.3 Thorn Height (*e*) to Mean Channel Height (*H*) Ratio Study

9.3.1 Thermal Considerations

Similar to the phenomena with the scale-inspired microchannel series, Nusselt number increases with Reynolds number and *e*/*H* ratio for the D microchannel series. In addition, Figure 9-6 shows that an increase in thorn height relative to mean channel height promotes early laminar-to-turbulent flow transition. The critical Reynolds number is 2,200, 1,500, 1,000 and 750, respectively, for the D microchannels with *e*/*H* ratio of 0.1, 0.3, 0.5, and 0.7. This postulation is also supported by the flow characteristics, as will be discussed using Figure 9-15 in Section 9.3.2.

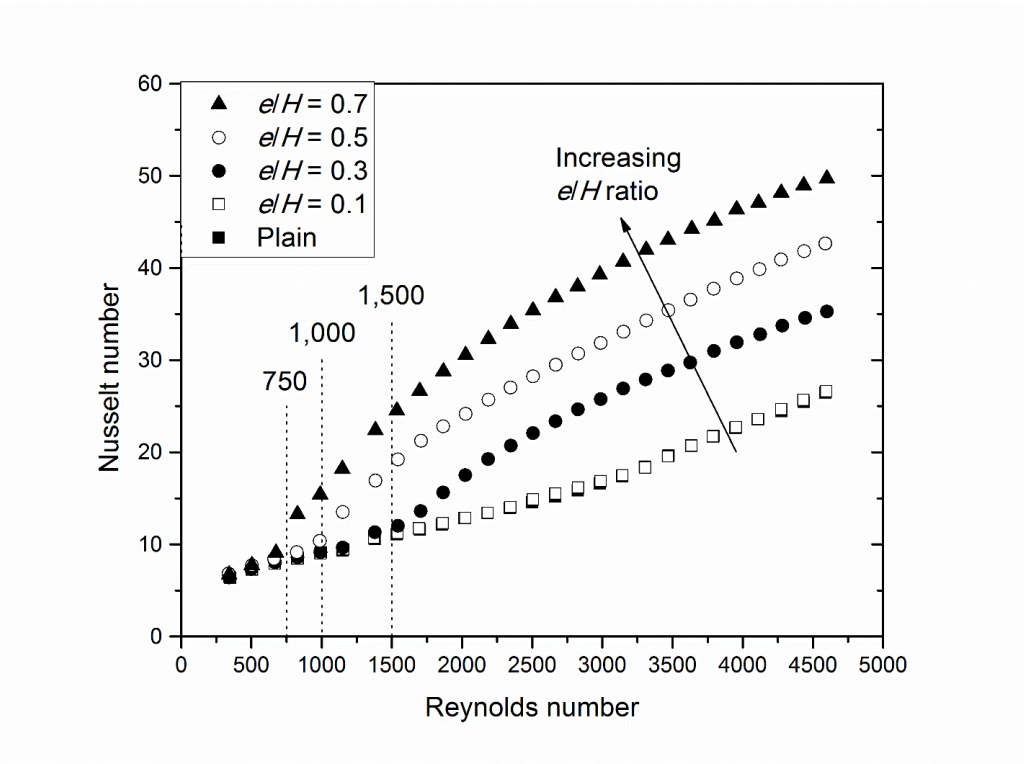

Figure 9-6: Nusselt number against Reynolds number, for different *e*/*H* ratio (D series)

As shown in Figure 9-7, the D microchannel with *e*/*H* ratio of 0.7 is observed to achieve a Nusselt number of up to nearly 2.5 times that of the Plain microchannel. The variation of normalised Nusselt number with Reynolds number is similar to that discussed for the scale-inspired microchannel series.

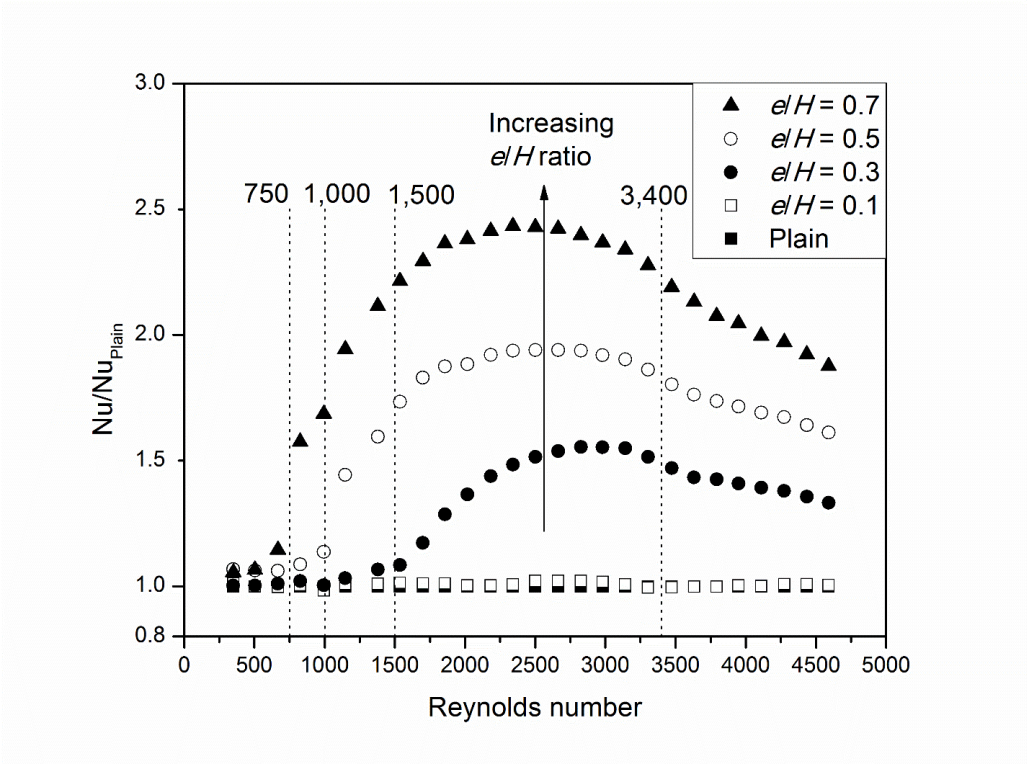

Figure 9-7: Normalised Nusselt number against Reynolds number, for different *e*/*H* ratio (D series)

As shown in Figure 9-8, the Nusselt number increases from 16 to 37, respectively, when the *e*/*H* ratio increases from 0.1 to 0.7 at *Re*≈2,664. Since the heat transfer enhancement mechanisms are similar to that for the scale-inspired microchannel series, the flow field and temperature distribution for the Plain microchannel and D microchannels with *e*/*H* ratio of 0.1 and 0.7 are presented in Figures D-1 to D-6 in Appendix D instead.

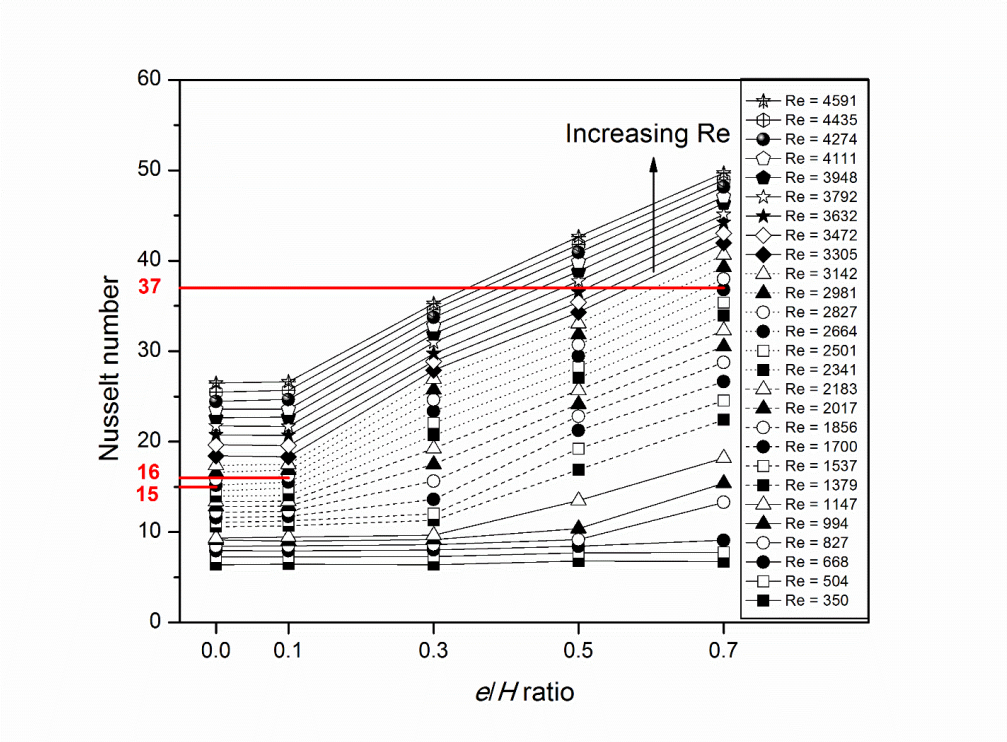

Figure 9-8: Nusselt number against *e*/*H* ratio, at different Reynolds number (D series)

Comparing across the three microchannel series, the Nusselt number is 37, 33 and 37, respectively, for the IFS, FS and D microchannel profiles with *e*/*H* ratio of 7 at *Re*≈2,664. This can be explained by comparing the corresponding flow fields and temperature distributions, as shown in Figures 9-9 to 9-14. As explained in the earlier sections, the IFS profile induces a high maximum fluid velocity of 7.5 m/s, which results in a high Nusselt number of 37.

On the other hand, the FS and D profiles incur a comparable maximum fluid velocity at about 6.65 m/s, as shown in Figures 9-10 and 9-11. However, a close examination of the D flow field reveals that the flow channel contracts and expands in a more gradual manner due to the wavy D profile. As a result, the D microchannel has a larger region of higher bulk fluid velocity both upstream and downstream of the thorn tip, as characterised by the yellow and orange colour contours in Figure 9-11. This results in a larger region of thinner thermal boundary layer, as illustrated in Figure 9-14, and therefore a higher Nusselt number for the D microchannel. On the other hand, the FS profile has a smaller

region of higher bulk fluid velocity due to the expansion of the flow channel downstream of the scale tip. This results in a smaller region of thinner thermal boundary layer, as illustrated in Figure 9-13, and therefore lower Nusselt number for the FS microchannel.

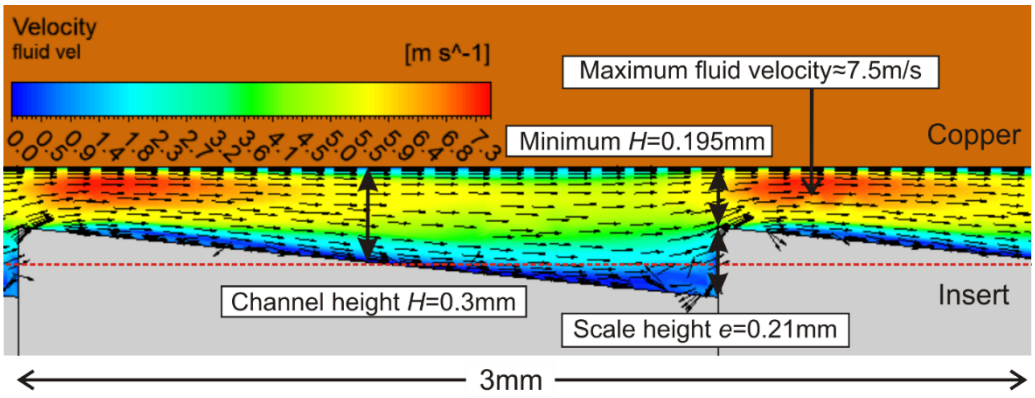

Figure 9-9: Flow field of IFS microchannel with *e*/*H* ratio of 0.7 at *Re* ≈ 2,664

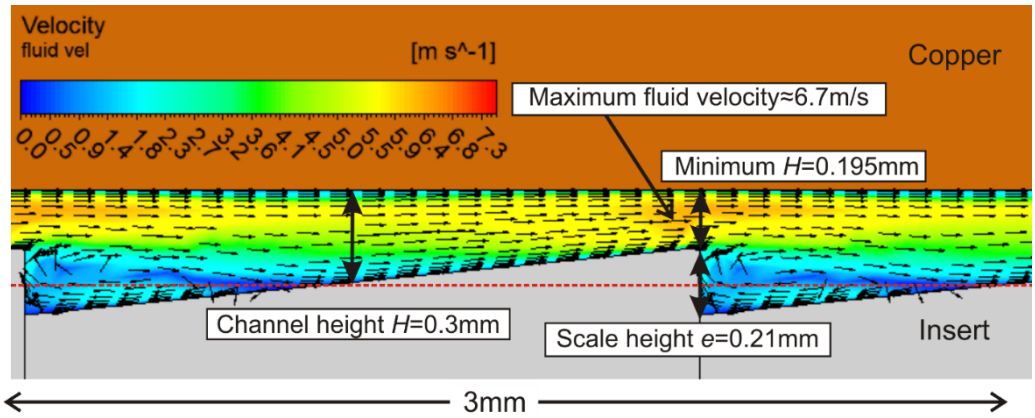

Figure 9-10: Flow field of FS microchannel with *e*/*H* ratio of 0.7, at *Re* ≈ 2,664

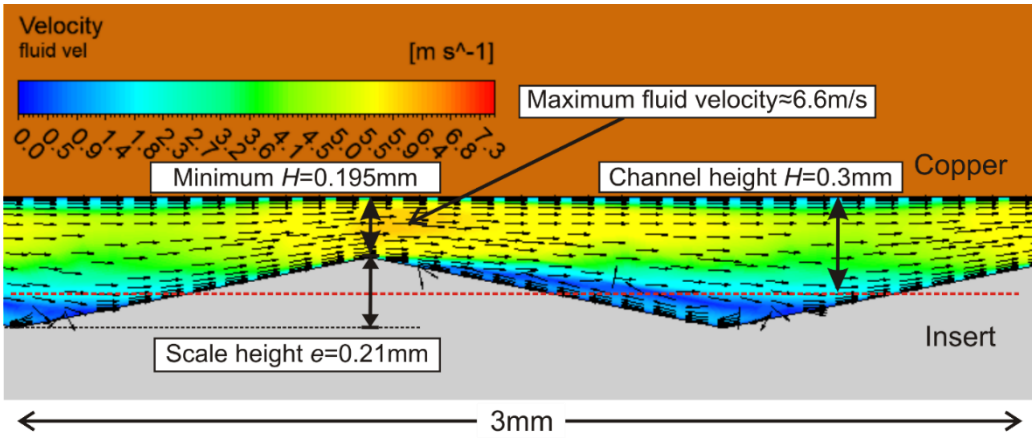

Figure 9-11: Flow field of D microchannel with *e*/*H* ratio of 0.7, at *Re* ≈ 2,664

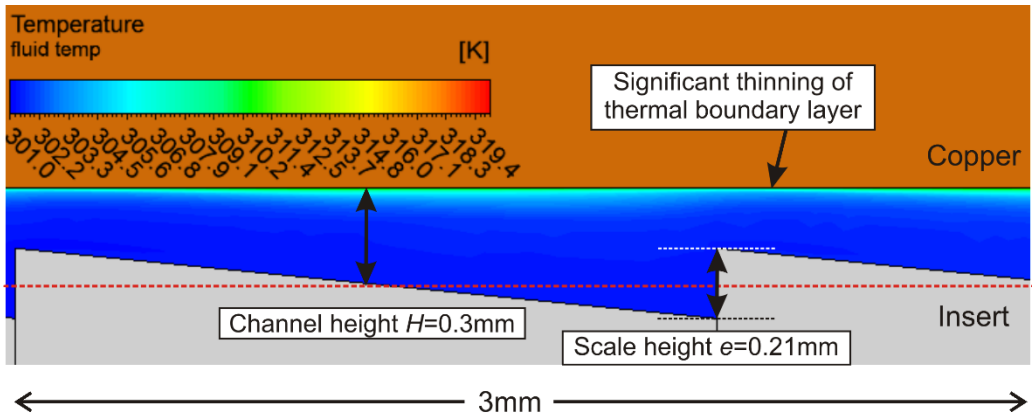

Figure 9-12: Temperature distribution of IFS microchannel with *e*/*H* ratio of 0.7, at *Re* ≈ 2,664

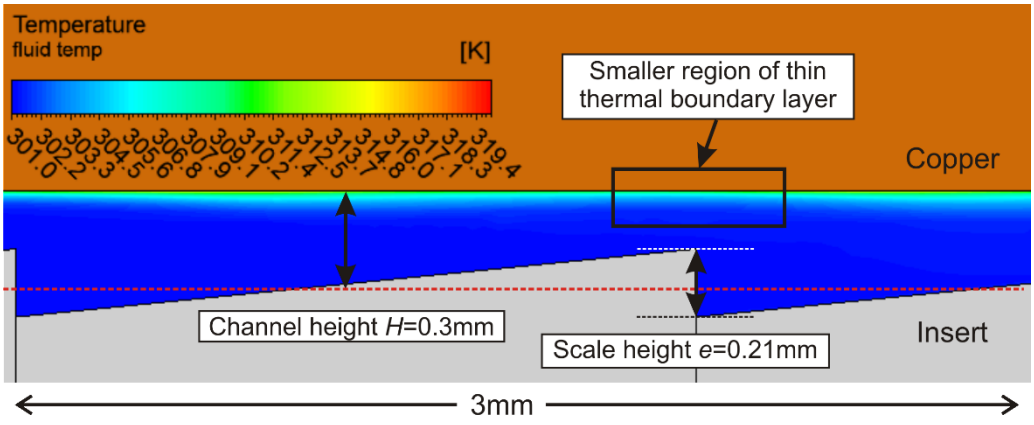

Figure 9-13: Temperature distribution of FS microchannel with *e*/*H* ratio of 0.7, at *Re* ≈ 2,664

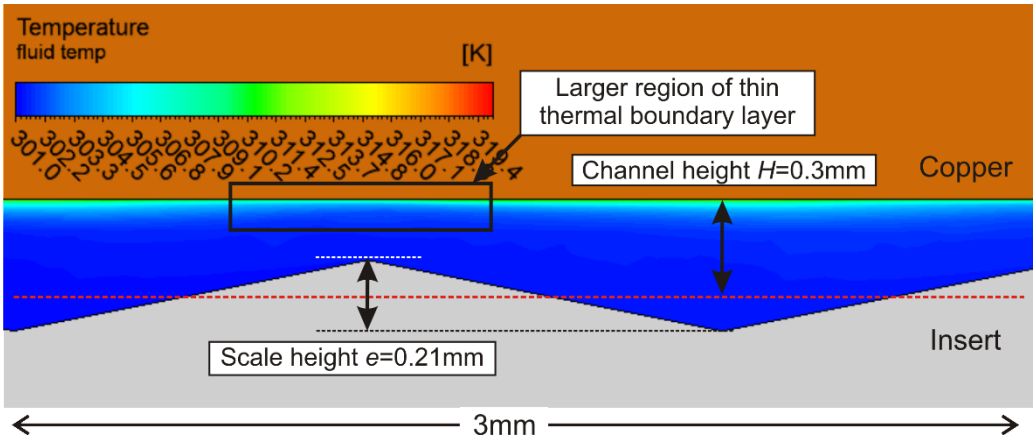

Figure 9-14: Temperature distribution of D microchannel with *e*/*H* ratio of 0.7, at *Re* ≈ 2,664

9.3.2 Hydrodynamic Considerations

As shown in Figure 9-15, the D_*e*0.21-*P*2.1 profile yields a maximum friction factor of 0.56, at Reynolds number of 350. This value is lower than those of the scale-inspired microchannel series, where the FS_*e*0.21-*P*2.1 and IFS_*e*0.21-*P*2.1 profiles yield 0.58 and 0.73, respectively, at the same flow condition.

As listed in Section 9.3.1, the critical Reynolds number is 2,200, 1,500, 1,000 and 750, respectively, for the D profile with *e*/*H* ratio of 0.1, 0.3, 0.5, and 0.7. This is supported by the change in flow behaviour in Figure 9-15. Additionally, the D microchannel with *e*/*H* ratio of 0.1 is observed to resemble the flow characteristics of the Plain microchannel up to Reynolds number of 3,400, beyond which the friction factor becomes slightly higher. This is because at higher Reynolds numbers, the flow disturbances caused by the thorn protrusions, albeit of a low height, are amplified by the dominant inertia forces.

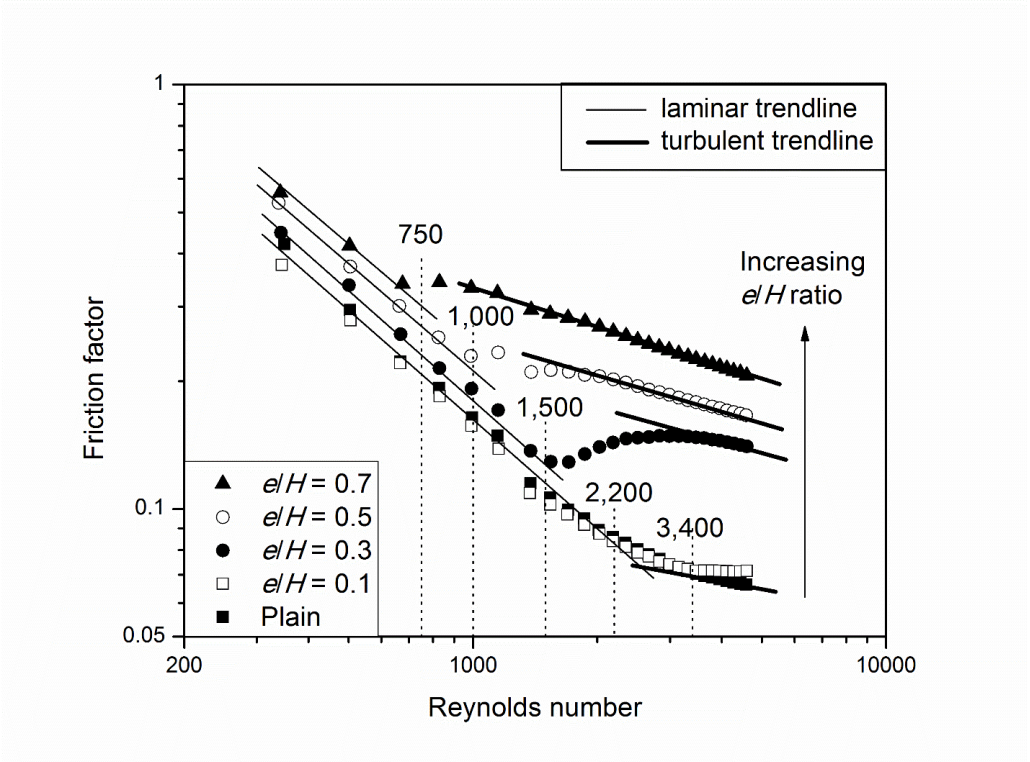

Figure 9-15: Friction factor against Reynolds number, for different *e*/*H* ratio (D series)

Referring to Figure 9-16, the normalised friction factor for the D series is visibly low, using the same y-axis range of 0 to 8 throughout the thesis. In particular, the maximum normalised friction factor is only 3.2.

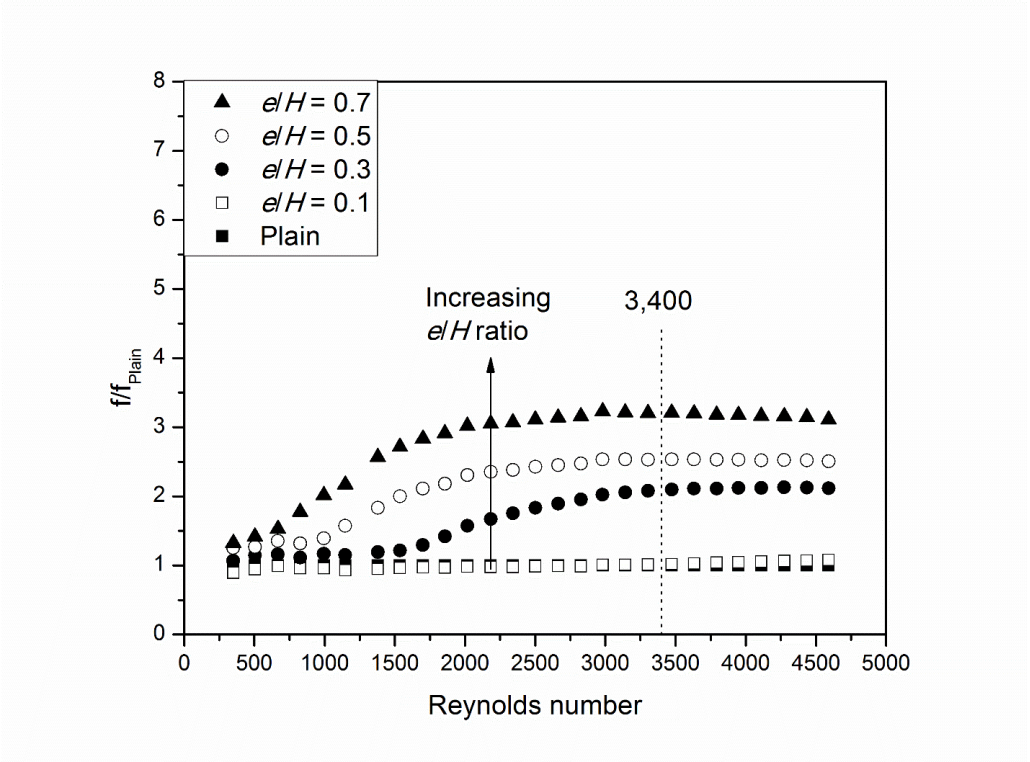

Figure 9-16: Normalised Friction factor against Reynolds number, for different *e*/*H* ratio (D series)

Figure 9-17 shows that the friction factor increases from 0.08 to 0.25, when the *e*/*H* ratio increases from 0.1 to 0.7 at *Re*≈2,664. The increase of friction factor with *e*/*H* ratio has been explained in earlier sections using the scale-inspired microchannel series. The supporting velocity distributions for the D microchannel series can be found in Figures D-7 to D-9 in Appendix D.

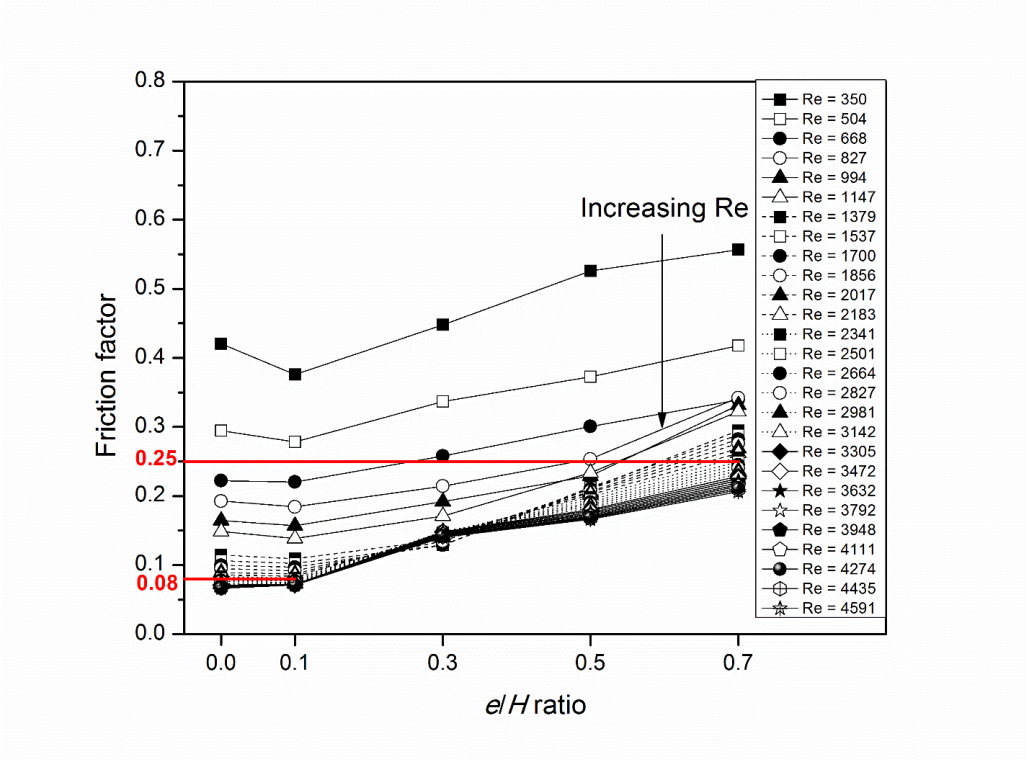

Figure 9-17: Friction factor against *e*/*H* ratio, at different Reynolds number (D series)

In addition, the friction factor is 0.36, 031 and 0.25, respectively, for the IFS, FS and D profiles with *e*/*H* ratio of 0.7 at *Re*≈2,664. The lowest friction factor for the D microchannel is likely due to the more gradual wavy profile, which causes the least pressure drop as can be seen from the pressure distribution presented in Figure 9-20. On the other hand, the flow disruptions caused by the sudden flow channel constriction/expansion in the IFS/FS microchannel result in a larger pressure drop, as can be seen from the pressure distributions presented in Figures 9-18 and 9-19.

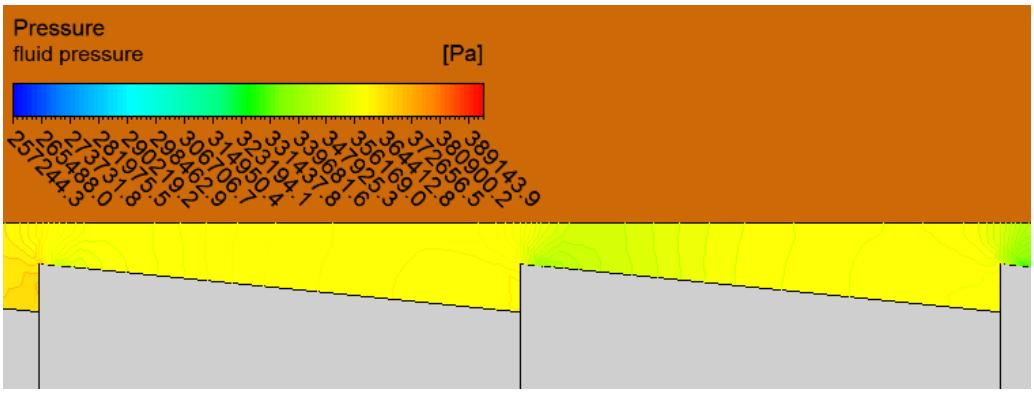

Figure 9-18: Pressure distribution of IFS microchannel with *e*/*H* ratio of 0.7 at *Re* ≈ 2,664

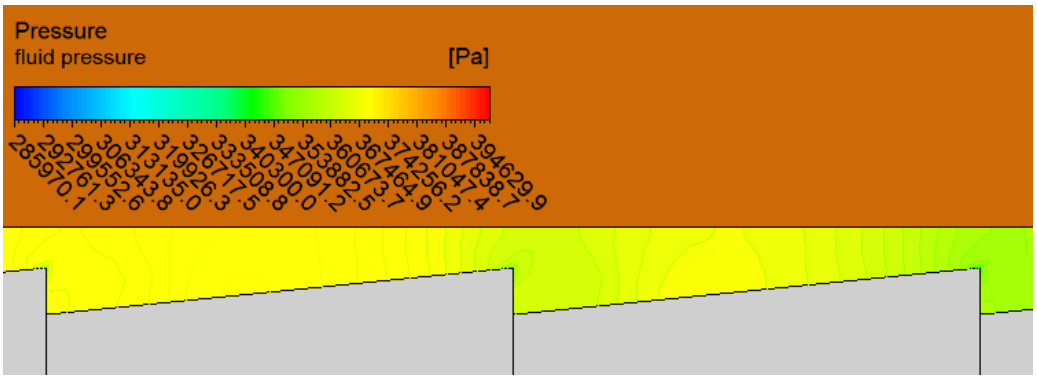

Figure 9-19: Pressure distribution of FS microchannel with *e*/*H* ratio 0.7, at *Re* ≈ 2,664

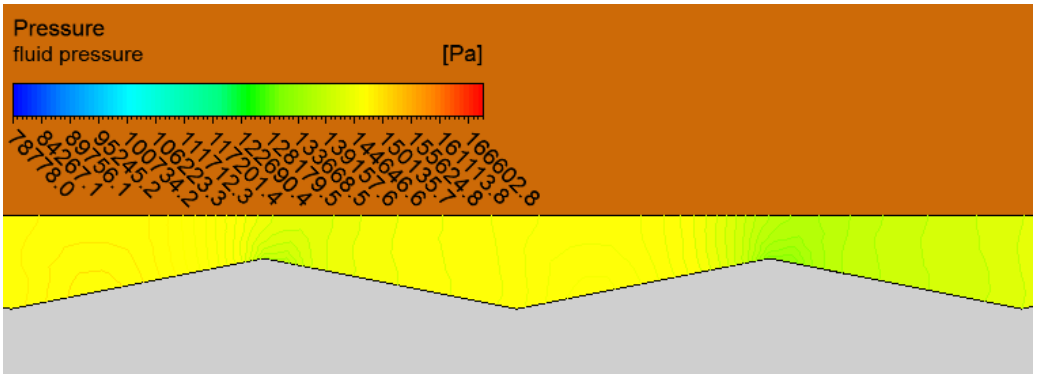

Figure 9-20: Pressure distribution of D microchannel with *e*/*H* ratio 0.7, at *Re* ≈ 2,664

9.3.3 Thermo-hydraulic Performance

Once again, this parametric study concludes that the largest *e*/*H* ratio of 0.7 exhibits the highest thermo-hydraulic performance, as shown in Figure 9-21. Given a fixed heat transfer surface area and pumping power, the D microchannel with *e*/*H* ratio of 0.7 improves the heat transfer capacity by 67% relative to the Plain microchannel, at Reynolds number of 2,350.

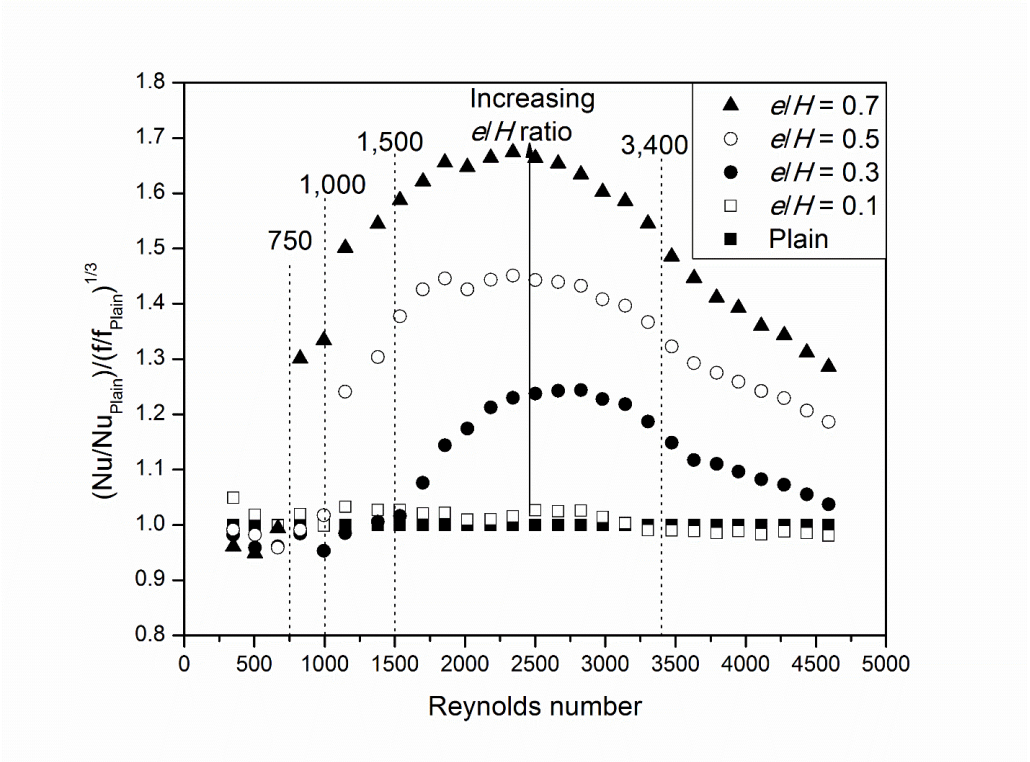

Figure 9-21: Thermo-hydraulic performance against Reynolds number, for different *e*/*H* ratio (D series)

9.4 Thorn Pitch (*P*) to Thorn Height (*e*) Ratio Study

9.4.1 Thermal Considerations

As shown in Figure 9-22, the maximum Nusselt number achieved is 43, at Reynolds number of 4,110 using the D microchannel with *P*/*e* ratio of 5. The critical Reynolds number is 800, 1,000, 1,500, 1,800, respectively, for the D microchannels with *P*/*e* ratio of 5, 10, 15 and 20. This indicates that the increase in number of thorn protrusions helps to promote early laminar-to-turbulent flow transition. This postulation is also supported by the flow characteristics, as will be discussed using Figure 9-25 in Section 9.4.2.

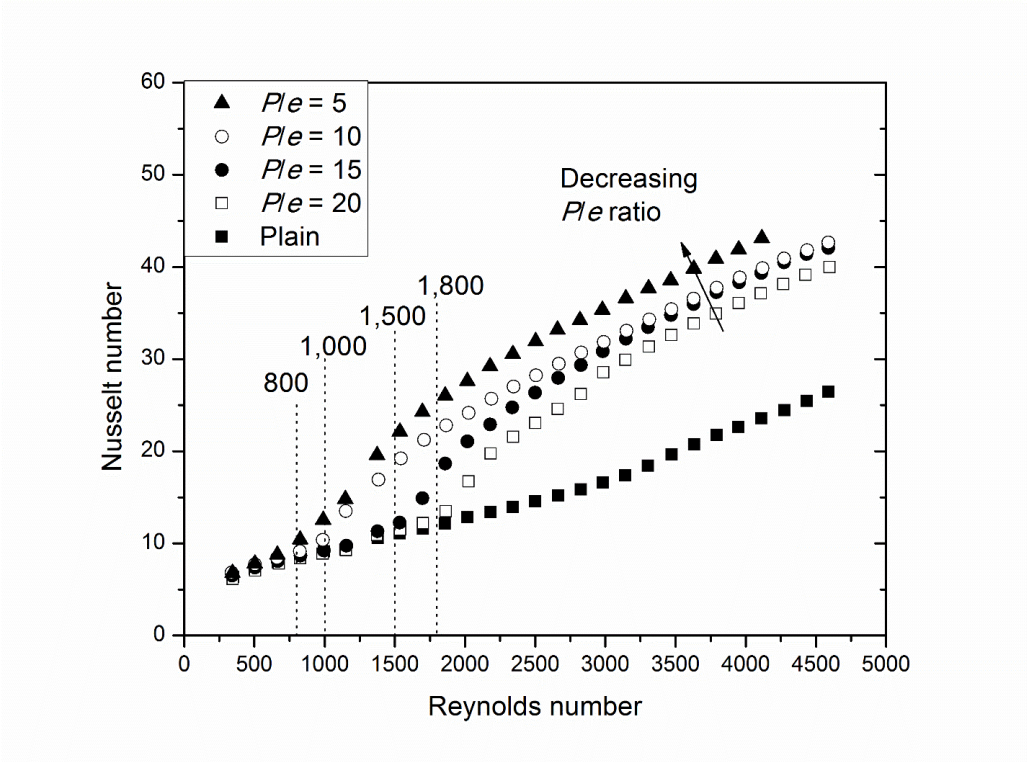

Figure 9-22: Nusselt number against Reynolds number, for different *P*/*e* ratio (D series)

Using the same y-axis range of 0.8 to 3.0 throughout the thesis, Figure 9-23 shows that the normalised Nusselt number is moderately high in the *P*/*e* ratio study for the D microchannel series. The D microchannel with *P*/*e* ratio of 5 is observed to achieve a Nusselt number of up to 2.2 times that of the Plain microchannel. For the same *P*/*e* ratio and within the same range of Reynolds number from 350 to 3,948, the normalised Nusselt number of the FS and IFS microchannels are 1.9 and 2.6, respectively,

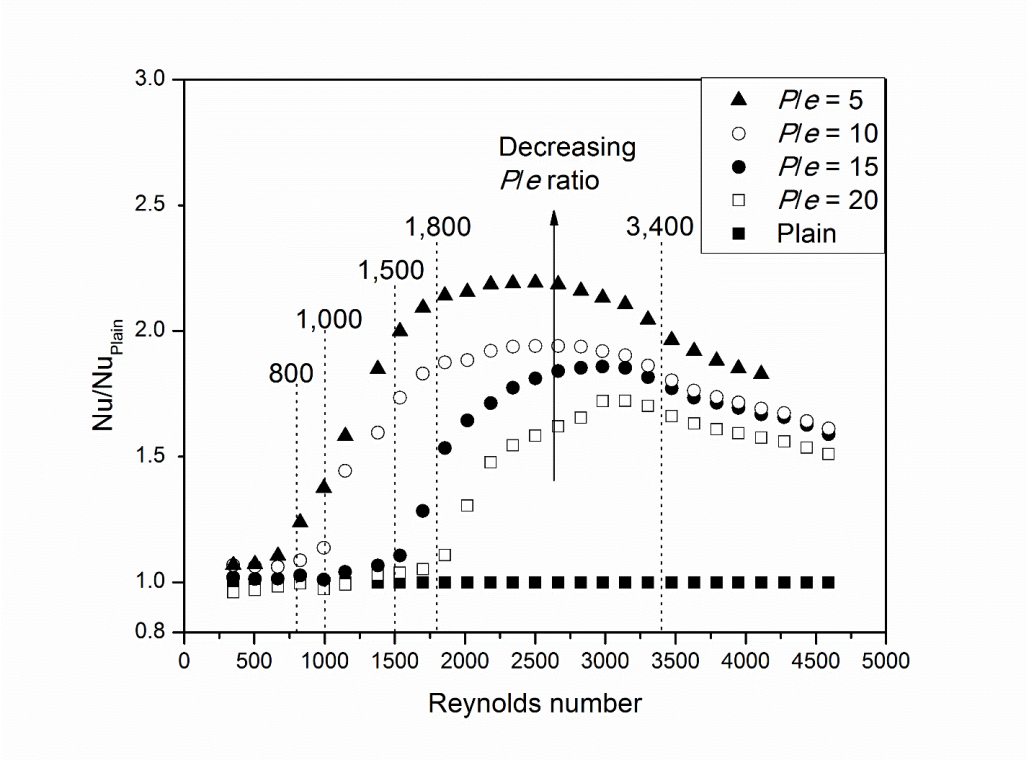

Figure 9-23: Normalised Nusselt number against Reynolds number, for different *P*/*e* ratio (D series)

Figure 9-24 shows that Nusselt number increases from 25 to 33, when the *P*/*e* ratio decreases from 20 to 5, at Reynolds number≈2,664. Since the heat transfer enhancement mechanisms are similar to that for the IFS microchannel series, the flow field and temperature distribution for the D microchannels with *P*/*e* ratio of 20 and 5 are thus presented in Figures D-10 to D-13 in Appendix D.

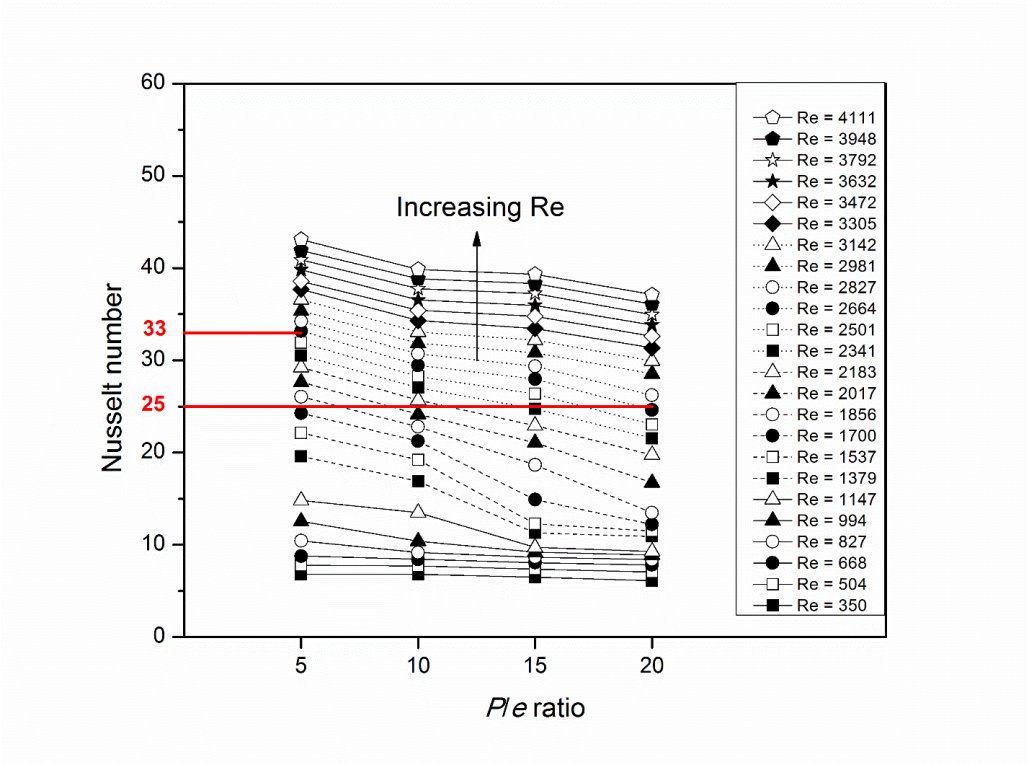

Figure 9-24: Nusselt number against *P*/*e* ratio, at different Reynolds number (D series)

9.4.2 Hydrodynamic Considerations

The friction factor variation, as presented in Figure 9-25, shows that the critical Reynolds number for each D profile matches those listed in Section 9.4.1. It is also observed that the D_*e*0.15-*P*0.75 profile yields a maximum friction factor of 0.55, at Reynolds number of 350. This value is lower than those of the scale-inspired microchannel series, where the FS_*e*0.15-*P*0.75 and IFS_*e*0.15-*P*0.75 profiles yield 0.63 and 0.73, respectively, at the same flow condition. In other words, the D profile with *P*/*e* ratio of 5 exhibits the lowest friction factor at lower Reynolds numbers. This is likely due to the more gradual wavy profile, as explained earlier in Section 9.3.2.

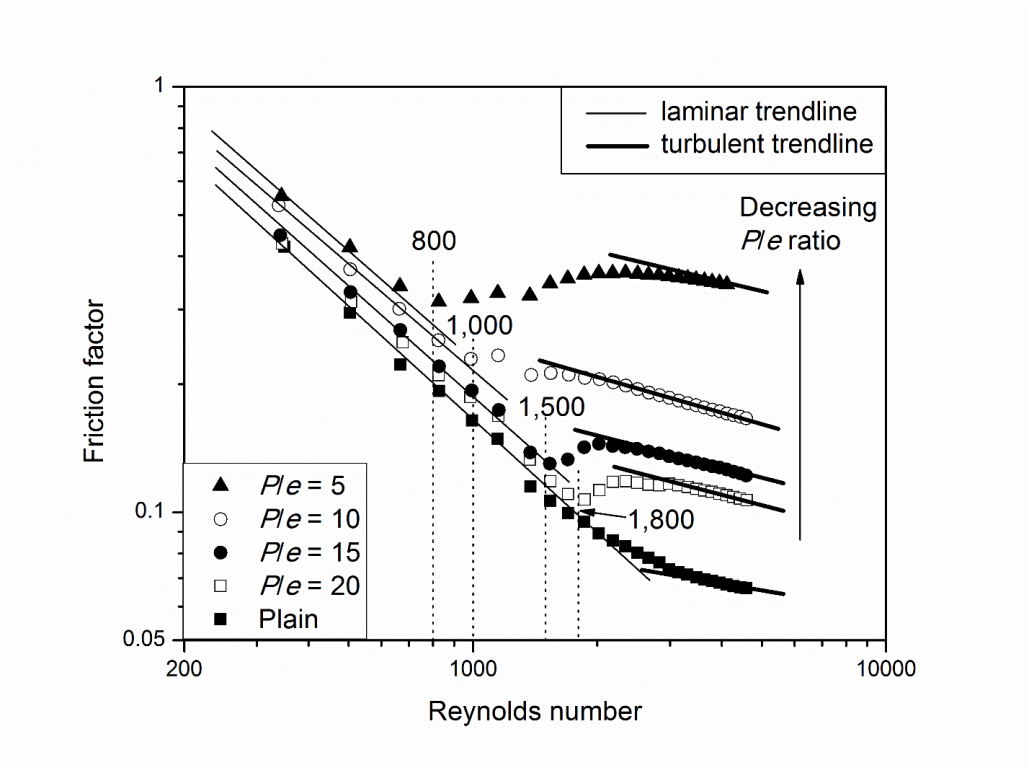

Figure 9-25: Friction factor against Reynolds number, for different *P*/*e* ratio (D series)

However, the D profile with *P*/*e* ratio of 5 does not exhibit the lowest friction factor at higher Reynolds numbers. Figure 9-26 shows that the normalised friction factor for the D profile with *P*/*e* ratio of 5 is moderately high, with a value of 5.1 at *Re*≈3948. While it is lower than the value of 6.7 for the IFS profile, it is higher than the value of 4.2 for the FS profile, at the same flow conditions. Hence, it appears that increasing the number of thorn protrusions by decreasing the *P*/*e* ratio has a strong effect in increasing the friction factor at higher Reynolds numbers.

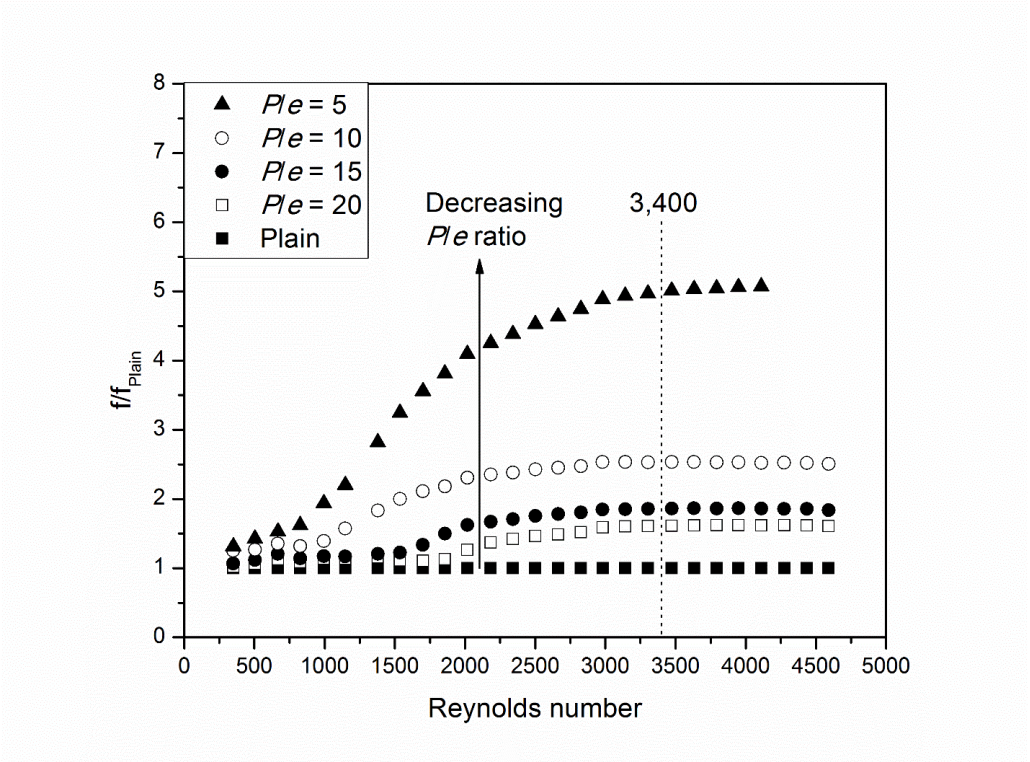

Figure 9-26: Normalised friction factor against Reynolds number, for different *P*/*e* ratio (D series)

The strong influence of the number of thorns on friction factor for the D microchannel series is analysed using the numerical results. The pressure distributions for the IFS, D and FS microchannel with *P*/*e* ratio of 5 at *Re*≈2,664 are respectively presented in Figures 9-27 to 9-29. It is observed that the region of pressure recovery for the D microchannel becomes smaller when there are more thorn protrusions. Since the pressure recovery for the D microchannel is less than that for the FS microchannel, the friction factor for the D microchannel is higher than that of the FS microchannel.

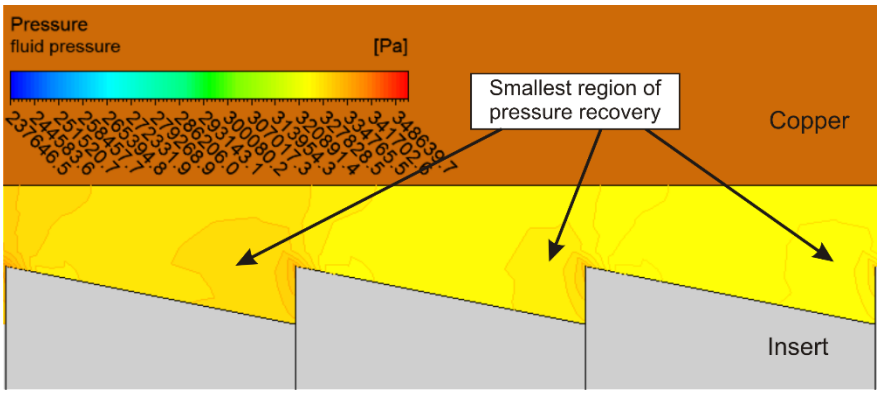

Figure 9-27: Pressure distribution of IFS microchannel with *P*/*e* ratio of 5, at *Re* ≈ 2,664

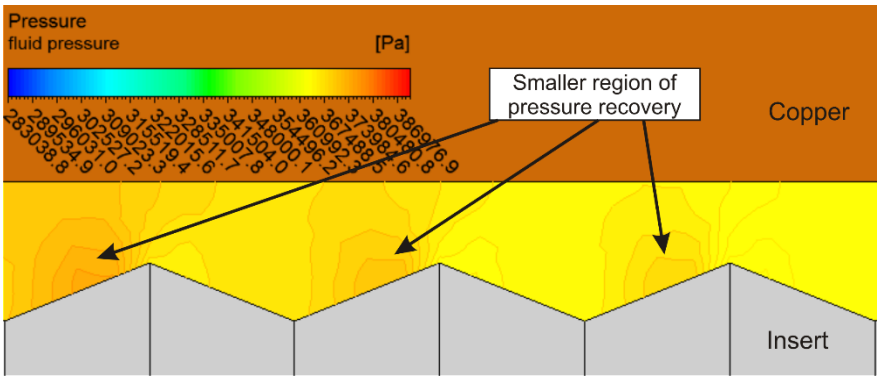

Figure 9-28: Pressure distribution of D microchannel with *P*/*e* ratio of 5, at *Re* ≈ 2,664

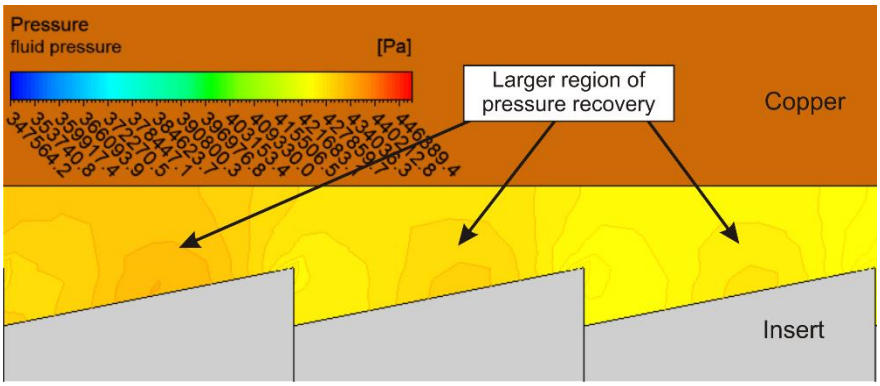

Figure 9-29: Pressure distribution of FS microchannel with *P*/*e* ratio of 5, at *Re* ≈ 2,664

Similarly, the friction factor is observed to increase when *P*/*e* ratio decreases for the D microchannel series, as shown in Figure 9-30. For example, the friction factor increases from 0.12 to 0.36, when the *P*/*e* ratio decreases from 20 to 5, at Reynolds number≈2,664. The figures illustrating the velocity boundary layers for the D microchannels with *P*/*e* ratio of 20 and 5 are presented in Figures D-14 and D-15 in Appendix D.

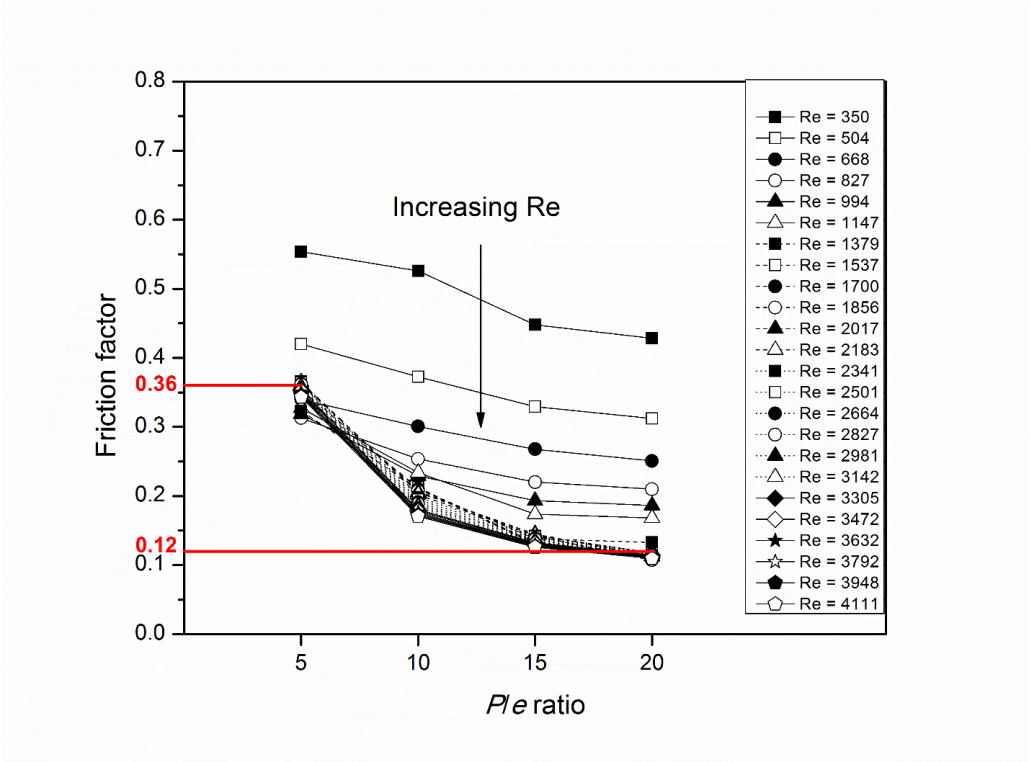

Figure 9-30: Friction factor against *P*/*e* ratio, at different Reynolds number (D series)

9.4.3 Thermo-hydraulic Performance

Figure 9-31 shows that there is no clear relationship between thermo-hydraulic performance and *P*/*e* ratio, at constant Reynolds numbers. This is contrary to a distinct relationship for the IFS microchannel series, where a smaller *P*/*e* ratio corresponds to a higher thermo-hydraulic performance at lower Reynolds numbers, and that for the FS microchannel series, where a larger *P*/*e* ratio corresponds to a higher thermo-hydraulic performance at higher Reynolds numbers. The D microchannel series seems to display both aforementioned characteristics. The D microchannel with *P*/*e* ratio of 15 performs the best at *Re*≈2,750. Given a fixed heat transfer surface area and pumping power, this D profile improves the heat transfer capacity by 52% relative to the Plain profile, at Reynolds number of 2,750. This could be due in part to the relatively low friction losses while the Nusselt number remains relatively high.

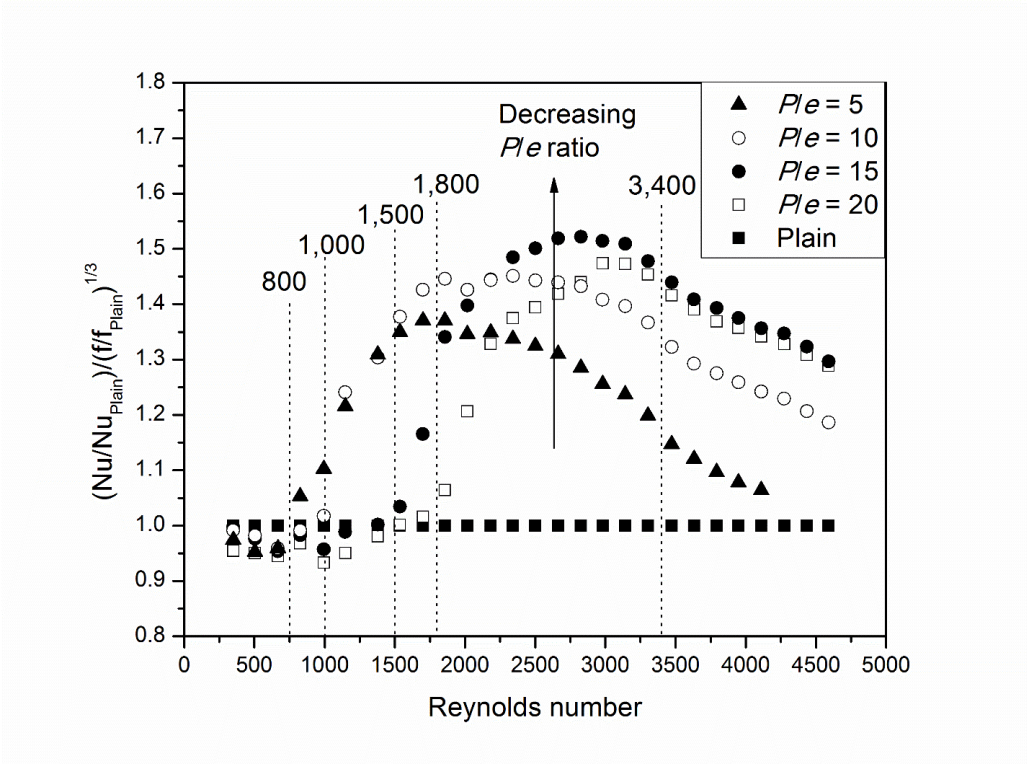

Figure 9-31: Thermo-hydraulic performance against Reynolds number, for different *P*/*e* ratio (D series)

Chapter 10 New Correlations

This chapter presents the newly proposed working correlations to evaluate the average Nusselt number and friction factor for the nature-inspired enhanced microchannels. Both the laminar and turbulent flow regimes are discussed. The mathematical form of the new correlations follows that of existing classical correlations, but with an additional term added to account for the effect of the scale or thorn protrusions. The correlations are formulated based on about 600 steady-state measurements, as well as the underlying physics which governs the heat transfer and flow behaviours, within the scope of investigation. These correlations are useful in the design of compact microchannel heat exchangers.

10.1 Proposed Correlations for Average Nusselt Number

10.1.1 Laminar Flow Regime

As discussed in Section 6.3, the Shah and London's correlation for circular pipes, as presented using Eqn. (2-28) in Section 2.1.3.2, can be used to predict the Nusselt number for the Plain microchannel in the laminar flow regime. The Reynolds number range for the laminar flow regime has been identified as $350 \lesssim Re \lesssim 2{,}200$ in Section 6.4.

For the Inverted Fish Scale (IFS) series, the IFS profile with e/H ratio of 0.1 exhibits similar heat transfer behaviour to that of the Plain microchannel for $350 \lesssim Re \lesssim 2{,}200$. The other six profiles exhibit early laminar-to-turbulent flow transition at $Re \approx 600$. Hence, the heat transfer behaviour can be largely predicted by the correlation proposed for the turbulent flow regime in Section 10.1.2.

For the Fish Scale (FS) series, the FS profiles with *e*/*H* ratio of 0.1, 0.3, 0.5, and 0.7 exhibit laminar-to-turbulent flow transition at Reynolds number of about 2,200, 1,850, 1,300 and 700, respectively. The FS profiles with *P*/*e* ratio of 20, 15, 10 and 5 exhibit laminar-to-turbulent flow transition at Reynolds number of about 1,600, 1,600, 1,300 and 800, respectively. Before the onset of transition at the respective critical Reynolds number, the FS profiles exhibit similar heat transfer behaviour to that of the Plain microchannel in the laminar flow regime.

For the Durian (D) series, the D profiles with *e*/*H* ratio of 0.1, 0.3, 0.5, and 0.7 exhibit laminar-to-turbulent flow transition at Reynolds number of about 2,200, 1,500, 1,000 and 750, respectively. The D profiles with *P*/*e* ratio of 20, 15, 10 and 5 exhibit laminar-to-turbulent flow transition at Reynolds number of about 1,800, 1,500, 1,000 and 800, respectively. Before the onset of transition at the respective critical Reynolds number, the D profiles also exhibit similar heat transfer behaviour to that of the Plain microchannel in the laminar flow regime.

Since the enhanced microchannels exhibit similar heat transfer behaviour to that of the Plain microchannel in the laminar flow regime, which can be predicted by the Shah and London's correlation for circular pipes, there is no need to propose any new Nusselt number correlations for the laminar flow regime. For the purpose of convenience, Table 10-1 re-presents the Shah and London's correlation for circular pipes. The applicable Reynolds number ranges for the enhanced microchannels are listed in Table 10-2.

Table 10-1: Nusselt number correlation for laminar flow regime

Thermal conditions	Correlation	Applicable range
Thermally developing, constant q_s	$\overline{Nu} = 1.953(Re\ Pr\ D_h/L)^{1/3}$ **Shah and London, 1978** [18]	$Re\ Pr\ D_h/L \geq 33.3$ $Re < 2{,}200$

Table 10-2: Applicable *Re* range of Nusselt number correlation for laminar flow regime

e/*H* ratio	*P*/*e* ratio	Reynolds number range		
		IFS series	FS series	D series
0.1	10	350≲*Re*≲2,200	350≲*Re*≲2,200	350≲*Re*≲2,200
0.3	10	-	350≲*Re*≲1,850	350≲*Re*≲1,500
0.5	10	-	350≲*Re*≲1,300	350≲*Re*≲1,000
0.7	10	-	350≲*Re*≲700	350≲*Re*≲750
0.5	20	-	350≲*Re*≲1,600	350≲*Re*≲1,800
0.5	15	-	350≲*Re*≲1,600	350≲*Re*≲1,500
0.5	5	-	350≲*Re*≲800	350≲*Re*≲800

10.1.2 Turbulent Flow Regime

As discussed in Section 6.3, the Gnielinski's correlation, as presented using Eqn. (2-34) in Section 2.1.3.2, is sufficient as a first approximation to predict the Nusselt number for the Plain microchannel in the turbulent flow regime. The Reynolds number range for the turbulent flow regime has been identified as 3,400≲*Re*≲4,600 in Section 6.4. However, the Gnielinski's correlation is relatively complex, and a simpler form as presented in Eqn. (10-1) has been suggested and used by several resources [12,14,17,166]. The terms outside the square brackets represent the general expression for Nusselt number in fully-developed internal turbulent flow, and A, B and C are coefficients to be determined. The last term within the square brackets accounts for the entrance effect, since the entrance length is a function of L/D_h, while D is another coefficient to be determined.

$$Nu_{Plain,turbulent} = ARe^{B}Pr^{C}\left[1+\frac{D}{L/D_h}\right] \quad (10\text{-}1)$$

A non-linear least-squares curve-fitting approach is performed on the measured Nusselt number data for the Plain microchannel in the range 3,400≲*Re*≲4,600. The Nusselt number correlation for the Plain microchannel is then proposed as follows:

$$Nu_{Plain,turbulent} = 0.034Re^{0.7}Pr^{1/3}\left[1+\frac{7}{L/D_h}\right] \quad (10\text{-}2)$$

Applicable for: 3,400≲*Re*≲4,600;
Pr≈5.5;
L/D_h =50
Type of fluid: Single-phase water
Maximum discrepancy: 5%
Mean discrepancy: 3%

The proposed Nusselt number correlation for the Plain microchannel for turbulent flow serves as the basis for the derivation of new correlations for the enhanced microchannels. An additional term is added to account for the increase in Nusselt number due to the scale/thorn protrusions, which promote early laminar-to-turbulent flow transition and cause significant thinning of the velocity and thermal boundary layers. When the scale/thorn protrusion height (*e*) becomes zero, the Nusselt number correlation reduces to that for the Plain microchannel. The new Nusselt number correlation for the enhanced microchannels is of the form:

$$Nu_{profile} = 0.034Re^{0.7}Pr^{1/3}\left[1+\frac{7}{L/D_h}+\frac{E(e/H)^F}{(P/e)^G}\right] \quad (10\text{-}3)$$

where *e*/*H* refers to the scale/thorn height (*e*) to mean channel height (*H*) ratio, *P*/*e* refers to the scale/thorn pitch (*P*) to scale/thorn height (*e*) ratio, and E, F and G are coefficients to be determined.

A non-linear least-squares curve-fitting approach is performed on the measured Nusselt number for each of the three nature-inspired enhanced microchannel series in their respective turbulent regime. The Nusselt number correlation for the IFS microchannel series is proposed as follows:

$$Nu_{IFS} = 0.034Re^{0.7}Pr^{1/3}\left[1 + \frac{7}{L/D_h} + \frac{8(e/H)^{1.1}}{(P/e)^{0.6}}\right] \quad (10\text{-}4)$$

Applicable for: $Pr \approx 5.5$; $L/D_h = 50$
Type of fluid: Single-phase water
Maximum discrepancy: 16%
Mean discrepancy: 3%

The applicable Reynolds number range of the proposed correlation for each IFS microchannel profile is listed in Table 10-3.

Table 10-3: Applicable Reynolds number range for the Nu_{IFS} correlation in Eqn. (10-4)

***e*/*H* ratio**	***P*/*e* ratio**	***Re* range**
0.1	10	3,400≲*Re*≲4,600
0.3	10	350≲*Re*≲4,600
0.5	10	350≲*Re*≲4,600
0.7	10	350≲*Re*≲4,600
0.5	20	350≲*Re*≲4,600
0.5	15	350≲*Re*≲4,600
0.5	5	350≲*Re*≲4,600

The proposed Nusselt number correlation for the IFS microchannel series fits the measured values well, as illustrated in Figure 10-1 and Figure 10-2.

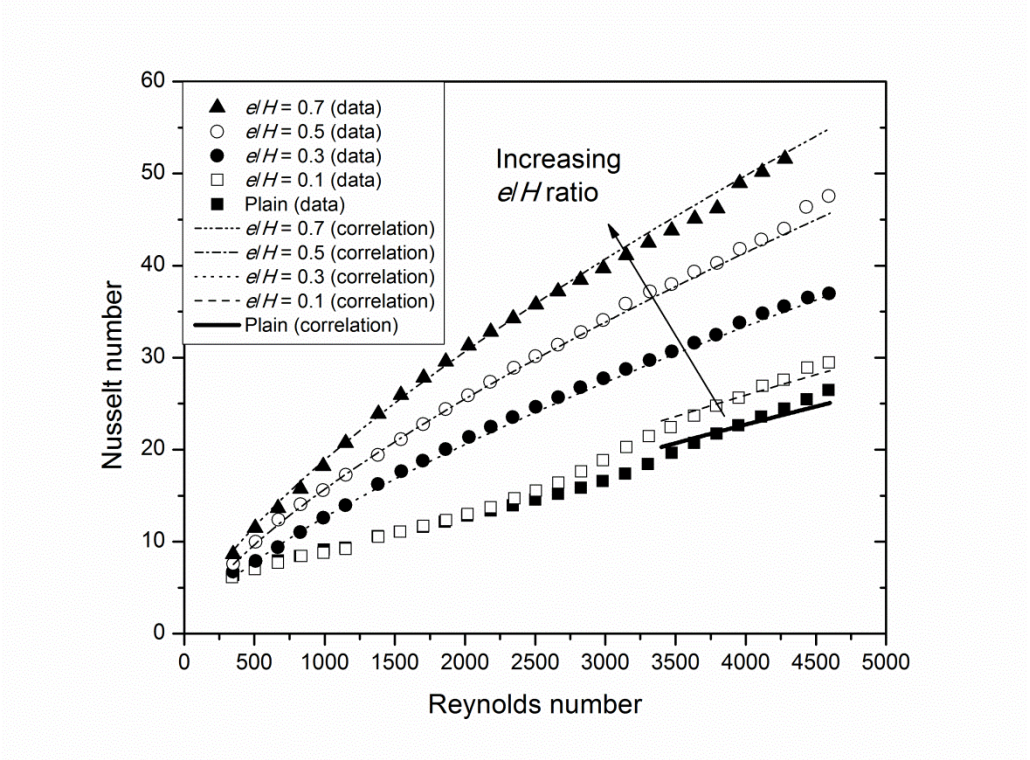

Figure 10-1: Proposed Nu_{IFS} correlation in Eqn. (10-4) applied to the e/H ratio study

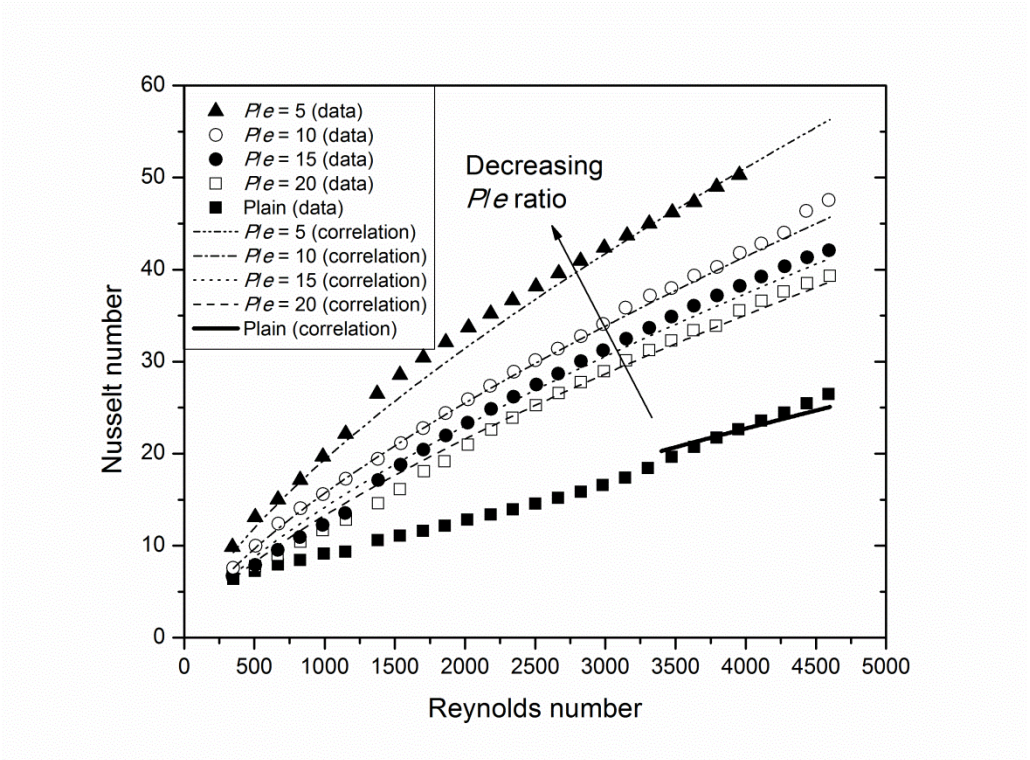

Figure 10-2: Proposed Nu_{IFS} correlation in Eqn. (10-4) applied to the P/e ratio study

The Nusselt number correlation for the FS microchannel series is proposed as follows:

$$Nu_{FS} = 0.034Re^{0.7}Pr^{1/3}\left[1 + \frac{7}{L/D_h} + \frac{2.75(e/H)^{1.5}}{(P/e)^{0.15}}\right] \quad (10\text{-}5)$$

Applicable for: $Pr \approx 5.5$; $L/D_h = 50$
Type of fluid: Single-phase water
Maximum discrepancy: 16%
Mean discrepancy: 4%

The applicable Reynolds number range of the proposed correlation for each FS microchannel profile is listed in Table 10-4.

Table 10-4: Applicable Reynolds number range for the Nu_{FS} correlation in Eqn. (10-5)

***e*/*H* ratio**	***P*/*e* ratio**	***Re* range**
0.1	10	3,400≲*Re*≲4,600
0.3	10	2,500≲*Re*≲4,600
0.5	10	1,600≲*Re*≲4,600
0.7	10	1,200≲*Re*≲4,600
0.5	20	2,200≲*Re*≲4,600
0.5	15	2,200≲*Re*≲4,600
0.5	5	1,600≲*Re*≲4,600

The proposed Nusselt number correlation for the FS microchannel series fits the measured values well, as illustrated in Figure 10-3 and Figure 10-4.

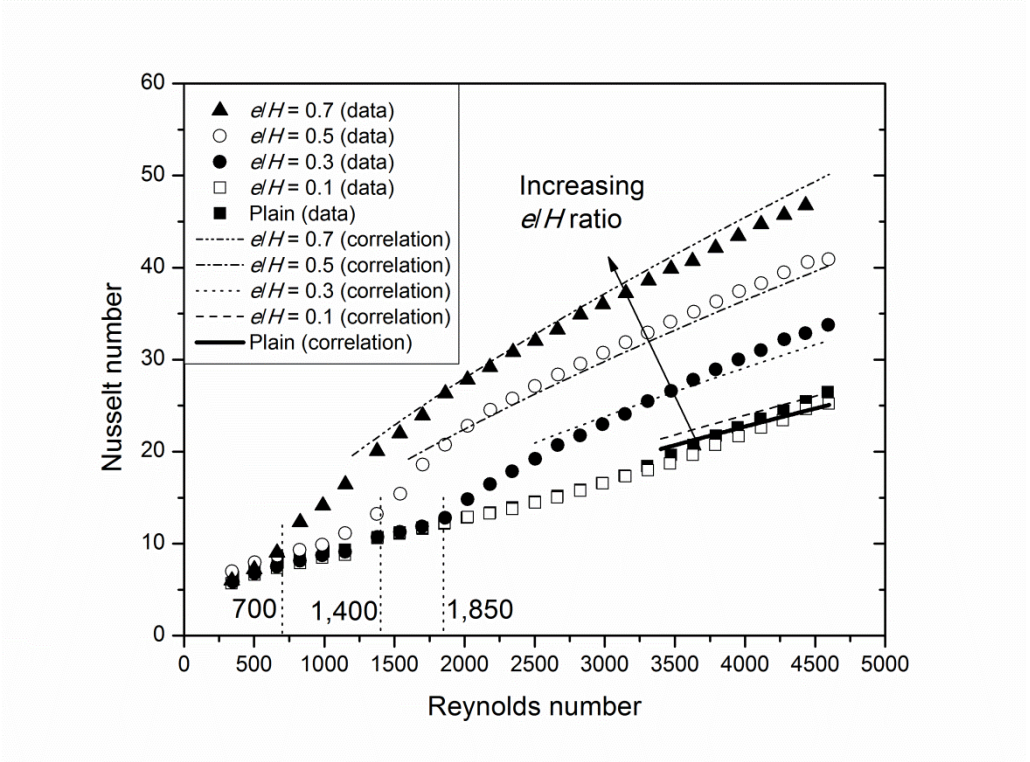

Figure 10-3: Proposed Nu_{FS} correlation in Eqn. (10-5) applied to the e/H ratio study

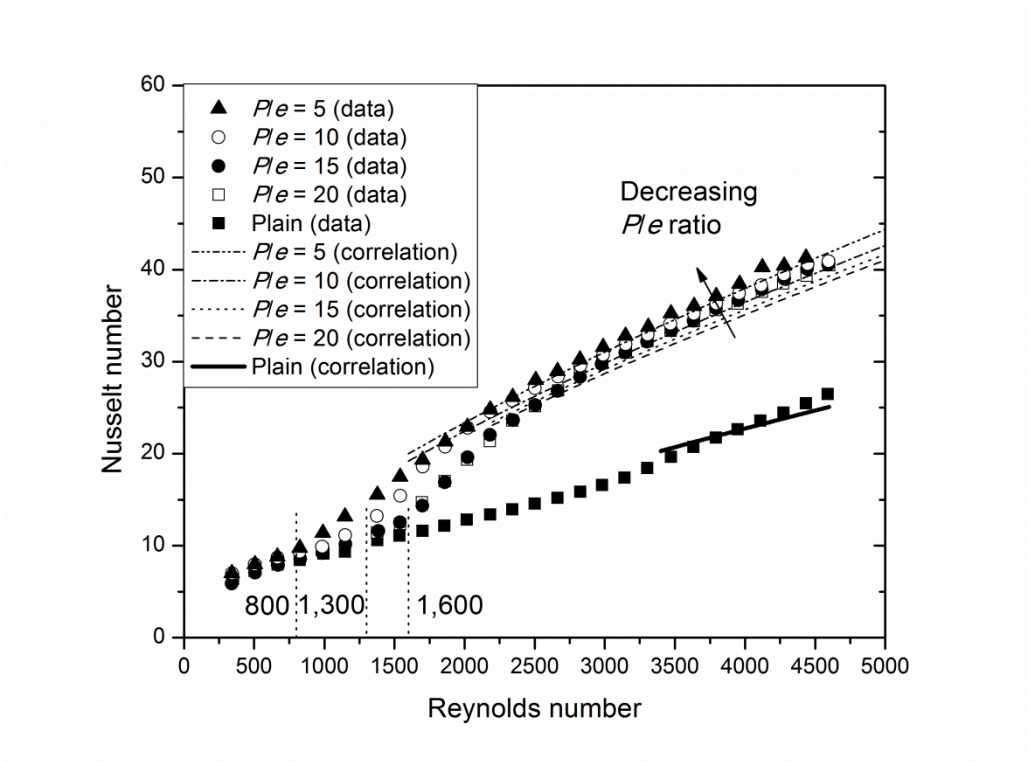

Figure 10-4: Proposed Nu_{FS} correlation in Eqn. (10-5) applied to the P/e ratio study

The Nusselt number correlation for the D microchannel series is proposed as follows:

$$Nu_D = 0.034Re^{0.7}Pr^{1/3}\left[1 + \frac{7}{L/D_h} + \frac{5(e/H)^{1.4}}{(P/e)^{0.375}}\right] \quad (10\text{-}6)$$

Applicable for: $Pr \approx 5.5$; $L/D_h = 50$
Type of fluid: Single-phase water
Maximum discrepancy: 13%
Mean discrepancy: 3%

The applicable Reynolds number range of the proposed correlation for each D microchannel profile is listed in Table 10-5.

Table 10-5: Applicable Reynolds number range for the Nu_D correlation in Eqn. (10-6)

***e*/*H* ratio**	***P*/*e* ratio**	***Re* range**
0.1	10	3,400≲*Re*≲4,600
0.3	10	2,000≲*Re*≲4,600
0.5	10	1,300≲*Re*≲4,600
0.7	10	1,000≲*Re*≲4,600
0.5	20	2,600≲*Re*≲4,600
0.5	15	2,000≲*Re*≲4,600
0.5	5	1,300≲*Re*≲4,600

The proposed Nusselt number correlation for the D microchannel series fits the measured values well, as illustrated in Figure 10-5 and Figure 10-6.

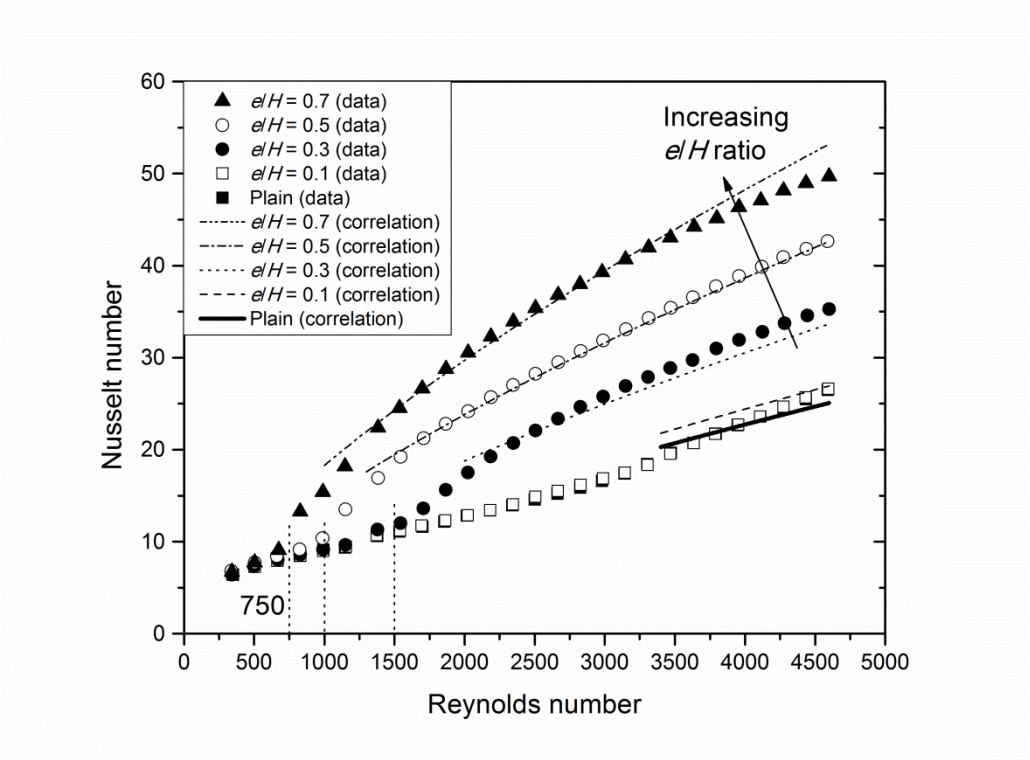

Figure 10-5: Proposed Nu_D correlation in Eqn. (10-6) applied to the e/H ratio study

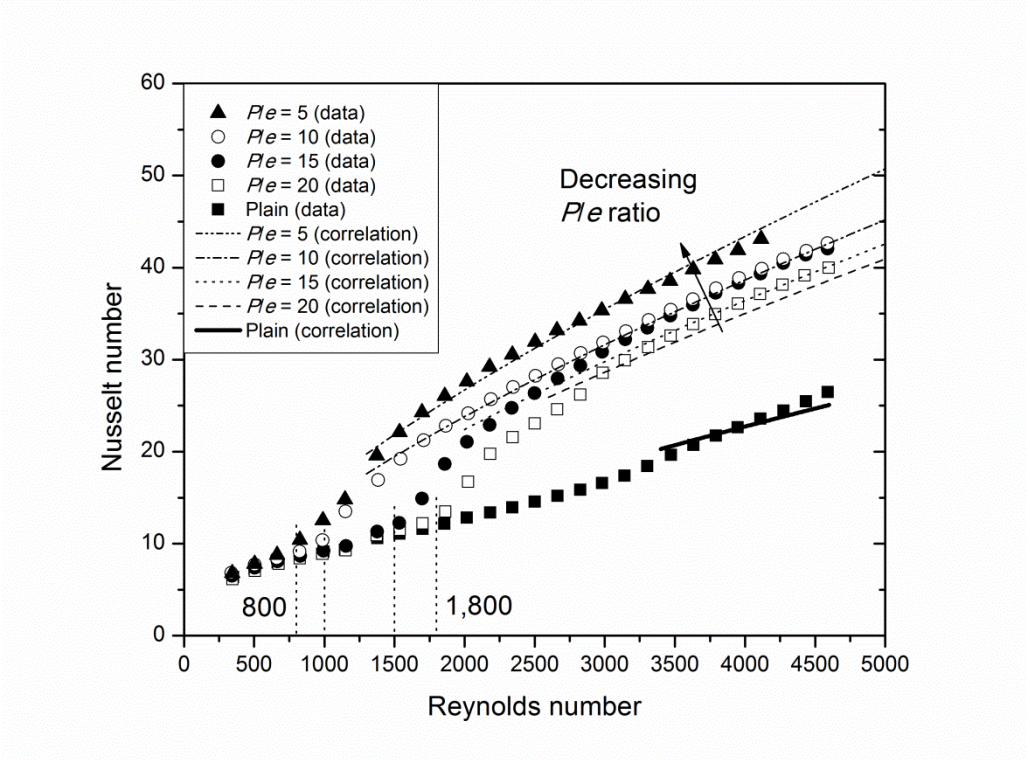

Figure 10-6: Proposed Nu_D correlation in Eqn. (10-6) applied to the P/e ratio study

Several interesting observations can be made from the coefficients used in Eqns. (10-3) to (10-6).

The coefficient F represents the effect of the scale/thorn height (e) on the heat transfer performance, for a fixed mean channel height (H) and P/e ratio. It is 1.1 and 1.5 for the scale-inspired IFS and FS microchannel series, respectively. This implies that increasing the scale height has a stronger influence in increasing the Nusselt number for the FS microchannel series, as compared to the IFS microchannel series. This is logical because the Fish Scale profile naturally causes the least disruption to the flow. Hence, the decrease in minimum channel gap by increasing the scale height plays a more dominant role in enhancing heat transfer by promoting early transition to turbulent flow and thinning of thermal boundary layer. On the other hand, the Inverted Fish Scale profile naturally causes the most disruption to the flow, such that heat transfer enhancement is achieved even for the lowest e/H ratio of 0.1 for $Re \gtrsim 2{,}200$. In addition, early transition to turbulent flow at $Re \approx 600$ is observed for the remaining IFS profiles. Since the heat transfer enhancement mechanisms are triggered by the naturally disruptive IFS profile, increasing the scale height plays a less dominant role in further enhancing heat transfer. For the thorny D microchannel series, the coefficient F is 1.4. This implies that increasing the thorn height also has a strong influence in increasing the Nusselt number for the D microchannel series.

Nonetheless, the overall effect of the scale/thorn height (e) on the heat transfer performance cannot simply be determined from the coefficient F alone. It is also influenced by the coefficients E and G. As can be seen from Table 10-6, increasing the scale height from 0 to 0.21 mm results in the least increment in Nusselt number from 15 to 33 for the FS microchannel series, even though the coefficient F is the highest. This is because the coefficient E is the lowest at only 2.75, as compared to 8 and 5 for the IFS and D microchannel series, respectively.

Table 10-6: Effect of *e*/*H* ratio on Nusselt number at *Re*≈2,664

e/*H* ratio	*P*/*e* ratio	Scale height (mm)	Nusselt number		
			IFS	FS	D
0 (Plain)	10	0	15	15	15
0.1	10	0.03	16	15	16
0.7	10	0.21	37	33	37

The coefficient G represents the effect of the number of scales/thorns of the same height (*e*) on the heat transfer performance, for a fixed channel length (*L*) and mean channel height (*H*). The coefficient G is 0.6 and 0.15 for the scale-inspired IFS and FS microchannel series, respectively. This implies that increasing the number of scales by decreasing the scale pitch (*P*) has a stronger influence in increasing the Nusselt number for the IFS microchannel series, as compared to the FS microchannel series. This is logical because the IFS profile is naturally the most disruptive and the FS profile is naturally the least disruptive. For the thorny D microchannel series, the coefficient G is 0.375. This implies that increasing the number of thorns by decreasing the thorn pitch (*P*) has a relatively strong influence in increasing the Nusselt number for the D microchannel series.

It appears that the overall effect of the number of scales/thorns of the same height (*e*) on the heat transfer performance can be observed from the coefficient G alone, at least within the scope of investigation. As can be seen from Table 10-7, increasing the number of scales/thorns from 10 to 40 results in the largest increment in Nusselt number from 27 to 40 for the IFS microchannel series, and the least increment in Nusselt number from 27 to 29 for the FS microchannel series. The D microchannel series falls in between with Nusselt number increment from 25 to 33.

Table 10-7: Effect of *P*/*e* ratio on Nusselt number at *Re*≈2,664

P/*e* ratio	*e*/*H* ratio	Number of scales/thorns	Nusselt number		
			IFS	FS	D
20	0.5	10	27	27	25
5	0.5	40	40	29	33

To determine the possibility of applying the correlations in Eqns. (10-4) to (10-6) beyond the measurement limits of the present study, the coefficient E is examined. The coefficient E can be interpreted as the effect of the scale/thorn profile on the heat transfer performance, when both ratios of *e*/*H* and *P*/*e* are set to unity. Referring to Eqns. (10-4) to (10-6), the right hand side (RHS) term within the square brackets is reduced to the coefficient E alone, which are 8, 2.75 and 5, respectively, for the IFS, FS and D microchannel series. Since the mean channel height (*H*) is fixed at 0.3 mm, the ratios of *e*/*H* and *P*/*e* equal unity implies that the scale/thorn height (*e*) and scale/thorn pitch (*P*) are both 0.3 mm. In other words, there would be 100 protrusions with a scale/thorn height (*e*) of 0.3 mm for a microchannel length of 30 mm. As can be seen from Table 10-8, the correlation predicts that the Nusselt number is 137, 58 and 92 for the IFS, FS and D microchannel series, respectively.

Table 10-8: Prediction of Nusselt number for *e*/*H* ratio and *P*/*e* ratio of 1, at *Re*≈2,664

P/*e* ratio	*e*/*H* ratio	Scale height (mm)	Number of scale/thorns	Nusselt number		
				IFS	FS	D
1	1	0.3	100	137	58	92

This seems logical in theory, since the Inverted Fish Scale profile is the most effective in disrupting the flow and enhancing heat transfer, followed by the Durian and Fish Scale profiles. However, this may not make practical sense, because if there were to be 100 scale/thorn protrusions within a microchannel length of 30 mm, the profiles would converge into a plain profile of higher height with a very rough surface, as shown in Figure 10-7. In this case, the

Nusselt number values are expected to converge to a single value for the three different profiles. Hence, the correlations must be used with caution beyond the current measurement limits.

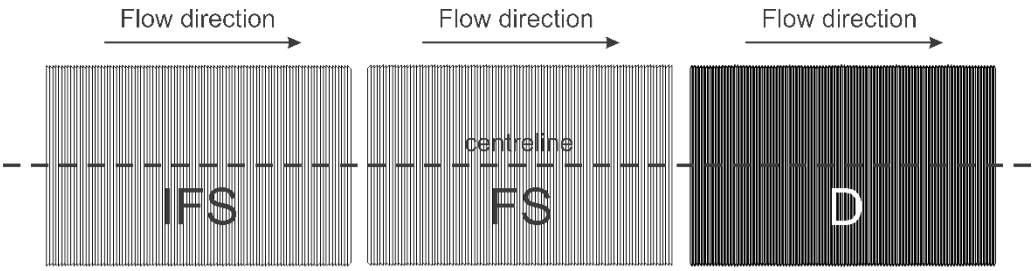

Figure 10-7: Front view of the profiles when both ratios of *e*/*H* and *P*/*e* equal unity

10.2 Proposed Correlations for Average Friction Factor

10.2.1 Laminar Flow Regime

Throughout the whole study, the variation of thermo-hydraulic performance with Reynolds number exhibits the same relationship, in which the nature-inspired enhanced microchannels perform better than the Plain microchannel only after the critical Reynolds number is exceeded. This is because the Nusselt number of the nature-inspired enhanced microchannels is similar to that of the Plain microchannel in the laminar flow regime. Conversely, the friction factor of the nature-inspired enhanced microchannels is higher than that of the Plain microchannel in the laminar flow regime. As a result, the thermo-hydraulic performance of the nature-inspired enhanced microchannels can be less than 1.0. In other words, there is no increased heat exchange capacity for equal heat transfer surface area and pumping power in the laminar flow regime.

As such, it is of no real benefit to consider the flow in the laminar regime. Hence, the friction factor correlation in the laminar flow regime is not proposed.

10.2.2 Turbulent Flow Regime

As discussed in Section 6.2, the Phillips correlation (Eqn. 2-13) is used to compare with the friction factor for the Plain microchannel in the turbulent flow regime. The Reynolds number range for the turbulent flow regime has been identified as 3,400≲*Re*≲4,600 in Section 6.4. It is of the form:

$$f_{Plain,turbulent} = \frac{1}{Re^{P}}\left[Q + \frac{R}{L/D_h}\right] \tag{10-7}$$

A non-linear least-squares curve-fitting approach is performed on the measured friction factor data for the Plain microchannel in the range 3,400≲*Re*≲4,600. The friction factor correlation for the Plain microchannel is then proposed as follows:

$$f_{Plain,turbulent} = \frac{1}{Re^{0.15}}\left[0.2 + \frac{2}{L/D_h}\right] \tag{10-8}$$

Applicable for: 3,400≲*Re*≲4,600;
L/D_h=50
Type of fluid: Single-phase water
Maximum discrepancy: 2%
Mean discrepancy: 2%

The proposed friction factor correlation for the Plain microchannel for turbulent flow serves as the basis for the derivation of new correlations for the enhanced microchannels. An additional term is added to account for the increase in friction factor due to the scale/thorn protrusions, which cause significant thinning of the velocity boundary layer and promote early transition to turbulent flow. When the scale/thorn protrusion height (*e*) becomes zero, the friction factor correlation reduces to that for the Plain microchannel. The new friction factor correlation for the enhanced microchannels is of the form:

$$f_{profile} = \frac{1}{Re^{P}}\left[Q + \frac{R}{L/D_h} + \frac{S(e/H)^{T}}{(P/e)^{U}}\right] \tag{10-9}$$

where e/H refers to the scale/thorn height (e) to mean channel height (H) ratio, P/e refers to the scale/thorn pitch (P) to scale/thorn height (e) ratio, and S, T and U are coefficients to be determined.

A non-linear least-squares curve-fitting approach is performed on the measured friction factor for each of the three enhanced microchannel series in their respective turbulent regime. The friction factor correlation for the IFS microchannel series is proposed as follows:

$$f_{IFS} = \frac{1}{Re^{0.15}}\left[0.2 + \frac{2}{L/D_h} + \frac{15(e/H)^{1.2}}{(P/e)^1}\right] \quad (10\text{-}10)$$

Applicable for: $Pr \approx 5.5$; $L/D_h = 50$
Type of fluid: Single-phase water
Maximum discrepancy: 13%
Mean discrepancy: 4%

The applicable Reynolds number range of the proposed correlation for each IFS microchannel profile is listed in Table 10-9.

Table 10-9: Applicable *Re* range for the f_{IFS} correlation in Eqn. (10-10)

***e*/*H* ratio**	***P*/*e* ratio**	***Re* range**
0.1	10	4,000≲*Re*≲4,600
0.3	10	900≲*Re*≲4,600
0.5	10	700≲*Re*≲4,600
0.7	10	600≲*Re*≲4,600
0.5	20	1,300≲*Re*≲4,600
0.5	15	800≲*Re*≲4,600
0.5	5	800≲*Re*≲4,600

The proposed friction factor correlation for the IFS microchannel series fits the measured values well, as illustrated in Figure 10-8 and Figure 10-9. The labelled number of 600 inside the figures represents the critical Reynolds number for all but the IFS profile with e/H ratio of 0.1. The critical Reynolds number corresponds to the onset of laminar-to-turbulent flow transition.

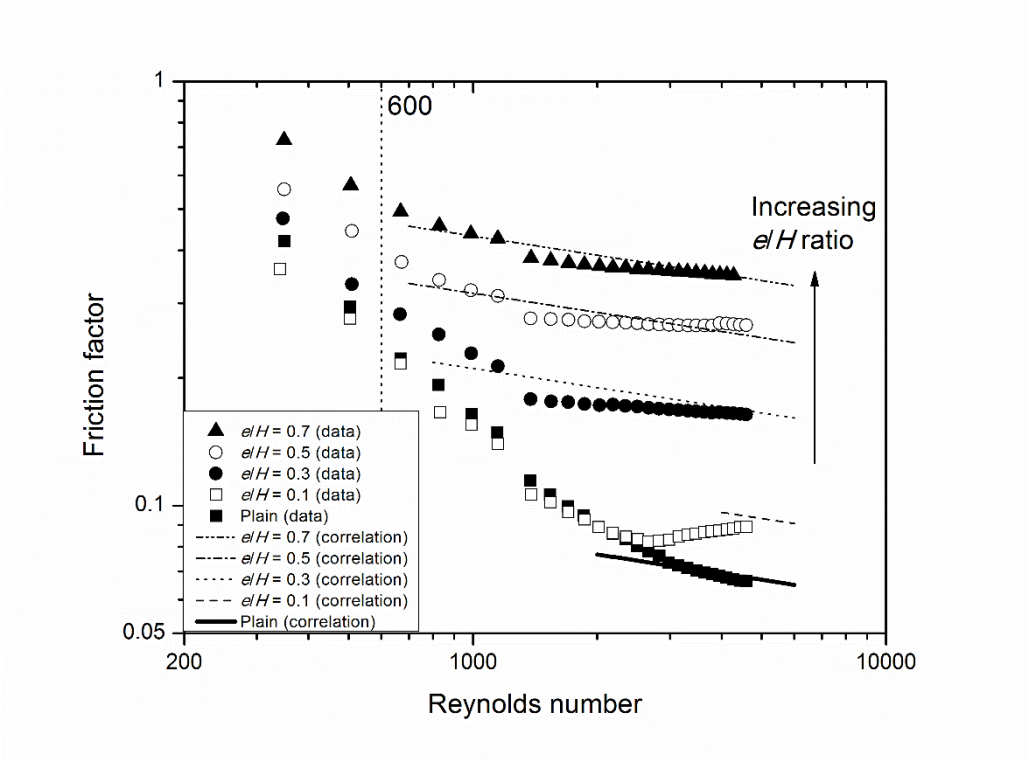

Figure 10-8: Proposed f_{IFS} correlation in Eqn. (10-10) applied to the e/H ratio study

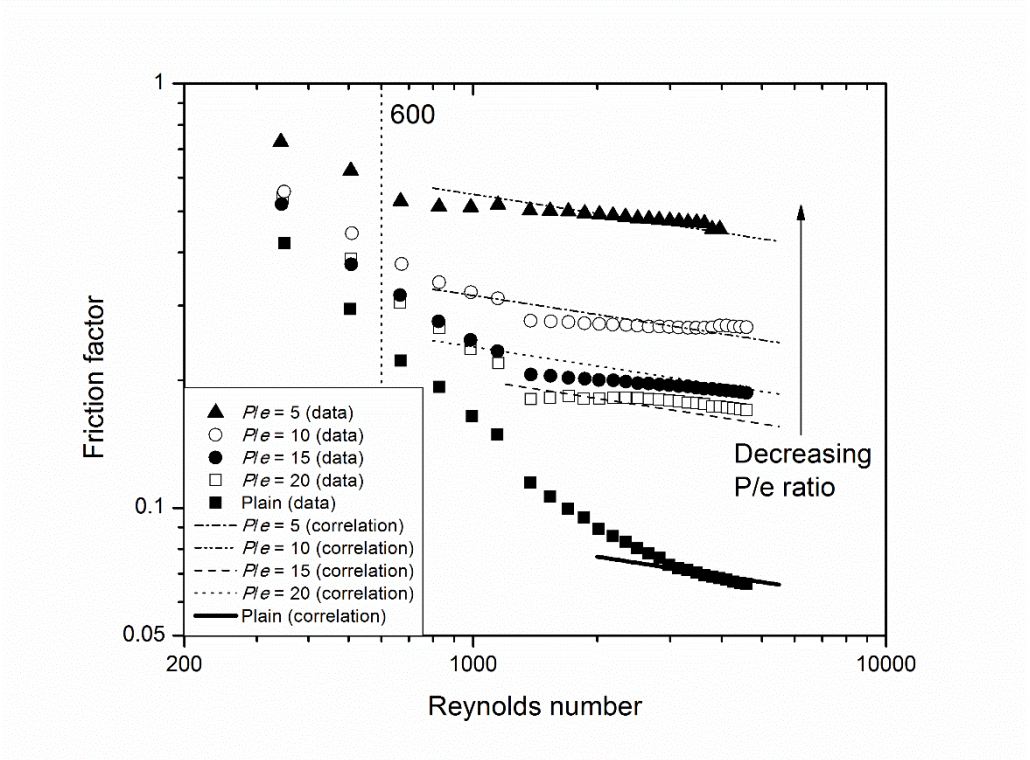

Figure 10-9: Proposed f_{IFS} correlation in Eqn. (10-10) applied to the P/e ratio study

The friction factor correlation for the FS microchannel series is proposed as follows:

$$f_{FS} = \frac{1}{Re^{0.15}}\left[0.2 + \frac{2}{L/D_h} + \frac{7(e/H)^{1.6}}{(P/e)^{0.7}}\right] \quad (10\text{-}11)$$

Applicable for: $Pr \approx 5.5$; $L/D_h = 50$
Type of fluid: Single-phase water
Maximum discrepancy: 11%
Mean discrepancy: 3%

The applicable Reynolds number range of the proposed correlation for each FS microchannel profile is listed in Table 10-10.

Table 10-10: Applicable *Re* range for the f_{FS} correlation in Eqn. (10-11)

***e*/*H* ratio**	***P*/*e* ratio**	***Re* range**
0.1	10	$3{,}400 \lesssim Re \lesssim 4{,}600$
0.3	10	$2{,}400 \lesssim Re \lesssim 4{,}600$
0.5	10	$1{,}800 \lesssim Re \lesssim 4{,}600$
0.7	10	$700 \lesssim Re \lesssim 4{,}600$
0.5	20	$2{,}300 \lesssim Re \lesssim 4{,}600$
0.5	15	$2{,}300 \lesssim Re \lesssim 4{,}600$
0.5	5	$1{,}800 \lesssim Re \lesssim 4{,}600$

The proposed friction factor correlation for the FS microchannel series fits the measured values well, as illustrated in Figure 10-10 and Figure 10-11. Similarly, the labelled numbers inside the figures represent the critical Reynolds number for each FS profile.

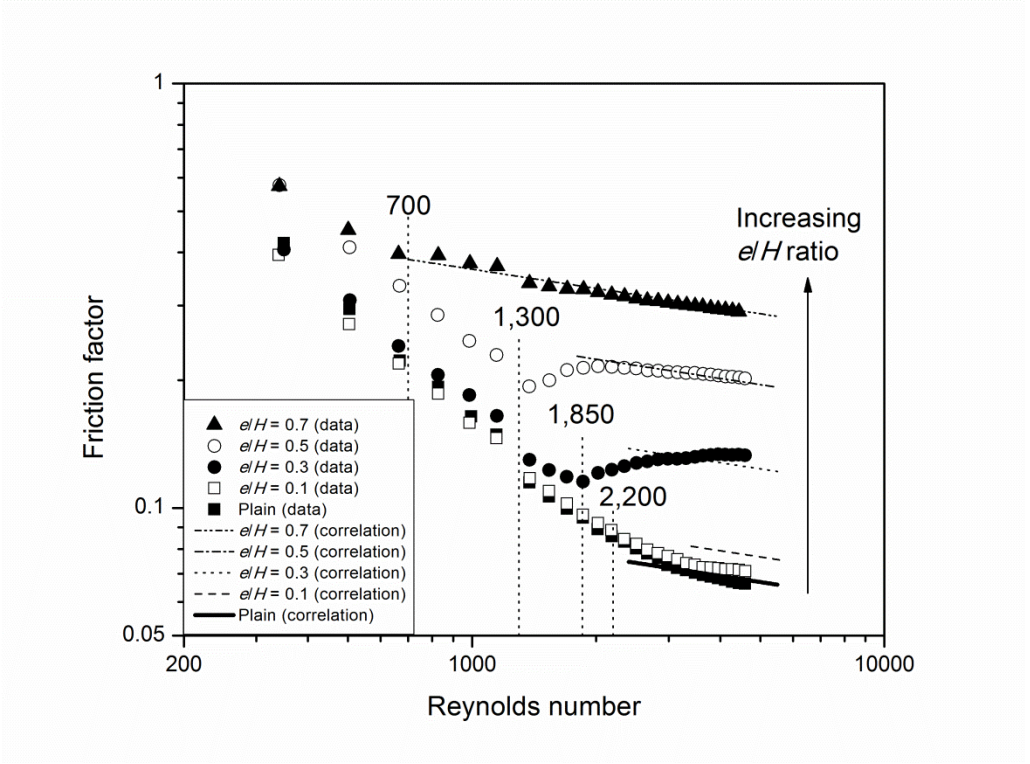

Figure 10-10: Proposed f_{FS} correlation in Eqn. (10-11) applied to the *e*/*H* ratio study

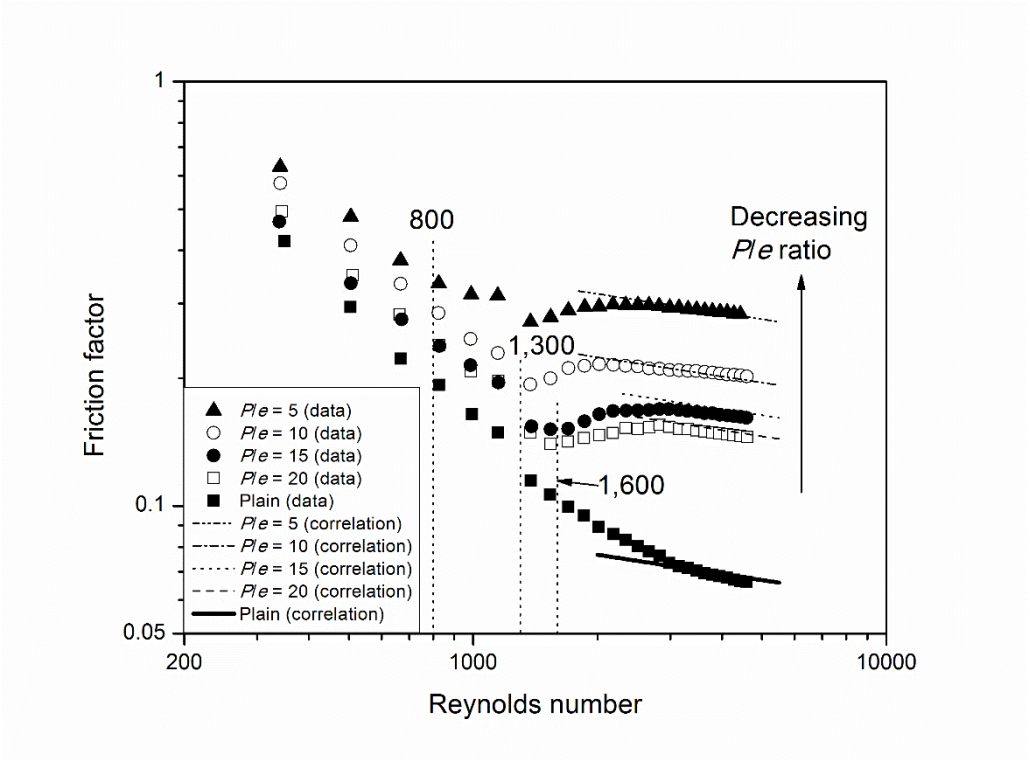

Figure 10-11: Proposed f_{FS} correlation in Eqn. (10-11) applied to the *P*/*e* ratio study

The friction factor correlation for the D microchannel series is proposed as follows:

$$f_D = \frac{1}{Re^{0.15}}\left[0.2 + \frac{2}{L/D_h} + \frac{18(e/H)^{1.1}}{(P/e)^{4/3}}\right] \quad (10\text{-}12)$$

Applicable for: $Pr \approx 5.5$; $L/D_h = 50$
Type of fluid: Single-phase water
Maximum discrepancy: 12%
Mean discrepancy: 4%

The applicable Reynolds number range of the proposed correlation for each D microchannel profile is listed in Table 10-11.

Table 10-11: Applicable *Re* range for the f_D correlation in Eqn. (10-12)

***e*/*H* ratio**	***P*/*e* ratio**	***Re* range**
0.1	10	Not applicable
0.3	10	$2{,}000 \lesssim Re \lesssim 4{,}600$
0.5	10	$1{,}000 \lesssim Re \lesssim 4{,}600$
0.7	10	$1{,}300 \lesssim Re \lesssim 4{,}600$
0.5	20	$2{,}000 \lesssim Re \lesssim 4{,}600$
0.5	15	$1{,}800 \lesssim Re \lesssim 4{,}600$
0.5	5	$1{,}800 \lesssim Re \lesssim 4{,}600$

The proposed friction factor correlation for the D microchannel series fits the measured values well, as illustrated in Figure 10-12 and Figure 10-13. Once again, the labelled numbers inside the figures represent the critical Reynolds number for each D profile.

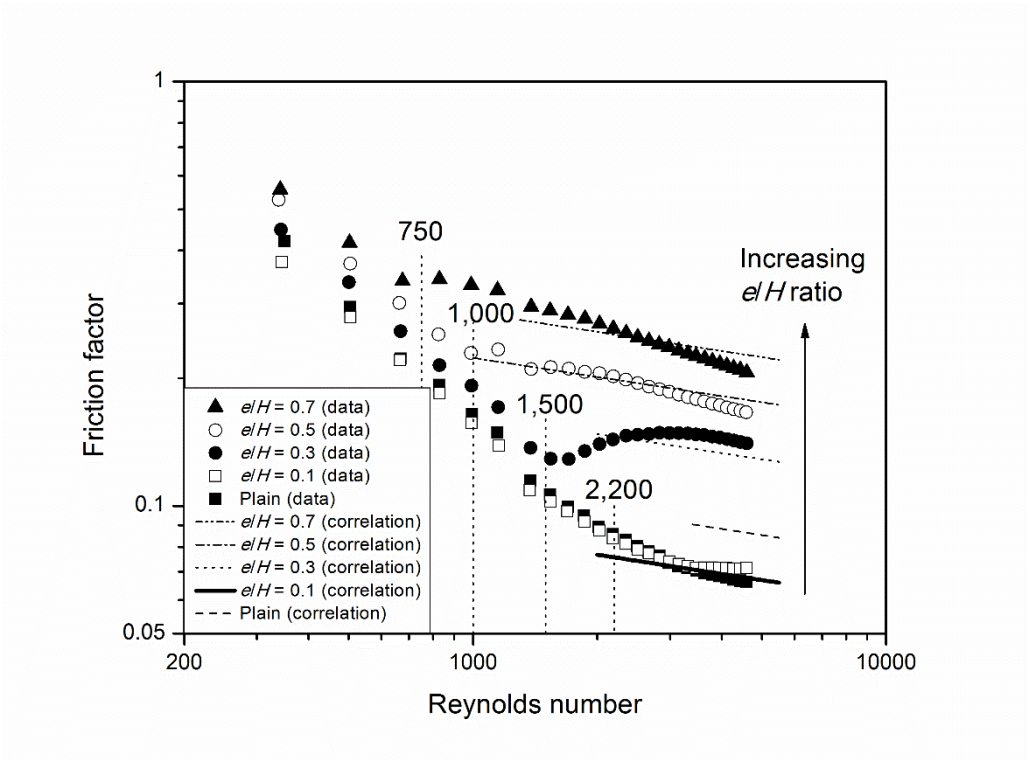

Figure 10-12: Proposed f_D correlation in Eqn. (10-12) applied to the *e*/*H* ratio study

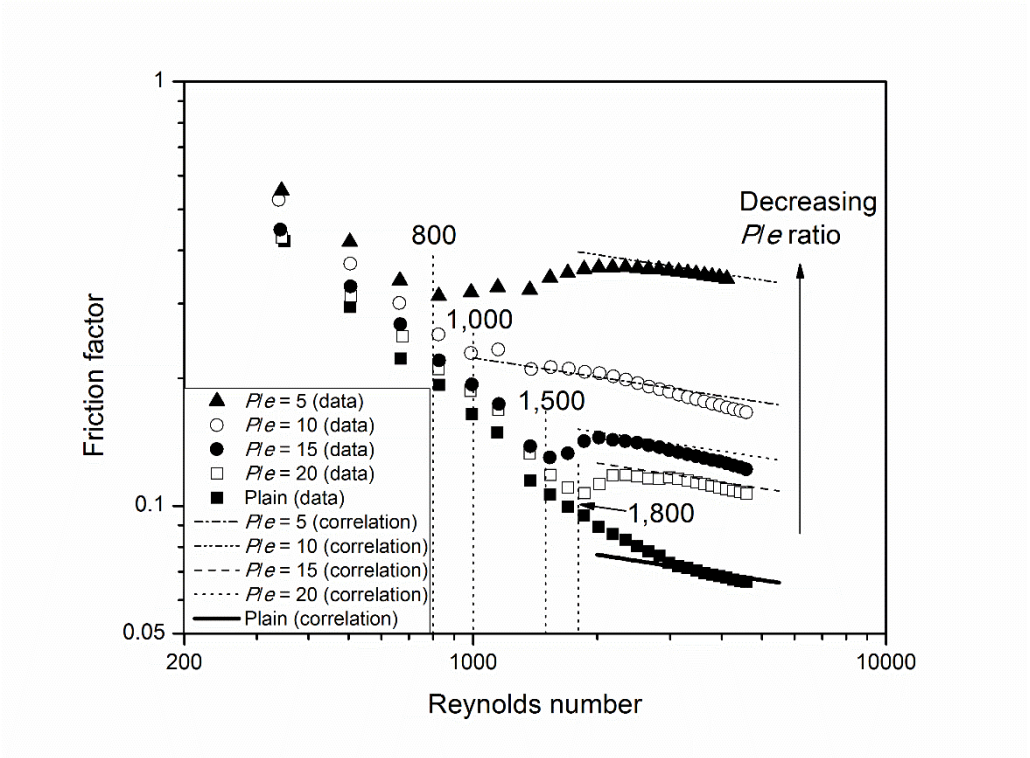

Figure 10-13: Proposed f_D correlation in Eqn. (10-12) applied to the *P*/*e* ratio study

Several interesting observations can be made from the coefficients used in Eqns. (10-9) to (10-12).

The coefficient T represents the effect of the scale/thorn height (*e*) on the friction losses, for a fixed mean channel height (*H*) and *P*/*e* ratio. It is 1.2 and 1.6 for the scale-inspired IFS and FS microchannel series, respectively. This implies that increasing the scale height has a stronger influence in increasing the friction factor for the FS microchannel series, as compared to the IFS microchannel series. The reasoning is similar to that with the coefficient F in the Nusselt number correlation. For the thorny D microchannel series, the coefficient T is 1.1. This implies that increasing the thorn height has the least influence in increasing the friction factor for the D microchannel series, as compared to the scale-inspired microchannel series.

Similarly, the overall effect of the scale/thorn height (*e*) on the heat transfer performance cannot simply be determined from the coefficient T alone. It is also influenced by the coefficients S and U. As can be seen from Table 10-12, increasing the scale height from 0 to 0.21 mm results in a moderate increment in friction factor from 0.08 to 0.31 for the FS microchannel series, even though the coefficient T is the highest. This is because the coefficient S is the lowest at only 7, as compared to 15 and 18 for the IFS and D microchannel series, respectively.

Table 10-12: Effect of *e*/*H* ratio on friction factor at *Re*≈2,664

***e*/*H* ratio**	***P*/*e* ratio**	**Scale height (mm)**	**Friction factor**		
			IFS	**FS**	**D**
0 (Plain)	10	0	0.08	0.08	0.08
0.1	10	0.03	0.08	0.08	0.08
0.7	10	0.21	0.36	0.31	0.25

The coefficient U represents the effect of the number of scale/thorn protrusions of the same height (*e*) on the friction losses, for a fixed channel length (*L*) and mean channel height (*H*). The coefficient U is 1 and 0.7 for the scale-inspired IFS and FS microchannel series, respectively. This implies that increasing the number of scales by decreasing the scale pitch (*P*) has a stronger influence in increasing the friction factor for the IFS microchannel series, as compared to the FS microchannel series. This is logical since the Inverted Fish Scale profile is naturally more disruptive than the Fish Scale profile. For the thorny D microchannel series, the coefficient U is 4/3. This implies that increasing the number of thorns by decreasing the thorn pitch (*P*) has the strongest influence in increasing the friction factor for the D microchannel series. This is likely due to the smaller region of pressure recovery as discussed in Section 9.4.2.

Similarly, it appears that the overall effect of the number of scales/thorns of the same height (*e*) on the friction losses can be observed from the coefficient G alone. As can be seen from Table 10-13, increasing the number of scales/thorns from 10 to 40 results in a 3 times increment in friction factor from 0.12 to 0.36 for the D microchannel series. The friction factor increases by 2.9 times from 0.16 to 0.47 for the IFS microchannel series, and increases by only 2 times from 0.15 to 0.30 for the FS microchannel series.

Table 10-13: Effect of *P*/*e* ratio on friction factor at *Re*≈2,664

P*/*e **ratio**	***e*/*H*** **ratio**	**Number of scales/thorns**	**Friction factor**		
			IFS	**FS**	**D**
20	0.5	10	0.16	0.15	0.12
5	0.5	40	0.47	0.30	0.36

To determine the possibility of applying the correlations in Eqns. (10-10) to (10-12) beyond the measurement limits of the present study, the coefficient S is examined. It represents the effect of the scale/thorn profile on the friction losses, when both ratios of e/H and P/e are set to unity. Referring to Eqns. (10-10) to (10-12), the RHS term within the square brackets is reduced to the coefficient S alone, which are 15, 7 and 18, respectively, for the IFS, FS and D microchannel series. As can be seen from Table 10-14, the correlation predicts that the friction factor is 4.67, 2.22 and 5.59 for the IFS, FS and D microchannel series, respectively, when there are 100 protrusions with a scale/thorn height (e) of 0.3 mm for a microchannel length of 30 mm.

Table 10-14: Prediction of friction factor for e/H ratio and P/e ratio of 1, at Re≈2,664

P/e ratio	e/H ratio	Scale height (mm)	Number of scale/thorns	Friction factor		
				IFS	FS	D
1	1	0.3	100	4.67	2.22	5.59

Once again, this may not make practical sense, since the profiles would converge into a plain profile of higher height with a very rough surface, as previously shown in Figure 10-7. The friction factor values are therefore expected to converge to a single value for the three different microchannel profiles. Hence, the correlations must be used with caution beyond the current measurement limits.

Chapter 11 Conclusions and Recommendations

This chapter concludes the work accomplished by the author during the course of the Ph.D. research study, and summarises the key findings of this research. The results for the Plain, Inverted Fish Scale (IFS), Fish Scale (FS) and Durian (D) microchannels are first individually concluded, before the newly proposed correlations for the average Nusselt number and friction factor are listed. After a thoughtful reflection on the key findings from the present study, the opportunities and strategies for future work are identified and recommended.

11.1 Conclusions

In essence, the present Ph.D. research study aims to develop a novel nature-inspired configuration to enhance the microscale heat transfer in macro geometry using conventional machining processes, and formulate working correlations to evaluate the heat transfer and pressure drop for practical applications. The enhancement profiles are the IFS and FS microchannel series inspired by fish scales, as well as the D microchannel series inspired by the thorny husk of the durian fruit. The research focuses on the forced convective steady-state internal flow of single-phase liquid water in an annular microscale passage, which is created by securing a cylindrical insert of mean diameter 19.4 mm within a cylindrical pipe of internal diameter 20 mm. The present study considers the flow of a constant-property incompressible Newtonian fluid through a stationary, nonporous channel, where the continuum mechanics theory is still valid.

Both physical measurements and numerical simulations have been carried out. A measurement system has been designed, fabricated, instrumented and commissioned for data collection. The system provides accurate pressure and

heat transfer measurements with a mean discrepancy of 7.8% and 13.4%, respectively, as well as consistent pressure and heat transfer measurements within 0.57% and 0.39%, respectively. In addition, a conjugate heat transfer numerical model has been developed using a Computational Fluid Dynamics (CFD) code. The numerical model is validated through the comparison of its predictions with the measurements, which shows a mean discrepancy of 8.5% and 20.2%, respectively, for the pressure and heat transfer predictions.

The investigations have been carried out for plain and enhanced annular microchannels, with a fixed mean gap size (H) of 300 μm and length (L) of 30 mm, using liquid-phase distilled water. About 600 steady-state measurements have been collected for a total of 22 microchannel profiles, using up to 27 flow conditions for each profile, and 2 wall heat fluxes of 13.3 and 53.0 W/cm^2. With a Reynolds number range of 350-4600, the laminar, transitional and turbulent flow regimes are studied. The 22 microchannel profiles include 7 for each of the three nature-inspired IFS, FS and D microchannel series, and the Plain microchannel. The measurements for the Plain microchannel are used as the basis to determine the extent of heat transfer enhancement.

Within the nature-inspired enhanced IFS, FS and D microchannel series, the effects of two geometrical ratios are studied. They are the ratio of scale/thorn height (e) to mean channel height (H), and the ratio of scale/thorn pitch (P) to scale/thorn height (e). In the first study, four e/H ratios of 0.1, 0.3, 0.5 and 0.7 are employed, with a fixed P/e ratio of 10. In the second study, four P/e ratios of 5, 10, 15 and 20 are employed, with a fixed e/H ratio of 0.5. A larger e/H ratio corresponds to a narrower minimum gap through which the fluid flows, while a lower P/e ratio corresponds to a larger number of scale/thorn protrusions, of the same protrusion height, for a given microchannel length.

The dependent variables include the convective heat transfer coefficient, pressure drop, Nusselt number, friction factor, and thermo-hydraulic performance factor. The thermo-hydraulic performance factor is computed from the normalised Nusselt number and normalised friction factor, with respect to the Plain microchannel. In the design of practical heat exchangers, this performance factor represents the increased heat transfer capacity for equal heat transfer surface area and pumping power.

The results show that enhanced microscale heat transfer effects have indeed been achieved in macro geometry, using conventional machining processes. The highest convective heat transfer coefficient achieved in the whole study is 52.8 $kW/m^2 \cdot K$, at 6.5 L/min ($Re \approx 4280$) using the IFS microchannel with a scale height (e) of 0.21 mm and scale pitch (P) of 2.1 mm. This means that the system is able to remove heat flux of up to 375 W/cm^2, for a temperature difference of 71 K. The highest pressure drop in the whole study is 3.3 bars, which can be easily overcome by a commercially available pump. In terms of the thermo-hydraulic performance, the D microchannel performs the best, with a thorn height (e) of 0.21 mm and thorn pitch (P) of 2.1 mm. Given a fixed heat transfer surface area and pumping power, this profile can improve the heat transfer capacity by 67% relative to the Plain microchannel, at Reynolds number of 2,350.

Most importantly, working correlations have been proposed to evaluate the Nusselt number and friction factor for each of the nature-inspired enhanced IFS, FS and D microchannel series. The mathematical form of the new correlations follows that of existing classical correlations, but with an additional term added to account for the effect of the scale or thorn protrusions. The correlations are formulated based on about 600 steady-state measurements, as well as the underlying physics which governs the heat transfer and flow behaviours, within the scope of investigation.

11.1.1 Plain Microchannel

- For single-phase liquid water in conventionally-sized channels, the typical convective heat transfer coefficient *h* values are at most 10 kW/m^2·K [14,27]. In the present study, the heat transfer coefficient for the 300 μm Plain microchannel ranges from 10.9 to 27.1 kW/m^2·K, for flow rates between 2 and 7 L/min. This confirms the feasibility of achieving microscale heat transfer effects in macro geometry.

- Comparison of Nusselt number and friction factor with classical theory confirms the applicability of the continuum theory to microchannel flows. The results also suggest that the variation in fluid properties due to a large temperature difference between the wall and the bulk fluid in microchannel flows could possibly account for the deviation from the classical theory.

- The critical Reynolds number corresponding to laminar-to-turbulent flow transition for the Plain microchannel is found to range between 2,200 and 3,400. This range agrees well with those for the macro-scale channels, which is 2,200–3,400 for parallel plates and approximately 2,300 for circular pipes.

- If the scale-inspired and durian-inspired microchannel profiles are able to trigger early laminar-to-turbulent flow transition at a Reynolds number lower than 2,200, heat transfer enhancement may be achieved.

11.1.2 Inverted Fish Scale (IFS) Microchannels

- The IFS microchannel series is best suited for applications where high convective heat transfer coefficient values are of utmost priority, with less stringent pressure drop restrictions.

- The highest convective heat transfer coefficient achieved is 52.8 kW/m^2·K, at 6.5 L/min (Re≈4280) using the IFS microchannel with a scale height (e) of 0.21 mm and scale pitch (P) of 2.1 mm. In comparison to the Plain microchannel, this demonstrates the effectiveness of the Inverted Fish Scale profile in enhancing heat

transfer performance. In addition, a microchannel study conducted on a MEMS-based pin fin heat sink using water flow reported a maximum heat transfer coefficient of around 55 kW/m^2·K at *Re*≈112 [133]. Therefore, the present study demonstrates that the nature-inspired enhanced microscale flow in macro geometry can achieve high heat transfer coefficient values comparable to those in a typical microchannel, without involving complex and costly manufacturing methods.

- The highest pressure drop is 3.3 bars, at 6 L/min using the IFS microchannel with a scale height (*e*) of 0.15 mm and scale pitch (*P*) of 0.75 mm. It is also the highest pressure drop incurred for the whole study, which is below the imposed pressure drop limit of 3.5 bars.

- The highest Nusselt number is 52, at Reynolds number of 4,280 using the IFS microchannel with a scale height (*e*) of 0.21 mm and scale pitch (*P*) of 2.1 mm.

- The highest friction factor is 0.73, at Reynolds number of 343 using the IFS microchannel with a scale height (*e*) of 0.15 mm and scale pitch (*P*) of 0.75 mm, as well as at Reynolds number of 349 using the IFS microchannel with a scale height (*e*) of 0.21 mm and scale pitch (*P*) of 2.1 mm.

- For the ease of reference, the above data is summarised in Table 11-1.

Table 11-1: Summary of results for the IFS microchannel series

IFS profile (*H* = 0.3 mm)	***h*** **(kW/m^2·K)**	**Δ*p*** **(bars)**	**Flow rate (L/min)**	***Nu***	***Re***	***f***	***Re***
Height *e* = 0.21 mm Pitch *P* = 2.1 mm	**52.8**	3.0	6.5	**52**	4,280	**0.73**	349
Height *e* = 0.15 mm Pitch *P* = 0.75 mm	51.5	**3.3**	6.0	50	3,953	**0.73**	343

- In the *e*/*H* ratio parametric study, a larger *e*/*H* ratio corresponds to higher Nusselt number and friction factor. Table 11-2 shows the effect of *e*/*H* ratio on Nusselt number and friction factor for Reynolds number of approximately 2,664.

Table 11-2: Effect of *e*/*H* ratio on Nusselt number and friction factor for IFS microchannel (*Re*≈2,664)

***e*/*H* ratio**	**Nusselt number**	**Friction factor**
0 (Plain)	15	0.08
0.1	16	0.08
0.7	37	0.36

- In addition, a larger *e*/*H* ratio exhibits higher thermo-hydraulic performance for 350≲*Re*≲4,600. Given a fixed heat transfer surface area and pumping power, the IFS microchannel with the largest *e*/*H* ratio of 0.7 can improve the heat transfer capacity by 54% relative to the Plain microchannel, at Reynolds number of 1,800.

- For an *e*/*H* ratio larger than 0.3, the Inverted Fish Scale profile is able to promote early laminar-to-turbulent flow transition at *Re*≈600, as shown in Table 11-3.

Table 11-3: Effect of *e*/*H* ratio on critical Reynolds number for IFS microchannel

***e*/*H* ratio**	**Critical Reynolds number**
0.1	2,200
0.3	600
0.5	600
0.7	600

- In the *P*/*e* ratio parametric study, a lower *P*/*e* ratio corresponds to higher Nusselt number and friction factor. Table 11-4 shows the effect of *P*/*e* ratio on Nusselt number and friction factor for Reynolds number of approximately 2,664.

Table 11-4: Effect of *P*/*e* ratio on Nusselt number and friction factor for IFS microchannel (*Re*≈2,664)

***P*/*e* ratio**	**Nusselt number**	**Friction factor**
5	40	0.47
20	27	0.16

- In addition, a smaller *P*/*e* ratio exhibits higher thermo-hydraulic performance for $350 \lesssim Re \lesssim 3{,}000$. Given a fixed heat transfer surface area and pumping power, the IFS microchannel with the smallest *P*/*e* ratio of 5 can improve the heat transfer capacity by 54% relative to the Plain microchannel, at Reynolds number of 1,500.

- For a scale height to mean channel height ratio of 0.5, the Inverted Fish Scale profile is able to promote early laminar-to-turbulent flow transition at $Re \approx 600$, regardless of the number of scales, as shown in Table 11-5.

Table 11-5: Effect of *P*/*e* ratio on critical Reynolds number for IFS microchannel

***P*/*e* ratio**	**Critical Reynolds number**
5	600
10	600
15	600
20	600

11.1.3 Fish Scale (FS) Microchannels

- The FS microchannel series is best suited for heat transfer applications where low pressure drop values are of higher priority.

- The highest convective heat transfer coefficient is 47.9 $kW/m^2 \cdot K$, at 6.75 L/min using the FS microchannel with a scale height (*e*) of 0.21 mm and scale pitch (*P*) of 2.1 mm.

- The highest pressure drop for the FS series is 2.6 bars, at 6.75 L/min using the FS microchannel with a scale height (*e*) of 0.21 mm and scale pitch (*P*) of 2.1 mm as well as the FS microchannel with a scale height (*e*) of 0.15 mm and scale pitch (*P*) of 0.75 mm.

- The highest Nusselt number is 47, at Reynolds number of 4,433 using the FS microchannel with a scale height (*e*) of 0.21 mm and scale pitch (*P*) of 2.1 mm.

- The highest friction factor is 0.63, at Reynolds number of 341 using the FS microchannel with a scale height (e) of 0.15 mm and scale pitch (P) of 0.75 mm.

- For the ease of reference, the above data is summarised in Table 11-6.

Table 11-6: Summary of results for the FS microchannel series

FS profile (H = 0.3 mm)	h (kW/m^2·K)	Δp (bars)	Flow rate (L/min)	Nu	Re	f	Re
Height e = 0.21 mm Pitch P = 2.1 mm	**47.9**	**2.6**	6.75	**47**	4,433	0.57	341
Height e = 0.15 mm Pitch P = 0.75 mm	42.3	**2.6**	6.75	41	4,435	**0.63**	341

- In the e/H ratio parametric study, a larger e/H ratio corresponds to higher Nusselt number and friction factor, as shown in Table 11-7 for Reynolds number of approximately 2,664.

Table 11-7: Effect of e/H ratio on Nusselt number and friction factor for FS microchannel (Re≈2,664)

e/H ratio	Nusselt number	Friction factor
0 (Plain)	15	0.08
0.1	15	0.08
0.7	33	0.31

- In addition, a larger e/H ratio exhibits higher thermo-hydraulic performance, after the critical Reynolds number for each profile is exceeded, due to the early transition to non-laminar flow. Given a fixed heat transfer surface area and pumping power, the FS microchannel with the largest e/H ratio of 0.7 can improve the heat transfer capacity by 43% relative to the Plain microchannel, at Reynolds number of 1,850.

- An increase in scale height (e) for a fixed mean channel height (H) promotes early laminar-to-turbulent flow transition, as shown in Table 11-8.

Table 11-8: Effect of *e*/*H* ratio on critical Reynolds number for FS microchannel

***e*/*H* ratio**	**Critical Reynolds number**
0.1	2,200
0.3	1,850
0.5	1,300
0.7	700

- In the *P*/*e* ratio parametric study, a lower *P*/*e* ratio corresponds to higher Nusselt number and friction factor, as shown in Table 11-9 for Reynolds number of approximately 2,664.

Table 11-9: Effect of *P*/*e* ratio on Nusselt number and friction factor for FS microchannel (*Re*≈2,664)

***P*/*e* ratio**	**Nusselt number**	**Friction factor**
5	29	0.30
20	27	0.15

- In addition, a larger *P*/*e* ratio exhibits higher thermo-hydraulic performance for 2,500≲*Re*≲4,600. Given a fixed heat transfer surface area and pumping power, the FS microchannel with the largest *P*/*e* ratio of 20 can improve the heat transfer capacity by 44% relative to the Plain microchannel, at Reynolds number of 2,800.

- Increasing the number of scales of the same height (*e*) by decreasing the scale pitch (*P*) for a fixed microchannel length helps to promote early laminar-to-turbulent flow transition, as shown in Table 11-10.

Table 11-10: Effect of *P*/*e* ratio on critical Reynolds number for FS microchannel

***P*/*e* ratio**	**Critical Reynolds number**
5	800
10	1,300
15	1,600
20	1,600

11.1.4 Durian (D) Microchannels

- The D microchannel series is best suited for heat exchanger applications where the highest heat transfer capacity (in Watts) for a given heat transfer surface area and pumping power is desired.

- The highest convective heat transfer coefficient is 50.8 kW/m^2·K, at 7 L/min using the D microchannel with a thorn height (*e*) of 0.21 mm and thorn pitch (*P*) of 2.1 mm.

- The highest pressure drop is 2.7 bars, at 6.25 L/min using the D microchannel with a thorn height (*e*) of 0.15 mm and thorn pitch (*P*) of 0.75 mm.

- The highest Nusselt number is 50, at Reynolds number of 4,600 using the D microchannel with a thorn height (*e*) of 0.21 mm and thorn pitch (*P*) of 2.1 mm.

- The highest friction factor is 0.56, at Reynolds number of 342 using the D microchannel with a thorn height (*e*) of 0.21 mm and thorn pitch (*P*) of 2.1 mm.

- For the ease of reference, the above data is summarised in Table 11-11.

Table 11-11: Summary of results for the D microchannel series

D profile (*H* = 0.3 mm)	*h* (kW/m^2·K)	Δ*p* (bars)	Flow rate (L/min)	*Nu*	*Re*	*f*	*Re*
Height *e* = 0.21 mm Pitch *P* = 2.1 mm	**50.8**	2.0	7	**50**	4,600	**0.56**	342
Height *e* = 0.15 mm Pitch *P* = 0.75 mm	44.1	**2.7**	6.25	43	4,114	0.55	344

- In the *e*/*H* ratio parametric study, a larger *e*/*H* ratio corresponds to higher Nusselt number and friction factor, as shown in Table 11-12 for Reynolds number of approximately 2,664.

Table 11-12: Effect of *e*/*H* ratio on Nusselt number and friction factor for D microchannel (*Re*≈2,664)

e/*H* ratio	Nusselt number	Friction factor
0 (Plain)	15	0.08
0.1	16	0.08
0.7	37	0.25

- In addition, a larger *e*/*H* ratio exhibits higher thermo-hydraulic performance, after the critical Reynolds number for each profile is exceeded, due to the early transition to non-laminar flow. Given a fixed heat transfer surface area and pumping power, the D microchannel with the largest *e*/*H* ratio of 0.7 can improve the heat transfer capacity by 67% relative to the Plain microchannel, at Reynolds number of 2,350.

- An increase in thorn height (*e*) for a fixed mean channel height (*H*) promotes early laminar-to-turbulent flow transition, as shown in Table 11-13.

Table 11-13: Effect of *e*/*H* ratio on critical Reynolds number for D microchannel

e/*H* ratio	Critical Reynolds number
0.1	2,200
0.3	1,500
0.5	1,000
0.7	750

- In the *P*/*e* ratio parametric study, a lower *P*/*e* ratio corresponds to higher Nusselt number and friction factor, as shown in Table 11-14.

Table 11-14: Effect of *P*/*e* ratio on Nusselt number and friction factor for D microchannel (*Re*≈2,664)

P/*e* ratio	Nusselt number	Friction factor
5	33	0.36
20	25	0.12

- In addition, a smaller *P*/*e* ratio exhibits higher thermo-hydraulic performance for 350≲*Re*≲1,500, while a larger *P*/*e* ratio exhibits higher thermo-hydraulic performance for 3,250≲*Re*≲4,600. Given a fixed heat transfer surface area and pumping power, the D microchannel with *P*/*e*

ratio of 15 can improve the heat transfer capacity by 52% relative to the Plain microchannel, at Reynolds number of 2,750.

- Increasing the number of thorns of the same height (*e*) by decreasing the thorn pitch (*P*) for a fixed microchannel length helps to promote early laminar-to-turbulent flow transition, as shown in Table 11-15.

Table 11-15: Effect of *P*/*e* ratio on critical Reynolds number for D microchannel

***P*/*e* ratio**	**Critical Reynolds number**
5	800
10	1,000
15	1,500
20	1,800

11.1.5 Thermo-hydraulic Performance

For the ease of reference, the thermo-hydraulic performance for the three nature-inspired microchannel series are summarised in Table 11-16. The results indicate that the increased heat transfer capacity for equal heat transfer surface area and pumping power occurs when the flow transits to the non-laminar region after the critical Reynolds number is exceeded. The D microchannel with *e*/*H* ratio of 0.7 exhibits the best performance of 67%, at $Re \approx 2{,}350$.

Table 11-16: Thermo-hydraulic Performance for the nature-inspired microchannel series

	Increased heat transfer capacity for equal heat transfer surface area and pumping power	**Corresponding *Re***	**Critical *Re***
IFS microchannel			
e/*H* ratio = 0.7	54%	1,800	600
P/*e* ratio = 5	54%	1,500	600
FS microchannel			
e/*H* ratio = 0.7	43%	1,850	700
P/*e* ratio = 20	44%	2,800	1,600
D microchannel			
e/*H* ratio = 0.7	**67%**	2,350	750
P/*e* ratio = 15	52%	2,750	1,500

11.1.6 New Correlations for Average Nusselt Number

New correlations have been proposed to evaluate the average Nusselt number of the nature-inspired enhanced microscale flow in macro geometry under a constant heat flux condition.

Plain microchannel

$$Nu_{Plain,turbulent} = 0.034Re^{0.7}Pr^{1/3}\left[1 + \frac{7}{L/D_h}\right]$$

Applicable for: 3,400≲*Re*≲4,600;
Pr≈5.5;
L/D_h =50
Type of fluid: Single-phase water
Maximum discrepancy: 5%
Mean discrepancy: 3%

Inverted Fish Scale (IFS) microchannels

$$Nu_{IFS} = 0.034Re^{0.7}Pr^{1/3}\left[1 + \frac{7}{L/D_h} + \frac{8(e/H)^{1.1}}{(P/e)^{0.6}}\right]$$

Applicable for: *Pr*≈5.5; L/D_h=50
Type of fluid: Single-phase water
Maximum discrepancy: 16%
Mean discrepancy: 3%

***e*/*H* ratio**	***P*/*e* ratio**	**Applicable *Re* range**
0.1	10	3,400≲*Re*≲4,600
0.3	10	350≲*Re*≲4,600
0.5	10	350≲*Re*≲4,600
0.7	10	350≲*Re*≲4,600
0.5	20	350≲*Re*≲4,600
0.5	15	350≲*Re*≲4,600
0.5	5	350≲*Re*≲4,600

Fish Scale (FS) microchannels

$$Nu_{FS} = 0.034Re^{0.7}Pr^{1/3}\left[1 + \frac{7}{L/D_h} + \frac{2.75(e/H)^{1.5}}{(P/e)^{0.15}}\right]$$

Applicable for: $Pr \approx 5.5$; $L/D_h = 50$
Type of fluid: Single-phase water
Maximum discrepancy: 16%
Mean discrepancy: 4%

***e*/*H* ratio**	***P*/*e* ratio**	**Applicable *Re* range**
0.1	10	3,400≲*Re*≲4,600
0.3	10	2,500≲*Re*≲4,600
0.5	10	1,600≲*Re*≲4,600
0.7	10	1,200≲*Re*≲4,600
0.5	20	2,200≲*Re*≲4,600
0.5	15	2,200≲*Re*≲4,600
0.5	5	1,600≲*Re*≲4,600

Durian (D) microchannels

$$Nu_D = 0.034Re^{0.7}Pr^{1/3}\left[1 + \frac{7}{L/D_h} + \frac{5(e/H)^{1.4}}{(P/e)^{0.375}}\right]$$

Applicable for: $Pr \approx 5.5$; $L/D_h = 50$
Type of fluid: Single-phase water
Maximum discrepancy: 13%
Mean discrepancy: 3%

***e*/*H* ratio**	***P*/*e* ratio**	**Applicable *Re* range**
0.1	10	3,400≲*Re*≲4,600
0.3	10	2,000≲*Re*≲4,600
0.5	10	1,300≲*Re*≲4,600
0.7	10	1,000≲*Re*≲4,600
0.5	20	2,600≲*Re*≲4,600
0.5	15	2,000≲*Re*≲4,600
0.5	5	1,300≲*Re*≲4,600

11.1.7 New Correlations for Average Friction Factor

Similarly, new correlations have been proposed to predict the average friction factor of the nature-inspired enhanced microscale flow in macro geometry.

Plain microchannel

$$f_{Plain,turbulent} = \frac{1}{Re^{0.15}}\left[0.2 + \frac{2}{L/D_h}\right] \quad (11\text{-}1)$$

Applicable for: 3,400≲*Re*≲4,600;
L/D_h=50
Type of fluid: Single-phase water
Maximum discrepancy: 2%
Mean discrepancy: 2%

Inverted Fish Scale (IFS) microchannels

$$f_{IFS} = \frac{1}{Re^{0.15}}\left[0.2 + \frac{2}{L/D_h} + \frac{15(e/H)^{1.2}}{(P/e)^{1}}\right]$$

Applicable for: *Pr*≈5.5; L/D_h=50
Type of fluid: Single-phase water
Maximum discrepancy: 13%
Mean discrepancy: 4%

***e*/*H* ratio**	***P*/*e* ratio**	**Applicable *Re* range**
0.1	10	4,000≲*Re*≲4,600
0.3	10	900≲*Re*≲4,600
0.5	10	700≲*Re*≲4,600
0.7	10	600≲*Re*≲4,600
0.5	20	1,300≲*Re*≲4,600
0.5	15	800≲*Re*≲4,600
0.5	5	800≲*Re*≲4,600

Fish Scale (FS) microchannels

$$f_{FS} = \frac{1}{Re^{0.15}}\left[0.2 + \frac{2}{L/D_h} + \frac{7(e/H)^{1.6}}{(P/e)^{0.7}}\right]$$

Applicable for: $Pr \approx 5.5$; $L/D_h = 50$
Type of fluid: Single-phase water
Maximum discrepancy: 11%
Mean discrepancy: 3%

***e*/*H* ratio**	***P*/*e* ratio**	**Applicable *Re* range**
0.1	10	$3{,}400 \lesssim Re \lesssim 4{,}600$
0.3	10	$2{,}400 \lesssim Re \lesssim 4{,}600$
0.5	10	$1{,}800 \lesssim Re \lesssim 4{,}600$
0.7	10	$700 \lesssim Re \lesssim 4{,}600$
0.5	20	$2{,}300 \lesssim Re \lesssim 4{,}600$
0.5	15	$2{,}300 \lesssim Re \lesssim 4{,}600$
0.5	5	$1{,}800 \lesssim Re \lesssim 4{,}600$

Durian (D) microchannels

$$f_D = \frac{1}{Re^{0.15}}\left[0.2 + \frac{2}{L/D_h} + \frac{18(e/H)^{1.1}}{(P/e)^{4/3}}\right]$$

Applicable for: $Pr \approx 5.5$; $L/D_h = 50$
Type of fluid: Single-phase water
Maximum discrepancy: 12%
Mean discrepancy: 4%

***e*/*H* ratio**	***P*/*e* ratio**	**Applicable *Re* range**
0.1	10	Not applicable
0.3	10	$2{,}000 \lesssim Re \lesssim 4{,}600$
0.5	10	$1{,}000 \lesssim Re \lesssim 4{,}600$
0.7	10	$1{,}300 \lesssim Re \lesssim 4{,}600$
0.5	20	$2{,}000 \lesssim Re \lesssim 4{,}600$
0.5	15	$1{,}800 \lesssim Re \lesssim 4{,}600$
0.5	5	$1{,}800 \lesssim Re \lesssim 4{,}600$

11.2 Recommendations for Future Work

11.2.1 Extend the Applicability Range of the New Correlations

The newly proposed correlations are only applicable for a limited range, and may not be useful for predictions beyond the current measurement limits. The range of *e*/*H* ratio in the present study is from 0 to 0.7. However, the upper limit of the *e*/*H* ratio can reach up to 2. As illustrated in Figure 11-1, *e*/*H* ratio = 0 corresponds to the Plain microchannel, whereas *e*/*H* ratio = 2 corresponds to the case where the tip of the scale is in contact with the heated copper wall, and the fluid cannot flow through.

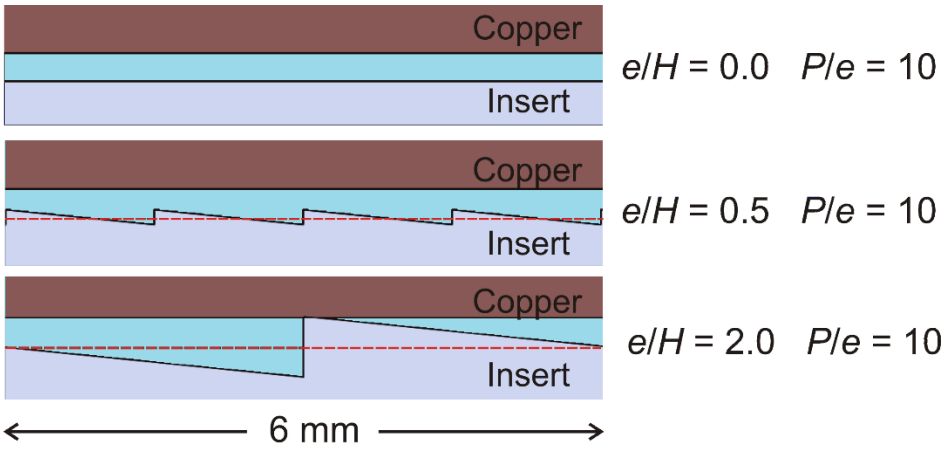

Figure 11-1: Practical limits of *e*/*H* ratio

The range of *P*/*e* ratio in the present study is from 5 to 20. However, the lower and upper limits of the *P*/*e* ratio are 0 and infinity, respectively. For a given scale height (*e*), *P*/*e* ratio = 0 implies that the scale pitch is 0. This corresponds to a Plain microchannel with a reduced gap size of (300 – *e*/2) µm. There are two cases where the *P*/*e* ratio tends to infinity, namely when the scale height is 0 and when the scale pitch tends to infinity. Both cases are reduced to the Plain microchannel with a gap size of 300 µm.

Table 11-17 shows the predictions of Nusselt number and friction factor by the newly proposed correlations at $Re \approx 2{,}664$. For the first three cases, the predictions need to be further verified. For case 4 where e/H ratio = 2, the correlations predict a finite value for both the Nusselt number and friction factor, even though there is no flow. For case 5 where P/e ratio = 0, the correlations predict an infinite value for both the Nusselt number and friction factor, when it should be a finite value. For the last two cases, the correlations offer reliable predictions. Therefore, further numerical and/or experimental investigations are recommended to extend the applicability range of the newly proposed correlations.

Table 11-17: Prediction of Nusselt number and friction factor by new correlations at $Re \approx 2{,}664$

Case	e/H ratio	P/e ratio	Scale height (mm)	Number of scales/thorns	Nusselt number			Friction factor		
					IFS	FS	D	IFS	FS	D
1	1	10	0.3	10	47	46	49	0.53	0.50	0.33
2	0.5	1	0.15	200	73	32	46	2.07	0.78	2.65
3	1	1	0.3	100	137	58	92	4.67	2.22	5.59
4	2	10	0.6	5	Finite			Finite		
5	(0,2)	0	(0,0.6)	-	Infinity			Infinity		
6	(0,2)	Infinity	(0,0.6)	-	Plain			Plain		
7	0	(0, infinity)	0	-	Plain			Plain		

11.2.2 Translate the New Correlations for Practical Applications

For practical use by design engineers, it is recommended to present the correlations as a graphical plot of Nusselt number/friction factor as a function of Re, e/H and P/e, similar to the well-established Moody diagram. As such, the Nusselt number/friction factor can be easily and quickly determined by referring to the graphical plots, for specified values of Re, e/H and P/e. Conversely, for a desired value of Nusselt number/friction factor, the corresponding geometrical dimensions to be used at various flow conditions could be promptly known without involving complex calculations.

For the correlations to be practically usable in design applications, they must be insensitive to machining tolerance. The predictions from the correlations should give roughly the same value, when the geometrical parameters are fabricated within a specified machining tolerance. It is recommended to verify this first before publishing the graphical plots for real-world applications.

11.2.3 Combine the Three Microchannel Series into One Series

It appears that the three enhanced microchannel series could possibly be combined into one series, where the profiles could be mathematically described by two additional angles, α and β. As illustrated in Figure 11-2, $\alpha = \tan^{-1}(e/P)$ and $\beta = 90°$ for the FS profile, while $\alpha = \beta = \tan^{-1}(2e/P)$ for the D profile. On the other hand, $\alpha = 90°$ and $\beta = \tan^{-1}(e/P)$ for the IFS profile.

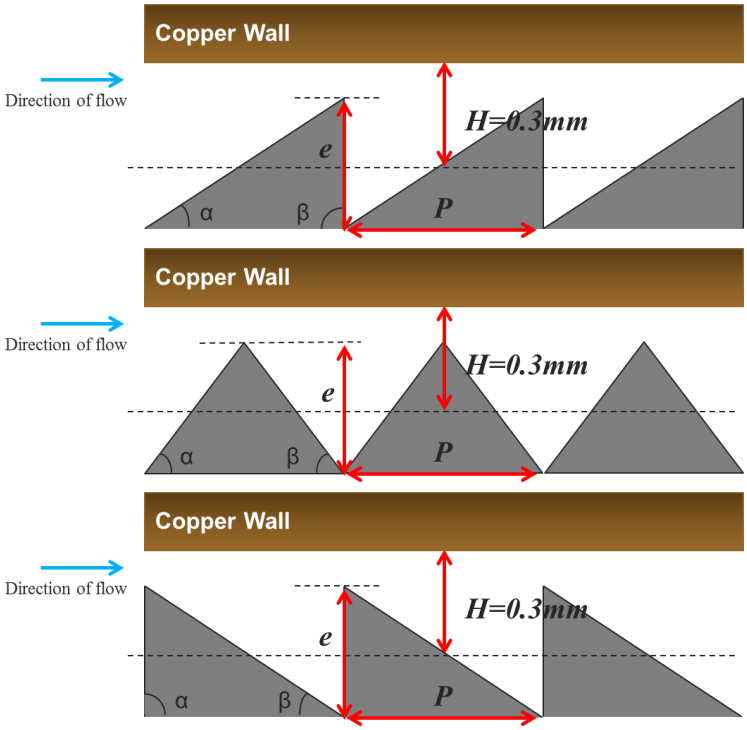

Figure 11-2: Profile parameters for the nature-inspired microchannel series

However, it may not be possible to simply classify all the profiles into one series, since the nature of flow differs among the IFS, FS and D microchannel series. Nonetheless, it would be practically useful to have a single correlation to describe the flow/heat transfer behaviour for all the three nature-inspired enhanced microchannel series.

11.2.4 Investigate Configurations with Varying Angles of Attack

The current investigation deals with a maximum α/β value of 90°. Further investigations could be conducted on configurations where α/β exceeds 90°, as illustrated in Figure 11-3. However, caution must be taken when designing the insert profiles, such that they can be practically fabricated using conventional machining processes.

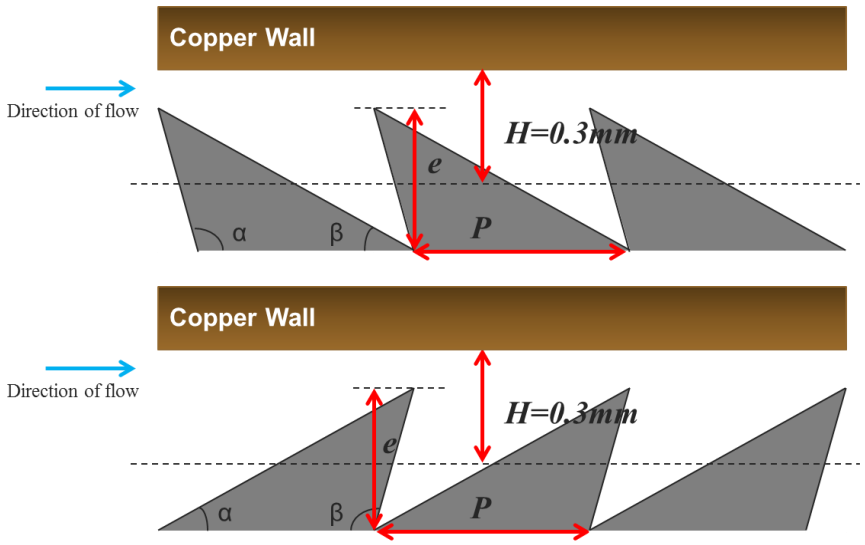

Figure 11-3: New configurations with α/β > 90°

11.2.5 Extend the Range of the Measurement System

The current measurement system is designed for a flow rate of up to 10 L/min, pressure drop of 3.5 bars, and heat rate of 2000 W or heat flux of 106 W/cm^2. As a result of the pressure drop limit, the Reynolds number range in the present study is between 350 and 4,600. It would be useful to extend the Reynolds number range to more than 4,600, in order to study the flow in the turbulent regime. In addition, the higher heat transfer coefficient values which could be achieved at higher Reynolds number are yet to be known. Hence, it is recommended to improve the measurement system to allow for a higher pressure drop, in order to extend the Reynolds number range to beyond 4,600.

11.2.6 Apply the Enhancement Profiles on the Heat Transfer Surface

In the present study, the enhancement profiles are introduced on the non-heated insert surface, while the heat is supplied to the opposite copper surface. The design intention is to increase the heat transfer coefficient by using the enhancement profiles to disturb the velocity and thermal boundary layers, thus improving the heat transfer for a fixed heat transfer surface area. Furthermore, it is practically simpler and relatively straightforward to fabricate the test module for the purpose of this study. By fixing the heating cable onto the copper block, the test pieces i.e. the inserts with the enhancement profiles could easily be removed and installed into the test module, without the tricky issue of having to supply heat to the test pieces.

On the other hand, future work could focus on introducing the enhancement profiles on the heat transfer surface. The new test module could be designed to supply heat to the test pieces. Should this tricky issue be resolved, there is great potential to achieve a significant improvement in heat transfer, since the heat transfer coefficient and heat transfer surface area are simultaneously increased.

11.2.7 Reducing the Friction Factor using Constructal Theory

While the pressure drop values are less than 3.5 bars in the present study, it is observed that the friction factor of the enhanced IFS microchannel can reach up to 6.7 times that of the Plain microchannel. In addition, the normalised friction factor is often higher than the normalised Nusselt number. This means that the percentage increase in friction factor is often higher than the percentage increase in Nusselt number. It is worthy to look into a new enhancement profile which can achieve a lower percentage increase in friction factor relative to the percentage increase in Nusselt number. This would result in a high thermo-hydraulic performance in excess of 67%, which is the maximum value achieved in the present study.

It is interesting to consider the Constructal theory [118–120] in the design of the new enhancement profiles. Introduced by Bejan in 1996 [167], the Constructal law states that "For a finite-size system to persist in time (to live), it must evolve in such a way that it provides easier access to the imposed currents that flow through it." In essence, the Constructal theory can be understood as the inverse of biomimicry. Instead of looking to nature/biology to guide design, the Constructal theory involves understanding the Constructal law, and applying the rules and principles of this law in the design process.

A preliminary study has been conducted, in which two insert enhancement profiles were designed based on the Constructal theory, in the attempt to reduce the flow resistance of the microscale flow. The two designs, namely the Tree and Cfin inserts, are shown in Figure 11-4 and Figure 11-5.

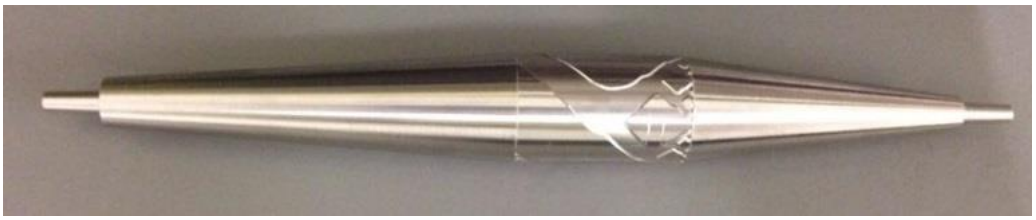

Figure 11-4: Tree insert

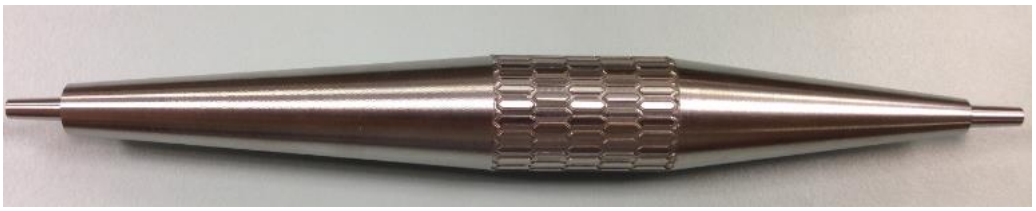

Figure 11-5: Constructal fin (Cfin) insert

The preliminary results show that the heat transfer coefficient increased by at least 30% with only 20% increase in pressure drop at 2 L/min using the Cfin insert, relative to a control insert. Analysis of the results suggests that the bifurcation of flow is effective in reducing the increment in pressure drop relative to heat transfer enhancement. More details can be found in the conference publication [168].

The research on designing new enhancement profiles based on the Constructal theory is still ongoing. Since the Cfin insert shows potential to achieve a high thermo-hydraulic performance, the ongoing research is focused on the variation of the fin height and the bifurcation angle. Optimising the geometrical parameters of the Constructal fins on the insert surface could possibly lead to exciting breakthroughs in the research on enhanced microscale heat transfer in macro geometry.

List of Publications

[1] A.L. Goh, K.T. Ooi, Nature-inspired Inverted Fish Scale microscale passages for enhanced heat transfer, Int. J. Therm. Sci. 106 (2016) 18–31.

[2] A. Deshpande, A.L. Goh, A. Goossens, S. Javdani, Biomimicry for coastal eco-cities: Towards a carbon neutral Dover, UK, University of Southampton, 2013. ISBN: 9780854329717

[3] A.L. Goh, K.T. Ooi, U. Stimming, Nature-inspired Enhanced Microscale Heat Transfer in Macro Geometry, in: Intersoc. Conf. Therm. Thermomechanical Phenom. Electron. Syst., IEEE, Orlando, FL, USA, 2014: pp. 397–403.

[4] A.L. Goh, B. Han, K.T. Ooi, Experimental Study of Nature-inspired Enhanced Microscale Heat Transfer, in: 5th Micro/Nanoscale Heat Mass Transf. Int. Conf., ASME, Singapore, 2016: p. 6733.

[5] K.X. Cheng, A.L. Goh, K.T. Ooi, Reducing Pressure Drop in Microscale Channel Using Constructal Theory, in: 18th Int. Conf. Heat Transf. Appl., WASET, London, 2016: pp. 170–178.

[6] K.T. Ooi, A.L. Goh, Enhanced Microchannel Heat Transfer in Macro-Geometry using Conventional Fabrication Approach, in: 7th Eur. Therm. Conf., Krakow, Poland, 2016.

List of References

[1] D.B. Tuckerman, R.F.W. Pease, High-performance heat sinking for VSLI, Electron Device Lett. 2 (1981) 126–129.

[2] T. Bayraktar, S.B. Pidugu, Characterization of liquid flows in microfluidic systems, Int. J. Heat Mass Transf. 49 (2006) 815–824.

[3] G.L. Morini, Single-phase Convective Heat Transfer in Microchannels: A Review of Experimental Results, Int. J. Therm. Sci. 43 (2004) 631–651.

[4] Y. Fan, L. Luo, Recent Applications of Advances in Microchannel Heat Exchangers and Multi-Scale Design Optimization, Heat Transf. Eng. 29 (2008) 461–474.

[5] M.G. Khan, A. Fartaj, A review on microchannel heat exchangers and potential applications, Int. J. Energy Res. 35 (2011) 553–582.

[6] N.T. Obot, Toward a better understanding of friction and heat/mass transfer in microchannels — a literature review, Microscale Thermophys. Eng. 6 (2002) 155–173.

[7] B. Agostini, M. Fabbri, J.E. Park, L. Wojtan, J.R. Thome, B. Michel, State of the Art of High Heat Flux Cooling Technologies, Heat Transf. Eng. 28 (2007) 258–281.

[8] S.G. Kandlikar, S. Colin, Y. Peles, S. Garimella, R.F. Pease, J.J. Brandner, D.B. Tuckerman, Heat Transfer in Microchannels — 2012 Status and Research Needs, ASME J. Heat Transf. 135 (2013) 091001.

[9] M.E. Steinke, S.G. Kandlikar, Single-phase heat transfer enhancement techniques in microchannel and minichannel flows, in: ASME 2004 2nd Int. Conf. Microchannels Minichannels, ASME, Rochester, NY, USA, 2004: pp. 141–148.

[10] T. Kishimoto, S. Sasaki, Cooling characteristics of diamond-shaped interrupted cooling fin for high-power LSI devices, Electron. Lett. 23 (1987) 456–457.

[11] K.S. Kong, K.T. Ooi, A numerical and experimental investigation on microscale heat transfer effect in the combined entry region in macro geometries, Int. J. Therm. Sci. 68 (2013) 8–19.

[12] K.S. Kong, Enhanced Microscale Heat Transfer in Macro Geometries, Ph.D. Thesis, Nanyang Technological University, 2014.

[13] T.L. Bergman, A.S. Lavine, F.P. Incropera, D.P. Dewitt, Fundamentals of Heat and Mass Transfer, 7th ed., John Wiley & Sons, 2011.

[14] S. Kakaç, R.K. Shah, W. Aung, Handbook of Single-phase Convective Heat Transfer, Wiley, New York, 1987.

[15] J.F. Douglas, J.M. Gasiorek, J.A. Swaffield, Fluid Mechanics, 4th ed., Prentice Hall, 2001.

[16] W. George, Is there a universal log law for turbulent wall-bounded flows?, Trans. R. Soc. 365 (2007) 789–806.

[17] W.M. Kays, M.E. Crawford, B. Weigand, Convective heat and mass transfer, 4th ed., McGraw-Hill Higher Education, Boston, 2005.

[18] R.K. Shah, A.L. London, Laminar flow forced convection in ducts - Supplement 1 to Advances in Heat Transfer, Academic Press, New York, 1978.

[19] A. Faghri, Y. Zhang, J. Howell, Advanced Heat and Mass Transfer, Global Digital Press, 2010.

[20] R.D. Blevins, Applied Fluid Dynamics Handbook, Van Nostrand Reinhold Company Inc, New York, N.Y., 1984.

[21] Y.A. Çengel, Heat and Mass Transfer: A Practical Approach, 3rd ed., Mcgraw-Hill Education, 2006.

[22] R.J. Phillips, Forced-Convection, Liquid-Cooled, Microchannel Heat Sinks, M.S. Thesis, Massachusetts Institute of Technology, 1987.

[23] P.R.H. Blasius, Das Aehnlichkeitsgesetz bei Reibungsvorgangen in Flüssigkeiten, Forschungsheft. 131 (1913) 1–41.

[24] Y. Taitel, A.E. Dukler, A model for predicting flow regime transition in horizontal and near horizontal gas-liquid flow, AIChE J. 22 (1976) 47–55.

[25] B.S. Petukhov, Heat Transfer and Friction in Turbulent Pipe Flow with Variable Physical Properties, Adv. Heat Transf. 6 (1970) 503–564.

[26] C.F. Colebrook, Turbulent Flow in Pipes, with Particular Reference to the Transition Region between the Smooth and Rough Pipe Laws, J. Inst. Civ. Eng. 11 (1939) 133–156.

[27] A. Bejan, Heat Transfer, Wiley, New York, 1993.

[28] W.M. Kays, M.E. Crawford, Convective Heat and Mass Transfer, McGraw-Hill, New York, 1993.

[29] D.K. Edwards, V.E. Denny, A.F. Mills, Transfer Processes, 2nd ed., Hemisphere, Washington, DC, 1979.

[30] H. Hausen, Neue Gleichungen fur dieWarmeubertragung bei freier oder erzwungener Stromung, Allg. Waermetechnik. 9 (1959) 75–79.

[31] E.N. Sieder, G.E. Tate, Heat Transfer and Pressure Drop of Liquids in Tubes, Ind. Eng. Chem. 28 (1936) 1429–1435.

[32] W.H. McAdams, Heat Transmission, 2nd ed., McGraw-Hill, New York, 1942.

[33] G. Filonenko, Hydraulic Resistance in Pipes, Teploenergetika. 1 (1954) 40–44.

[34] V. Gnielinski, New Equations for Heat and Mass Transfer in Turbulent Pipe and Channel Flow, Int. Chem. Eng. 16 (1976) 359–368.

[35] R.K. Shah, A Correlation for Laminar Hydrodynamic Entry Length Solutions for Circular and Noncircular Ducts, J. Fluids Eng. 100 (1978) 177–179.

[36] S.G. Kandlikar, History, Advances, and Challenges in Liquid Flow and Flow Boiling Heat Transfer in Microchannels: A Critical Review, ASME J. Heat Transf. 134 (2012) 034001–1.

[37] S.G. Kandlikar, Fundamental issues related to flow boiling in minichannels and microchannels, Exp. Therm. Fluid Sci. 26 (2002) 389–407.

[38] J.B. Marcinichen, J.A. Olivier, V. de Oliveira, J.R. Thome, A review of on-chip micro-evaporation: Experimental evaluation of liquid pumping and vapor compression driven cooling systems and control, Appl. Energy. 92 (2012) 147–161.

[39] A.E. Bergles, M.K. Jensen, B. Shome, The Literature on Enhancement of Convective Heat and Mass Transfer, J. Enhanc. Heat Transf. 4 (1996) 1–6.

[40] Z.S. Kareem, M.N. Mohd Jaafar, T.M. Lazim, S. Abdullah, A.F. Abdulwahid, Passive heat transfer enhancement review in corrugation, Exp. Therm. Fluid Sci. 68 (2015) 22–38.

[41] C.A. Balaras, A review of augmentation techniques for heat transfer surfaces in single-phase heat exchangers, Energy. 15 (1990) 899–906.

[42] A.E. Bergles, Recent developments in enhanced heat transfer, Heat Mass Transf. Und Stoffuebertragung. 47 (2011) 1001–1008.

[43] W.Q. Tao, Y.L. He, Q.W. Wang, Z.G. Qu, F.Q. Song, A unified analysis on enhancing single phase convective heat transfer with field synergy principle, Int. J. Heat Mass Transf. 45 (2002) 4871–4879.

[44] J. Xu, Y. Gan, D. Zhang, X. Li, Microscale heat transfer enhancement using thermal boundary layer redeveloping concept, Int. J. Heat Mass Transf. 48 (2005) 1662–1674.

[45] J. Xu, Y. Song, W. Zhang, H. Zhang, Y. Gan, Numerical simulations of interrupted and conventional microchannel heat sinks, Int. J. Heat Mass Transf. 51 (2008) 5906–5917.

[46] Y.J. Lee, P.K. Singh, P.S. Lee, Fluid flow and heat transfer investigations on enhanced microchannel heat sink using oblique fins with parametric study, Int. J. Heat Mass Transf. 81 (2015) 325–336.

[47] D. Deng, W. Wan, Y. Tang, H. Shao, Y. Huang, Experimental and numerical study of thermal enhancement in reentrant copper microchannels, Int. J. Heat Mass Transf. 91 (2015) 656–670.

[48] Y. Sui, C.J. Teo, P.S. Lee, Y.T. Chew, C. Shu, Fluid flow and heat transfer in wavy microchannels, Int. J. Heat Mass Transf. 53 (2010) 2760–2772.

[49] Y. Sui, P.S. Lee, C.J. Teo, An experimental study of flow friction and heat transfer in wavy microchannels with rectangular cross section, Int. J. Therm. Sci. 50 (2011) 2473–2482.

[50] G. Yang, Z.F. Dong, M.A. Ebadian, Laminar forced convection in a helicoidal pipe with finite pitch, Int. J. Heat Mass Transf. 38 (1995) 853–862.

[51] L. Wang, T. Yang, Bifurcation and stability of forced convection in curved ducts of square cross-section, Int. J. Heat Mass Transf. 47 (2004) 2971–2987.

[52] C.. Kalb, J.. Seader, Heat and mass transfer phenomena for viscous flow in curved circular tubes, Int. J. Heat Mass Transf. 15 (1972) 801–817.

[53] H.A. Mohammed, P. Gunnasegaran, N.H. Shuaib, Numerical simulation of heat transfer enhancement in wavy microchannel heat sink, Int.

Commun. Heat Mass Transf. 38 (2011) 63–68.

[54] R.. Webb, E.R.. Eckert, Application of rough surfaces to heat exchanger design, Int. J. Heat Mass Transf. 15 (1972) 1647–1658.

[55] D.L. Gee, R.L. Webb, Forced convection heat transfer in helically rib-roughened tubes, Int. J. Heat Mass Transf. 23 (1980) 1127–1136.

[56] P.M. Ligrani, M.M. Oliveira, T. Blaskovich, Comparison of Heat Transfer Augmentation Techniques, AIAA J. 41 (2003) 337–362.

[57] M.E. Taslim, Darryl E. Metzger Memorial Session Paper: Experimental Heat Transfer and Friction in Channels Roughened With Angled, V-Shaped, and Discrete Ribs on Two Opposite Walls, J. Turbomach. 118 (2008) 20.

[58] J.C. Han, J.S. Park, Developing heat transfer in rectangular channels with rib turbulators, Int. J. Heat Mass Transf. 31 (1988) 183–195.

[59] X. Gao, B. Sundén, Heat transfer and pressure drop measurements in rib-roughened rectangular ducts, Exp. Therm. Fluid Sci. 24 (2001) 25–34.

[60] P.S. Kathait, A.K. Patil, Thermo-hydraulic performance of a heat exchanger tube with discrete corrugations, Appl. Therm. Eng. 66 (2014) 162–170.

[61] J. Marschewski, R. Brechbühler, S. Jung, P. Ruch, B. Michel, D. Poulikakos, Significant heat transfer enhancement in microchannels with herringbone-inspired microstructures, Int. J. Heat Mass Transf. 95 (2016) 755–764.

[62] M. Asadi, G. Xie, B. Sunden, A review of heat transfer and pressure drop characteristics of single and two-phase microchannels, Int. J. Heat Mass Transf. 79 (2014) 34–53.

[63] C.B. Sobhan, S. V. Garimella, A comparative analysis of studies on heat transfer and fluid flow in microchannels, Microscale Thermophys. Eng. 5 (2001) 293–311.

[64] G.L. Morini, M. Lorenzini, S. Salvigni, M. Spiga, Thermal performance of silicon micro heat-sinks with electrokinetically-driven flows, Int. J. Therm. Sci. 45 (2006) 955–961.

[65] M.J. Kohl, S.I. Abdel-Khalik, S.M. Jeter, D.L. Sadowski, An experimental investigation of microchannel flow with internal pressure measurements, Int. J. Heat Mass Transf. 48 (2005) 1518–1533.

[66] G.L. Morini, M. Lorenzini, S. Salvigni, M. Spiga, Analysis of laminar-to-turbulent transition for isothermal gas flows in microchannels, Microfluid. Nanofluidics. 7 (2008) 181–190.

[67] G.H. Tang, Z. Li, Y.L. He, W.Q. Tao, Experimental study of compressibility, roughness and rarefaction influences on microchannel flow, Int. J. Heat Mass Transf. 50 (2007) 2282–2295.

[68] K. Vijayalakshmi, K.B. Anoop, H.E. Patel, P.V. Harikrishna, T. Sundararajan, S.K. Das, Effects of compressibility and transition to turbulence on flow through microchannels, Int. J. Heat Mass Transf. 52 (2009) 2196–2204.

[69] Z. Liu, C. Zhang, Y. Huo, X. Zhao, Flow and Heat Transfer in Rough Micro Steel Tubes, Exp. Heat Transf. 20 (2007) 289–306.

[70] P. Wu, W.A. Little, Measurement of friction factors for the flow of gases in very fine channels used for microminiature Joule-Thomson refrigerators, Cryogenics (Guildf). 23 (1983) 273–277.

[71] C.Y. Yang, J.C. Wu, H.T. Chien, S.R. Lu, Friction characteristics of water, R-134a and air in small tubes, Microscale Thermophys. Eng. 7 (2003) 335–348.

[72] D. Yu, R.O. Warrington, R. Barron, T. Ameel, An experimental and theoretical investigation of fluid flow and heat transfer in microtubes, in: ASME/JSME Therm. Eng. Jt. Conf., ASME/JSME, Maui, 1995: pp. 523–530.

[73] Z.X. Li, D.X. Du, Z.Y. Guo, Experimental Study on Flow Characteristics of Liquid in Circular Microtubes, Microscale Thermophys. Eng. 7 (2003) 253–265.

[74] S.B. Choi, R.F. Barron, R.O. Warrington, Fluid flow and heat transfer in microtubes, in: Micromechanical Sensors, Actuators Syst. ASME DSC, ASME, Georgia, 1991: pp. 123–134.

[75] V. Kumar, M. Paraschivoiu, K.D.P. Nigam, Single-phase fluid flow and mixing in microchannels, Chem. Eng. Sci. 66 (2011) 1329–1373.

[76] G.P. Celata, Single-Phase Heat Transfer and Fluid Flow in Micropipes, Heat Transf. Eng. 25 (2004) 13–22.

[77] X.F. Peng, B.X. Wang, G.P. Peterson, H.B. Ma, Experimental investigation of heat transfer in flat plates with rectangular microchannels, Int. J. Heat Mass Transf. 38 (1995) 127–137.

[78] X.F. Peng, B.-X. Wang, Forced convection and flow boiling heat transfer for liquid flowing through microchannels, Int. J. Heat Mass Transf. 36 (1993) 3421–3427.

[79] X.F. Peng, G.P. Peterson, Convective heat transfer and flow friction for water flow in microchannel structures, Int. J. Heat Mass Transf. 39 (1996) 2599–2608.

[80] W. Qu, G.M. Mala, D. Li, Heat transfer for water flow in trapezoidal silicon microchannels, Int. J. Heat Mass Transf. 43 (2000) 3925–3936.

[81] B.X. Wang, X.F. Peng, Experimental investigation on liquid forced-convection heat transfer through microchannels, Int. J. Heat Mass Transf. 37 (1994) 73–82.

[82] P. Gao, S. Le Person, M. Favre-Marinet, Scale effects on hydrodynamics and heat transfer in two-dimensional mini and microchannels, Int. J. Therm. Sci. 41 (2002) 1017–1027.

[83] S.G. Kandlikar, W.J. Grande, Evolution of Microchannel Flow Passages--Thermohydraulic Performance and Fabrication Technology, Heat Transf. Eng. 24 (2003) 3–17.

[84] M.M. Rahman, Measurements of heat transfer in microchannel heat sinks, Int. Commun. Heat Mass Transf. 27 (2000) 495–506.

[85] P.-F. Hao, F. He, K.-Q. Zhu, Flow characteristics in a trapezoidal silicon microchannel, J. Micromechanics Microengineering. 15 (2005) 1362–1368.

[86] T.M. Adams, S.I. Abdel-Khalik, S.M. Jeter, Z.H. Qureshi, An experimental investigation of single-phase forced convection in microchannels, Int. J. Heat Mass Transf. 41 (1998) 851–857.

[87] T.S. Ravigururajan, Impact of Channel Geometry on Two-Phase Flow Heat Transfer Characteristics of Refrigerants in Microchannel Heat Exchangers, J. Heat Transfer. 120 (1998) 485.

[88] G.R. Warrier, C.-J. Kim, Y. Sungtaek Ju, Microchannel cooling device with perforated side walls: Design and modeling, Int. J. Heat Mass Transf. 68 (2014) 174–183.

[89] W. Qu, I. Mudawar, Experimental and numerical study of pressure drop and heat transfer in a single-phase micro-channel heat sink, Int. J. Heat Mass Transf. 45 (2002) 2549–2565.

[90] H.. Wu, P. Cheng, An experimental study of convective heat transfer in

silicon microchannels with different surface conditions, Int. J. Heat Mass Transf. 46 (2003) 2547–2556.

[91] T.M. Harms, M.J. Kazmierczak, F.M. Gerner, Developing convective heat transfer in deep rectangular microchannels, Int. J. Heat Fluid Flow. 20 (1999) 149–157.

[92] R.E. Acosta, R.H. Muller, C.W. Tobias, Transport processes in narrow (capillary) channels, AIChE J. 31 (1985) 473–482.

[93] A. Bucci, G.P. Celata, M. Cumo, E. Serra, G. Zummo, Water Single-Phase Fluid Flow and Heat Transfer in Capillary Tubes, in: 1st Int. Conf. Microchannels Minichannels, ASME, 2003: pp. 319–326.

[94] T.. Adams, M.. Dowling, S.. Abdel-Khalik, S.. Jeter, Applicability of traditional turbulent single-phase forced convection correlations to non-circular microchannels, Int. J. Heat Mass Transf. 42 (1999) 4411–4415.

[95] X.F. Peng, G.P. Peterson, B.X. Wang, Frictional Flow Characteristics of water flowing through rectangular microchannels, Exp. Heat Transf. 7 (1994) 249–264.

[96] W. Qu, G.M. Mala, D. Li, Pressure-driven water flows in trapezoidal silicon microchannels, Int. J. Heat Mass Transf. 43 (2000) 353–364.

[97] B. Xu, K.T. Ooi, N.T. Wong, W.K. Choi, Experimental investigation of flow friction for liquid flow in microchannels, Int. Commun. Heat Mass Transf. 27 (2000) 1165–1176.

[98] P.-X. Jiang, M.-H. Fan, G.-S. Si, Z.-P. Ren, Thermal–hydraulic performance of small scale micro-channel and porous-media heat-exchangers, Int. J. Heat Mass Transf. 44 (2001) 1039–1051.

[99] J. Judy, D. Maynes, B.W. Webb, Characterization of frictional pressure drop for liquid flows through microchannels, Int. J. Heat Mass Transf. 45 (2002) 3477–3489.

[100] D. Liu, S. V. Garimella, Investigation of Liquid Flow in Microchannels, J. Thermophys. Heat Transf. 18 (2004) 65–72.

[101] X.F. Peng, G.P. Peterson, B.X. Wang, Heat Transfer Characteristics of Water Flowing Through Microchannels, Exp. Heat Transf. 7 (1994) 265–283.

[102] N.T. Nguyen, D. Bochnia, R. Kiehnscherf, W. Dötzel, Investigation of forced convection in microfluid systems, Sensors Actuators A Phys. 55 (1996) 49–55.

[103] Z.-Y. Guo, Z.-X. Li, Size effect on single-phase channel flow and heat transfer at microscale, Int. J. Heat Fluid Flow. 24 (2003) 284–298.

[104] M.E. Steinke, S.G. Kandlikar, Control and effect of dissolved air in water during flow boiling in microchannels, Int. J. Heat Mass Transf. 47 (2004) 1925–1935.

[105] P.S. Lee, S. V. Garimella, D. Liu, Investigation of heat transfer in rectangular microchannels, Int. J. Heat Mass Transf. 48 (2005) 1688–1704.

[106] M.E. Steinke, S.G. Kandlikar, Single-phase liquid friction factors in microchannels, Int. J. Therm. Sci. 45 (2006) 1073–1083.

[107] G. Mohiuddin Mala, D. Li, Flow characteristics of water in microtubes, Int. J. Heat Fluid Flow. 20 (1999) 142–148.

[108] G.P. Celata, M. Cumo, M. Guglielmi, G. Zummo, Experimental Investigation of Hydraulic and Single Phase Heat Transfer in 0.130μm CapillaryTube, Microscale Thermophys. Eng. 6 (2002) 85–97.

[109] K. V. Sharp, R.J. Adrian, Transition from laminar to turbulent flow in liquid filled microtubes, Exp. Fluids. 36 (2004) 741–747.

[110] F.J. Gui, R.P. Scaringe, Enhanced heat transfer in the entrance region of microchannels, in: 30th Intersoc. Energy Convers. Eng. Conf., 1995: pp. 289–294.

[111] X.F. Peng, G.P. Peterson, The effect of thermofluid and geometrical parameters on convection of liquids through rectangular microchannels, Int. J. Heat Mass Transf. 38 (1995) 755–758.

[112] L.S. Ding, H. Sun, X.L. Sheng, B.D. Lee, Measurement of Friction Factors for R134A and R12 Through Microchannels, in: Proc. Symp. Energy Eng. 21st Century, 2000: pp. 650–657.

[113] D. Pfund, D. Rector, A. Shekarriz, A. Popescu, J. Welty, Pressure drop measurements in a microchannel, AIChE J. 46 (2000) 1496–1507.

[114] F. Debray, J.P. Franc, T. Maı̂tre, S. Reynaud, Mesure des coefficients de transfert thermique par convection forcée en mini-canaux, Mécanique Ind. 2 (2001) 443–454.

[115] H.E. Hegab, A. Bari, T. Ameel, Friction and Convection Studies of R-134a in Microchannels within the Transition and Turbulent Flow Regimes, Exp. Heat Transf. 15 (2002) 245–259.

[116] H. Schlichting, Boundary Layer Theory, McGraw-Hill, New York, 1979.

[117] A. Bejan, Convection Heat Transfer, 4th ed., John Wiley & Sons, Inc., Hoboken, NJ, USA, 2013.

[118] A. Bejan, Shape and Structure, from Engineering to Nature, Cambridge University Press, Cambridge, UK, 2000.

[119] A. Bejan, J.P. Zane, Design in Nature, Doubleday, New York, 2012.

[120] A. Bejan, The Physics of Life, St. Martin's Press, New York, 2016.

[121] J.M. Benyus, Biomimicry: Innovation Inspired By Nature, HarperCollins, 1997.

[122] R. Paul, Design Inspiration from Nature – Biomimicry for a Better Planet, Inhabitat. (2016). http://inhabitat.com/finding-design-inspiration-in-nature-biomimicry-for-a-better-planet/ (accessed May 26, 2016).

[123] The Biomimicry Institute, Shinkansen Train, Ask Nat. (2016). www.asknature.org (accessed May 26, 2016).

[124] R. Mittal, H. Dong, M. Bozkurttas, G. Lauder, P. Madden, Locomotion with flexible propulsors: II. Computational modeling of pectoral fin swimming in sunfish., Bioinspir. Biomim. 1 (2006) S35–S41.

[125] Y. Yang, N. Nguyen, N. Chen, M. Lockwood, C. Tucker, H. Hu, H. Bleckmann, C. Liu, D.L. Jones, Artificial lateral line with biomimetic neuromasts to emulate fish sensing., Bioinspir. Biomim. 5 (2010) 16001.

[126] H.-T. Lin, G.G. Leisk, B. Trimmer, GoQBot: a caterpillar-inspired soft-bodied rolling robot., Bioinspir. Biomim. 6 (2011) 026007.

[127] R. Dewan, S. Fischer, V.B. Meyer-Rochow, Y. Özdemir, S. Hamraz, D. Knipp, Studying nanostructured nipple arrays of moth eye facets helps to design better thin film solar cells., Bioinspir. Biomim. 7 (2012) 016003.

[128] C. Greiner, M. Schäfer, Bio-inspired scale-like surface textures and their tribological properties., Bioinspir. Biomim. 10 (2015) 044001.

[129] N. Huebsch, D.J. Mooney, Inspiration and application in the evolution of biomaterials., Nature. 462 (2009) 426–32.

[130] S.W. Chang, T.-M. Liou, M.H. Lu, Heat transfer of rectangular narrow channel with two opposite scale-roughened walls, Int. J. Heat Mass Transf. 48 (2005) 3921–3931.

[131] A. Deshpande, A.L. Goh, A. Goossens, S. Javdani, Biomimicry for coastal eco-cities: Towards a carbon neutral Dover, UK, University of Southampton, 2013.

[132] S. Ashman, S.G. Kandlikar, A Review of Manufacturing Processes for Microchannel Heat Exchanger Fabrication, in: ASME 4th Int. Conf. Nanochannels, Microchannels, Minichannels, ASME, Limerick, Ireland, 2006: pp. 855–860.

[133] A. Koşar, Y. Peles, Thermal-Hydraulic Performance of MEMS-based Pin Fin Heat Sink, J. Heat Transfer. 128 (2006) 121.

[134] A. Dominic, J. Sarangan, S. Suresh, V.S. Devah Dhanush, An Experimental Investigation of Wavy and Straight Minichannel Heat Sinks Using Water and Nanofluids, J. Therm. Sci. Eng. Appl. 7 (2015) 031012.

[135] A.M. Siu-Ho, W. Qu, F. Pfefferkorn, Pressure drop and heat transfer in a single-phase micro-pin-fin heat sink, in: 2006 ASME Int. Mech. Eng. Congr. Expo., ASME, Chicago, IL, United states, 2006.

[136] Y.J. Lee, P.S. Lee, S.K. Chou, Enhanced Thermal Transport in Microchannel Using Oblique Fins, ASME J. Heat Transf. 134 (2012) 101901.

[137] G. Lu, J. Wang, Experimental investigation on heat transfer characteristics of water flow in a narrow annulus, Appl. Therm. Eng. 28 (2008) 8–13.

[138] W. Wagner, A. Pruss, The IAPWS Formulation 1995 for the Thermodynamic Properties of Ordinary Water Substance for General and Scientific Use, J. Phys. Chem. Ref. Data. 31 (2002) 387–535.

[139] J.D. Anderson, Ludwig Prandtl's Boundary Layer, Phys. Today. 58 (2005) 42–48.

[140] ANSYS, ANSYS CFX-Solver Theory Guide, ANSYS Inc., 2011.

[141] O. Reynolds, On the Dynamical Theory of Incompressible Viscous Fluids and the Determination of the Criterion, Philos. Trans. R. Soc. London. A. 186 (1895) 123–164.

[142] J. Boussinesq, Essai sur la Théorie des Equaux Courantes, Mém. Présentés Acad. Sci. 23 (1877) 46.

[143] P.R. Spalart, S.R. Allmaras, A one-equation turbulence model for aerodynamic flows, La Rech. Aérospatiale. 0 (1994) 5–21.

[144] P.Y. Chou, On velocity correlations and the solutions of the equations of turbulent fluctuation, Q. Appl. Math. 3 (1945) 38.

[145] A.N. Kolmogorov, Equations of Turbulent Motion of an Incompressible Fluid, Izv. Acad. Sci. USSR; Phys. 6 (1942) 56–58.

[146] D.C. Wilcox, Turbulence Modeling for CFD, 3rd ed., DCW Industries, Inc, La Canada, CA, 2006.

[147] D.C. Wilcox, Reassessment of the scale-determining equation for advanced turbulence models, AIAA J. 26 (1988) 1299–1310.

[148] D.C. Wilcox, Multiscale Model for Turbulent Flows, AIAA J. 26 (1988) 1311–1320.

[149] F.R. Menter, Influence of freestream values on k-w turbulence model predictions, AIAA J. 30 (1992) 1657–1659.

[150] F.R. Menter, Zonal two-equation k-ω turbulence model for aerodynamic flows, in: AIAA 23rd Fluid Dyn. Plasmadynamics, Lasers Conf., Orlando, FL, 1993: pp. 93–2906.

[151] F.R. Menter, Two-equation eddy-viscosity turbulence models for engineering applications, AIAA J. 32 (1994) 1598–1605.

[152] S.E. Rogers, F.R. Menter, P.A. Durbin, N.N. Mansour, A Comparison Of Turbulence Models In Computing Multi-Element Airfoil Flows, in: AIAA 32nd Aerosp. Sci. Meet. Exhib., Reno, NV, 1994: pp. 94–0291.

[153] ANSYS, ANSYS CFX - Solver Modelling Guide, 2011.

[154] P.J. Roache, Perspective: A method for unifrom reporting of grid refinement studies, ASME J. Fluids Eng. 116 (1994) 405–413.

[155] L.E. Schwer, Is your mesh refined enough? Estimating Discretization Error using GCI, 7th LS-DYNA Anwenderforum. 1 (2008) 45–54.

[156] M.S.M. Ali, C.J. Doolan, V. Wheatley, Grid convergence study for a two-dimensional simulation of flow around a swuare cylinder at a low reynolds number, in: Seventh Int. Conf. CFD Miner. Process Ind., Melbourne, Australia, 2009: pp. 1–6.

[157] A. Dominic, J. Sarangan, S. Suresh, V.S. Devah Dhanush, An Experimental Investigation of Wavy and Straight Minichannel Heat Sinks Using Water and Nanofluids, J. Therm. Sci. Eng. Appl. 7 (2015) 031012–1 – 031012–9.

[158] E.W. Lemmon, M.O. McLinden, M.L. Huber, REFPROP: Reference Fluid Thermodynamic and Transport Properties, NIST Stand. Ref. Database 23. (2007).

[159] S. Bell, A Beginner's Guide to Uncertainty of Measurement, National Physical Laboratory, 2001.

[160] (UKAS), M3003 - The Expression of Uncertainty and Confidence in Measurement, United Kingdom Accreditation Services, 2012.

[161] (JCGM), Evaluation of measurement data—Guide for the expression of uncertainty in measurement, Joint Committee for Guides in Metrology, 2008.

[162] B.N. Taylor, C.E. Kuyatt, NIST Technical Note 1297 1994 Edition - Guidelines for Evaluating and Expressing the Uncertainty of NIST Measurment Results, 1994.

[163] J. Kim, T. Simon, R. Viskanta, Journal of heat transfer policy on reporting uncertainties in experimental measurements and results, J. Heat Transfer. 115 (1993) 5–6.

[164] BIPM, IEC, IFCC, ILAC, IUPAC, IUPAP, ISO, OIML, The international vocabulary of metrology—basic and general concepts and associated terms (VIM), JCGM 200:2008, (2008).

[165] R.W. Hanks, H. Ruo, Laminar-Turbulent Transition in Ducts of Rectangular Cross Section, Ind. Eng. Chem. Fundam. 5 (1966) 558–561.

[166] F.P. Incropera, D.P. DeWitt, Introduction to heat transfer, 5th ed., Wiley, Hobokenm, NJ, 2007.

[167] A. Bejan, Constructal-theory network of conducting paths for cooling a heat generating volume, Int. J. Heat Mass Transf. 40 (1997) 799–816.

[168] K.X. Cheng, A.L. Goh, K.T. Ooi, Reducing Pressure Drop in Microscale Channel Using Constructal Theory, in: 18th Int. Conf. Heat Transf. Appl., WASET, London, 2016: pp. 170–178.

Appendix A – Calibration Procedures

Calibration of Type-J thermocouples

The Type-J thermocouples are connected to the DAQ system, and calibration is carried out for the whole system. Four-point calibration is carried out for the 12 Type-J thermocouples, from 120 °C to 30 °C at an interval of 30 °C. For each calibration point, three sets of readings are taken and then averaged. The temperature reading is recorded when the following two conditions are met. First, the reference probe reading is stable, i.e. fluctuations are within tolerance of 0.05 °C for 1 minute. Second, the reference probe reading is accurate, i.e. the probe reading is within the setpoint temperature ± 0.05 °C.

After collecting the raw data, the variation of the standard known temperature with DAQ reading is plotted for each thermocouple using the calibration points. Next, a best fit line is plotted based on the calibration points, obtaining a best fit equation and R-squared value. The best fit equation provides the relationship between the temperature reading captured by the DAQ system and the known fluid temperature in which the thermocouple is immersed. For the purpose of illustration, the graph for the TC-J-01 thermocouple is shown in Figure A-1.

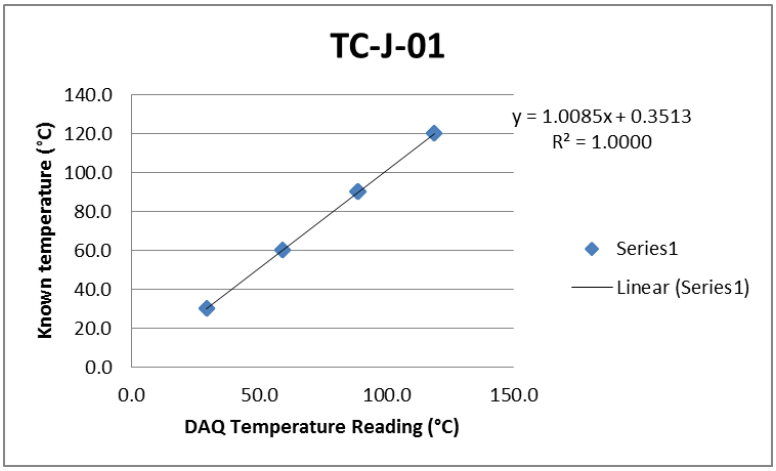

Figure A-1: Known temperature against DAQ reading for Type-J Thermocouple

The best fit equations for the Type-J thermocouples are then programmed into the LabVIEW software, such that it displays a more accurate temperature reading. In order to verify that the DAQ system works as intended, the thermocouples are immersed into the calibration bath and tested again. For a quick verification, the highest and lowest calibration points were sampled. The temperature readings provided by the DAQ system are found to be closer to the known temperature values than before, as shown in Figure A-2. This implies that the DAQ temperature readings are indeed more accurate after calibration.

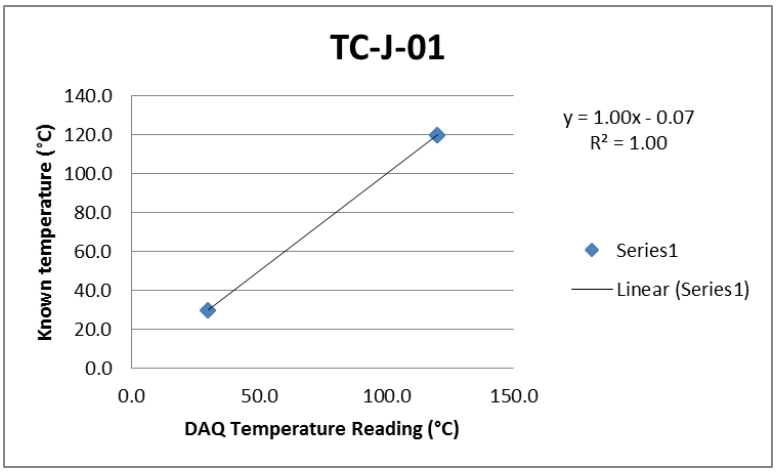

Figure A-2: Known temperature against DAQ reading for Type-J thermocouple after inputting the best fit equation

Calibration of Type-T thermocouples

Since the Type-T thermocouples are used to measure the temperature of liquid water only, the calibration points are different. Preliminary calculations suggest that the temperature range of water along the flow loop is 30 to 40 °C. Hence, the calibration points are chosen as: 85, 65, 45, 35 and 25 °C. The same procedure as described for the Type-J thermocouples was carried out for the Type-T thermocouples. For the purpose of illustration, Figure A-3 shows the variation of the standard known temperature with the DAQ reading, using the TC-T-01 thermocouple.

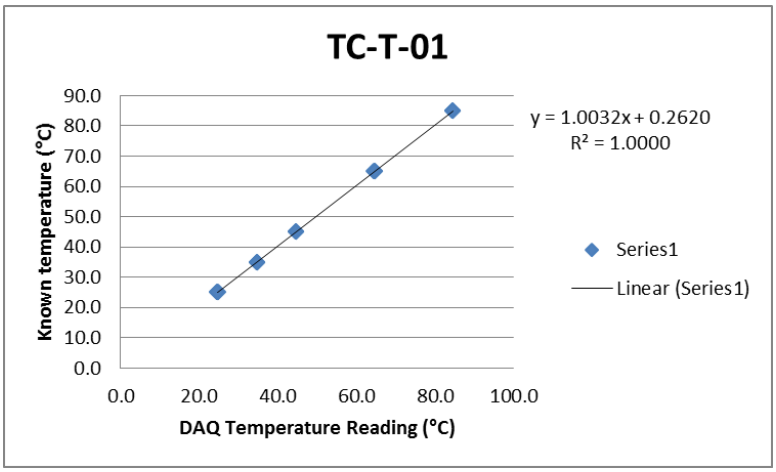

Figure A-3: Known temperature against DAQ reading for Type-T Thermocouple

After inputting the best fit equations into the LabVIEW software, the temperature readings provided by the DAQ system are found to be more accurate, as shown in Figure A-4.

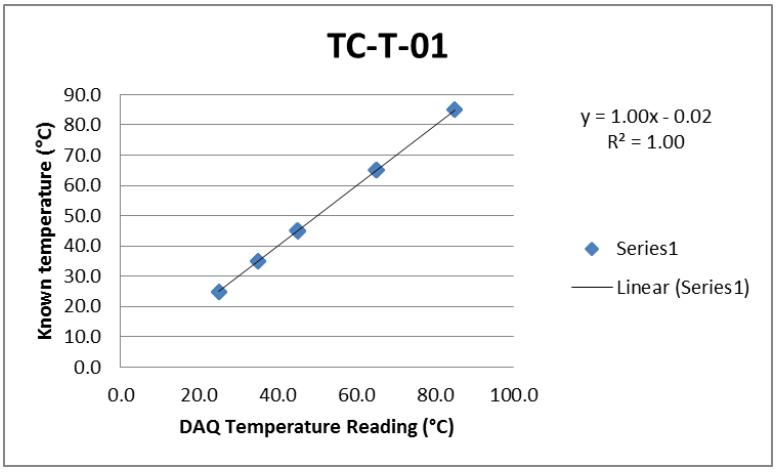

Figure A-4: Known temperature against DAQ reading for Type-T Thermocouple after inputting the best fit equation

Calibration of Pressure transducer

The pressure transducer to be calibrated is connected to its respective channel in the NI 9208 module, and calibration is carried out for the whole DAQ system. The pressure transducer to be calibrated is connected to the dead weight tester via a gauge connector. It is exposed to the pressurised gas inside the container, of which the pressure is known through the use of dead weights. Once the dead weights corresponding to a certain pressure level are purely supported by the pressurised gas, the pressure reading recorded by the pressure transducer is captured as a current output by the DAQ system.

After collecting the raw data, a graph of pressure against current is plotted for each pressure transducer using the calibration points. Next, a best fit line is plotted based on the calibration points, obtaining a best fit equation and R-squared value. The best fit equation provides the relationship between the current output reading of the DAQ system and the actual fluid pressure being measured by the pressure transducer. For the purpose of illustration, the graph for the PT-01 pressure transducer is shown in Figure A-5.

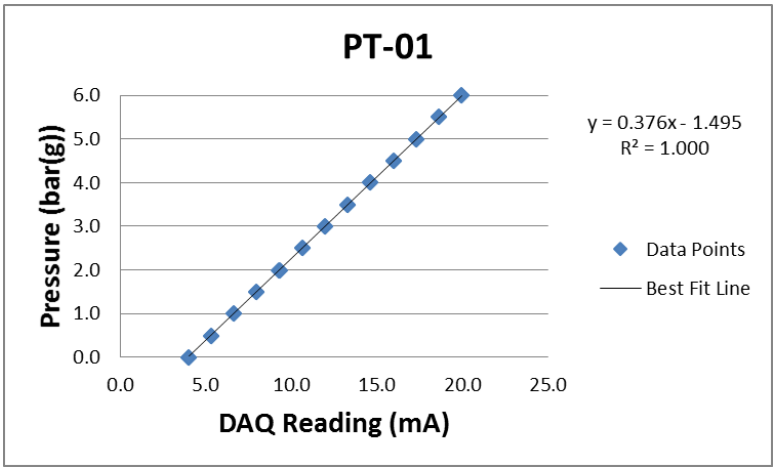

Figure A-5: Pressure-current relationship for the pressure transducers

The best fit equations for the pressure transducers are then programmed into the LabVIEW software, such that the screen displays the actual pressure readings. In order to verify that the system works as intended and the pressure transducers correctly measures the applied pressure load, the pressure transducer is again connected to the dead weight tester, and the procedure described above is repeated. Figure A-6 shows the graph of applied known pressure against the DAQ pressure readings. The results indicate that the pressure readings provided by the DAQ system are accurate.

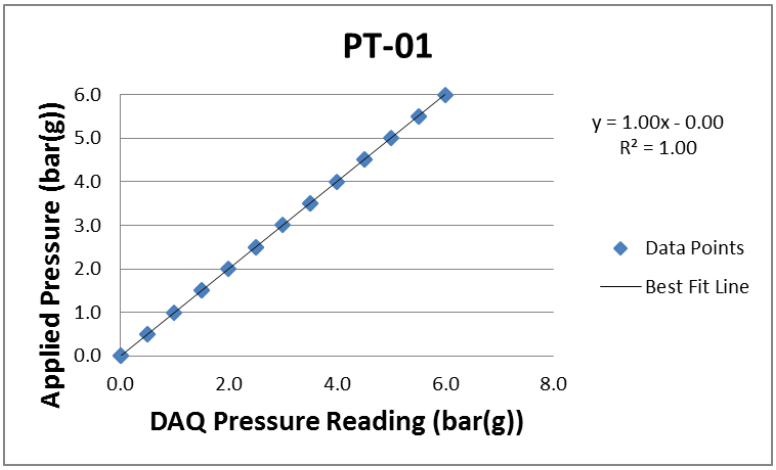

Figure A-6: Known pressure against DAQ pressure readings after inputting the best fit equation

Appendix B – Uncertainty Calculations

Uncertainty calculation for Type J thermocouple	
Sources of uncertainty	
- Maximum deviation from best fit line (maximum S.E.E.)	0.179
- Lack of repeatability due to unsteadiness	0.00631
Combined standard uncertainty	0.179
Expanded uncertainty (°C)	0.358

Uncertainty calculation for Type T thermocouple	
Sources of uncertainty	
Maximum deviation from best fit line (maximum S.E.E.)	0.0611
Lack of repeatability due to unsteadiness	0.000691
Combined standard uncertainty	0.0611
Expanded uncertainty (°C)	0.122

Uncertainty calculation for pressure transducer	
Sources of uncertainty	
Maximum deviation from best fit line (maximum S.E.E.)	0.00230
Lack of repeatability due to unsteadiness	0.000487
Combined standard uncertainty	0.00235
Expanded uncertainty (barg)	0.00470

Uncertainty calculation for flow meter	
Sources of uncertainty	
Uncertainty provided by calibration certificate (maximum)	0.1% of reading
Lack of repeatability due to unsteadiness	0.0000977 (negligible)
Combined standard uncertainty	0.1% of reading
Expanded uncertainty (L/min)	0.2% of reading

Uncertainty calculation for dimensions

Measuring Instrument	**Half-width *a* (mm)**	**Standard uncertainty (mm)**	**Expanded uncertainty (mm)**
Intec electronic internal micrometer	0.0005	0.000289	0.000577
Intec electronic calliper	0.005	0.00289	0.00577

Appendix C – Numerical Results for the Fish Scale Microchannels

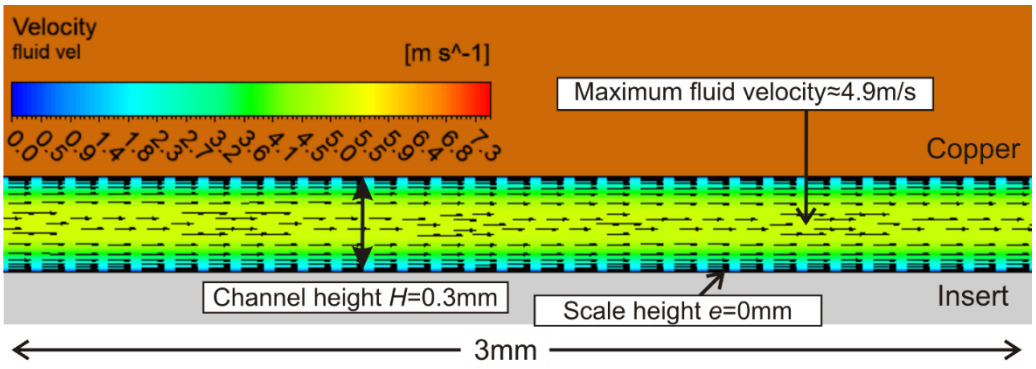

Figure C-1: Flow field of Plain microchannel at *Re* ≈ 2,664

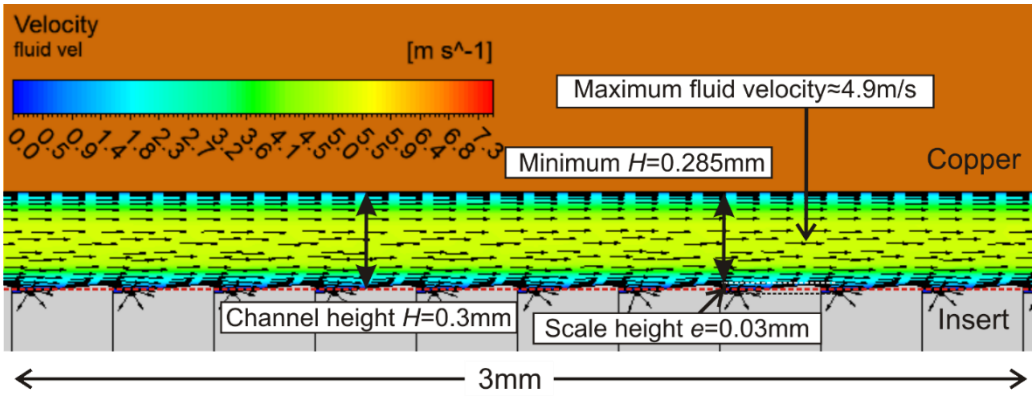

Figure C-2: Flow field of FS microchannel with *e*/*H* ratio of 0.1, at *Re* ≈ 2,664

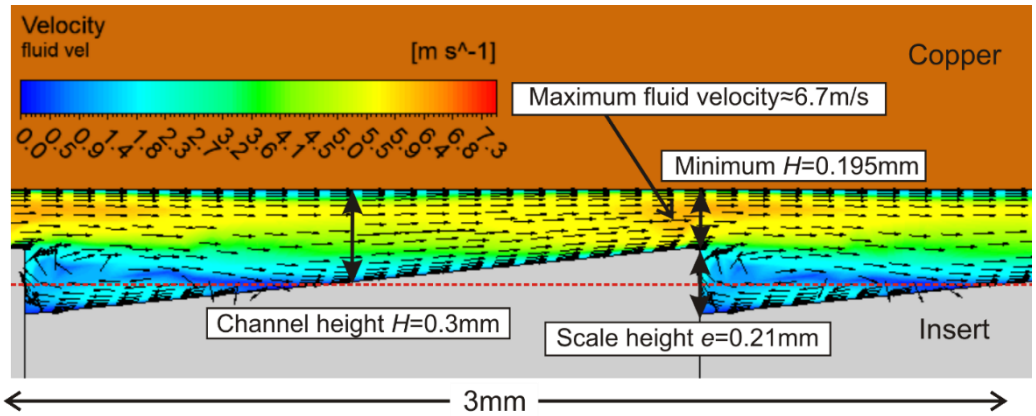

Figure C-3: Flow field of FS microchannel with *e*/*H* ratio of 0.7, at *Re* ≈ 2,664

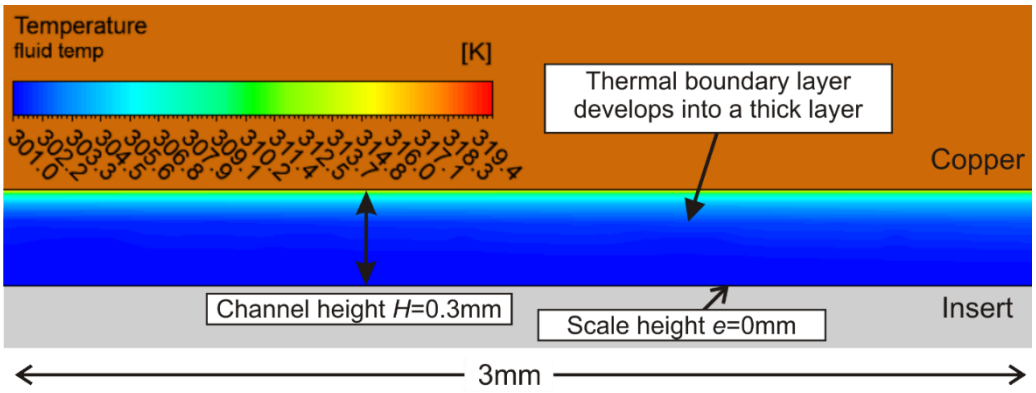

Figure C-4: Temperature distribution of Plain microchannel at *Re* ≈ 2,664

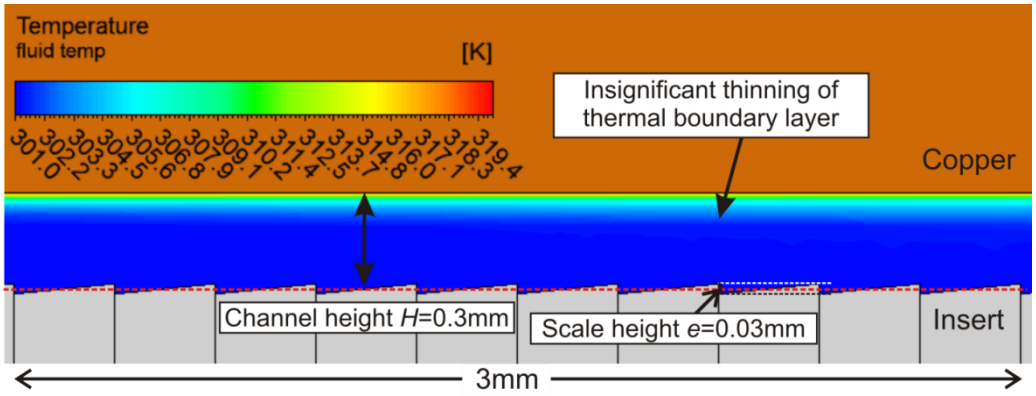

Figure C-5: Temperature distribution of FS microchannel with *e*/*H* ratio of 0.1, at *Re* ≈ 2,664

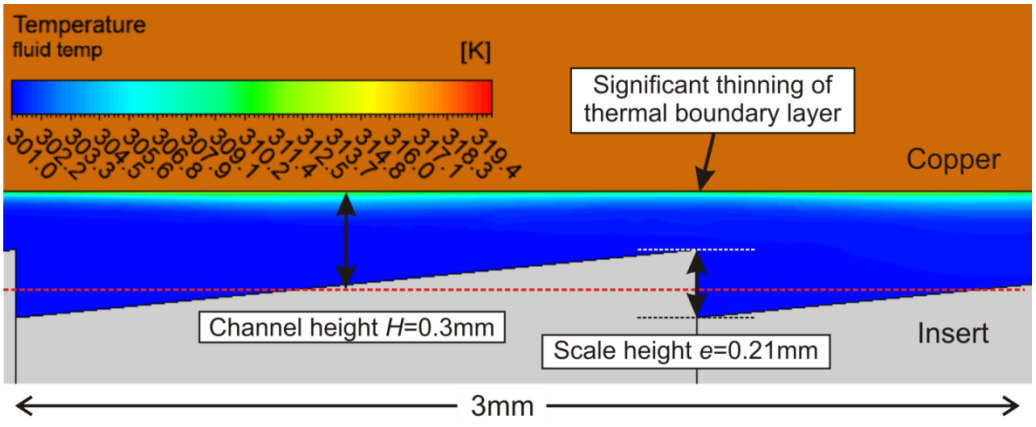

Figure C-6: Temperature distribution of FS microchannel with *e*/*H* ratio of 0.7, at *Re* ≈ 2,664

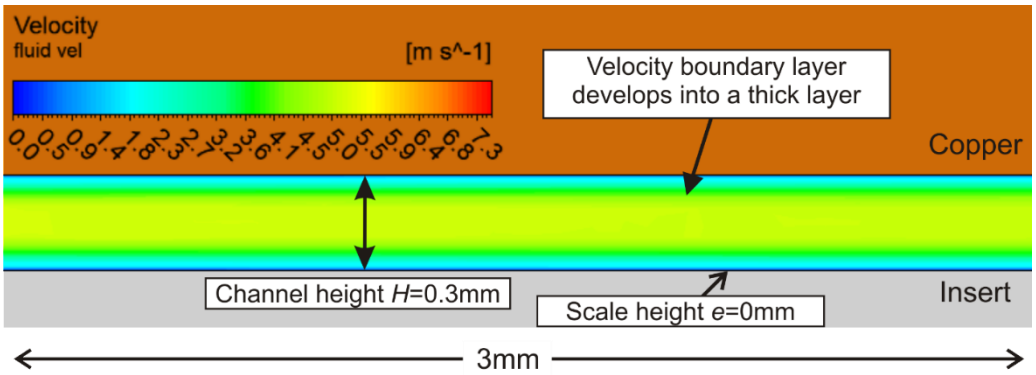

Figure C-7: Velocity distribution of Plain microchannel at *Re* ≈ 2,664

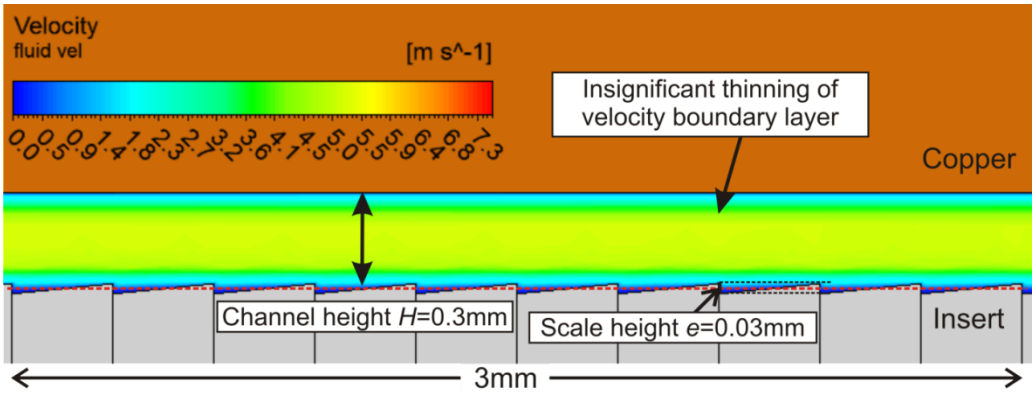

Figure C-8: Velocity distribution of FS microchannel with *e*/*H* ratio of 0.1, at *Re* ≈ 2,664

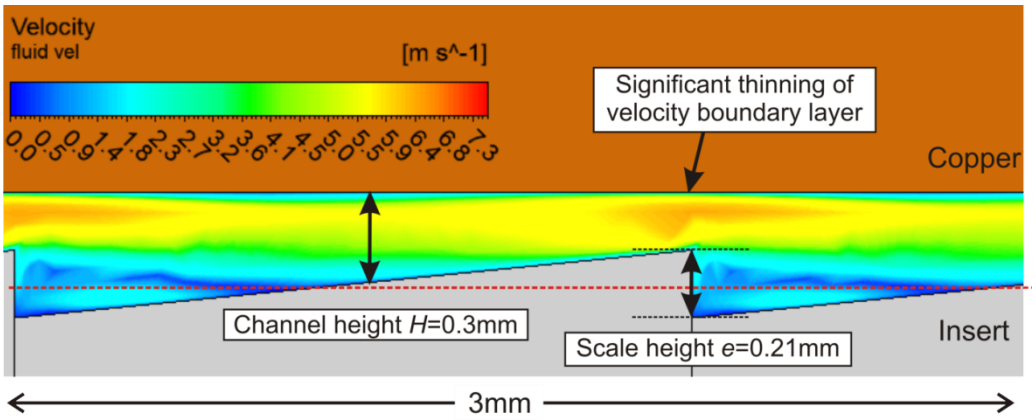

Figure C-9: Velocity distribution of FS microchannel with *e*/*H* ratio 0.7, at *Re* ≈ 2,664

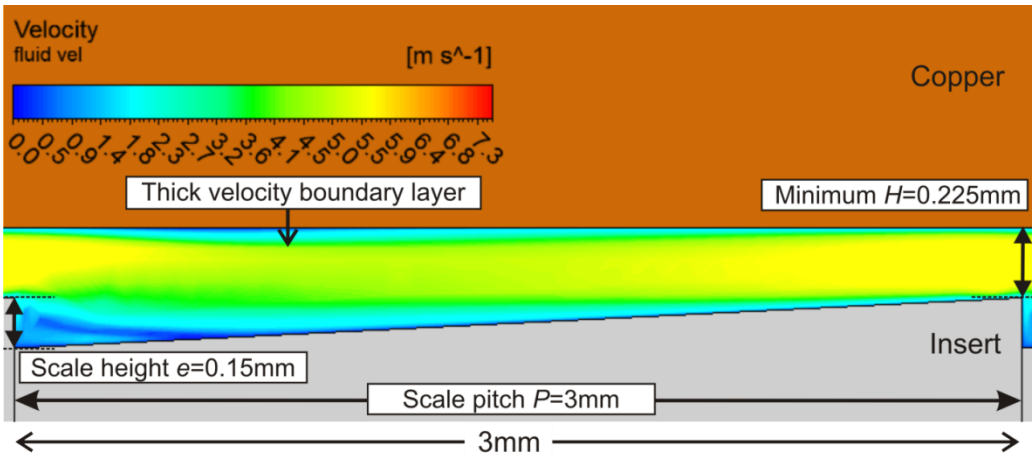

Figure C-10: Velocity distribution of FS microchannel with *P*/*e* ratio of 20, at *Re* ≈ 2,664

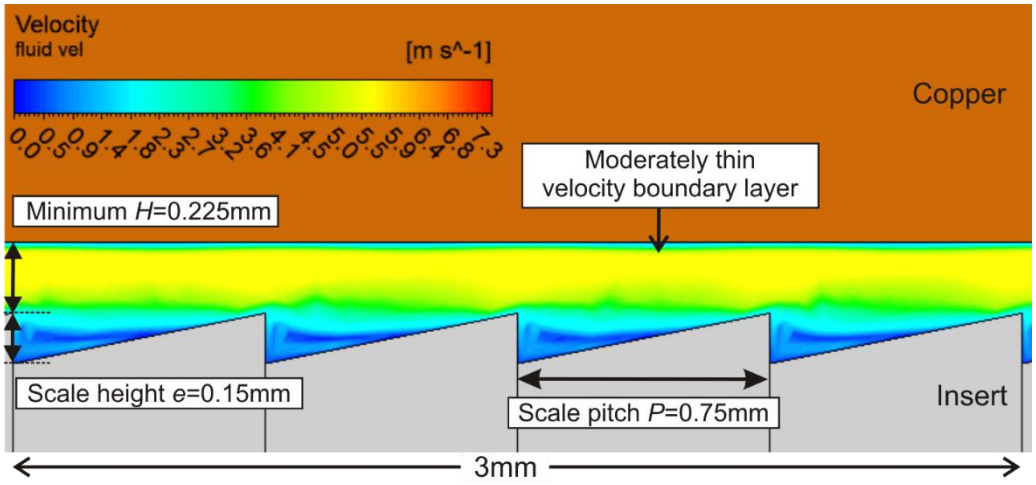

Figure C-11: Velocity distribution of FS microchannel with *P*/*e* ratio of 5, at *Re* ≈ 2,664

Appendix D – Numerical Results for the Durian Microchannels

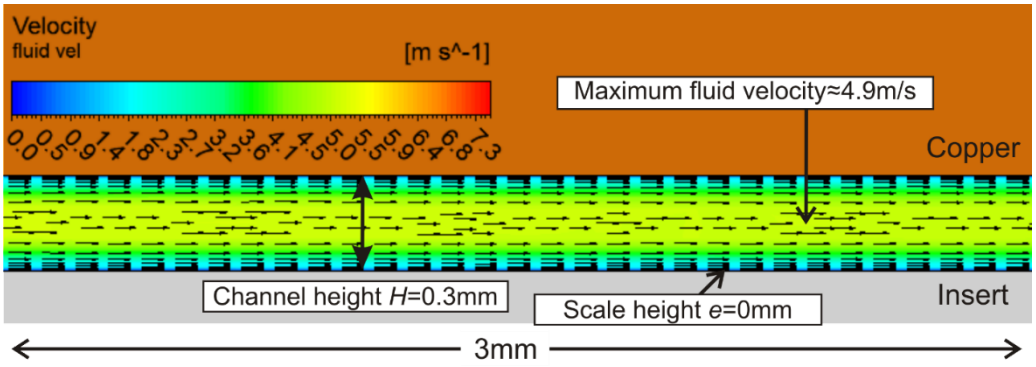

Figure D-1: Flow field of Plain microchannel at *Re* ≈ 2,664

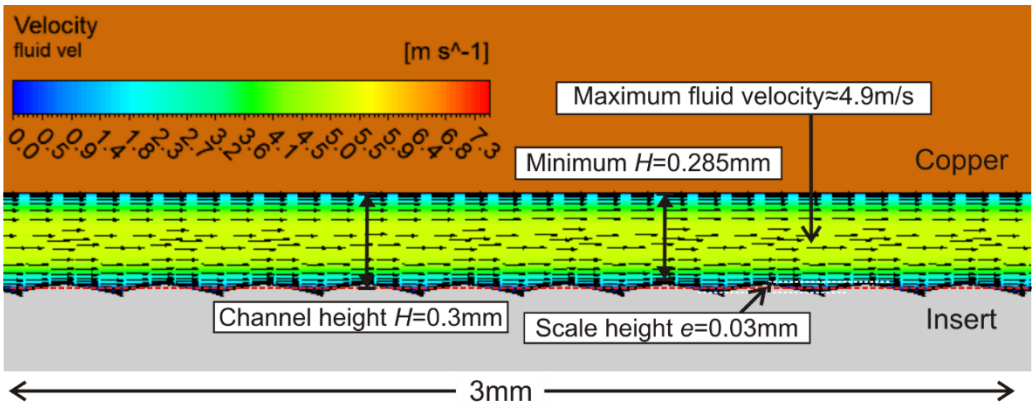

Figure D-2: Flow field of D microchannel with *e*/*H* ratio of 0.1, at *Re* ≈ 2,664

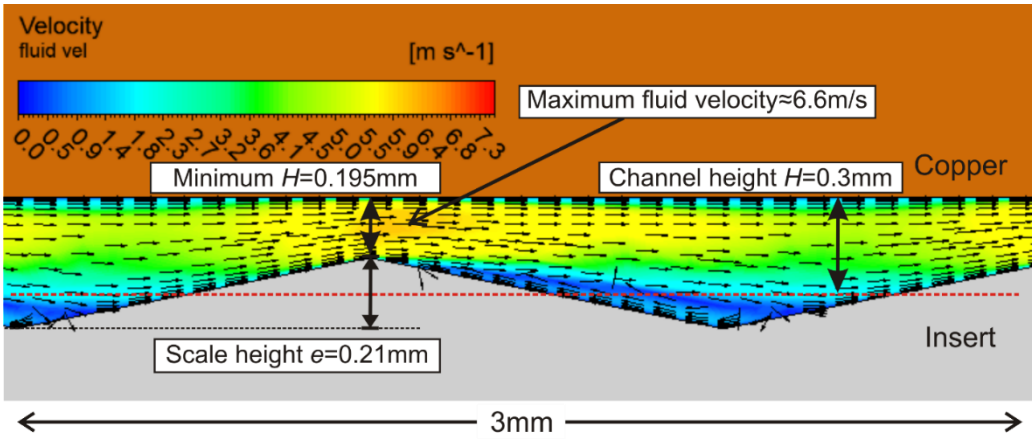

Figure D-3: Flow field of D microchannel with *e*/*H* ratio of 0.7, at *Re* ≈ 2,664

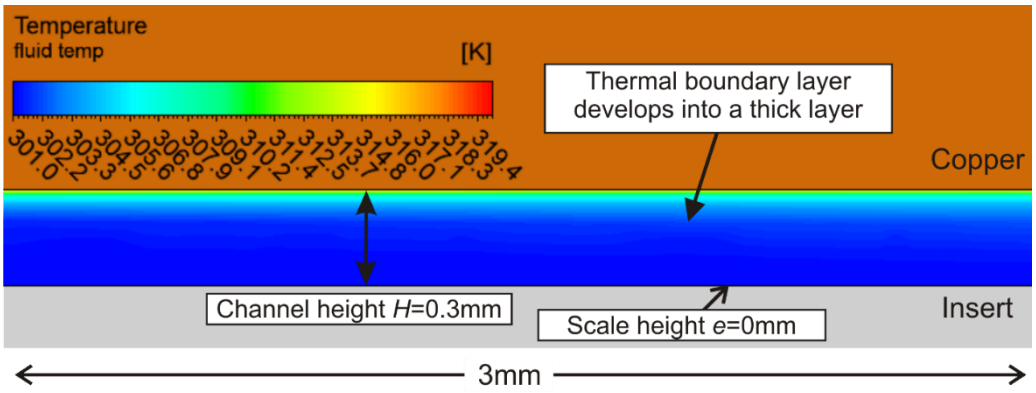

Figure D-4: Temperature distribution of Plain microchannel at *Re* ≈ 2,664

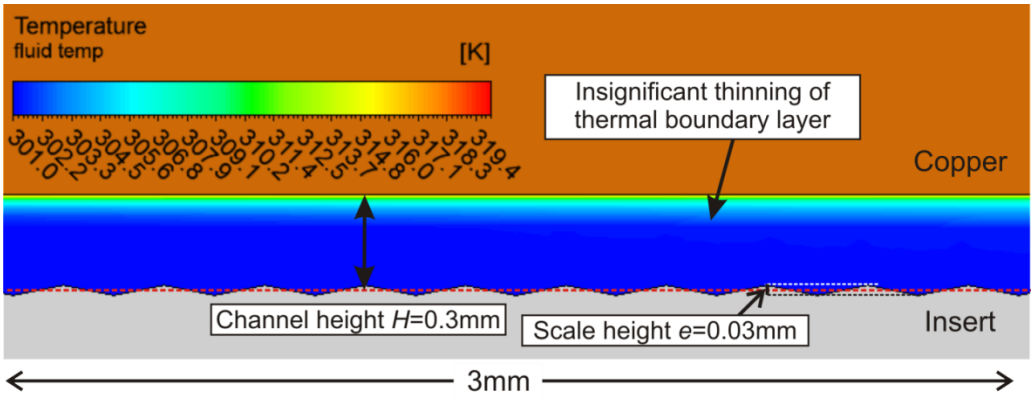

Figure D-5: Temperature distribution of D microchannel with *e*/*H* ratio of 0.1, at *Re* ≈ 2,664

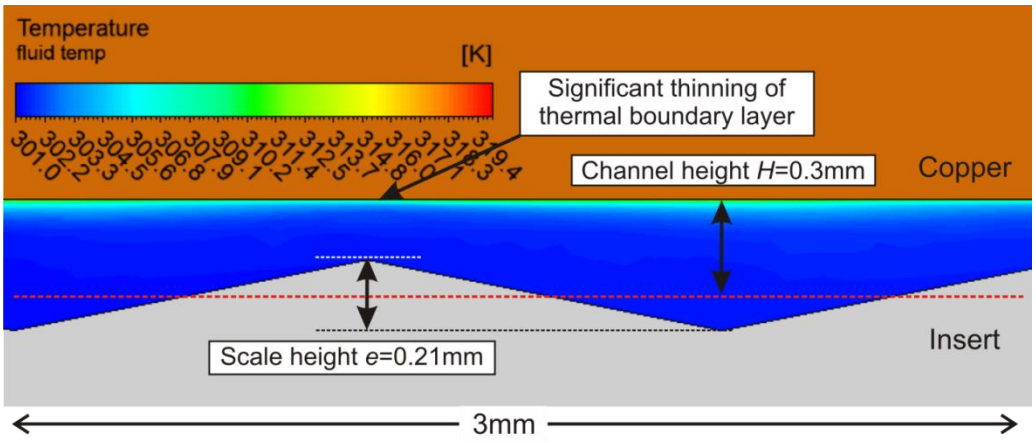

Figure D-6: Temperature distribution of D microchannel with *e*/*H* ratio of 0.7, at *Re* ≈ 2,664

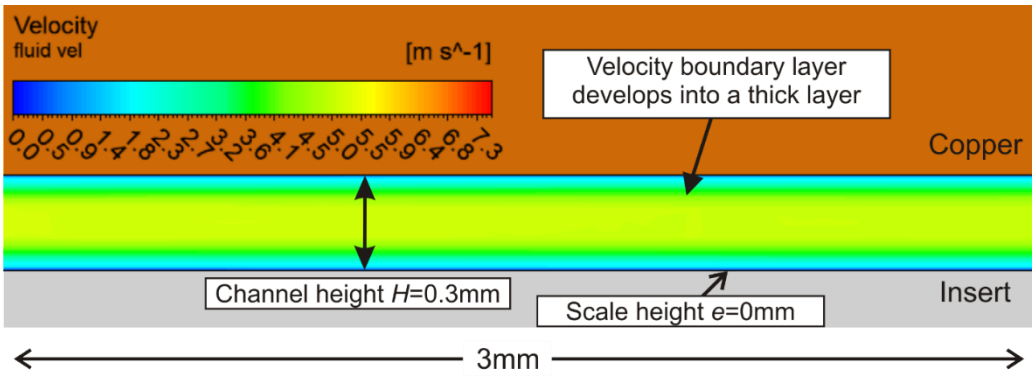

Figure D-7: Velocity distribution of Plain microchannel at *Re* ≈ 2,664

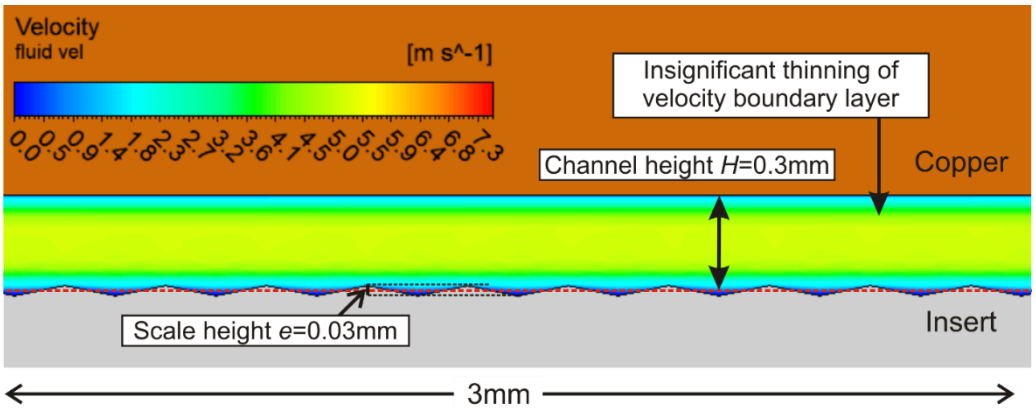

Figure D-8: Velocity distribution of D microchannel with *e*/*H* ratio of 0.1, at *Re* ≈ 2,664

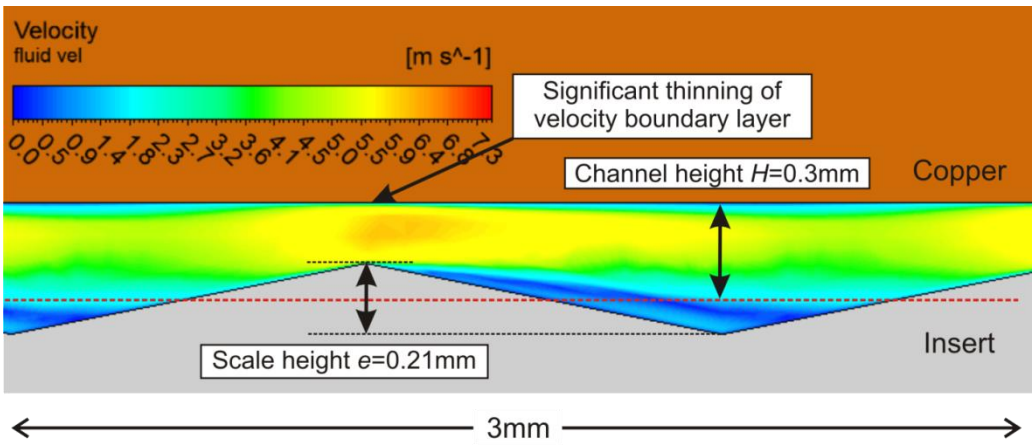

Figure D-9: Velocity distribution of D microchannel with *e*/*H* ratio 0.7, at *Re* ≈ 2,664

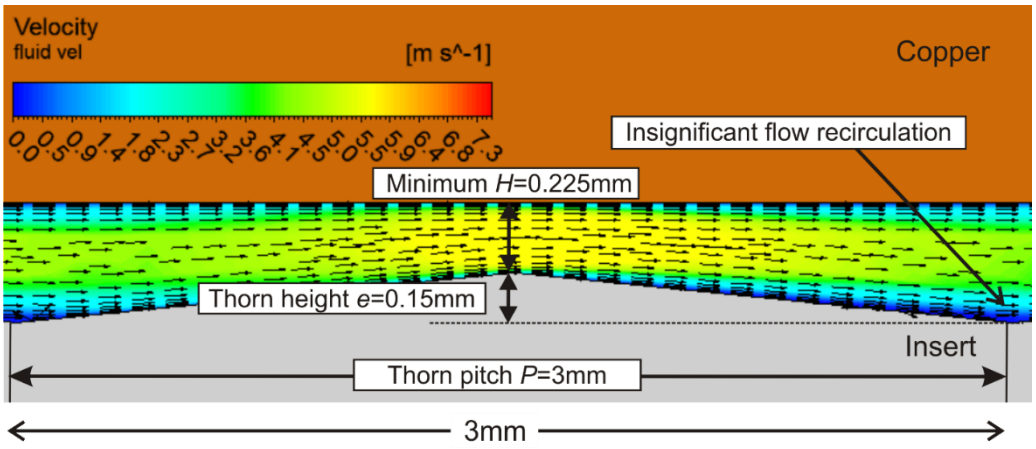

Figure D-10: Flow field of D microchannel with *P*/*e* ratio of 20, at *Re* ≈ 2,664

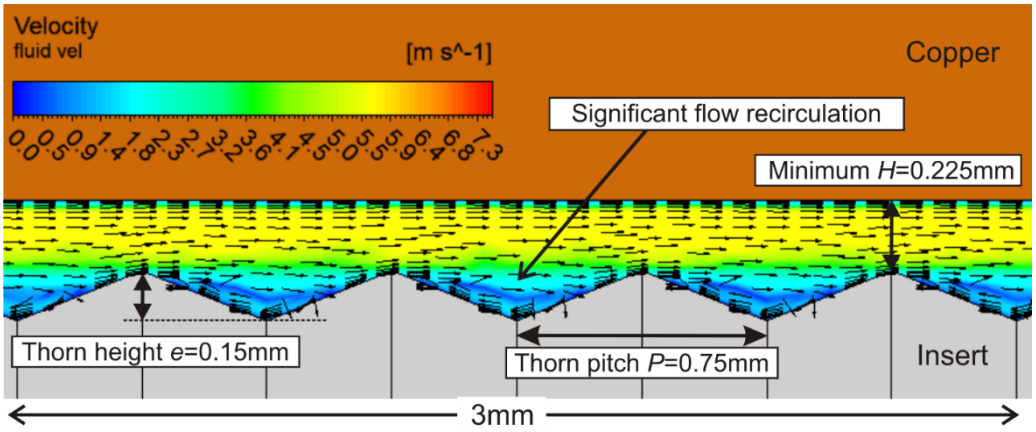

Figure D-11: Flow field of D microchannel with *P*/*e* ratio of 5, at *Re* ≈ 2,664

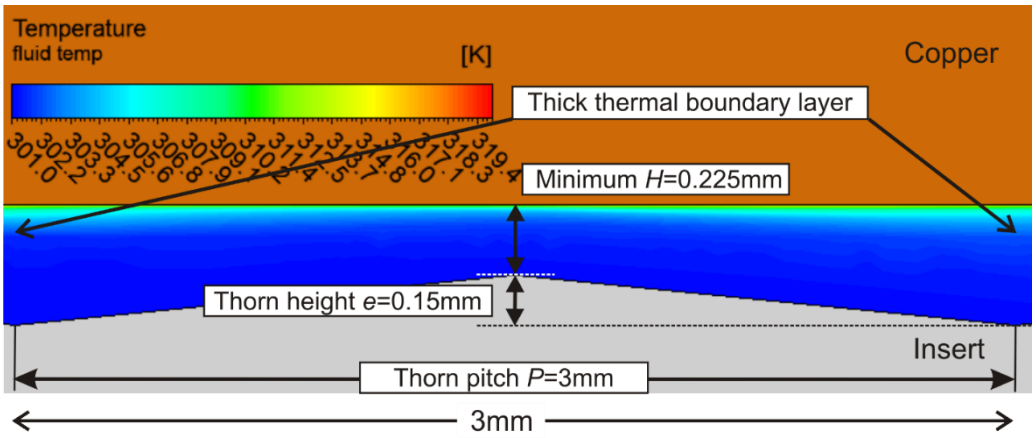

Figure D-12: Temperature distribution of D microchannel with *P*/*e* ratio of 20, at *Re* ≈ 2,664

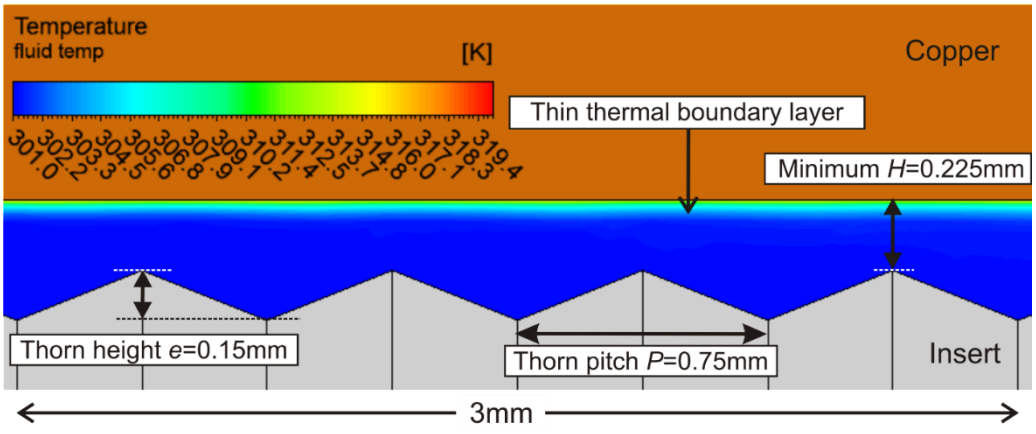

Figure D-13: Temperature distribution of D microchannel with *P*/*e* ratio of 5, at *Re* ≈ 2,664

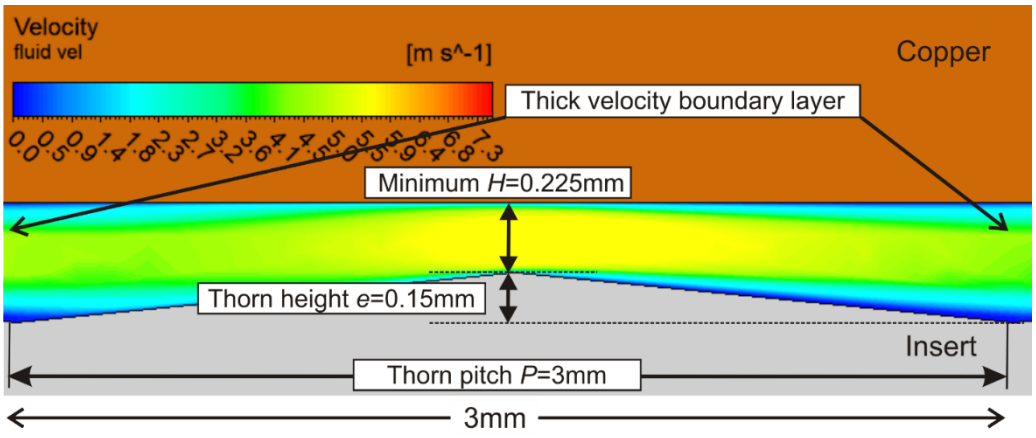

Figure D-14: Velocity distribution of D microchannel with *P*/*e* ratio of 20, at *Re* ≈ 2,664

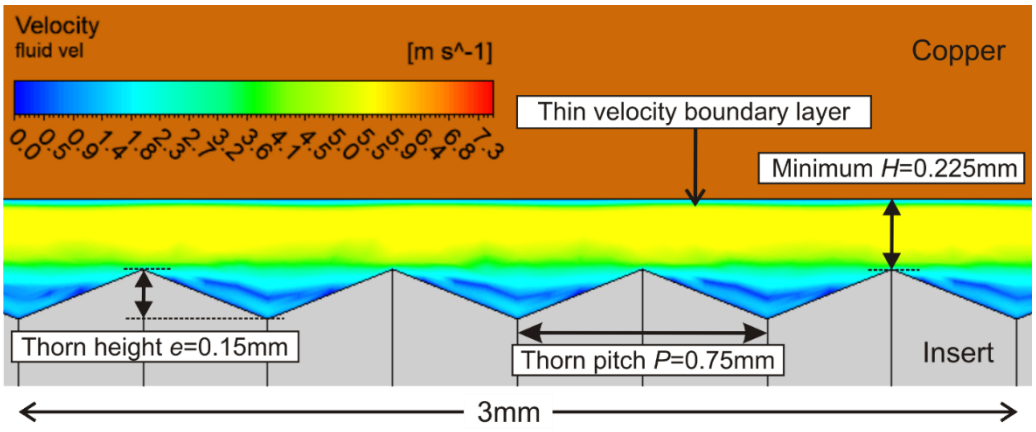

Figure D-15: Velocity distribution of D microchannel with *P*/*e* ratio of 5, at *Re* ≈ 2,664